Analysis of Potential Impacts of Climate Change and Deforestation on Surface Water Yields from the Mau Forest Complex Catchments in Kenya

By

Stephen Kibe Rwigi
I80/80641/2009
Department of Meteorology
School of Physical Sciences
University of Nairobi

A thesis submitted in fulfilment of the requirements for the degree of
Doctor of Philosophy (PhD) in Meteorology
Department of Meteorology
University of Nairobi

July 2014

DECLARATION

This thesis is my original work and has not been presented for a degree in any other university.

Signature………………………… ……….Date……………..

Stephen Kibe Rwigi

This thesis has been submitted for examination with our approval as University supervisors.

Signature………………………………… Date………………..

Prof. Nzioka J. Muthama

Department of Meteorology

University of Nairobi

Signature……………………….………….. Date……..…………..

Dr. Alfred O. Opere

Department of Meteorology

University of Nairobi

Dedication

To my dear father the late Mark Rwigi Senior who inculcated in me a desire for academic excellence but unfortunately did not live to see this day (may God bless his soul), my dear wife Lucy who has patiently been by my side providing moral support, my dear mother Sarah Warima for her love and prayers for me, my children Mark and Sarah for always keeping me on my toes and my niece Jacqueline for her faith in me.

Acknowledgement

The success of this PhD study would not have been realised without the support obtained from various individuals and institutions from within and outside Kenya. I therefore wish to unreservedly acknowledge those individuals and institutions who contributed in one way or another towards the successful completion of this study.

I am particularly grateful to the University of Nairobi for financial support in form of fees waiver and research grant through the Dean's Committee that enabled me undertake the study, and all the staff of the Department of Meteorology for creating an enabling environment during the entire period of this study. I am also specially grateful to my two supervisors and mentors Prof. Nzioka J. Muthama and Dr. Alfred O. Opere, both of the University of Nairobi, for their invaluable guidance and encouragement throughout the period of this study.

I also wish to make special mention to the following individuals and institutions and their respective staff for their contributions towards the completion of the study: Dr. Franklin Opijah of the University of Nairobi, who meticulously read the first draft of this report and made very useful suggestions, Dr. Francis Gichuki of the University of Nairobi, who introduced and guided me through the SWAT model, Dr. Philip A. Omondi of ICPAC, who introduced and guided me through PRECIS model, Dr. Wilson Gitau of the University of Nairobi who designed the necessary scripts for extraction of data from PRECIS outputs, the staff of the Department of Resource Survey and Remote Sensing (DRSRS) through Dr. James M. Kinyanjui, who made available landuse data from LANDSAT images, Kenya Meteorological Services (KMS) who provided observed climate data, UK Met Office who provided boundary data to run PRECIS model, Ministry of Water and Irrigation through Water Resources Management Authority (WRMA) who provided observed stream flow data, Kenya Soil Survey (KSS) who provided soil data, and Kenya Forest Service (KFS) who offered use of their facilities during the field trip. I also wish to sincerely thank all those not mentioned here but provided support in one way or another. Please accept my sincere thanks because there isn't enough space to list all of you. Your contribution is highly valued.

Last but not least I wish to appreciate most sincerely the patience and moral support from my dear wife Lucy and children, Mark Rwigi and Sarah Warima. Knowing that you always held me in your thoughts and prayer gave me the extra energy and courage to move on. Above all I am grateful to the Almighty God for it is His grace that has brought me this far.

ABSTRACT

This study focuses on an in-depth understanding of the extent to which climate change and deforestation impact on the surface water yields in the Mau forest complex, the largest of the five water towers in Kenya. The forest complex forms the source of important national and international rivers including Sondu, Nyando, the Nile, Mara and Ewaso Ng'iro which are economic life lines for three sectors of the country's economy: Tourism, Agriculture, and Energy. Demand for more arable land to support the area's growing population has led to large tracts previously preserved as gazetted forests being excised since late 1940s which has affected the hydrology of the water tower. The study analysed the past climate and forest cover changes and modelled future changes in climate and the extent to which these changes impact on the surface water yields in this region.

Potential impacts of climate change and deforestation on surface water yields were analysed using a modelling approach in which observed and projected climate outputs from a regional climate model, commonly referred to as PRECIS, which stands for Providing Regional Climate for Impacts Studies, and changes in forest cover were used to drive a hydrologic model, the Soil and Water Assessment Tool (SWAT). Outputs from SWAT were used to assess the impacts of changes in climate and forest cover on the surface water yields from the Mau forest complex water tower as exemplified by changes in river flow volumes. The study analysed historical climate, forest cover and streamflow changes that have taken place within these catchments with a focus on South West Mau forest block located within Sondu River basin. Projections of future climates under the Special Report on Emissions Scenarios (SRES) A2 emissions scenario were obtained from the third generation Hadley Centre Regional Climate model (HadRM3) using PRECIS regional climate model while Landuse/Landcover (LULC) changes were obtained from LANDSAT satellite image analysis using supervised classification methods.

It was shown from the analyses of historical data that the climate of the area has progressively become warmer and wetter since the 1970s. Analysis of temperature and rainfall indicated increasing trends while streamflow indicated a decreasing trend. Analysis of forest cover indicated increasing deforestation trends over the Mau forest complex of about 27% between 1973 and 2010. Analyses of mean daily maximum and minimum temperatures indicate that days and nights in this area have become warmer since the 1961-1990 baseline period by about 0.5°C and 0.4°C respectively. In the same period monthly rainfall distribution has shown increasing trends in the relatively dry DJF and SON seasons which have become wetter by about 7.5% and 9.2%

respectively, and decreasing trends in the relatively wet MAM and JJA seasons which have become drier by about 2.2% and 4.5% respectively. The changes in the distribution of monthly rainfall translate into redistribution of seasonal water yields from the catchments.

Analysis of projected temperature and rainfall shows strong indications that the climate of the area will significantly change in future under the SRES A2 emissions scenario with warmer and wetter climates being experienced by 2030 and beyond. The annual average temperatures and rainfall are expected to change by about 2.7°C and 4.7% respectively by 2030, and by 4.7°C and 18.9% respectively by 2050, relative to the baseline. The projected monthly rainfall distribution show increasing trends in the relatively dry DJF and SON seasons while showing decreasing trends in the relatively wet MAM and JJA seasons.

Simulated water yields under climate change at the baseline forest cover scenario show an increasing trend but show decreasing trends as forest cover over South West Mau forest block diminishes. Projected water yields in 2010s and 2030s indicate a decreasing trend in potential water yields of about 0.69 MCM/yr in 2010s and 0.71 MCM/ yr in 2030s

Results of the study indicate that indeed deforestation of the Mau forest catchment has notable impacts on water yields from the water tower. The study has shown that the overall impacts of climate change coupled with deforestation on the water yielding capacity of the Mau forest catchments will be a reduction in the potential annual water yields in the range of 15% and 16% per decade of the baseline yields to between 28% and 45% in 2010s and between 31% and 50% in 2030s respectively.

Results of this study have provided useful insights into the impacts of climate change and deforestation on surface water yields which can be used to inform short, medium to long term planning of water resources. The results, methods and products of the study should be incorporated in the mainstream economic development strategies especially in the development of the national water resources master plan. To ensure adequate flow in rivers from this important water tower to sustain both the socio-economic and environmental uses, it is recommended that efforts to rehabilitate the Mau forest complex be stepped up and sustained.

TABLE OF CONTENTS

LIST OF TABLES

LIST OF FIGURES

LIST OF EQUATIONS

LIST OF ABBREVIATIONS AND SPECIAL TERMS

AGRR	Agricultural Land Row Crops
ArcGIS	Geographic Information System for Working with Maps
ASALs	Arid and Semi-Arid Lands
AWC	Available Soil Water Capacity
BCM	Billion Cubic Meters
Blai	Maximum Potential Leaf Area Index
CANMX	Maximum Canopy Storage
CCC	Climate Change Cell
CMS	Catchment Management Strategy
CN	Curve Number
CO_2	Carbon Dioxide
DEM	Digital Elevation Model
DRSRS	Department of Resource Surveying and Remote Sensing
DMS	Dimethyl Sulphate
ECHAM4	European Community Hamburg Model Version 4
ENSDA	Ewaso Ng'iro South Development Authority
ECMWF	European Centre for Medium Range Weather Forecast
ERA-40	ECMWF Re-Analysis of 40 years
Esco	Soil Evaporation Coefficient
ETM	Enhanced Thematic Mapper
ETM+	Enhanced Thematic Mapper Plus
ET	Evapotranspiration
FAO	Food and Agriculture Organisation
FC	Field Capacity
FRSD	Open Forest
FRSE	Evergreen Forest
GCM	Global Climate Model
GDP	Gross Domestic Product
GIS	Geographical Information System
GOK	Government of the Republic of Kenya
GWD	Gravity Wave Drag

GUI	Graphical User Interface
HadCM3	Hadley Centre Coupled Model Version 3
HadRM3	Hadley Centre Regional Climate Model Version 3
HadAM3P	Hadley Centre Atmosphere only Model Version 3P
HRU	Hydrological Response Unit
IHP	International Hydrological Programme
IYF	International Year of Fresh Water
ICWE	International Conference on Water and the Environment
IVM	Institute for Environmental Studies
IPCC	Intergovernmental Panel on Climate Change
ISRIC	International Soil Reference and Information Centre
ITCZ	Inter Tropical Convergence Zone
JICA	Japan International Cooperation Agency
JJA	June-July-August
KARI	Kenya Agricultural Research Institute
KENSOTER	Kenya Soil and Terrain
KIFCON	Kenya Indigenous Forest Conservation Programme
KSS	Kenya Soil Survey
KFWG	Kenya Forest Working Group
KMS	Kenya Meteorological Service
KWS	Kenya Wildlife Service
KWTA	Kenya Water Towers Agency
LANDSAT	Land Satellite
LAI	Leaf Area Index
LVB	Lake Victoria Basin
LBC	Lateral Boundary Conditions
LBDA	Lake Basin Development Authority
LH	Latin Hypercube
LH-OAT	Latin Hypercube and One-Factor-At-A-Time
LLGHG	Long-Lived Greenhouse Gases
LVSCA	Lake Victoria South Catchment Area
LULC	Landuse / Landcover
MAM	March-April-May

MFC	Mau Forest Complex
MDG	Millennium Development Goals
MSS	Multi-spectral Scanner System
MW	Mega Watts
NASA	National Aeronautical and Space Administration
NCEP	National Centre for Environmental Prediction
NE	North East
NGA	National Geospatial-Intelligence Agency
NRCS	National Resource Conservation Service
NSE	Nash-Sutcllife Efficiency
OAT	One-Factor-At-A-Time
OAGCM	Ocean Atmosphere Global Climate Model
PAST	Pasture
PCPD	Precipitation Days in a Month
PCPMM	Mean Monthly Precipitation
PCPSKW	Skew Coefficient of Daily Precipitation in a Month
pcpSTAT	Precipitation Statistics software
PCPSTD	Standard Deviation of Daily Precipitation in a Month
PET	Potential Evapotranspiration
PBIAS	Percentage Bias
PRECIS	Providing Regional Climate for Impact Studies
PR_W1	Probability of a wet day following a dry day
PR_W2	Probability of a wet day following a wet day
RGB	Red-Green-Blue
RMSE	Root Mean Square Error
RNGE	Range Grass
RSR	Ratio of Root-Mean-Square Error to the Standard Deviation
RCM	Regional Climate Model
RF	Radiative Forcing
RGS	River Gauging Station
RH	Relative Humidity
SBC	Surface Boundary Conditions
SCS	Soil Conservation Service

SON	September-October-November
SOTER	Soil Terrain
SO_4	Sulphate Particles
SO_2	Sulphur Dioxide
Sol_Z	Depth from the soil surface to the bottom of layer
SRES	Special Report on Emissions Scenarios
SRTM	Shuttle Radar Topography Mission
SS_E	Sum of Square Errors
SS_T	Total Sum of Squares
SST	Sea Surface Temperature
SWAT	Soil and Water Assessment Tool
TM	Thematic Mapper
TM^+	Thematic Mapper Plus
TMPMN	Mean Monthly Minimum Air Temperature
TMPMX	Mean Monthly Maximum Air Temperature
TMPSTDMN	Standard Deviation of Daily Minimum Temperature in a Month
TMPSTDMX	Standard Deviation of Daily Maximum Temperature in a Month
UK	United Kingdom
UN	United Nations
UNDP	United Nations Development Programme
UNEP	United Nations Environment Programme
UNESCO	United Nations Educational, Scientific and Cultural Organization
UNFCCC	United Nations Framework Convention on Climate Change
USA	United States of America
USDA	United States Department Of Agriculture
USGS	United States Geological Survey
UTC	Coordinated Universal Time
UTM	Universal Transverse Mercator
WATR	Water
WCMC	World Conservation Monitoring Centre
WMO	World Meteorological Organisation
WP	Permanent Wilting Point
WRMA	Water Resources Management Authority

CHAPTER 1

INTRODUCTION

1.1 Background

Water is an essential component in all aspects of our life (IPCC 2007). It is an economic as well as a social good that pervades all human activities and undoubtedly one of the most important natural resources for man's survival. Besides being a vital ingredient for the maintenance of the natural ecosystems on which we ultimately depend for existence, water is a key driver of human economic productivity, societal development, and social well-being (Young, 2009). It is also an important catalyst necessary to accelerate both economic and social development of a nation (GOK, 1999).

During the last century freshwater has become increasingly limited by an ever increasing demand resulting from the rapid growth in population, unsustainable use, and increasing incidences of pollution due to emissions from anthropogenic activities. Warning of freshwater scarcity issued at the close of the twentieth century has become a reality to the extent of insufficient freshwater which now threatens food security, livelihoods and human health (Liebscher, 2009).

Climate change observed over the last several decades affects freshwater through a number of mechanisms as it is closely linked to changes in a number of components of the hydrological systems such as changing precipitation patterns, intensity and extremes of climatic indicators such as temperature and rainfall, increasing atmospheric water vapour content, increasing rate of evaporation, changes in soil moisture levels, and runoff (Bates *et al*, 2008). The interaction between human, environment and natural resources such as water is vital for life support but can also be a potential hazard like floods and droughts. Thus hydrological knowledge in relation to climate change is valuable in providing for man's continuity and well being (WMO, 2008).

Provision of adequate water for both domestic and agricultural use would significantly reduce the poverty levels by addressing the Millennium Development Goal (MDG) of development and environmental sustainability which seeks to minimise hunger and famine (UNEP, 2009a). This particular MDG recognises the fact that issues of degraded environment and the declining health of water resources increase the gap between the rich and the poor with poverty levels remaining high and the inequalities continuing to grow (Liebscher, 2009). At the national level, Kenya has incorporated this MDG in its new development blue print, Vision 2030, which covers the period

2008 to 2030 with the aim of steering Kenya to a middle income nation providing high quality life for all its citizens by the year 2030 (GOK, 2007; GOK, 2010a).

Kenya is a water scarce country with only 647 m^3 per capita of water against the global benchmark of 1000 m^3 (WRMA, 2009; Mogaka *et al*, 2006). With the projected population of about 56 million by the year 2030, the amount of water available per capita will reduce to about 359 m^3 if no measures are taken to increase and secure the water resources in the country (WRMA, 2009).

Vision 2030 is based on three pillars of development namely the economic, social and political pillar. This study seeks to address the social pillar of the vision which seeks, among other things, to build a just and cohesive society with social equity in a clean and secure environment (GOK, 2007). The study focuses on two out of the eight sectors that fall under this pillar: water and sanitation which aims to ensure that improved water and sanitation are available and accessible to all; environment through which Kenya aims to be a nation living in a clean, secure and sustainable environment by the year 2030 through increased forest cover from below 3% to about 10%.

The environment sector of the vision's social pillar also aims at improving the capacity for adaptation to global climate change where some of the flag ship projects include the water catchment management initiative which encompasses the rehabilitation of the country's five water towers: Mau Forest Complex, Mt Kenya, Aberdare Ranges, Cherengani Hills and Mt Elgon. This study seeks to understand how climate change and deforestation impact on water yields from forested catchments with particular reference to the Mau Forest Complex water tower, since water is a critical factor of these two sectors of the social pillar (GOK, 2002; GOK, 1999**).**

1.2 Problem Statement

Mau Forest Complex (MFC) is Kenya's largest indigenous forest and the largest of the five water towers in the country with more than twelve rivers originating from it (KWTA, 2013). The forest complex is endowed with a rich diversity of resources ranging from direct forest products, water supply, tourism, and micro-climate regulation (KIFCON, 1994). However, despite its national and international importance as a natural resource, the forest complex has been widely deforested (Kinyanjui, 2010).

Demand for more land suitable for tea farming, settlement and other agricultural activities has led to large tracts previously preserved as gazetted forests for purposes of water conservation and regulation, being excised since late 1940s (Kinyanjui, 2009; Edwards and Blackie, 1979). Conducive conditions for rain fed agriculture, fertile soils, and ample rainfall in the area have attracted a rapidly growing population that has encroached the forest reserve.

Experts have warned that continued destruction of this vital water tower will cause environmental disaster resulting in reduced rainfall and drying up of rivers in the region. This is likely to cause a water crisis of national and international proportions that could extend far beyond the Kenyan territory (Baldyga *et al,* 2007). The extensive destruction of MFC water tower is therefore a matter of national concern as it presents real economic threats and underlies a breakdown of law and order with ramifications for internal security and conflict (GOK, 2010a).

Analysis of 50-year daily discharge data for the rivers in the LVSCA shows significant variations in high and low flows during wet and dry seasons respectively. The flash flood incidents have continued to increase during wet seasons and base flows have continued to decrease during dry seasons (WRMA 2009). Changes in flow regimes of rivers from this water tower have resulted in heightened tensions among various water users with regard to reduced water yields during the dry seasons. Continued degradation of this critical watershed coupled with the effects of climate change is likely to worsen conflicts over this vital natural resource and this is a major source of concern for policy makers (UNEP/GOK, 2008; Mogaka *et al*, 2006).

The causes of the problem of water yields in the area of study can be attributed to global, local or both systems; global because of changes in the water cycle as a result climate change and variability and local because of changes in the forest cover (Bates *et al,* 2008; Muhati *et al,* 2008; Kundzewicz *et al*, 2007). The problem can be solved by first understanding the impacts of climate change (global) and deforestation (local) on water yields as set out in the objective of this study.

1. 3 Objectives of the Study

The overall objective of this study is to analyse the potential impacts of climate change and deforestation on surface water yields from the Mau Forest Complex water tower by the year 2050. Specific objectives used to achieve the broad objective are:

i. To determine the trends in observed rainfall, temperature, stream flow and forest cover between 1961 and 2010

ii. To simulate temperature and rainfall for the periods 1961-1990, 2001-2030 and 2021-2050 under the Special Report on Emissions Scenarios (SRES A2) and analyse the trends

iii. To simulate streamflow for the periods 1961-1990, 2001-2030 and 2021-2050 under different climate and forest cover scenarios and analyse the trends

iv. To conduct sensitivity analysis using rainfall and forest cover changes on the hydrological regime of the catchment to determine their impacts on surface water yields

1.4 Hypothesis

If the amount of rainfall that transforms into runoff is determined by the level of forest cover, then deforestation in the Mau forest complex water catchments will lead to changes in flow volumes in rivers that originate from these catchments under different climate change scenarios.

1.4.1 Assumptions

The underlying assumptions in this study include:

i. Observed climatic and forest cover trends influence trends in water yields from catchment areas

ii. Simulated rainfall and climatic conditions have the same statistical characteristics observed and influence water yields from the catchment areas

iii. Simulated stream flow has the same characteristics as the observed stream flow

iv. Changes in streamflow in the Sondu catchment area are applicable to other catchment areas whose upper catchments comprise the Mau forest complex

1.5 Conceptual Framework of the Study

Rainfall, the ultimate source of freshwater, is a function of a combination of several factors: air temperature, wind patterns, moisture content in the atmosphere, etc. Condensation of atmospheric moisture which originates from vapour evaporated mainly from the oceans and other continental water bodies such as lakes and rivers as well as evapotranspiration from forest and other ground vegetation cover is the source of rainfall. The moisture from the oceans and other sources is distributed horizontally to various parts of the world by the global and regional wind patterns which can be modelled by global and regional climate models respectively.

The atmospheric moisture contents as well as the wind patterns are likely to change with the rising global temperatures and with the ongoing deforestation thus affecting the timing, distribution and possibly the quantity of fresh surface water that is available for various uses. In order to analyse the impacts of climate change on the water yields from the area of study, a modelling approach proposed by Di Baldessarre *et al* (2011) was adopted. The approach was (i) to choose a scenario from the Intergovernmental Panel on Climate Change (IPPC) Special Report on Emissions Scenarios (SRES); in this study, SRES A2 was chosen, (ii) to choose a global circulation model from which to downscale climate scenarios; in this study, (HadAM3) and (ECHAM4) were chosen, (ii) to downscale the GCM climate output (rainfall and temperature) to the river basin scale (Sondu) using a regional climate model; in this study, PRECIS (providing regional climates for impacts studies) regional climate model was used, (iv) to use the downscaled GCM outputs as inputs to a hydrological model; in this study, rainfall and temperature outputs from PRECIS were used as inputs to the Soil and Water Assessment Tool (SWAT) hydrological model under different land cover scenarios, and (v) to analyse the hydrological model (SWAT) results by comparing them to the corresponding results related to the baseline climate and land cover scenario (Figure 1.1).

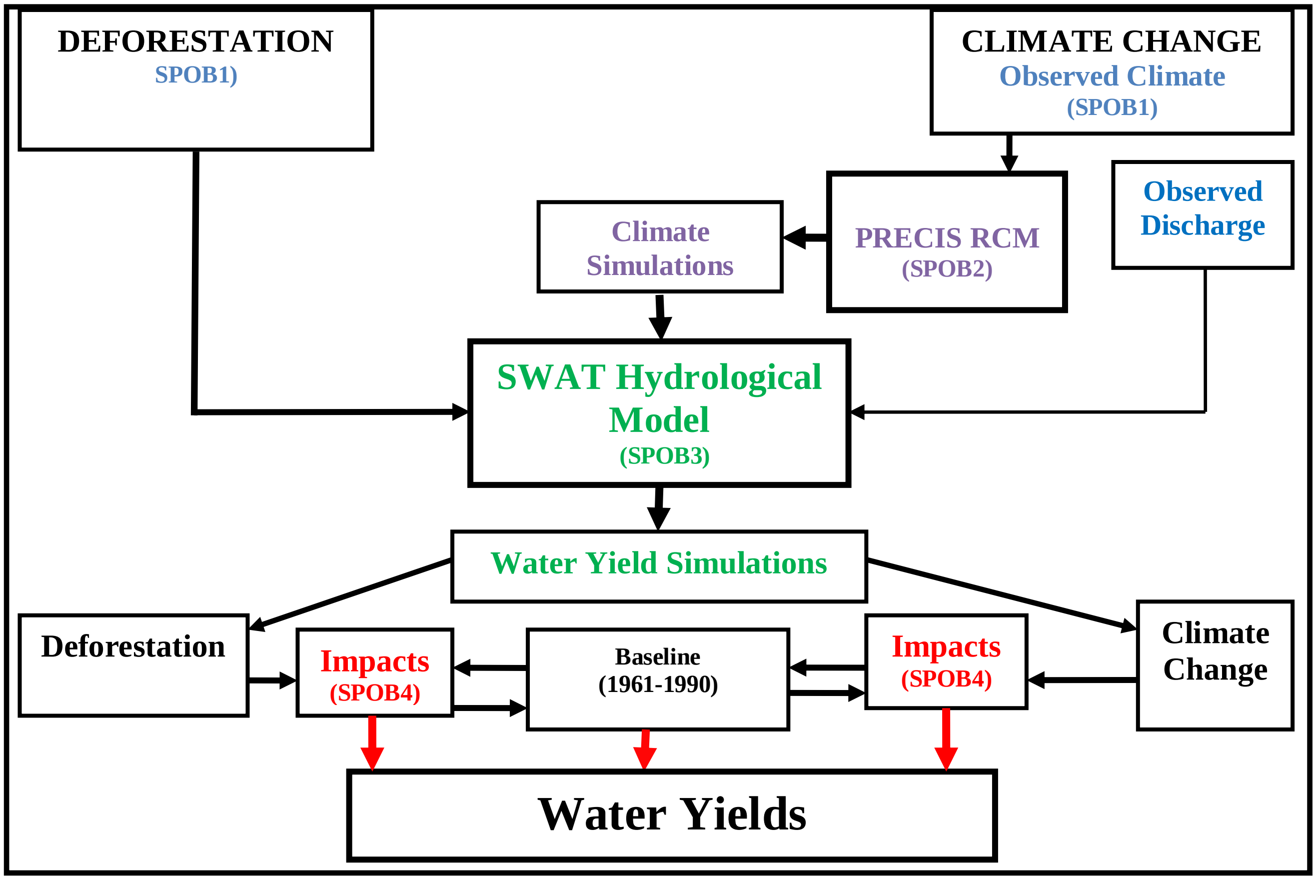

Figure 1.1: Flow chart of the study procedure showing critical stages in the study where SPOB1, SPOB2, SPOB3, and SPOB4 stand for specific objectives 1, 2, 3, and 4 respectively

Figure 1.1 shows the logical framework of the study. PRECIS regional climate model was used to simulate 30-year climates at daily time-steps for the periods 1961-1990, 2001-2030, and 2021-2050 from which the past, current and projected climates of the Mau forest catchment areas could be described. Climate outputs from PRECIS regional climate model were calibrated using the observed baseline climate. Calibrated PRECIS outputs were then used as inputs to the SWAT hydrologic model. Observed discharge data from the catchment were used to calibrate the SWAT model input parameters. Outputs from the calibrated SWAT model under different climate and forest cover scenarios were then used to determine the impacts of climate change and deforestation on surface water yields for the periods 2001-2030 and 2021-2050 relative to 1961-1990 yields.

1.6 Justification of the Study

The Mau Forest Complex (MFC) ecosystems are important drivers of Kenya's economy as they provide invaluable ecological services in terms of river flow regulations, flood mitigation, water storage, recharge of ground water, and micro-climate regulations. The forest complex forms the source of important international rivers such as the Nile, Mara and Ewaso Ng'iro which are economic life lines for three main sectors of the country's economy: Tourism, Agriculture, and Hydropower generation (GOK, 2007). These three sectors form the bulk of the economies of the countries that share at least a part of the basins of these rivers.

The MFC is a critical component of the water catchments in Lake Victoria Basin (LVB). It provides a source of rivers that serve a population of over six million people who depend directly or indirectly on water from the MFC for their subsistence livelihoods. UNEP (2009a) has estimated that the value of goods and services generated annually by sectors supported by the MFC is in excess of 20 billion Kenya shillings which is equivalent to 5% of the country's Gross domestic product (GDP).

The macro-economic costs of the MFC destruction are gradually manifesting themselves. Hydropower capacity of rivers originating from the forest complex and particularly the Sondu Miriu River is severely constrained by the reduced flow levels during the dry seasons. Sondu Miriu River, which originates from the SWM forest block, is set to contribute about 60 MW of hydropower when the hydropower plant becomes fully operational. Flow levels of this river and others that originate from MFC have been declining lately (GOK, 2010a) and this is likely to impact negatively on the proposed hydropower generation.

The world renowned Maasai Mara game reserve is losing its wondrous attraction, the wildebeest annual migration, to progressively longer drought spells. The same applies to the tea industry in the Rift Valley where tea harvests are fluctuating widely. All this is believed to be as a result of degradation of the MFC, which has widely been documented (Kinyanjui, 2009; Baldyaga, 2007). The degradation has impacted negatively on the various roles of the forest including that of water catchment.

Rivers from MFC contribute a substantial amount of surface inflows to Lake Victoria, the second largest freshwater lake in the world. The average total annual surface inflow into the lake from its catchments is about 2 x 10^{10} m^3 out of which 8.4 x 10^9 m^3; about 42% of the total inflows come from Kenyan forests, mainly the MFC (Albinus *et al*, 2008). The lake is the source of River Nile, and therefore the MFC is not only important as a water catchment area in Kenya but also to the international community who depend on River Nile for their water needs. Over the past four decades about a quarter of this essential ecosystem has been destroyed through deforestation for timber, farming and human settlements (GOK, 2010a).

This study is anchored on the legal framework as set out in the Constitution of Kenya (2010), section 69 which spells out obligations in respect of the environment and exploitation of natural resources such as water (GOK, 2010b), and three other documents: the Sessional Paper Number 1 (1999) on the National Policy on Water Resources Management and Development (GOK, 1999), the Water Act (2002) (GOK, 2002), the Forest Act (2005) (GOK, 2005), and the Environmental management coordination act (1999) (GOK, 2000) enacted in the Kenyan Parliament to guide the management of water resources in Kenya.

The Water Act (2002) provides for the management, conservation, use and control of water resources among others. The Act vests all the water resources within Kenyan territory in the National Government so that it manages these vital resources for the benefit of all its citizens. It encourages investigation of water resources, which by this act include stream flow, throughout Kenya. This study mainly investigates characteristics of stream flow in relation to climate change under different land use scenarios and hence finds its anchor in this particular provision of the Act. The terms used in the study relating the surface phase of the water cycle are in line with the interpretation of the Act.

For efficient management of water resources throughout Kenya, the Act provided for setting up of the Water Resources Management Authority (WRMA) as the lead national agency in the management of water resources. The mandate of WRMA includes, among others: regulation and protection of water resources from adverse impacts such as climate change, management and protection of water catchment areas, gathering and maintaining information on water resources, publishing forecasts, projections and information on water resources which are provided for in the National Policy on Water Resources Management and Development (1999). In order for WRMA to fully carry out its mandate of managing the water resources, it requires backing from research findings. This study seeks to provide advice to policy makers in the water sector as it seeks to identify and quantify the impacts of climate change and deforestation on water yields at the catchment level.

The Forest Act (2005) provides for the establishment, development and sustainable management of forest resources for socio-economic development of the people of Kenya. The Act recognizes, among others issues, the vital role played by the forests in the protection of water catchments, and stabilization of soils and groundwater, and moderation of microclimates. Part of the area of study comprises indigenous forests and section 8 of the Act requires that all forests and woodlands be managed on a sustainable basis for purposes of water conservation and water catchment protection among others. The Act describes a number of forest products and water is clearly described as one of the main forest products. Hence deforestation, which for the purpose of this study refers to conversion of forest land to other landuse activities as a result of excision or encroachment, is relevant in this study. The Act vests all forests in the State and for better management of this vital resources in Kenya, the Act provides for the establishment of the Kenya Forest Service (KFS) which is the lead national agency charged with the responsibility of managing forests for the benefit of the people of Kenya.

Some of the mandates of KFS are conservation of all types of forests in Kenya, collaboration with individuals, private and public research institutions in identifying research needs and applying research findings. This study finds relevance in this particular mandate as it seeks to establish how one of the vital forest products, water, is affected by deforestation and climate change. Of particular interest is the fact that KFS manages and protects forests for purposes of water conservation on water catchment areas such as the MFC in general and South West Mau in particular, which is the focus of this study. This was done through estimation of changes in simulated stream flow under different climate and forest cover scenarios using a hydrological model (SWAT) driven by outputs from a regional climate model (PRECIS) over the Sondu River basin whose upper catchment comprises the SWM forest reserve; the largest of the 22 forest blocks comprising the Mau forest complex. Changes in observed and simulated stream flows in the Sondu catchment area were assumed to be applicable to the entire Mau forest complex catchment.

1.7 Area of Study

Kenya lies between latitudes 6°N and 5°S and longitudes 34°E and 42°E and is divided into six hydrological catchment areas: Athi, Ewaso Ng'iro, Lake Victoria North, Lake Victoria South, Rift Valley, and Tana (Figure 1.2a). The area of study is located on the western part of Kenya and lies within Lake Victoria South Catchment Area (LVSCA). LVSCA is located at the south-western part of Kenya and borders Lake Victoria North catchment Area (LVNCA) to the north, Rift Valley Catchment Area (RVCA) to the east, Tanzania to the south, and Lake Victoria to the west (Figure 1.2). the Mau forest complex (MFC), the largest of the five water towers in Kenya, lies in the north-eastern part of the catchment area (Figure 1.3).

LVSCA covers an area of about 31000 km^2 out of which about 4000 km^2 is under Lake Victoria water (WRMA, 2009). The catchment area is divided into three distinct zones namely: the upper catchment comprising mainly the Mau Forest Complex (MFC), the middle catchment comprising undulating hills bisected by the four main rivers in the basin (Figure 1.2b), and the lower catchment comprising mainly the Kano plains, lower Gucha-Migori, lower Awach Tende, Lower Awach Kubuon, and Masaai Mara. The major rivers in LVSCA are Sondu, Nyando, Mara, and Kunja originating from the MFC, and other small rivers on the northern and southern shorelines of Lake Victoria. The catchment area is therefore further subdivided into six river catchment areas: Kunja, Mara, Nyando, Sondu, Northern, and Southern shore Streams (Figure 1.2b and Table 1.1). Table 1.1 shows the respective river catchment code, length of the main river, catchment area, and the mean annual discharge volume of the main rivers in Billion Cubic Metres per year (BCM/yr). Three of these rivers; Nyando, Sondu and Mara originate from the MFC (WRMA, 2009).

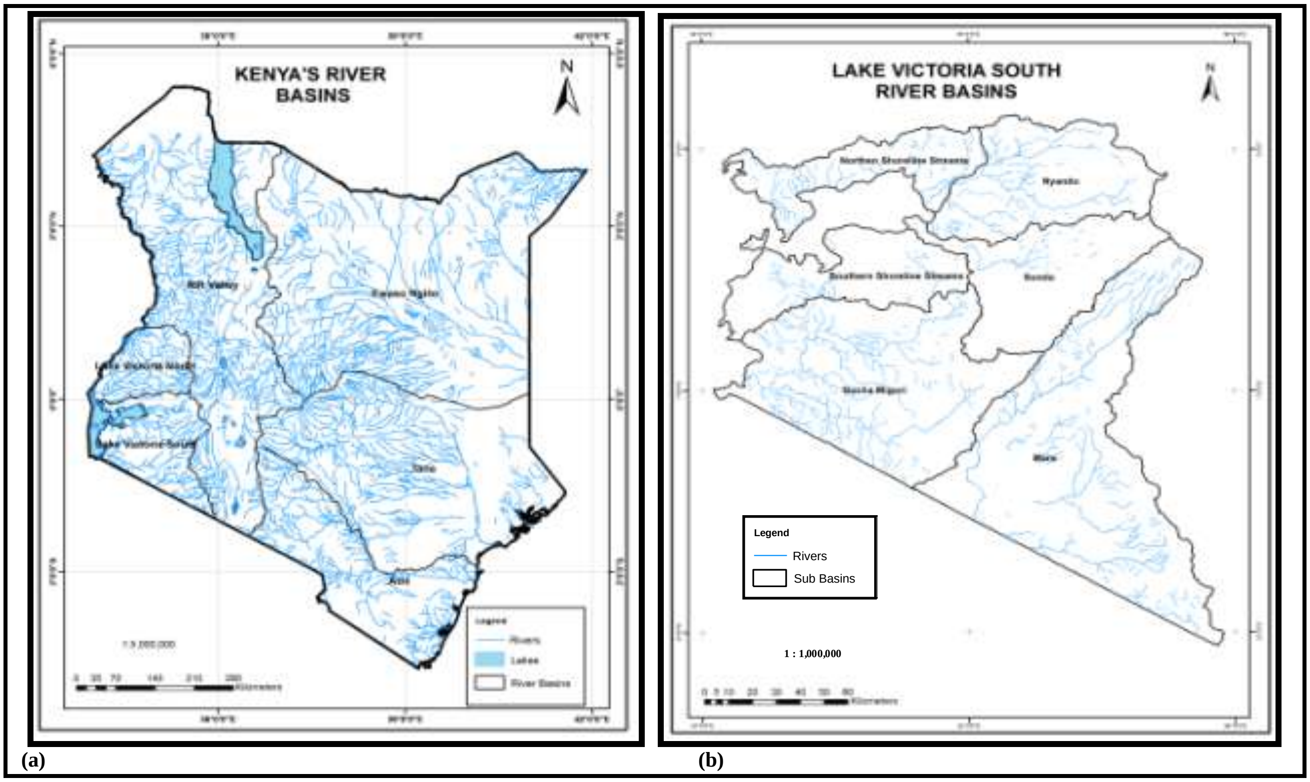

Figure 1.2: (a) Kenya's six drainage basins (b) the six river basins comprising Lake Victoria south catchment area

Table 1.1: The six main river basins of Lake Victoria south catchment area

No	**River**	**Code**	**Length (km)**	**Catchment area (km^2)**	**Mean annual discharge (BCM/yr)**
1	Nyando	1G	120	3652	0.66
2	Sondu	1J	173	3500	1.37
3	Mara	1L	181	8705	1.18
4	Kuja	1K	149	6600	1.83
5	Northern Shoreline	1H	27	1985	0.12
6	Southern Shoreline	1H	65	3156	0.19

(Source: WRMA, 2009)

Based on the 2009 Census published in 2010, LVSCA has a population about 7.37 million (19.1% of the country's total population) with a population density of over 2273 persons per km^2 (WRMA, 2009; JICA, 2013), making it one of the most densely populated areas in the country. As a result of the high population density, pressure on high potential agricultural land has increased leading to the encroachment of water catchment areas; mainly the Mau forest complex and South West Mau (SWM) forest reserve in particular. This has resulted in the degradation of the catchment's main water tower (Kinyanui, 2011; WRMA, 2009; Edwards and Blackie, 1979).

LVSCA has undergone drastic changes as a result of anthropogenic activities in the last fifty years. Analysis of 50-year daily discharge data for the rivers in the LVSCA shows significant variations in high and low flows during wet and dry seasons respectively. The flash flood incidents have continued to increase during wet seasons and base flows have continued to decrease during dry seasons (WRMA 2009). This has been attributed to catchment degradation, mainly the Mau forest complex, which has resulted in an increase in runoff coefficient as a result of decreased infiltration capacity.

1.7.1 Mau Forest Complex

The Mau Forest Complex (MFC), the most important source of water in the Rift Valley and the Western parts of Kenya, forms the upper catchments of all but one of the main Kenyan rivers west of the Rift Valley. MFC is one of the most important sources of water in Kenya providing water for multiple uses to millions of people in both Rift Valley and Lake Victoria drainage basins (UNEP/GOK, 2008). It is dissected by numerous rivers, river tributaries, and streams which form at least a part of the twelve main rivers whose sources are found within this forest complex and flow into three of Kenya's six main drainage basins, the Rift Valley, Lake Victoria North, and Lake Victoria South. These rivers include Yala, Nyando, Sondu and Mara, which drain into the Lake Victoria drainage basins (LVBs), and Kerio, Ewaso Ng'iro South, Molo and Njoro which drain into the Rift Valley drainage basin. Through these rivers, the MFC is the single most important source of water for domestic, agricultural, and wildlife uses in Rift Valley and Western Kenya regions (UNEP/GOK, 2008; Gereta *et al*, 2003).

Rivers from the Mau forests are important economically and ecologically not only to Kenya but also to the East African region and the Nile basin countries. Mara River, for instance is a trans-boundary water resource, which is the only permanent source of water in the Maasai-Mara Game Reserve in Kenya and the northern part of the Serengeti National Park in Tanzania (Gereta *et al*, 2003). River Ewaso Ng'iro is the only permanent source of water on the whole of northern front of Lake Natron. River Nile, which passes through Uganda, Sudan and Egypt before emptying its waters into the Mediterranean Sea, has its furthest source in Lake Victoria, the largest freshwater lake in Africa and the second largest in the world (Jayakrishnan *et al*, 2005; JICA, 2013).

The Mau complex sits on the western side of the Great Rift Valley in Kenya spanning north–south from Eldama Ravine to Narok and east-west from Nakuru to Kericho (Figure 1.3). The forest complex comprises 22 forest blocks including South West Mau, Eastern Mau, Transmara, Mau Narok, Maasai Mau, Western Mau, and Southern Mau, covering a total area of slightly over 400,000 hectares. MFC are undeniably the largest closed canopy montane forest ecosystem in East Africa (GOK, 2010a; WRMA, 2009; UNEP/KWS/KFWG/ENSDA 2008; UNEP/GOK, 2008).

To the east, the East Mau forest is the head water for the Njoro River which drains into Lake Nakuru, one of Kenya's prime tourist attractions. To the west, the West Mau forms the source of river Mara, which passes through Maasai Mara National Reserve, known worldwide for its annual migration of animals and therefore a major tourist attraction in the country. The forest complex, therefore occupies a central place in the country's economy particularly in the tourism sector, where it is key to conservation areas such as Lake Nakuru National Park and the Maasai Mara national reserve both of which earn the country in excess of Ksh 6 billion annually as tourism attraction sites (UNEP, 2009a) where Ksh 1.16 billion comes from entry fees and Ksh. 5 billion comes from direct and indirect revenue; and agriculture and hydropower sectors (UNEP/KWS/KFWG/ENSDA, 2008).

MFC further provides environmental services essential to both food and cash crop production such as continuous river flows and favourable microclimates particularly for tea growing. As a result of these favourable conditions, the largest tea growing areas in the country are found near the forest complex particularly around South West Mau Forest reserve in Kericho, Tinderet and Northern Tinderet forests where conditions for optimum tea production are readily present. Such conditions include constant moisture, soil temperature of between 16°C and 25°C and air temperatures of between 10°C and 30°C. Tea from this area earns the country in excess of Ksh. 8 billion annually in revenue (UNEP/KWS/KFWG/ENSDA, 2008; WRMA, 2009).

Despite its critical importance in sustaining current and future ecological and socio-economic development in Kenya, the MFC water tower, together with other smaller water towers in LVSCA, have been invaded for human settlement, agriculture, logging, and charcoal production (Figure 1.4). Excisions and widespread encroachments have led to the destruction of over 27% of the MFC in the last two decades resulting in the degradation of these critical water catchment areas (WRMA, 2009). Between years 2003 and 2005 a decrease of over 9800 ha of forest cover was witnessed in this 400000 ha plus forest complex (UNEP, 2009a). This has negatively impacted on four main river catchments in the complex namely Sondu, Mara, Njoro, Molo and Lake Nakuru.

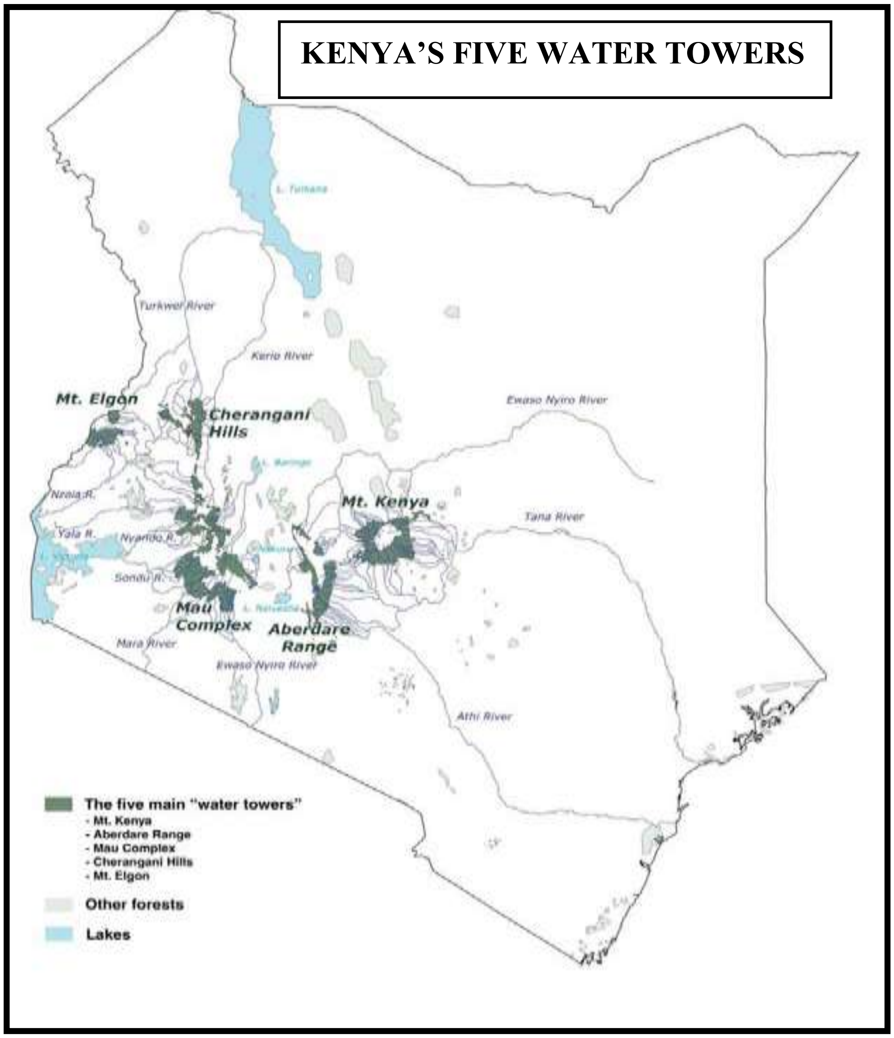

Figure 1.3: Location of Kenya's five water towers (source: DRSRS/KFWG, 2006)

South West Mau (SWM) forest reserve is the largest of all the blocks of the Mau forest complex covering about 84000 ha; about 20% of the MFC. This forest block forms the upper catchment of River Sondu, the lifeline of Sondu Miriu hydropower plant and the major source of water for other users that include domestic, industrial and agricultural use in the Sondu catchment area. The forest is characterised by an afromontane vegetation type (Kinyanjui, 2009) and consists of tall, broad-leaved evergreen species that give way to bamboo at the higher altitudes. The forest reserve lies within 0.5° south of the equator and between 2000 m and 2800 m in altitude. The forest and its surrounding areas receive an annual rainfall ranging from 1500 mm to 2100 mm. The perennial streams emanating from this area form a critical source of water to the main Sondu River, which serves the surrounding tea estates and the densely populated lake shores of LVSCA (Edwards and Blackie, 1979).

Figure 1.4: Aerial view of Mau forest complex heavily impacted by encroachment on the western part of the Maasai Mau (Source: UNEP/KFWG/KWS, 2005)

For purposes of this study, South West Mau forest reserve was chosen as the representative subset of the Mau forest complex. The forest reserve is the largest of the 22 forest blocks comprising the Mau forest complex, has all the characteristics of whole complex (Kinyanjui, 2009), and above all, is the most deforested block since 1973 (UNEP/KFWG, 2006). A study of the South West Mau and Eastern Mau forest reserves by UNEP/KFWG (2006) has shown South West Mau as the most deforested of all the blocks comprising the MFC and has proposed reforestation and rational land use as some of the measures needed to curb the degradation of the MFC catchments.

This study sought to examine the extent to which deforestation of the Mau forest complex has affected surface water yields from this important water tower in view of climate change. River Sondu, which originates form the largest and the most deforested of the forest blocks comprising the Mau forest complex (South West Mau), was identified as the most affected by deforestation of the MFC. South West Mau (SWM) is mainly located on the upper parts of the Sondu catchment area and forms the source of River Sondu (Figure 1.5). Sondu catchment area was therefore selected to study the impacts of climate change and deforestation on water yields using Kiptiget sub catchment, which is located within the SWM forest reserve, as the unit of study.

1.7.2 Sondu River Basin

Sondu River basin, code 1J, covers an area of about 3500 km^2 and is located within latitudes 00°23'S and 01°10'S and longitudes 34°46'E and 35°45'E. The main water course in this basin is River Sondu which is fed by several tributaries, whose head waters originate from the SWM forest block. The river crosses the basin in a general east-west direction (Figure 1.5), and drains its waters into Lake Victoria at an annual rate of about 1.37 BCM/yr (WRMA, 2009). Figure 1.5 presents Sondu River catchment area showing the location in Kenya, SWM forest reserve, river system, river and climate gauging stations networks that were used in this study. Between the source, SWM forest, at about 2680 m above mean sea level, and the river mouth, Lake Victoria at about 1134 m above mean sea level, the river covers a total length of about 173 km (WRMA, 2009).

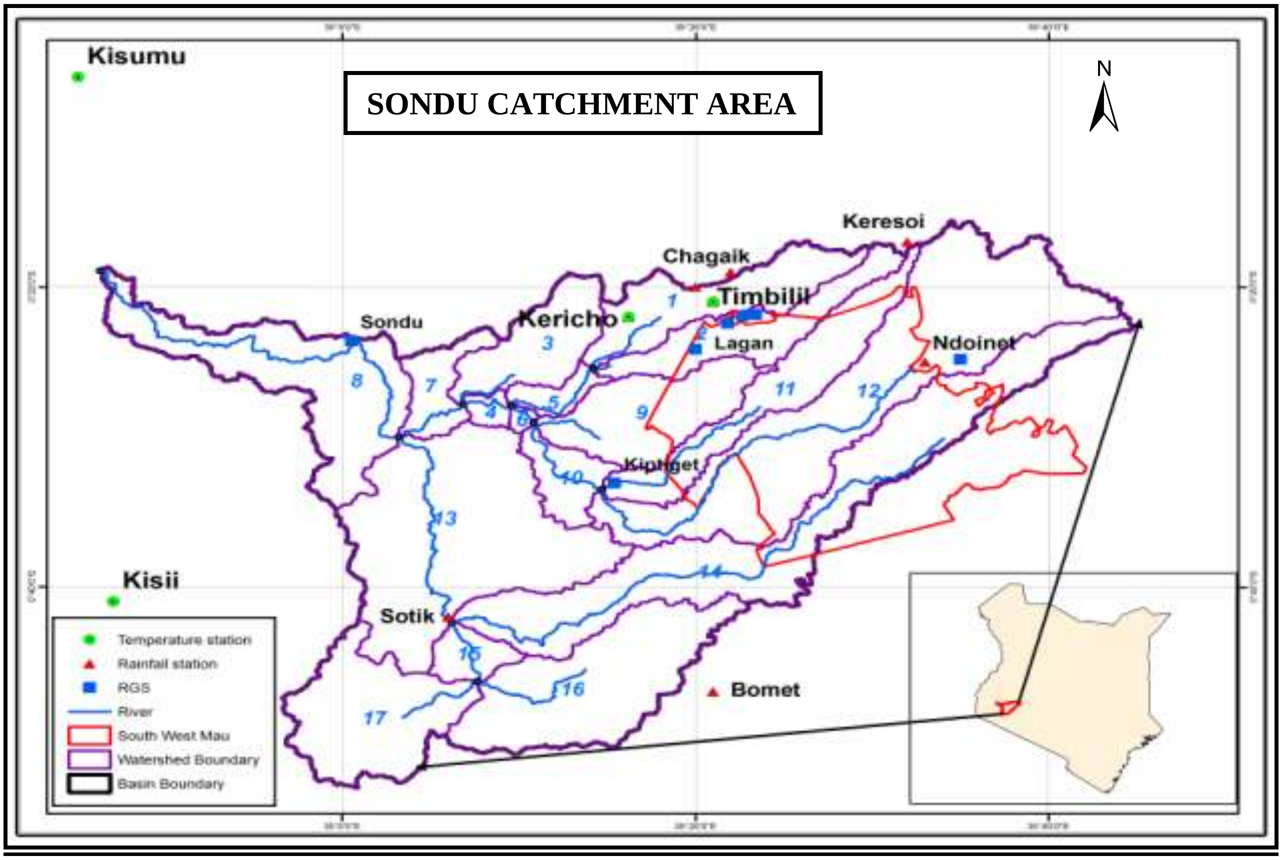

Figure 1.5: Sondu River catchment area and the river, rainfall and temperature gauging stations networks

Sondu River is important not only as a source of water for agricultural and domestic uses, but also as an important source of hydropower. According to a joint presentation by UNEP (2008) and others, the river has a potential for hydropower production of about 209 MW out of which only 64

MW have been developed; 60 MW of these are at Sondu-Miriu hydropower complex and 4 MW at the upper tributaries of the river which mainly serve the Tea Estates around Kericho. Being the primary source of such an important river as the Sondu, SWM forest reserve is therefore critical to key economic sectors such as agriculture and hydropower generation in the Sondu basin. Excisions and wanton encroachments of the forest reserve have impacted negatively on River Sondu (WRMA, 2009; Jayakrishnan *et al*, 2005).

1.7.3 Characteristics of Sondu Basin

The four primary basin characteristics that govern water yields into the river network (Arnold *et al*, 1998) include those that affect runoff response time (topography and size), those that affect subsurface baseflow (geology and soils), those that affect hydrologic abstraction and runoff volumes (landuse/landcover), and those that affect the amount of rain water arriving in the basin (climate). These characteristics affect different aspects of streamflow hydrograph and therefore deserve to be mentioned briefly.

1.7.3.1 Topography and Size

Topography and size of the basin influence how much and how quickly rain water reaches the river network. Topographic characteristics that affect runoff response time include watershed shape, drainage pattern, watershed slope and the stream channel slope. Steep-sloped basins are often associated with quick response to rainfall events in terms of flashy runoff unlike the case in the relatively flat basins.

The landform of the Sondu watershed consists of low plains near the lakeshore and rises eastwards to volcanic plateaus with dissected margins in the middle parts and rugged terrain with deep gorges and V-shaped valleys in the upper eastern parts of the catchment (JICA, 1987). These landforms comprise the Kano plains on the western side and the Londiani Mountains on the eastern side which form the lower and the upper Sondu catchment areas respectively. Land elevation in the basin varies from about 1134 m above sea level at the lakeshore to about 2900 m above sea level at the summit of Londiani Mountains. The basin generally slopes from east towards west with relatively flat areas towards Lake Victoria.

1.7.3.2 Geology and Soils

Characteristics that influence subsurface baseflow include soil type, channel bed material, and geology (Arnold *et al*, 1998). The solid geology of the South West Mau forest reserve and the surrounding areas consists of tertiary lavas extruded in a westerly and south-westerly direction from the Rift valley faults in early Miocene times (Edwards and Blackie, 1979). The lavas are notable for the number and thickness of their beds, their freedom from interbedded pyroclasic material and their low angle of dip. These phenolite lavas are remarkably uniform in composition and are reported to be free from fissures due to lack of subsequent tilting. They weather into deep stone free soils, and uniform in physical structure up to a depth of about 6 m (Edwards and Blackie, 1979).

Soils in the Sondu catchment area vary from the lower to the upper parts. The middle and upper parts of the catchment area have well drained soils, extremely deep, dark reddish-brown, friable clay with humic top soil and with high levels of fertility. The well drained characteristics of the soils in the upper catchment area make them more susceptible to erosion, which together with changes in land use tend to lead to serious catchment degradations whose impacts result in reduced stream flow volumes during dry seasons. The high levels of the soil fertility have attracted settlements, farming and other land use activities such as industrial development in the area (Nyangaga, 2008; Edwards and Blackie, 1979).There is therefore need to carry out research to establish the extent to which these changes in land use are affecting the water yielding capacity of the catchment area and to recommend measures to ensure sustainable water resources development taking into account the influence of climate change.

1.7.3.3 Landuse/Landcover

Landuse/landcover (LULC) influences the hydrologic abstractions and runoff volumes through canopy interception, evaporation and evapotranspiration dynamics. The dominant land use activities in the Sondu River basin include crop and dairy farming. Large areas of the basin have been deforested over time mainly for purposes of agricultural activities. The local economy is mainly subsistence farming, small and large scale tea plantations and other annual crops that are almost entirely rain fed. Other economic activities in the area include dairy farming, sheep rearing, fishing and industrial activities (Nyangaga, 2008).

These land use activities have significant impacts on the hydrological regime of the catchment area as they lead to the destruction of the natural vegetation cover resulting into faster overland flow, less infiltration, more erosion, less ground water recharge and thus the frequent flood events during wet seasons and to reduced discharge during dry seasons.

1.7.3.4 Climate

The climate of Sondu basin, just like that of the rest of the eastern side of Lake Victoria basin, is largely influenced by the north-south movement of the Inter Tropical Convergence Zone (ITCZ) modified by the local orography and the proximity of Lake Victoria, Atlantic and Indian oceans. The ITCZ is a zone characterised by low and medium level convergence. It is marked by a line of thunderstorms and showers in most areas and marks the boundary between the two inter-hemispheric monsoon wind systems over the region. This is the main synoptic scale system that affects the intensity, distribution and migration of seasonal rainfall over the Eastern Africa region (Omeny *et al*, 2008).

Generally, airstreams from the northern and the southern hemisphere converge over the ITCZ. However, over Africa, this generality is broken since the ITCZ breaks into two spatial components over the central parts of Africa to form the zonal and the meridional components. The division into the two components has been attributed to the geography of the Rift Valley and the mountain chains of the East African region (Okoola, 1996). The zonal component of the ITCZ is a zone of convergence between the NE and SW monsoons while the meridional component is observed as a quasi-permanent low over the Central African region. The meridional component of ITCZ fluctuates from East to West and vice versa with the most eastern extent occurring between July and August when the arm is located over the Rift Valley highlands of Kenya. This eastern extent of the meridional arm of the ITCZ enhances the penetration of westerly winds further eastwards giving rise to enhanced June-July-August (JJA) rainfall over the western side of Kenya, including the Sondu basin from the Atlantic Ocean, the Congo basin, and Lake Victoria (Kiangi *et al*, 1981). This is believed to be the cause of the third rainfall peak observed on the western parts of Kenya during the JJA season (Figure 1.7). The zonal component of the ITCZ migrates north and south of the equator following the seasonal match of the sun with a time lag of about one month. It traverses the Sondu catchment area twice a year bringing with it the long rains during the March-April-May (MAM) season and the short rains during the September-October-November (SON) season as shown in Figure 1.7 (Okoola, 1996).

The Atlantic and Indian Oceans are the major sources of moisture for the East African region and hence greatly influence the regional climate through interactions associated with Oceanic and atmospheric circulations (Nyakwanda *et al*, 2009). The above normal rainfall over the region are associated with the low level circulation patterns dominated by easterly inflows from the Indian Ocean and westerly inflows from the Atlantic Ocean and the Congo basin.

Lake Victoria trough induces a mesoscale circulation with a strong diurnal cycle over the lake basin region. The existence of a large water body (Lake Victoria) brings about a thermal contrast between the land and the water surfaces. This thermal contrast initiates local circulations that include land-sea breezes. The temperature contrast between the lake and the land during the day and night results in a land breeze during the day and a sea breeze during the night. The land-sea breeze contributes to the lake basin in general and the Sondu catchment area in particular having rainfall throughout the year which is enhanced during the three main rainfall seasons as shown in Figure 1.7 (Sabiiti, 2008).

Unlike the higher latitudes where climatic patterns are marked by a high seasonal variability of temperature and other climatic parameters, the climatic parameter with the highest variability within the tropics is rainfall. Being in the tropical zone, seasonal temperature changes are relatively small compared to the rainfall due to the insignificant seasonal changes in the solar radiation. The warmest month is normally February and July the coldest with an average range of about 10°C between the warmest and the coldest months (Ahrens, 2009).

1.7.3.4.1Temperature

Figure 1.6 shows the annual cycle of mean monthly temperatures for selected stations in and around the area of study. The temperatures range from about 16°C in the upper parts (Timbilil) in July to about 24°C in the lower parts (Kisumu) in March. The warmest temperatures in the area are observed in March while the coolest are observed in July.

The average temperature over the catchment area is at least 18°C in all the months and hence the area is warm throughout the year. The seasonal difference in average temperature over the area is small (2.2°C) while the difference between day time and night time temperatures is large (12.4°C). Hence the area can be described as being in a tropical type of climate zone (Ahrens, 2009).

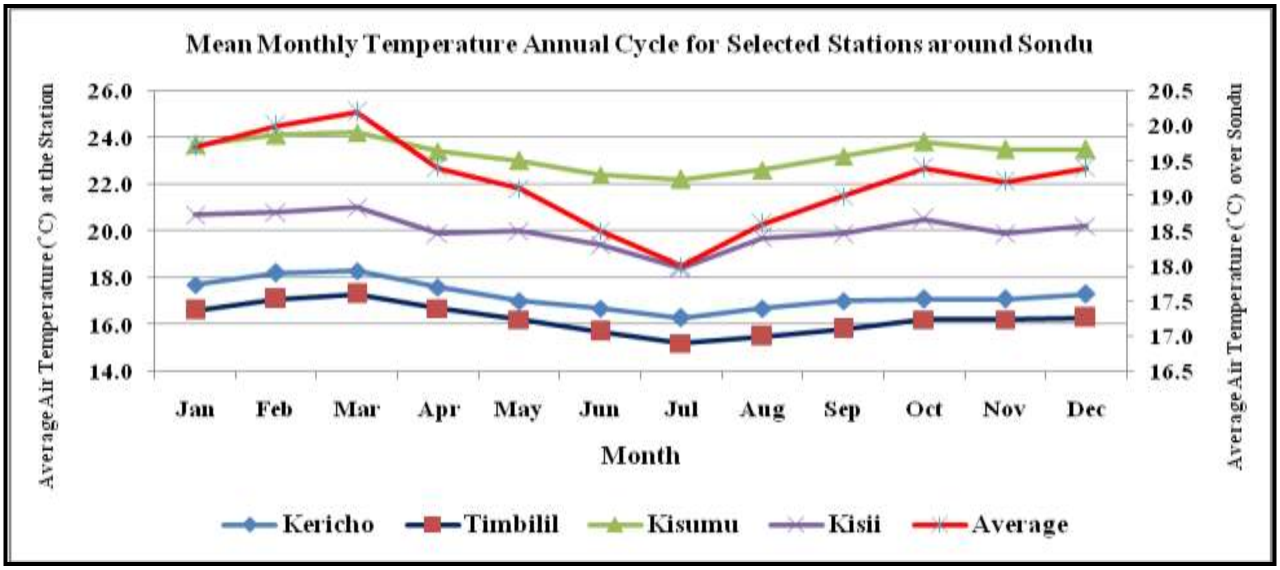

Figure 1.6: Mean monthly average air temperature distribution in and around the Sondu basin

1.7.3.4.2 Rainfall

Figure 1.7 shows the annual cycle of mean monthly total rainfall averaged over the period 1973-2006 at selected stations within and around the area of study. The figure shows that rainfall patterns in the area follow a trimodal pattern with the main rainfall season coming in the months of MAM followed by JJA and the short rains in SON with the mean monthly rainfall ranging from about 60 mm in January (Ndoinet) to about 284 mm in May (Timbilil).

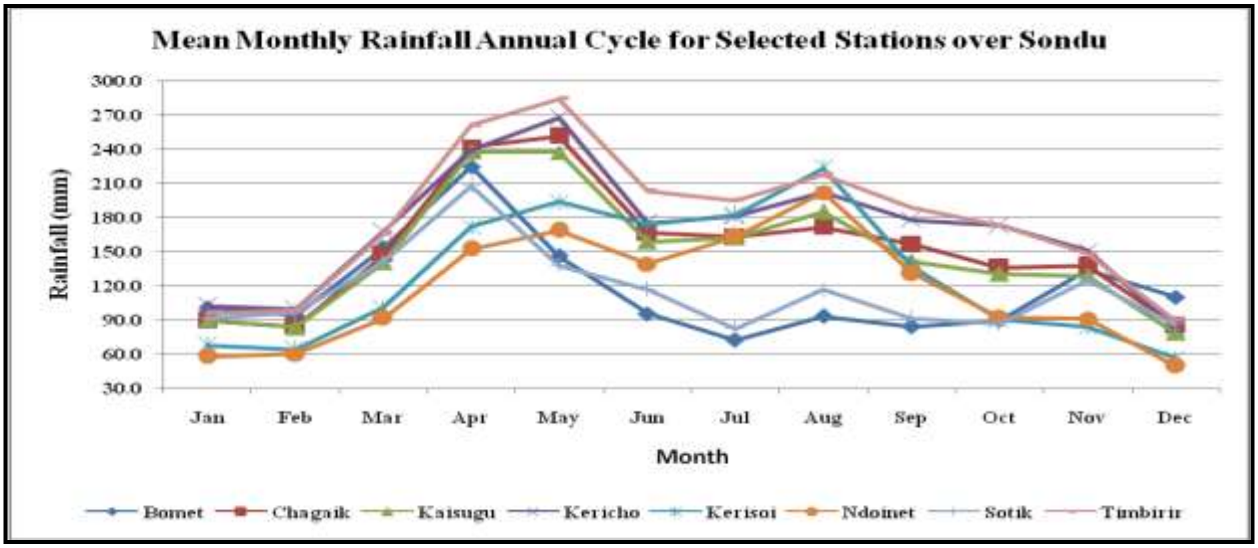

Figure 1.7: Mean monthly total rainfall distribution over the Sondu basin showing a trimodal pattern

The average monthly rainfall totals exceed 60 mm in all the months with a mean annual rainfall total of more that 1500 mm, the threshold values for a tropical wet type of climate (Ahrens, 2009). Hence the area can be described being under a tropical wet type of climate.

1.7.3.4.3 Hydrology

Figure 1.8 shows the hydrographs of observed mean monthly discharge at Kiptiget and Sondu RGSs showing the annual cycle of discharge distribution over the Sondu catchment area. From the figure it was evident that February has the lowest discharges in the area while May and September have the highest. Sondu RGS, at which over 94% of the catchment area is drained, shows a trimodal pattern of discharge while Kiptiget RGS, at which only about 5% of the catchment area is drained, shows a bimodal pattern. The lowest discharge values in the basin are observed in the month of February while the highest are in May and September. Hence the hydrological year in this basin may be considered to begin in February and end in January.

The peaks and low flows follow the general rainfall pattern in the area quite closely but generally lag by about one month except in the month of May where thy coincide. This can be attributed to antecedent soil moisture conditions in the month of May following April.

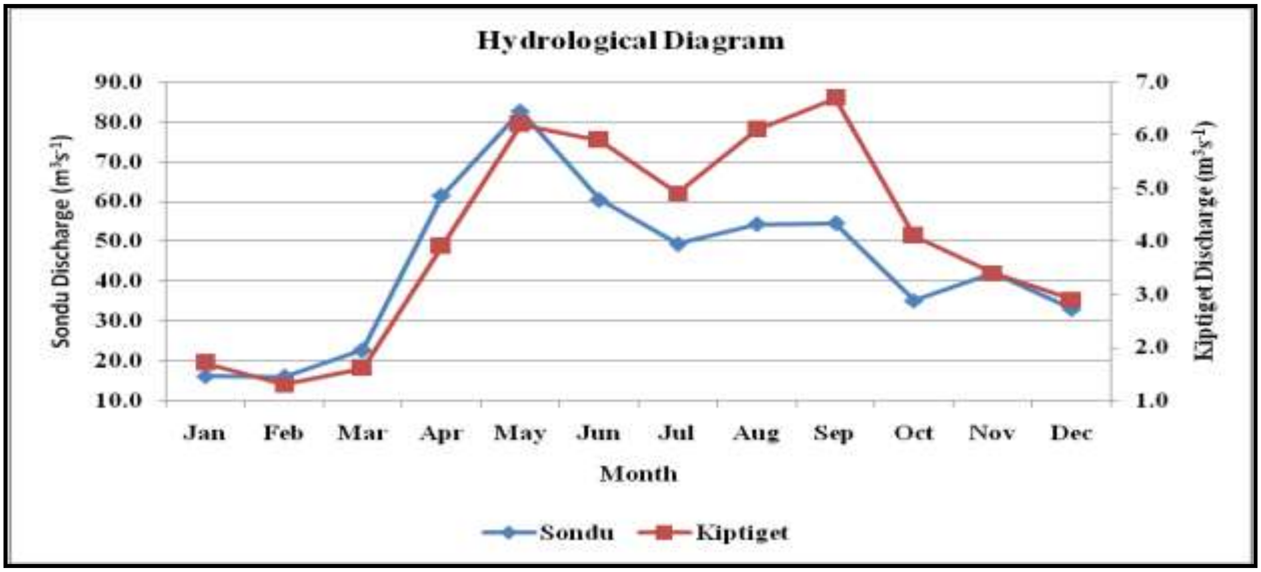

Figure 1.8: Mean monthly hydrographs at Sondu and Kiptiget RGSs

1.8 Data Availability and Challenges

The data required for this study were compiled from different sources and included: meteorological, hydrological, topographical, land use, soil type, and GCM outputs. Some of these data were obtained from various institutions in Kenya and the Met Office (UK) while others were downloaded from the internet.

Datasets obtained from various institutions in Kenya included: meteorological data from the Kenya Meteorological Service (KMS) and hydrological data from the Water Resources Management Authority (WRMA); Land use data from the Department of Resource Surveying and Remote Sensing (DRSRS) in form of processed LANDSAT satellite imageries; and soil data from the Kenya Soil Survey (KSS). Topographical data were obtained from the Digital Elevation Model (DEM) downloaded from the global USGS public domain geographic database (http://srtm.csi.cgiar.org/.) while GCM outputs were obtained from the Met Office (UK). This section presents brief descriptions of the type and source of the datasets used in this study.

1.8.1 Meteorological Data

Meteorological data used in this study for the analysis of long term trends in the past climate, calibration and validation of the climate model outputs are both daily and monthly records of rainfall, maximum and minimum temperature. These were obtained from KMS. Seven rainfall and three synoptic stations located in and around the area of study were selected to provide the required datasets. The selection of the eight stations was based on the length and the quality of their data records. All the eight stations had over 30 years of daily data up to 2010 and less than 10 % of missing records with the longest record starting in 1959 (Kaisugu House) and the shortest starting in 1975 (Ndoinet Forest Station). A few stations however did not have data spanning the entire period. The names, station codes, location, elevation, period with data, and percentage of missing data records are presented in Table 1.2.

Selection of these stations was guided by the fact that in order for the results to be dependable, rain gauge stations should generally be distributed across the basin in such a way that each of the main seven sub-catchments in the basin was represented. In selecting the eight stations, due care was taken to ensure that as far as possible the WMO recommended minimum network density was adhered to. For hilly areas such as the upper parts of the Sondu River catchment area, WMO (2008) recommends a minimum rainfall station network density of one station for every 575 km^2.

The eight selected stations were way above the recommended minimum threshold since on average each of the rainfall station serves about 437 km^2. The other criterion for selecting the rain gauge stations was their location relative to the stream gauging station. WMO (2008) recommends that the location of rain gauges be co-ordinated with the location of the stream flow gauges so that basin rainfall can be estimated for each stream gauging station. Such locations are generally on the upstream side of the River Gauging Stations (RGS).

Table 1.2: Table of the meteorological stations used in the study

No	**Station Identification**		**Location**			**Data Availability**			**(%) Missing**
	Name	**Code**	**Lat.**	**Long.**	**Alt. (m)**	**Start**	**End**	**Length (yrs)**	
1	Kaisugu	9035075	-0.3167	35.3667	2134	1960	2009	50	7.5
2	Chagaik	9035235	-0.3333	35.3333	1829	1960	2006	47	6.9
3	Keresoi	9035240	-0.2833	35.5333	2682	1962	2011	50	6.2
4	Timbilil	9035244	-0.3500	35.3500	2073	1964	2010	47	0.9
5	Sotik	9035262	-0.7000	35.1000	2134	1966	2007	42	7.1
6	Bomet	9035265	-0.7833	35.3500	1951	1967	2009	43	12
7	Kericho	9035279	-0.3667	35.2700	1976	1973	2011	39	0.9
8	Ndoinet	9035292	-0.4167	35.5500	2438	1975	2011	37	9.7

Of the eight meteorological stations selected from within the basin for the study only two, Kericho and Timbilil, had temperature data. All the others had only rainfall records. The spatial distribution of the rainfall and temperature stations is presented in Figure 1.5 which shows good coverage of the upper parts of the basin. The meteorological station network coverage progressively becomes sparse towards the lower parts of the basin.

1.8.2 Discharge Data

The main objective of the stream flow gauging network is to obtain as much information as possible on the availability of surface water resources and their spatial and temporal distributions. Specific locations of these gauges should therefore be governed by topographic, geologic and climatic considerations (WMO, 2008). Most countries in the world, Kenya included, operate national river discharge monitoring networks to meet primary multiple needs that include water resources management and development, as well as disaster mitigation. The river discharge data collected in an endeavour to meet the primary needs may also be utilised for research programmes, as is the case in this study, to improve our understanding of the catchment hydrology (WMO, 2009).

Hydrological data used in this study are mainly daily streamflow records obtained from a network of seven selected river gauging stations (RGSs) which are manned by the Water Resources Management Authority (WRMA). In selecting the network of RGSs, the minimum recommended density of 1875 square kilometres per station (WMO, 2008) was adhered to. The selected network covers about 188 square kilometres per station, which is well above the WMO recommended minimum threshold density. River discharge is a critical water cycle variable since it integrates all processes occurring in a river basin and also provides a hydrological output variable that can readily be measured besides serving as an indicator for climate change and variability by reflecting changes in rainfall and evapotranspiration (WMO, 2009).

Sondu River gauging station, 1JG01, is located near the main outlet of the study area whereas the rest are upstream tributary flow gauging stations. The observed discharge data for the Sondu Miriu River basin are available at the outlets of different sub-basins as presented in Table 1.3 which shows the names, station code, length of period with data, percentage of missing data, area upstream of station location, location and elevation of the station above mean sea level (msl), with their spatial distribution presented in Figure 1.3. The lengths of records in each sub-basin are not the same and span different time periods with at least 30 years of data.

Table 1.3: Table of River gauging stations (RGS) used in the study

No	**RGS Identification**		**RGS Location**			**Upstream Area**	**Data Availability**			**Missing (%)**
	Name	**Code**	**Lat.**	**Long.**	**Alt. (m)**		**Start**	**End**	**Length (yrs}**	
1	Kiptiget	1JA02	-0.5513	35.2569	1900	179	1956	1993	37	18.9
2	Lagan	1JC14	-0.4027	35.3333	2100	5	1957	1996	40	15.0
3	Ndoinet	1JA05	-0.4138	35.5833	2500	49	1957	1992	36	16.7
4	Sambret1	1JC13	-0.3736	35.3638	1920	8	1957	1995	39	10.2
5	Sambret2	1JC15	-0.3638	35.3902	1960	3	1960	1996	37	13.5
6	Sambret3	1JC16	-0.3652	35.3777	2180	5	1960	1996	37	8.1
7	Sondu	1JG01	-0.3930	35.0083	1500	3287	1946	1991	46	15.2

1.8.3 Surface Characteristics Data

In addition to the more conventional Hydro-meteorological measurements, there is need to measure other aspects of fresh water environment. This involves measurements of basin characteristics that influence the basin's hydrology, such as: Topography, land use, soil type, and land cover patterns. In this section topography, land use patterns, soil types, and land cover characteristics of the Sondu basin are presented as non climate data that influence hydrology of a watershed.

1.8.3.1 Topography Data

Topography data were obtained from the Shuttle Radar Topography Mission (SRTM) 90 m by 90 m grid resolution Digital Elevation Model (DEM) developed jointly by the National Aeronautical and Space Administration (NASA) and the National Geospatial Intelligence Agency (NGIA) and available from the United States Geological Survey (USGS) website (USGS, 2004). DEM is a three dimensional representation of the continuously varying topographic surface of the earth consisting of a sampled array of elevations for a number of ground positions at regularly spaced intervals (Thomson *et al,* 2001). The array of elevations represents the three-dimensional form of the earth's surface on a regular grid that describes the elevation of any point in a given area at a specified spatial resolution.

DEM data provide good terrain representation and are routinely applied in hydrological modelling to derive flow networks and watershed boundaries for given outlet points using GIS technology (Pryde *et al,* 2007). They serve as a common data source for terrain analysis and other spatial applications and are therefore critical in hydrological modelling. SWAT model uses DEM data for catchment and drainage network delineation, routing analysis, and HRU definition. DEM therefore forms one of the primary SWAT input datasets for hydrological modelling (Thomson *et al,* 2001) and was used in this study to define the topography of and to delineate Sondu catchment as well as to analyse the drainage patterns of the land surface terrain (Setegn *et al*, 2008).

1.8.3.2 Land Use/Land Cover Data

Land use is the phrase commonly used to describe human activities that modify the landscapes including the material covering the earth's surface while land cover is used to describe the physical material that actually covers the earth's surface (Gihui, 2008; Comber, 2007).

Anthropogenic land use activities that modify the landscapes include agriculture, commerce, settlement, and recreation while land cover includes crops, water, forest, and buildings among others. Land cover is a good indicator of prevailing land use activities since whatever covers the land surface is determined by the type of land use activities and hence the coupled use of the term land use/ land covers (LULC) (Tucker *et al*, 1985).

Accurate and timely information on the distribution of vegetation on the earth's surface is one of the requisites for understanding how changes in LULC affect the hydrologic cycle and hence water yields into the streams in a river basin. Traditionally the principal source of such information has been vegetation mapping by field survey but lately satellite remote sensing data has become a viable alternative (Tucker *et al*, 1985). Land cover mapping by field survey is labour-intensive and requires synthesis of different observations when large areas are being surveyed; which introduces further errors in the data. On the other hand satellite remote sensing data with its synoptic overview, accurately maps land cover types over large areas (Tucker *et al*, 1985). In this study, analyses of remotely sensed LANDSAT imageries were used to obtain LULC datasets over the area of study on account of their accuracy, affordability and accessibility.

LANDSAT imageries for four time periods; 1970s, 1980s, 1990s, and 2000s from Multispectral Scanner System (MSS), Thematic Mapper (TM), Enhanced Thematic Mapper (ETM), and Enhanced Thematic Mapper Plus (ETM+) sensors aboard the National Aeronautical and Space Administration (NASA) LANDSAT satellites were used to provide the LULC datasets for the area of study. The four processed LANDSAT imageries were obtained from the Department of Resource Survey and Remote Sensing (DRSRS) in Kenya. DRSRS carries out a number of surveys aimed at providing LULC data by use of sample aerial photography and processing of satellite images. The LULC data, which are a result of classifying raw satellite data into LULC categories based on the return value of the satellite image, were then processed to obtain LULC maps for the years 1973, 1986, 2000, and 2010 in digital format.

1.8.3.3 Soil Type Data

Soil data for this study were obtained in digital map format from the Kenya Soil and Terrain (KENSOTER) database compiled by the Kenya Soil Survey (KSS) in conjunction with the International Soil Reference and Information Centre (ISRIC) according to the Soil and Terrain (SOTER) methodology (www.isric.org/data/soil-and-terrain-database-kenya-primary-data, April

12, 2012). Soil data is a critical input for any hydrological simulation model (Nam *et al*, 2010; Melesse, 2006). Soil properties such as texture and hydraulic conductivity affect hydrologic processes such as infiltration and lateral transport of water in the soil.

The soil data used by SWAT is divided into two major groups according to their characteristics; physical and chemical. In this study, physical characteristics of the soil data were considered since they govern the movement of water through the soil profile and thus have a major impact on the cycling of water within each hydrologic response unit (Arnold *et al*, 2011). Soils are generally classified into four main hydrologic groups which comprise soils with similar runoff potential under similar storm and surface cover conditions namely: A, B, C, and D based mainly on their infiltration characteristics as described in Table 1.4.

Table 1.4: Soil hydraulic groups as defined by the United States Natural Resource Conservation Service (NRCS)

Soil class	Characteristics
A	Have a high infiltration rate even when thoroughly wetted, and low runoff potential. Consist mainly of deep, well drained to excessively drained sands and gravel
B	Have moderate infiltration rate when thoroughly wetted, hence moderate runoff potential. Consist mainly of moderately deep to deep, moderately well drained to well drained soils that have moderately fine to moderately course textures
C	Have low infiltration rates when thoroughly wetted and hence have moderate tending to high runoff potential. Consist mainly of a layer that impedes downward movement of water or have a moderately fine to fine texture
D	Have a very slow infiltration rate when thoroughly wetted and hence high runoff potential, have a permanent water table, have a clay pan or clay layer at or near the surface, and shallow soils over neatly impervious material

(Source: Neitsch et al, 2011)

In this classification, A has the highest rate of infiltration while D has the lowest. The soil properties that influence runoff potential in a watershed are those that impact the minimum rate of infiltration for a bare soil after prolonged wetting. These soil properties include depth to seasonally higher water table, saturated hydraulic conductivity, and depth to a very slowly varying permeable layer (Neitsch *et al*, 2011). Soils within the Sondu basin largely lie in group C which is characterized by slow infiltration rate when fully wetted. The soils have moderately fine to fine texture and a slow rate of water transmission which gives them a high runoff potential (Arnold *et al*, 2011).

Besides serving as a growth medium for vegetation that influences surface hydrology, soil also serves as a major source of water to streams and rivers. Essentially the soil particle size, distribution, and the soil structure determine the moisture characteristics of a particular soil class. Soil particles are mainly composed of sands, silts, clays, and organic matter. The fraction of each soil particle type in a given soil sample determines the soil moisture characteristics as well as the movement of water in the soil (Arnold *et al*, 2011). In general, the larger the soil particle, the better the soil drainage will be. On the other hand the fine sized soil particles such as clays and silts tend to have poor drainage characteristics but are able to hold onto more water and for a longer period which they release more slowly and thereby ensuring a longer period of water supply to a stream (Neitsch *et al*, 2011).

CHAPTER 2
LITERATURE REVIEW

2.1 Introduction

This Chapter presents an overview of the background information on climate and climate change, impacts of climate change on water resources, the role of forests in the climate system and hydrologic cycle, concept of water yields, climate modelling, and hydrological modelling.

2.2 Climate Variability and Climate Change

In the IPCC (2007) fourth assessment report climate is defined as the statistical description of weather elements in terms of the mean and variability over a period of time ranging from months to millions of years with thirty years being the classical averaging period of climatic variables in order to properly determine the climate of a particular region. Climate, whether global, regional or local, is a result of interactions between the five components of the climate system; the atmosphere, seas and oceans, ice, land surface and vegetation cover, and surface waters (Wilson *et al*, 2009; Miller and Yates, 2005). The interactive response of the components of the climate system to the external energy sources such as the solar radiation and anthropogenic changes in any of the components of climate system, determine the global as well as regional background conditions that govern the world's weather and climate patterns.

Solar radiation is the main source of energy that drives the climate system (UNEP, 2009c). This energy passes through and interacts with the atmosphere before reaching the earth's surface. Any human induced changes to the composition of the atmosphere and the land surface constitute another significant source of energy to the climate system because it alters the energy balance between the incoming solar and outgoing terrestrial radiation. Approximately 240 Wm^{-2} of solar energy reaches the top of the earth's atmosphere from the sun (Le Treut *et al*, 2007). About two thirds of this energy is absorbed by the earth's surface, and thus warms the atmosphere and the earth's surface while the rest is reflected back to space. To balance the incoming solar radiation, the Earth must radiate the same amount of energy back to space but in the long wave radiation band.

Within the atmosphere there are some gases that include carbon dioxide (CO_2), methane (CH_4), nitrous oxide (N_2O), chlorofluorocarbons (CFCs), hydro-fluorocarbons, per fluorocarbons, halons and sulphur hexafluoride that selectively absorb radiation. These gases are transparent to the incoming short wave radiation but absorb and radiate long wave radiation resulting in enhanced warming of the Earth's surface and the atmosphere. These gases are referred to as greenhouse gases (GHGs) because of their natural "greenhouse effect" that keeps the earth's average surface temperature approximately 33°C warmer than what simple radiation Physics would suggest for a transparent atmosphere (IPCC, 2007).

The climate of a particular region is determined by both local and distant processes with solar radiation providing the principal forcing. The effect of the solar radiation is generally modulated by the composition of the atmosphere and various feedback processes within the global climate system such as the extent of the surface vegetation cover (Wilson *et al*, 2009). Any changes in the characteristics of any of the components of the climate system such as the concentration of GHGs in the atmosphere or in the extent of the earth's vegetation cover as a result of changes in land use, shifts the energy balance between the external Radiative Forcings (RF) and the components of the climate system. This shift in the energy balance leads to long term changes in the global and regional climate patterns as reflected by positive trends in the global temperature which serves as an indicator of climate change (IPCC, 2007).

IPCC (2007) defines climate change as a change in the state of climate in terms of the mean and or variability over an extended period of time typically decades or longer due to internal or external forcings. Internal forcings of climate change include changes in either one or more of the five components of the climate system while external forcings include natural processes such as volcanic activities, changes in the solar cycles, or external Radiative Forcings (RF) resulting from persistent anthropogenic changes in the composition of the atmosphere or the physical properties of the land surface (Bates *et al*, 2008; Miller and Yates, 2005). Increased concentrations of GHGs in the atmosphere and changes in the albedo of the earth's surface as a result landuse change have resulted in enhanced global average surface temperatures. Climate is driven by solar radiation energy; if the energy reaching the climate system changes, the climate also changes. For example if the orbital distance of the Earth from the sun increases, the radiation reduces and the mean temperatures of the climate system decrease bringing about cold periods all over the globe known as glacier periods. On the other hand if the orbital distance decreases the energy increases bringing about warm periods.

Human activities have contributed to global climate change by altering the composition of the Earth's atmosphere through emission of GHGs and aerosols, and to regional climate change by changing the surface albedo through socio-economic activities that have altered the Earth's vegetation cover. Changes in the composition of the atmosphere have led to a warming of the climate system and thereby changing both the global and regional climate patterns (Forster *et al*, 2007; UNEP/IVM, 1998). It has been demonstrated beyond reasonable doubt that climate is changing due to anthropogenic green house gases (IPCC, 2007).

Globally we are already committed to future substantial climate change over the next thirty years and beyond. This change is likely to accelerate over the rest of the 21st century (IPCC, 2007). It is therefore critical that more detailed regional climate change predictions be made available so that cost effective adaptation and appropriate mitigation actions can be planned. If this is not done, the costs of adaptation are potentially high both economically and socially (Trenberth *et al*, 2007; Met Office, 2007). In this study detailed regional climate change predictions were made for the East African region with special focus on Sondu River catchment area. Results of these predictions were used to analyse the impacts of climate change on surface water yields from the Mau forest complex catchments.

Since the beginning of the industrial revolution in the 1750s, human activities, primarily the burning of fossil fuels and clearing of forests in pursuit of socio-economic activities have greatly intensified the natural green house effects. This has resulted in the addition of more of the long-lived greenhouse gases (LLGHGs) into the atmosphere and the destruction of carbon dioxide sinks leading to a general global warming condition (IPCC, 2007; McBean and Motiee, 2006; Miller and Yates, 2005). This has contributed to a shift in the radiation balance between the incoming solar radiation and the outgoing terrestrial radiation.

Climate of Kenya is mainly associated with the northward-southward movement of Inter Tropical Convergence Zone (ITCZ). The great differences in the country's topography bring about considerable variations of climate throughout Kenya. The sun crosses the Kenyan territory twice in a year where it is overhead on March 21st on its way to the northern hemisphere and again on September 21st on its way towards the southern hemisphere. The ITCZ is expected to be most active about a month after the sun is overhead. These periods correspond to the two main rainy seasons in Kenya; the long rains in the March-April-May (MAM) and the short rains in the

September-October-November (SON) seasons respectively (Mogaka *et al*, 2006; Okoola, 1996; JICA, 1992).

The climate of a region largely determines the volume of water supplied to the drainage basin through precipitation as well as the proportion of that precipitation that is returned to the atmosphere through evapotranspiration before it is converted into runoff, stream flow and ground water storage (Neitsh *et al*, 2011). Climate determines the drying power of the atmosphere (net radiation and vapour pressure deficit) and the supply of water in the catchment (intercepted by the canopy or stored on ground surface or in the soil) both of which influence evapotranspiration (Creed *et al*, 2014) Kenya's mean annual rainfall is about 500 mm varying between 250 mm in the ASALs in the northern and eastern parts of the country to over 2000 mm in the highlands and mountain ecosystems and generally follows the seasonal pattern of the ITCZ (Kiangi *et al*, 1981; Omeny *et al*, 2008). The area west of the Rift Valley that includes the Mau Forest Complex (MFC) and Lake Victoria Basin (LVB), has an almost continuous rainfall pattern with most of the rain falling between April and August which is the long rain season in this region.

In order to estimate the impacts of climate change on river flows from the MFC, different scenarios of future climate conditions are required as inputs to a hydrological model to calculate the corresponding discharges. Different future climate change scenarios are described in the next section.

2.2.1 Climate Change Scenarios

Climate change scenarios are representations of the difference between possible future climate scenarios, based on climate projections resulting from responses of the climate system to scenarios of greenhouse gas and aerosol emissions as simulated by climate models, and the baseline climate (Wilson *et al*, 2009; Jones *et al*, 2004). They are plausible descriptions of what future states of the global climate would be like based on coherent and internally consistent set of assumptions concerning the driving forces and their key relationships (Miller and Yates, 2005). Such scenarios are usually constructed for explicit use in investigating the potential impacts of anthropogenic climate change.

The driving forces of anthropogenic climate change include concentrations of GHGs and aerosols coming from emissions resulting from social-economic and technological developments (IPCC, 2007). There is increasing evidence that human activities have already influenced climate and that this influence continues to increase and will continue to increase into the future leading to hitherto unknown climate scenarios (Mitchell *et al*, 1999). It is therefore important to establish possible future scenarios of climate change resulting from human activities in order to be able to assess the economic, ecological and social consequences of climate change and thereby decide on the necessary adaptive and mitigative measures.

2.2.2 Emissions Scenarios

Many climate change scenarios examine the climate associated with the levels of concentration of carbon dioxide and other greenhouse gases in the atmosphere as a result of natural and anthropogenic emissions. Emissions scenarios are driven by demographic, technological and economic development. Since it is difficult to know exactly how anthropogenic emissions will change in future, IPCC (2000) developed and adopted plausible representations of future emissions of radiatively active substances in its Special Report on Emissions Scenarios (SRES) which are used to drive the Global Circulation Models (GCMs) to develop climate change scenarios using combinations of demographic change, social, economic, and broad technological developments. SRES provide a full suite of GHGs and aerosols that comprise the four scenario families namely A1, A2, B1 and B2 (Figure 2.3) which are all considered equally sound. Scenarios within each family follow the same storyline of how the world will develop demographically, socially, economically, technologically, and environmentally. It is important to note that none of these scenarios includes any future policies that explicitly address climate change. They are therefore only used for analysis of possible climate change, its impacts, and options to mitigate the climate change (IPCC, 2007; Jones *et al*, 2004).

SRES A2 scenario, which has been used in this study, is based on a continuously growing population scenario of about 8.2 billion by 2020, 11.3 billion by 2050, and 15.1 billion by 2100 (IPCC, 2000). SRES A2 scenario describes a heterogeneous world characterised by: a world of independently operating and self-reliant nations, a regionally oriented economic development, and a slower and more fragmented technological change and improvement to per capita income (CCC, 2009). This is the worst case scenario that assumes business as usual and no change in policy.

2.3 Impacts of Climate Change on Water Resources

Water resources are inextricably linked with climate (Kundzewicz *et al*, 2007). Hence the prospect of global climate change has serious implications on water resources and regional development. The driving force of the hydrologic cycle, the lifeline of all the world's water resources, is the state of the climate. The hydrologic cycle, whose main components are evapotranspiration, precipitation and runoff, is an integral component of the climate system. The climate of a watershed provides the moisture and energy inputs that control the water balance and determine the relative importance of the different components of the hydrologic cycle (Neitsch *et al*, 2011).

The character of precipitation is greatly influenced by temperature and other climatic elements (Bates *et al*, 2008). Elevated global mean temperatures will therefore result in changes in regional precipitation, evapotranspiration, and soil moisture content. Changes in precipitation, temperature and evaporative demand, the most dominant climate drivers for water availability, will alter the flow regimes in streams and rivers as well as the ground water recharge rates and depths of ground water tables and consequently water quality and quantity will be altered (Akhtar *et al*, 2008; Whitehead *et al*, 2006). This will have an impact on the freshwater yields from the existing storage facilities such as the MFC water tower (IPCC, 2007; UNEP/IVM, 1998).

Changes in river flow volumes as well as lake and wetland levels due to climate change are primarily functions of changes in the volume and timing of rainfall and the rate of evapotranspiration (Miller and Yates, 2005). Several studies of the potential effects of climate change on river flow volumes have been published (Bates *et al*, 2008); most of them are concentrated in Europe, North America and Australia with a small number from Asia but very few in Africa.

Widespread increases in heavy precipitation events as a result of global warming have been observed even in places where total precipitation amounts have decreased (IPCC, 2007). As climate changes, the probability of certain weather events occurring are also affected. Some become more frequent and intense while others become less frequent and mild. Depending on the condition of the other climatic parameters some regions will experience heavy precipitation events while others will experience less than average precipitation events. Both of these changes will impact on the freshwater yields from water catchment areas.

A consequence of global warming from human-induced enhanced green house effect will be increased evaporation subject to availability of adequate surface moisture. More precipitation will be associated with higher temperatures since the water holding capacity of the atmosphere will increase with the warmer conditions. According to the IPCC (2007) fourth assessment report the water holding capacity of the atmosphere increases by about 7% for every $1^{o}C$ increase in temperature. Climate model simulations and empirical evidence, indicate that warmer climates due to increased water vapour in the atmosphere, will lead to more intense precipitation events even when the total annual amount is reduced slightly (IPCC, 2007).

According to Bates *et al* (2008) in the IPCC technical paper IV, trends in major river basins in the world indicate about 17% decrease in runoff. Observational records and climate projections provide abundant evidence that fresh waters are vulnerable and have the potential to be strongly impacted by climate change, with wide ranging consequences for human societies and ecosystems. Impacts of particular concern to Africa are related to water resources, food production, human health, and desertification. Water resources are a key area of vulnerability affecting water supply for household use, agriculture, and industry. Population growth and degradation of water resources are significant threats to water security in many parts of Africa including Kenya.

One of Kenya's water vulnerability is the high variability with which annual rainfall occurs (Mogaka *et al*, 2006). This is further exacerbated by the extensive degradation of the country's water resources such as the Mau forest complex water tower (Kinyanjui, 2011). Alterations of the forest cover in this catchment are believed to have altered the catchment's response to rainfall, the ultimate source of water in a catchment area. This is likely to be made worse by climate change as heavy rains are expected to lead to increased erosion from degraded land surface leading to accelerated siltation, reduced recharge of groundwater and therefore loss of water storage capacity in Kenya's largest water tower (Mogaka *et al*, 2006).

2.4 The Role of Forests and their Impact on Water Resources

FAO (2008) warns that climate change will have a significant effect on hydrology and water resources manifested in increased catastrophes such as floods, droughts and landslides, all of which may be influenced by changes in forest cover. The world's forests fulfill many roles such as providing renewable raw materials and energy, providing environmental services that include maintaining biodiversity, protecting land and water resources and also play a critical role in climate change mitigation (Jacobs *et al*, 2007). Increasing areas of the world's forests, which occupy about 20 per cent (FAO, 2006) of the total land area, are designated primarily for soil, water and environmental conservation. Locally, forests protect water resources by reducing surface erosion and sedimentation, filtering water pollutants through infiltration and forest litter, regulating water yields, moderating floods, enhancing precipitation and mitigating salinity (GOK, 2010b). Although most of the earth's surface is water, there is insufficient water to meet the needs of the world's human population. The United Nations International Year of Fresh Water (IYF) in 2003 highlighted the critical need to have water available in the right place, in sufficient amounts, of sufficient quality and at the right time. In this regard forests play a key role.

Forests trap radiation in their multilayered canopies which results in a net warming of the ecosystem **(**GOK, 2010b). This warming generates more thermal turbulence above the forest cover which favours the formation of clouds and hence rainfall over and close to the forest areas. Evapotranpiration from the forests adds to the existing atmospheric moisture thus enhancing cloud formation. By intercepting precipitation, evaporating moisture from vegetative surfaces, transpiring soil moisture, capturing fog water and maintaining soil infiltration capacity, forests play a key role in influencing the amount of water available from groundwater, rivers and streams, and other surface water bodies (FAO, 2008). When rainfall reaches the forest floor surface, it distributes into various components that include surface runoff, interflow, ground water recharge, continental evaporation, and plant intake. In this regard, forests play a major role in moderating and regulating the hydrology of river catchments since they influence how the net rainfall is distributed into the various stream flow components.

By maintaining and improving soil infiltration and water storage capacity, forests influence the timing of fresh water delivery to streams and rivers in a catchment area. Along streams and rivers, forests provide a shading effect thereby reducing water temperatures and hence loss through evaporation. As catchment land cover, protected and well managed forests tend to increase the hydrological safety of a water catchment area and thereby leading to water being one of the most important products of the forested watershed (FAO, 2008).

2.5 Concept of Water Yields

Water yield from a water resource system is the amount of water that can be abstracted from the system at a certain rate over a specified period of time such as one year (WMO, 2009). The rate at which water is abstracted may vary throughout the year depending on the level of demand which in most cases depends on the season. In the case of unregulated natural stream flow, and for the purpose of this study, water yield is that average amount of water flowing in the catchment's stream channel system (Kienzle and Mueller, 2013). For the purpose of this study, a catchment area is defined as that basin-shaped area bounded by natural features from which surface and sub-surface water flows into streams, rivers and wetlands.

Rivers are significantly influenced by the catchment areas that they drain (Hynes, 1975). They receive their water from these catchments and therefore any changes in the characteristics of the catchments such as vegetative cover as a result of anthropogenic activities influence the volume and timing of water flowing in the river system within the catchment area. The changes occurring in the catchment area are always reflected in stream flow volumes and timing. Rivers are more than just channels with flowing water; they are part and parcel of the catchment area that they drain. These catchment areas have vegetative covers which under natural conditions are usually forests. The character of the vegetative cover in the catchment area together with the characteristics of their soils influence the volume and timing of water in the stream channel system.

Studies conducted by Hewlett and Helvey (1970) in the Coweeta Forest in North Carolina and reported by Hynes (1975) indicate that watersheds under natural forest cover rarely experience surface runoff since the soils under such conditions absorb most of the rain water and then go on yielding it to the stream channels long after the rain has ceased. Most of the water that enters the stream channel system has been in contact with the soil for some time. The water yielded to the streams is therefore a function of the soil characteristics, the slope of the valley, patterns of rainfall, as well as the type and extent of the vegetative cover which collectively determine the flow regimes in the rivers. Removal of the natural forest cover affects soil characteristics and therefore the water yielding capacity of the watershed.

Maintaining natural forest and other vegetative cover on the river's catchment areas enhance infiltration and the subsequent ground water recharge. It has been shown that forested catchments provide natural water storage facilities that release water slowly into the river system at a near constant rate throughout the year and this ensures higher water yields even during the dry seasons (WMO, 2009). Land use changes as a result of human activities such as deforestation and afforestation on the upper catchments of a river alter the natural stream flow characteristics leading to significant impacts on water yields. The loss of forest cover contributes to less infiltration and hence less storage of water for release during the dry seasons. Observed changes in surface water yields reflect the impacts of human activities on the upper catchments. In totally natural forest catchments, the observed stream flows reflect the natural flow conditions. Any long term deviation from the natural flow may be considered as an indicator of human impacts on the catchment area as a result of population growth and the consequent landuse changes, climate change or a combination of both (Di Baldassarre *et al,* 2011; FAO, 2008).

2.5.1 Impacts of Climate Change on Water Yields

There is growing evidence that global temperatures are currently rising at an unprecedented rate (WMO, 2009) with some GCMs showing evidence that this could cause changes in annual precipitation. According to WMO (2009) scenario analysis for assessing the potential impacts of climate change on stream flow, and hence water yields from river catchment areas, indicate that in some areas stream flow could decrease by as much as 10% by the year 2015. Such changes could have significant impacts on the water yield characteristics of water resources systems. It is therefore prudent to anticipate the inevitable eventuality of climate change and perform scenario analysis for areas that are vulnerable in order to assess the impacts that climate change might bring on the water yielding capacity of water resources such as the Mau forest complex water tower.

It is important that impacts of climate change on water yields be considered in the long term planning of water resources systems and the related economic activities such as hydropower, water supply, and irrigation. To do this, water management bodies and policy makers need reliable hydrological information on the likelihood and magnitude of the impacts of climate change on the regional as well as local water cycle. Previously, such planning has assumed that climate will remain unchanged. This is no longer feasible since climate change is now a certainty (Mauser and Marke, 2009; IPCC, 2007).

2.5.2 Impacts of Forests on Water Yields

Availability of clean water in many parts of the world is increasingly becoming threatened by overuse, misuse and pollution (Kundzewicz *et al,* 2007). In this context, it is important that the relationship between forests and freshwater be understood and be accorded high priority in the management of water resources. Forests have value in conservation and regulation of water supplies, soil conservation, and maintaining the natural flow regimes of rivers (Edwards and Blackie, 1979).

Until a few years ago, forests and water policies were based on the assumption that under any hydrological and ecological circumstances, forest is the best land cover for maximising water yields, regulating seasonal flows and ensuring high water quality (FAO, 2008). Going by this assumption, conservation of forest cover in upstream watersheds would be the most effective measure for enhancing water availability as well as for preventing floods in downstream areas. However, research on forest hydrology conducted between 1980s and 1990s (FAO, 2008) suggest that generalisation about the impact of such land cover on downstream annual and seasonal flows can be misleading.

Forests and other vegetation cover influence the water cycle because they are a primary component for the exchange of water between the land surface and the atmosphere. They also influence the local hydrology since the uncompacted forest soils are known to have the highest infiltration rates and storage capacities (FAO, 2008). Under natural forest conditions, infiltration levels are well above net rainfall intensities and therefore surface runoff is rare. Soils under such conditions retain large volumes of water and this has the effect of reducing the frequency and the degree of overland flow and therefore flooding which in turn ensures supply of stream flow water from interflow (Muhati *et al*, 2008; Hoover and Hursh, 1943).

When natural forest vegetation is converted to agriculture and other land uses, both opportunities for infiltration and storage are greatly reduced in the long term as a result of subsequent soil compaction and the high rate at which precipitation reaches the ground surface; often exceeding the infiltration rates. This reduces the period within which the catchment can continue yielding water to the stream channel system after the rainfall has ceased (Hoover and Hursh, 1943). The overall effect that changes from forest to various other types of land uses have on the local hydrology depends on the combined effect of differences in interception, transpiration and infiltration capacities. Rain falling on a forest canopy reaches the ground below the canopy through three different routes namely: the direct through fall, stem flow and crown drip (FAO, 2008). These three components constitute the net precipitation on the forest ground. The rest of the rainfall is intercepted by the forest canopy and evaporated back into the atmosphere before reaching the forest floor. Interception therefore constitutes a net loss of water to the forest ecosystem.

Where the forest soils are undisturbed, the net precipitation infiltrates the soil through the thick layer of dead organic matter that is so characteristic of natural forests. Some of the infiltrated water eventually drains into ground water bodies that feed the springs and therefore maintain the base flow of streams that emanate from the catchments associated with the particular forest ecosystem while the rest is lost from the soil through transpiration (UNESCO, 2000). Deforestation may therefore lead to a change in the hydrologic regime over an area such as Sondu basin where one of the issues is the conversion of natural forests to alternative land uses such as agriculture and settlements (Muhati *et al*, 2008).

Over the last four decades, the Sondu basin has undergone environmental changes on account of both natural and anthropogenic factors. The natural factors include prolonged droughts while anthropogenic factors include the massive deforestation of the South West Mau forest (Kinyanjui, 2009) that forms the upper catchment area which is the source of the majority of the tributaries that feed the main River Sondu (Nyangaga, 2008).

2.5.3 Forests as Major Sources of Water

All mountain forests have an important role in stabilising water quality and maintaining natural flow patterns of rivers and streams originating from them (Bubb *et al*, 2004). Tropical mountainous cloud forests have the unique additional value of capturing water from condensation of low level clouds and fog. This stripping of windblown fog by the forest vegetation becomes especially important during the non-rainy season and in areas with low rainfall but frequent low level clouds (FAO, 2008). The vegetative surfaces of these forests provide a *net* for capturing horizontally moving precipitation from fog and clouds and adding it as fog drip and stem flow to the water budget of the catchment. In this way such forests act as sources of water.

Of all forest types, cloud forests such as the Mau forest complex have the closest interrelationship with fresh water because of their role in water production and erosion control. On large mountains in equatorial regions away from the coast, cloud forests are usually found at high elevations of between 2000 m and 3000 m above sea level as is the case in Mau forest complex in Kenya. Such cloud forests have great value as water fountains and they have been described as water towers (KWTA and DRSRS, 2013; DRSRS and KFWG, 2006). Mau forest complex, Mt Elgon, Cherengani Hills, Aberderes and Mt Kenya forests are all examples of cloud forests which constitute the five water towers in Kenya. They act as stabilizers that guard the water quality and maintain the natural flow of the rivers that emanate from them (Bubb *et al*, 2004, UNESCO, 2000).

Within the cloud forest, transpiration is relatively low since most of its vegetation comprises small leaves and often wet and water logged soils both of which minimise loss by transpiration. This helps to minimise water uptake from the soil by the trees and hence reduces the overall water use by the forests. This reduction in forest water use translates to a twofold gain in water for cloud forests: the water stripped from the clouds and fog and added to the catchment water budget, and the water saved through minimised transpiration. As a result of this, discharge levels of streams and rivers that emanate from cloud forest catchments tend to be higher for a given rainfall event and also more dependable during dry periods than for those that emanate from other types of catchments (Bubb *et al*, 2004).

The amount of extra water obtained from cloud forests varies according to rainfall patterns, topography, frequency or persistence of clouds and the extent to which the clouds are wind driven (Bubb *et al*, 2004). Removal of cloud forests such as the Mau forest complex leads to loss of that extra water captured by the forest. Trees and other vegetation in cloud forests are of hydrological importance because of their water capturing function. This water capturing function is normally eliminated when deforestation takes place since deforestation results in the raising of the cloud base due to the associated drop in the total forest evapotranspiration (ET) and the rise in air temperature in the affected areas. Such a situation was observed in Luquillo Mountains, Puerto Rico in 1989 when Hurricane Hugo defoliated the forests. The rise of the average level of the cloud base gradually disappeared within a few months after the leaves regenerated (UNESCO, 2000).

Under humid conditions in cloud forests, the net precipitation ranges from 65% to 80% of the incident rainfall in the lower montane forests that do not experience much cloudy conditions. This figure may rise to between 115% and 130% of the incident rainfall in the case of the more exposed cloud forests. More often the net rainfall total in both upper and lower montane forests are in the range of 80% to 100% of the incident rainfall. This suggests an additional increase of about 15% to 20% of ordinary rainfall that comes from cloud and fog interception. This is an equivalent of about 300 mm to 600 mm of additional water for annual rainfall of about 2000 mm to 3000 mm and it can go up to between 50% and 60% under more exposed circumstances for the same rainfall range (Bubb *et al*, 2004; UNESCO, 2000). Low water levels in rivers originating from the Mau forest complex have been blamed on excision and encroachment of the forest catchments. This study investigated the extent to what this assertion is true.

2.6 Climate Modelling

Climate modelling involves the use of computer models of the climate system to simulate the interactions of the components of the Earth's climate system and their response to solar radiation between the top of the atmosphere and the surface of the Earth (Jones *et al*, 2004). A climate model is a mathematical representation of the climate system, expressed as computer codes and run on a powerful computer to provide a comprehensive and quantitative description of how atmospheric temperature, air pressure, winds, water vapour, clouds, and precipitation respond to the solar heating of the atmosphere (IPCC 2007; Jones *et al*, 2004).

Climate models also include equations that describe how the greenhouse elements of the atmosphere keep the lower atmosphere warmer than would ordinarily have been the case by providing a radiative blanket that controls how fast the Earth cools by loss of terrestrial infra-red radiation to the outer space. Climate models compute energy transfers through the atmosphere, the direct and indirect effects of aerosols, changes in snow cover and sea ice, the storage of heat in soils and oceans, surface flux of heat and moisture, and the large scale transport of heat and water by the atmosphere and oceans. Climate models are therefore fundamental research tools for understanding and predicting both natural and anthropogenic changes in the Earth's climate (Rummukainen, 2010; Wilby and Miller, 2009). This section describes the principle behind computer climate models, their construction and operation. The models are divided into two levels; global and regional climate models.

2.6.1 Global Climate Models

Global Climate Models (GCMs) are numerical representations of the climate system based on its physical, chemical and biological properties, component interactions and feedback mechanisms (Wilson *et al*, 2009). They are used to examine the influence of increased concentrations of GHGs and aerosols in the atmosphere through simulation of the processes and interactions that define the global climate. The three-dimensional climate system is represented by primary equations that describe the movement of energy and momentum, conservation of mass and water vapour behaviour (Met Office, 2002). The primary equations are governed by: the first law of thermodynamics, Newton's second law of motion, continuity equation, and the ideal gas law respectively (Wilby and Miller, 2009).

GCMs such as the Hadley Centre third generation Coupled Model (HadCM3) are used to solve these equations at discrete grid-points (Figure 2.5) across the surface of the Earth and between coupled layers in the atmosphere and ocean using concentration scenarios of GHGs as inputs to make climate projections (Wilson *et al*, 2009; Jones *et al*, 2004; UNEP/IVM, 1998). Figure 2.5 shows the horizontal and vertical grids together with the physical processes that are represented in a GCM.

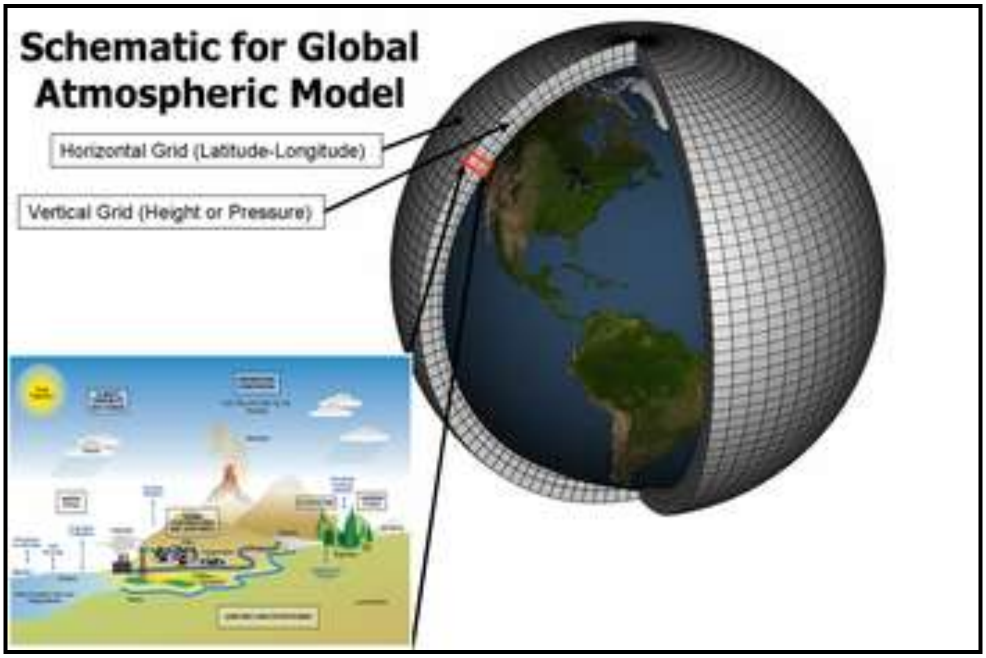

Figure 2.1: Model Earth-atmosphere system and the processes represented in a GCM (Source: Met Office, 2002)

Solving these equations for a large number of grid-points over the entire globe requires enormous computing resources such as the use of supercomputers. The task is usually made more manageable by using coarse horizontal resolutions of about 300 km (Rummukainen, 2010) with 20 levels in the vertical in order to reduce the number of grid points and hence the number of computations. As a result of this, GCMs are unable to capture and resolve the local details of the mesoscale forcings that include orographic and other local climate drivers such as inland waters and convection which are known to influence regional climates and which are important for climate change impacts assessments at regional and national levels; which is what is required for this study (Jones *et al* 2004).

GCMs can therefore only effectively address the large-scale climate features such as the general circulation of the atmosphere and the ocean, as well as the continental patterns of temperature and precipitation but cannot represent the fine scale details that characterise local climates in many regions of the world (Wilby and Miller, 2009; IPCC, 2007). One of the widely accepted methods of adding the finer details that are missed out by GCMs is the use of Regional Climate Models (RCMs) which are the subject of the next section

2.6.2 Regional Climate Models

Regional climate models (RCM) are comprehensive high resolution physical models of the atmosphere and land surface containing representations of the important processes in the climate system as found in GCMs but cover a limited area of the globe. They cover about 5000 km by 5000 km with a typical horizontal resolution of 50 km (Wilson *et al*, 2009; IPCC 2007; Jones *et al*, 2004). RCMs complement GCMs as climate change impacts research tools by making it possible to access the finer spatial details that are required for climate change impacts studies as is the case in the current study. The greatest potential in the use of RCMs for the study of climate processes and impacts studies derives from their high horizontal resolution which improves the representation of such landscape features as mountain ranges, lakes, as well as other surface features like land use change. All these are known to give rise to local and regional circulation and precipitation features, as well as modifying winds, temperature, and other climate variables (Rummukainen, 2010).

RCMs operate by taking the coarse resolution information from GCMs and developing temporary and spatially fine-scale information using their higher resolution representation of the climate system (Jones *et al* 2004). They therefore allow direct modelling of the dynamics of the physical systems that characterise the climate of the region of interest. The high resolution details required for impacts studies can be obtained from RCMs such as the third generation Hadley Centre Regional Climate models (HadRM3) which are higher resolution versions of the Hadley Centre Coupled Models (HadCM3) but covering a limited area of the globe (Jones *et al* 2004).

The concept of downscaling is the main motivation behind the use of RCM. RCMs are downscaling tools that add fine scale information to the large scale projections of GCMs. They are used to obtain regional as well as the local scale details from the low resolution GCM outputs. RCMs are therefore more appropriate for resolving the small scale features of topography and land use that have a major influence on such climatological variables as rainfall and temperature. They act like magnifying glasses by being able to “see” more details than what the GCMs can “see” as shown in Figure 2.6 which presents the RCM nested on a GCM. The figure shows the ability of the RCM to downscale details that are required for hydrological modelling but are otherwise missed out by the GCM. The ability to “see” these details is derived from the RCM’s ability to downscale the low resolution GCM information to the regional and local scale level (Akhtar *et al*, 2009). Hence RCMs provide a more accurate representation of many surface features such as complex mountain topographies.

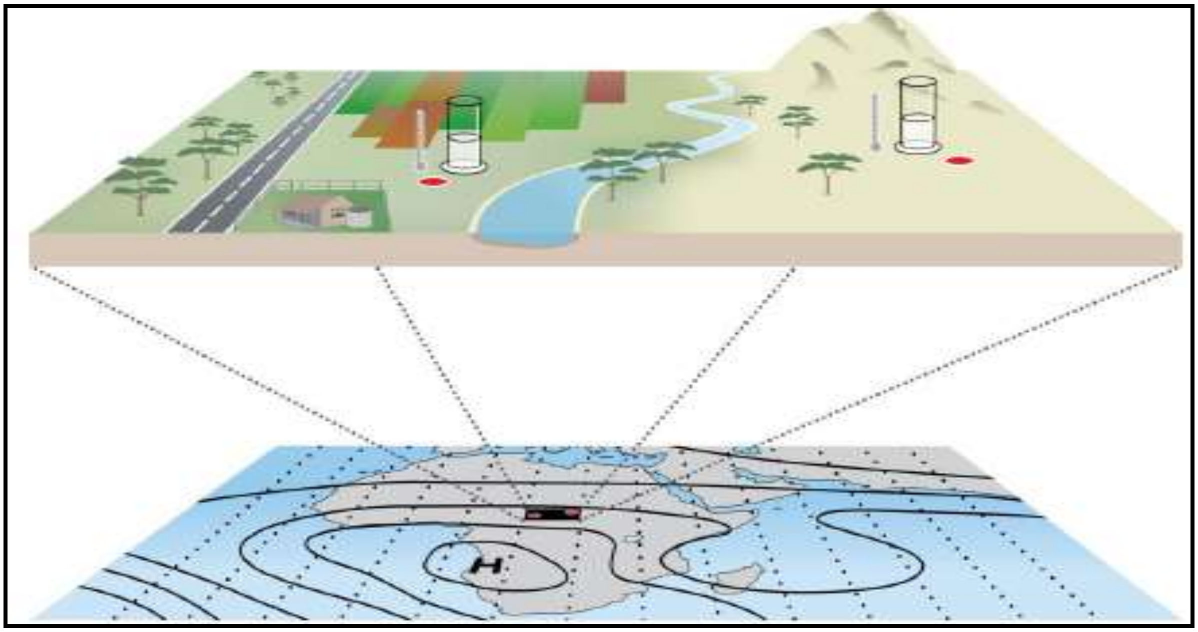

Figure 2.2: Regional Climate Model nested on a Global Climate Model
(Source: Met Office, 2002)

The primary assumption in regional climate modelling is that data from the large scale GCMs are used to drive the RCMs over limited domains such as the East African region that spans latitudes 12°S to 18°N and longitudes 22°E to 52°E (IPCC, 2007). Such a limited regional domain allows for the use of a higher resolution than that of the global domain without necessarily resulting to prohibitive increases in the computational costs. The data driving the RCMs are supplied as boundary conditions containing the basic set of lateral boundary conditions (LBC) data that include: temperature, moisture, and winds as well as the surface boundary conditions (SBC) data that include: sea surface temperature and sea ice (Wilson *et al*, 2009).

The climate of any region of the world is influenced by the rest of the globe. When large scale circulation impinges on a regional model domain such as the East African region, the boundary conditions of the RCMs consist of the information drawn from the GCM outputs. Since the two models have different resolutions, the RCM's domain should be large enough in order to allow for the desired phenomena related to topographic influence and the small scale atmospheric processes to develop. Still, the domain should not be too large as to allow the flow to deviate too much from the driving model (Wilson *et al,* 2009; Jones *et al,* 2004).

RCMs have some major limitations that include: the physics of the models; the quality of the driving boundary data derived from the GCMs; and the relatively high demand of computational resources which put a limit to the number, resolution, and length of RCM runs (Jones *et al*, 2004). Increased resolution carries a penalty in computational costs and a balance has to be reached between the cost and the quality of the RCM output (Rummukainen, 2010).

In order to get regional climate model projections for purposes of impacts studies, most RCM climate change runs have been done on time-slice modes (Christensen *et al*, 2007). This involves running the model for some recent past which may also be regarded as the present baseline period such as 1961-1990 and some future scenario period such as 2021-2050. Differences in the modelled climates are then analysed for climate change signals such as changes in the 30-year means of seasonal or annual and variability of climate elements such as temperature and precipitation. In addition to the time-slice modes, continuous periods spanning more than a century are currently being addressed through transient model runs. Such runs cover different time horizons from the past to 2100. Such continuous regional climate projections are useful in modelling impacts on systems with long characteristic time-scales such as forests and other ecosystems (Rummukainen, 2010; IPCC, 2007), and the Hadley centre has configured the third generation HadRCM3 for the purpose of Providing Regional Climates for Impacts Studies (PRECIS), over any region of the world as described in the next section.

2.6.3 PRECIS RCM

Providing Regional Climates for Impacts Studies (PRECIS) is a regional climate model developed by the Hadley Centre of the United Kingdom (UK) Meteorological Office based on the atmospheric component (HadAM3) of the third generation of the Hadley Centre's Coupled Climate Model (HadCM3). PRECIS RCM is used to generate regional scale climatology at high spatial resolutions of 50 km or less. PRECIS is extensively described in Wilson *et al* (2009) and Jones *et al* (2004). The model is a portable, flexible and easy-to-use atmospheric and land surface regional climate modelling system covering a limited area with high horizontal resolution that ranges between 25 and 50 km (Ahktar *et al,* 2009; Met office, 2008; Islam *et al*, 2008; UNFCCC, 2005).

PRECIS provides countries with a means of generating detailed, high quality climate predictions for their own regions at the earliest possible stage. The model is driven by prescribed LBCs which provide dynamical atmospheric information at the latitudinal and longitudinal edges of the model domain. LBCs comprise the standard atmospheric variables of surface pressure, horizontal wind components, atmospheric temperature and humidity which are updated every six hours. SBCs are only required over ocean and inland water points, where the model needs time series of sea surface temperatures and ice extents (Jones *et al*, 2004).

Timely access to detailed climate change scenarios is vital in developing countries where economic stresses are likely to increase vulnerability to impacts of climate change especially in the field of surface water yields from given precipitation events. PRECIS has special characteristics that make it adaptable for use in Kenya that include; the high resolution which makes it viable for both the Mau forest complex and Sondu River catchment area which are about 4000 km^2 and 3050 km^2 respectively; requirement of a basic resource of one fast personal computer, a reliable power supply and expertise to maintain the hardware and support system (Wilson *et al*, 2009).

PRECIS RCM has been applied in the Eastern Africa domain to project future climate scenarios for the region by among others Omondi, (2010) and Sabiiti (2008). Omondi (2010) used the model to generate regional climate scenarios over Eastern Africa while Sabiiti (2008) used it to simulate climate scenarios over Lake Victoria basin (LVB). They both found that the model performed fairly well in the region. Their results were on a regional level and could therefore not be used to determine the impacts of climate change at a river basin scale. The present study goes further to use the products of PRECIS RCM on a daily time-step to analyse the impacts of climate change on water yields from the Mau forest complex using a hydrological model.

PRECIS is a mathematical model of the atmosphere and land surface which is of higher resolution relative to GCMs. The advective and thermodynamic evolution of winds, pressure, temperature, and moisture are simulated by the model while including the effects of many other physical processes such as the land surface cover. The model comprises four modules: the atmospheric dynamics, the model grid, the physical parameterizations, and the boundary conditions which operate in harmony to accomplish the simulations. Details of these modules can be found in Jones et al (2004); only brief highlights are given in the following subsections**.**

2.6.3.1 Atmospheric Dynamics

Atmospheric dynamics is the part of the model which uses the three fundamental conservation principles; conservation of momentum, conservation of mass, and conservation of energy to simulate the evolution of the model state variables namely atmospheric pressure, winds, temperature, and moisture (Met Office, 2009). The conservation of momentum principle is a consequence of Newton's second law of motion. The horizontal equation of motion (Equation 2.1), which is used to simulate the advection of air round the atmosphere, is derived from Newton's second law of motion.

$$\frac{DU}{Dt} = -2\Omega \times U - \frac{1}{\rho}\nabla p + g + F_r \quad \ldots\ldots 2.1$$

$\frac{DU}{Dt}$ is the acceleration of an air parcel, $-2\Omega \times U$ is the Coriolis force, $-\frac{1}{\rho}\nabla p$ is the pressure gradient force, g is the effective gravity, and F_r is the friction force.

At the synoptic scale level of the model, the magnitudes of vertical motion due to conservation of momentum are small compared to horizontal velocities and accelerations. Hence hydrostatic balance (Equation 2.2), which essentially relates variation of pressure with height above the Earth's surface, was assumed.

$$\frac{\partial p}{\partial z} = -\rho g \quad \ldots\ldots 2.2$$

$-\frac{1}{\rho}\frac{\partial p}{\partial z}$ is the pressure gradient force, ρ is the mean density of the atmosphere, and g is the effective gravity. The presumed balance between the two forces, pressure gradient force and gravity, gives an air parcel neutral buoyancy and hence the model assumes no explicit vertical motion (Met Office, 2009). PRECIS is constructed in such a way that mass is conserved. The atmosphere is considered to be a continuum of gas and therefore does not allow any voids. As a consequence of conservation of mass principle, vertical motions are inferred in the atmosphere whenever the horizontal wind field is diverging or converging. The continuity equation (Equation 2.3) relates changes in density with divergence in the wind velocity field. From this equation, vertical motions which were ignored in the hydrostatic balance assumption are inferred. Areas of convergence or divergence in the horizontal diagnose a vertical transfer of mass between vertical layers (Met Office, 2009).

$$\frac{1}{\rho}\frac{D\rho}{Dt} + \nabla.\vec{U} = 0 \quad\ldots\ldots\ldots\ldots\ldots\ldots\ldots\ldots\ldots\ldots\ldots\ldots\ldots\ldots\quad 2.3$$

ρ is the mean density of air, $\vec{U}$ is the horizontal wind component.

The evolution of heat and moisture is modelled using the principle of conservation of energy which is applied to a moving atmospheric element according to the first law of thermodynamics (Equation 2.4) and the equation of state (Equation 3.18). By the first law of thermodynamics, the amount of heat added to a parcel of air is exactly balanced by the work done in increasing its volume and the change in internal energy.

$$dq = du + dw \quad\ldots\ldots\ldots\ldots\ldots\ldots\ldots\ldots\ldots\ldots\ldots\ldots\ldots\ldots\ldots\ldots\ldots\ldots\ldots\quad 2.4$$

dq is the differential increment of heat added to the air parcel, dw is the differential increment of work done by the air parcel, and du is the differential increase in internal energy of an air parcel. The equation of state (Equation 2.5) relates vapour pressure, specific volume, and temperature.

$$pv = RT \quad\ldots\ldots\ldots\ldots\ldots\ldots\ldots\ldots\ldots\ldots\ldots\ldots\ldots\ldots\ldots\ldots\ldots\ldots\ldots\ldots\quad 2.5$$

p is the atmospheric vapour pressure, v is the specific volume of the atmosphere, R is the gas constant, and T is the absolute temperature. These equations were used to describe the evolution of the model prognostic variables: temperature, pressure, moisture, and winds in both space and time.

The atmospheric component of the model has 19 levels which include the real geography, full diurnal and annual cycles, and a land surface scheme that allows for prescribed geographically varying vegetation and soil covers. Cloud amounts and radiative properties, snow cover and soil moisture are all modelled interactively by this model (Wilson *et al*, 2009; Jones *et al,* 2004). The model equations are solved numerically on a three-dimensional grid spanning the area of the model domain and the depth of the atmosphere. In this regard the model simulates values of the diagnostic variables at discrete and evenly spaced points in time.

The time gap between each of these points is the model's time step. The model time step is critical to its numerical stability and as such the length of the model time step must be chosen with utmost care. The model's numerical integration scheme is designed to adhere to the rule that a parcel of air can only be allowed to move at most one grid box length in one time step. Beyond this speed, the model becomes numerically unstable. The time step therefore depends on the models resolution and the maximum possible wind speed. Assuming the maximum possible wind speed of 166 ms^{-1}, the 50 km model resolution gives a time step of 5 minutes (Wilson *et al*, 2009).

2.6.3.2 Model Grid

The importance of the model grid lies in the fact that all the model output results are based on this grid. The vertical component of this grid uses a hybrid coordinate system where each vertical level is specified as a linear combination of a terrain following height-above-the-surface coordinate and an atmospheric pressure coordinate (Figure 2.8). In total there are 19 vertical levels with the lowest four being purely terrain following and the uppermost three being purely pressure levels. Within each pressure level is a horizontal grid which uses a latitude-longitude spherical polar coordinate system with regular grid spacing in both latitudinal and longitudinal directions. Within this horizontal grid, the wind variables are simulated on a grid that is offset by half a grid box in each direction from all other variables (Met Office, 2009).

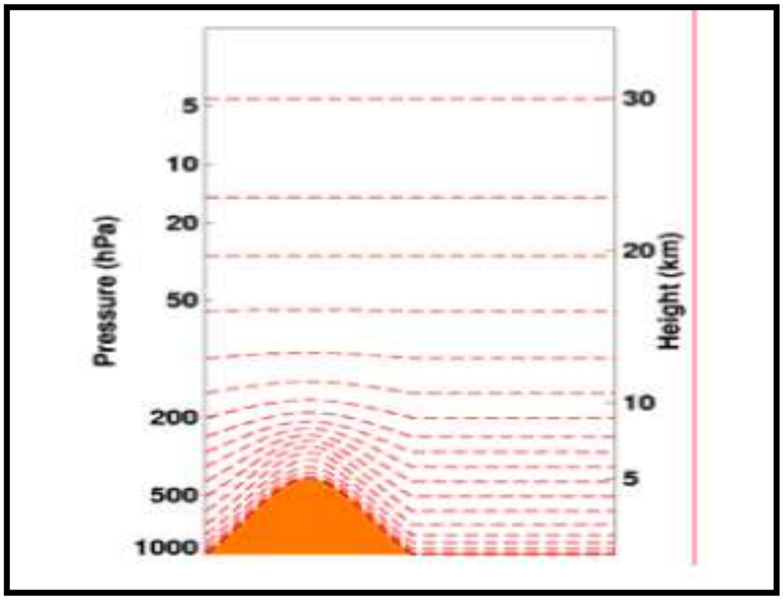

Figure 2.3: Schematic view of PRECIS vertical hybrid co-ordinate system
(Source: Met Office, 2009)

2.6.3.3 Physical Parameterisations

This section of the model is the one that deals with the effects of many of the physical processes in the atmosphere and the land surface of the climate system which are not accounted for by the grid scale simulation of the prognostic variables by the atmospheric dynamics but which are likely to change and therefore drive climate change (Figure 2.9). There are important processes that occur in the atmosphere on spatial scales that are much smaller than those which are resolved by the discrete three-dimensional grid on which the dynamical equations are simulated (Met Office, 2009).

The model deduces the grid scale effects of these unresolved processes from the large scale state of the atmosphere as given by the prognostic variables arising from the solutions of the dynamical equations. This procedure is called parameterisation. The physical parameterisation within the PRECIS model is split into six main groups comprising; clouds and precipitation, radiation, atmospheric aerosols, boundary layer, land surface, and gravity wave drag (Met Office, 2009).

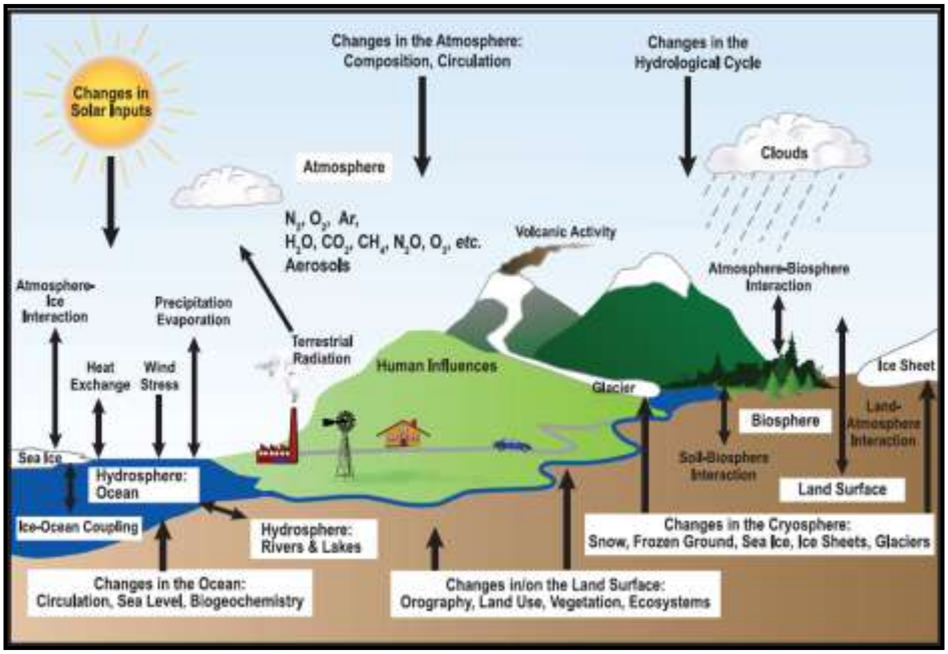

Figure 2.4: Schematic view of the components of climate system parameterized by the GCM (Source: IPCC, 2007)

Cloud formation and precipitation are portioned into two types within the model: the large scale and convective processes. Cloud water droplets may be liquid or frozen in the model as is the case with precipitation. Both solid and liquid precipitations are diagnosable from the large scale as well as the convective precipitation schemes. The large scale cloud model calculates the fraction of the grid box which is cloudy and also the mixing ratios for cloud water and cloud ice. The model holds explicit values of fractional cloud cover together with separate values for cloud water and cloud ice mixing ratios. Cloud water is converted to precipitation through a process known as auto-conversion (Met Office, 2009).

Frozen precipitation is assumed to fall as soon as it is formed. Evaporation and melting of precipitation is allowed to take place to the extent that temperature and humidity of the lower layers allow, with the attendant cooling of the environment by the latent heat exchange. Dynamical assent is the main cause of large scale cloud formation followed by radiative cooling and turbulent mixing (Met Office, 2009).

Convective clouds are modelled in the PRECIS model by an up-draught dependent on a vertical temperature instability balanced by a precipitation-induced cool downdraught. The resulting cloud in a grid box is also dependent on pressure, humidity, and aerosol particle concentration. Convection will continue as long as the air within the cloud continues to be buoyant. Dilution of the cloud is represented by entrainment of environmental air. Before the cloud detrains completely at the level where the air parcel ceases to be buoyant, the remaining mass, heat, water vapour, and cloud/ice are completely mixed into the environment at the cloud top. A single cloud model is used to represent a number of convective plumes within the grid box. Precipitation within the grid square is diagnosed if: the cloud water content exceeds a critical amount, and the cloud depth exceeds a critical value which is set at 1.5 km and 4 km over the sea and land surface respectively (Met Office, 2009).

The atmosphere is driven by solar radiation and therefore an accurate representation of radiative processes is essential for climate models. In the atmosphere, radiation is divided into short wave and long wave components. PRECIS models short wave and long wave energy fluxes separately. In the model, daily, seasonal and annual cycles of insolation are simulated. The model then treats short wave and long wave radiative fluxes differently within the atmosphere.

The short wave radiation flux depends essentially on the solar zenith angle, cloud cover, and the albedo of the surface. Long wave fluxes depend on the amount and temperature of the emitting medium as well as its emissivity. In order to account for the different effects of the atmospheric radiatively active constituents, long wave radiation is considered in six wave bands, and short wave radiation in four wave bands. Clouds interact quite significantly with both short wave and long wave radiation (Figure 2.11). Figure 2.11 is a schematic representation of atmospheric radiative processes showing the short wave radiation (red arrows) and long wave radiation (blue arrows) together with their interactions with the climate system. Their effects depend upon the fractional cover, height, phase, and the water content of the atmosphere (Met Office, 2009).

PRECIS simulates the spatial distribution and the life cycle of atmospheric sulphate aerosols. This simulation scheme is particularly important in the climate context since the presence of such particles tends to give a surface cooling effect and thus offset some of the GHG induced warming in some areas. There are two mechanisms simulated in the model which can lead to this cooling effect: the direct effect which involves scattering of insolation, and the indirect effect which involves increased cloud albedo due to smaller cloud droplets. In both cases more radiation is reflected back to space. Hence less energy reaches the surface of the earth leading to the cooling of the Earth's surface (Met Office, 2009).

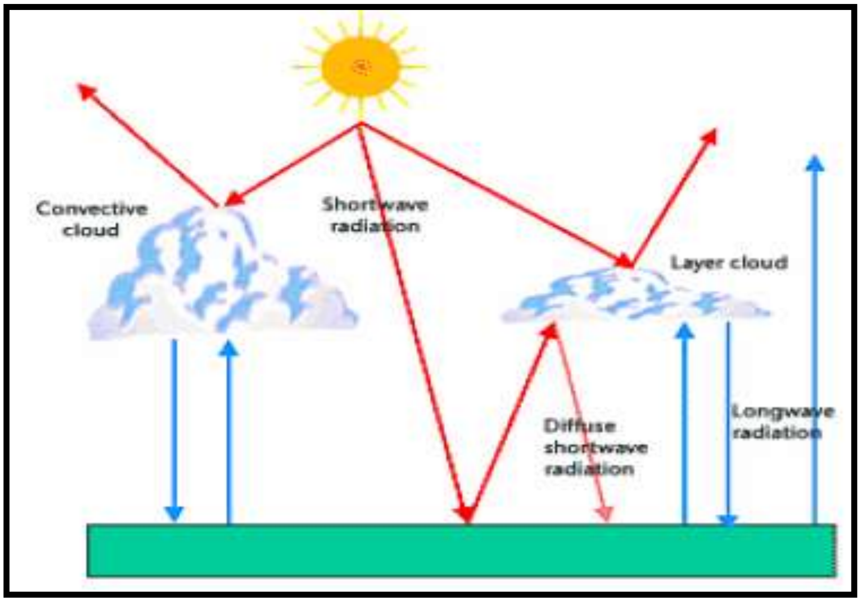

Figure 2.5: Schematic view of PRECIS atmospheric radiative processes
(Source: Met Office, 2009)

Within the PRECIS model, sulphate (SO_4) particles are simulated as existing in the atmosphere ultimately due to emission of chemicals from the surface of the Earth. The main sources of these emissions include; the natural sources such as sulphur dioxide (SO_2) from volcanic eruptions and the dimethyl sulphate (DMS) released from the surface of oceans, and also anthropogenic sources such as sulphur dioxide (SO_2) released from fossil fuel burning mainly in the industrial areas. In both cases the model has time varying source data that form part of the model spanning both current and future climates. Within the atmospheric boundary layer, heat, moisture, and momentum are mixed by sub-grid scale turbulence (Figure 2.12). This turbulent mixing is dependent on the large scale vertical temperature stability of the atmosphere as well as the nature of the land surface. Fluxes of momentum between the atmosphere are also modelled (Met Office, 2009).

The surface processes involve the exchange of heat and moisture between the surface of the Earth, the vegetation, and the atmosphere. The water stored in the vegetation canopy is released either to the soil via through-fall or back to the atmosphere via evaporation. The amount of water the canopy in the grid can hold depends on the vegetation types present in the grid box (Wilson *et al*, 2009).

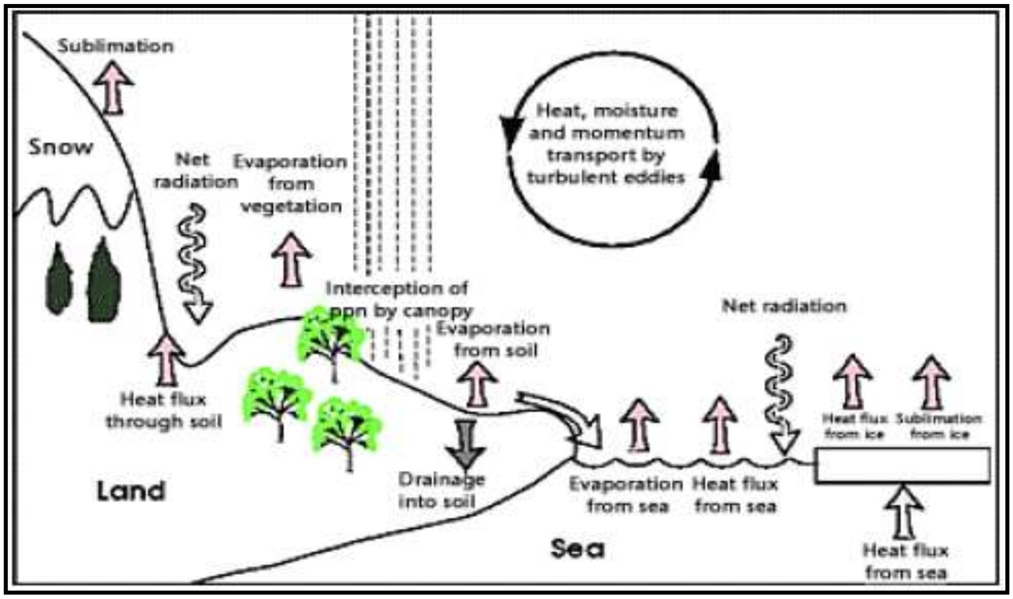

Figure 2.6: Schematic view of PRECIS boundary layer process (Source: Met Office, 2009)

Wilson *et al* (2009) further explains that beneath the earth's surface, fluxes of heat and moisture are simulated with a four-layer soil hydrology and thermodynamics model. This includes the effects of the roots which are responsible for removing water from the soil back to the atmosphere via transpiration. Vegetation plays an active role in the hydrology of the surface. Land surface vegetated canopy interacts with insolation and precipitation and also provides fluxes of heat and moisture to the atmosphere and transformation of rainfall to runoff. When precipitation falls, some of it is intercepted by the canopy of the vegetation while the rest reaches the soil surface via through fall. The part of precipitation reaching the soil surface is absorbed by the soil unless the intensity is too high or the soil is already saturated: in which case part of it is transformed into surface runoff into the river system, lakes and other reservoirs in the basin.

PRECIS model assigns each land point characteristics according to the soil type and the vegetation types within the grid box. These characteristics are important in the calculation of the heat, moisture and momentum fluxes at each of the grid points. The soil temperature and moisture are calculated in four separate levels (Figure 2.13). According to Met Office (2009) the temperature of the soil will change according to the radiation balance at the soil surface. Each of the land points has a value of the soil moisture content in four layers of different thicknesses (Figure 2.13). This moisture content is altered according to the rate of evapotranpiration and the amount of precipitation at that land point. Soil water is mainly lost through evapotranpiration and this is usually limited by the amount of the available soil moisture.

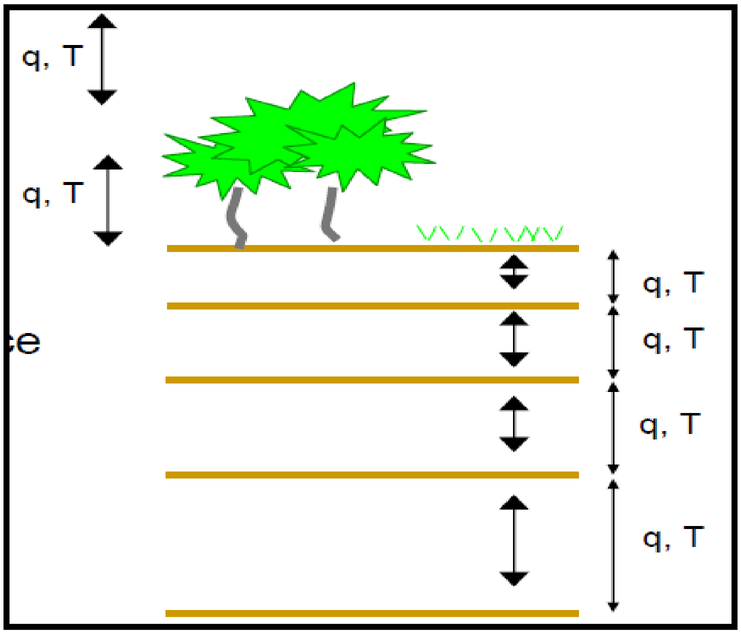

Figure 2.7: Schematic view of PRECIS exchange of heat (T) and moisture (q) between the Earth's surface, vegetation, and the atmosphere as well as the sub-surface fluxes (Source: Met Office, 2009)

The final parameterisation scheme in PRECIS is that of the Gravity Wave Drag (GWD) which describes how flow over mountain ranges generates sub-grid scale atmospheric waves. These waves form on the lee side of mountain ranges and propagate vertically, eventfully reducing atmospheric stability which exerts a drag on the prevailing horizontal flow. PRECIS includes within itself a scheme that parameterises GWD whereby flow over mountains in stable conditions excites waves. It is important to take GWD into account because, without the GWD scheme and the drag that it generates, the jet streams in the model tend to be too strong. This feeds back to unusually deep surface depressions leading to poorer surface climatology. The GWD scheme therefore reduces the strength of jet streams and causes surface depressions to be less deep and therefore quicker to fill than would otherwise have been the case (Met Office, 2009).

2.6.3.4 Boundary Conditions

The model boundary conditions supply information on all the factors that are external to the model but which, nonetheless affect the simulations. Boundary conditions are required to provide the meteorological remote forcing of the regional climate and consistent information on atmospheric composition. It is by carefully specifying the boundary conditions that the model is made to simulate future climates. The boundary conditions are categorised into three main classes namely the lateral boundary conditions (LBCs), the initial conditions, and other boundary conditions (Wilson *et al*, 2009; Met Office, 2009; Jones *et al*, 2004).

LBCs are meteorological conditions at the lateral boundaries of the RCM domain. They are large-scale time-dependent data that constrain the prognostic variables of the model at its edges throughout the simulation. LBC state variables include: winds, temperature, water vapour, surface pressure, and aerosol concentrations. Data for LBCs come either from existing GCM integrations or from reanalysis. In this study existing integrations from the European Community Hamburg Model version4 (ECHAM4) and European centre for medium range weather forecasts Re-Analysis of 40 years (ERA40) LBCs were used and applied over a buffer zone of 8 grid points in width, at the edge of the model domain and model output results over this rim were removed from the analysis of the output data (Wilson *et al*, 2009).

The initial condition is the instantaneous state of the atmosphere and land surface from which the model can progress forward in time. The model needs to be provided with initial data of all prognostic variables which come from the same source as the LBCs. This helps to prevent physical inconsistencies between the initial state of the interior of the model domain and the initial information being fed in at the lateral boundaries. Such inconsistencies would cause instabilities that could result in model failure (Met Office, 2009).

Other boundary conditions include the rest of the boundary conditions which provide information that is required throughout the duration of the model simulation. Spatially, these boundary conditions are applied either at the surface or throughout the depth of the atmosphere. Spatial surface boundary conditions include; land-sea mask, orographic fields, vegetation, and soil characteristics. Constant boundary conditions throughout the depth of the atmosphere include the sulphur cycle. Temporal boundary conditions are applied either as data which is constant in time or as time varying data. Time-varying data at the surface include: SST and Ice fractions, anthropogenic SO_2 emissions, and dimethyl Sulphide (DMS). Time varying data applied throughout the depth of the atmosphere include the Tropospheric ozone (Wilson *et al*, 2009).

The standard output data from PRECIS, which serve as the inputs to the impact models, are available as time series of temperature and precipitation in daily or hourly time-steps as well as climatic mean values for the river basin of interest such as Sondu, depending on the user's needs (Wilson *et al*, 2010; Akhtar *et al*, 2008; Jones *et al* 2004). In this study, the output data were time series of daily temperature and rainfall over the Sondu catchment area which was averaged over three grid boxes representing Kericho, Keresoi, and Sotik stations.

2.7 Hydrological Modelling

Hydrological modeling involves the application of mathematical equations to model the physical responses of a watershed to meteorological events in a catchment area (Miller *et al*, 2007). For purposes of hydrological modelling the river basin is the most appropriate scale to focus on for analyses of water management issues using hydrological models. Hydrological models are simplified, conceptual representations of a part of the hydrological cycle which attempt to represent the physical processes that control the transformation of rainfall (input) to runoff and streamflow (output) (Droogers *et al*, 2006). Streamflow and runoff are interplays of many physical processes that include: the hydrological, meteorological, topographical, landuse/landcover, and soil parameters. Hydrological models relate streamflow and these parameters and are primarily used for hydrologic predictions as well as for understanding the hydrologic processes in a catchment area (Mutua, 1986). The most important climatological inputs required for the calibration and validation of hydrological models are temperature and precipitation (Akhtar *et al*, 2009). These climatological inputs can be derived from either observational records or from simulations of regional climate models such as PRECIS.

This study examines stream flows, rainfall, and deforestation in the Sondu River basin, whose upper catchment comprises SWM forest, the largest of the 22 blocks (UNEP, 2009a) comprising the MFC in Kenya. The study examines how stream flows and hence surface water yields vary under different climate and forest cover scenarios. The extent of variation in stream flow was quantified in terms of changes in the mean as a central value. In order to achieve this, a physically based hydrological model: the Soil and Watershed Assessment Tool (SWAT) was applied. SWAT is extensively described in Neitsch *et al (*2011) and Winchell *et al (*2010) and Arnold *et al* (1998). Only a brief description of the model is given in the next sub-section.

2.7.1 The SWAT Model

The Soil and Watershed Assessment Tool (SWAT), developed by Arnold *et al* (1998) is a conceptual continuous time model. The model was initially developed to assist water resources managers in assessing the impacts of management on water supplies, sediments and agricultural chemical yields in large and complex watersheds with varying soils, land use and management conditions over long periods of time. Currently the model is also being used to estimate impacts of climate change and land use management on water resources. Arnold *et al* (1998) have described SWAT as a basin scale hydrologic model that is computationally efficient, allows considerable spatial detail, requires readily available inputs, is continuous time model that operates on a daily time step at basin scale level, is capable of simulating land management scenarios, and gives reasonable results. As input data, SWAT requires specific information about weather, soil properties, topography, vegetation, and land management practices that take place in the watershed from which the physical processes associated with water movement are directly modelled.

SWAT model includes procedures to describe how carbon dioxide concentration, precipitation, temperature and humidity affect plant growth, evaporation, and runoff generation among others and can therefore be used to investigate climate change impacts (Abbaspour *et al*, 2009). SWAT allows a number of different physical processes in the watershed to be simulated. These include: hydrology, weather, sedimentation, soil temperature, and agricultural management among others (Arnold *et al*, (1998). This study focused mainly on the simulation of the hydrology process.

In order to facilitate efficient analysis of the impacts of different watershed management scenarios on water yields, SWAT has been integrated with a Geographical Information System (GIS) interface (Van Griensven, *et al*, 2012). The SWAT-GIS interface allows the model to preserve the spatial nature of topography, soils, and land use databases and thereby preserving the distributed nature of the model parameters. This improves the model's effectiveness in developing input data files from GIS coverage (Neitsch *et al,* 2011). In this study, ArcSWAT2009 was used under ArcGIS9.3 environment for project development.

SWAT model is a very flexible and robust tool that can be used to simulate a variety of watershed problems (Van Griensven, *et al*, 2012). Its ability to replicate hydrologic and pollutant loads at a variety of spatial scales on an annual and monthly basis has been confirmed in numerous studies (Faramarzi *et al*, 2009; Gassman *et al*, 2007; Schuol *et al,* 2008; Githui, 2008). The model is capable of performing continuous, long-term simulations for watersheds composed of various sub-basins with different soils, land uses, crops, topography, and weather among others (Neitsch *et al,* 2011).

The basic model products simulated by SWAT include weather, surface runoffs, return flow, percolation, evapotranspiration, transmission loss, pond and reservoir storage, crop growth and irrigation, and ground water flows. For efficient simulation of these components, the model delineates the watershed into a number of sub-basins and Hydrological Response Units (HRUs). This is particularly important where different parts of the watershed are dominated by different land uses and soils so that they impact on the catchment's hydrology differently (Neitsch *et al,* 2011). Spatial heterogeneity in a watershed is taken into account in the model by considering information from the DEM, soil, and LULC maps (Schuol *et al*, 2008). Watershed delineation into different components is briefly discussed in the next sub-section.

2.7.2 Watershed Delineation

SWAT model automatically delineates the area of study using the Digital Elevation Model (DEM) data under ArcGIS environment. The purpose of delineation is to establish the general watershed attributes over the catchment area such as land area and stream network which are known to control a diversity of physical processes at the watershed level (Arnold *et al*, 2011). The model sets these parameters at default values. Model users can change the default values within certain limits to better reflect the characteristics of the watershed being studied.

2.7.2.1 Sub-Basin

Sub-basins constitute the first level of sub division during the watershed delineation process. They possess a geographical location in the watershed and are spatially related to one another. Each of the sub-basins delineated contains at least one area with unique soil-landuse-slope combination called Hydrological Response Unit (HRU), a tributary channel and a main channel. Input information for each sub-basin is organised into climate, groundwater, the main channel draining the sub basin, and HRUs. The next sub-section presents a brief discussion of the HRUs, main channels, canopy storage, potential evapotranspiration and sub-surface flow (Winchell *et al,* 2010).

2.7.2.2 HRU

Hydrological Response Units (HRUs) are lumped land areas within the sub-basin that comprise unique land cover, soil, slope, and management combinations. They allow the SWAT model to capture the diversity of land use and soils within each sub-basin. Unlike the sub-basins, HRUs are not geographically located; rather they represent the total area in the sub-basin with a particular land use, management system, soil and slope characteristics (Winchell *et al,* 2010; Arnold *et al,* 1998). Though HRUs may be scattered all over the sub-basin, SWAT lumps all of them together to form one HRU for each of the sub-basin delineated.

SWAT simulates the overall hydrologic balance for each HRU, including canopy interception of precipitation, partitioning of precipitation, snowmelt water, and irrigation water between surface runoff and infiltration, redistribution of water within the soil profile, evapotranspiration, lateral sub surface flow from the soil profile, and return flow from shallow aquifers. All these are then aggregated at the sub-basin level and then routed to the associated reach and catchment outlet through the channel network to obtain the total runoff and water yields for the whole watershed (Faramarzi *et al,* 2009; Abbaspour *et al,* 2009). This has been found to increase the accuracy as well as giving a much better physical description of the catchment's water balance (Winchell *et al,* 2010).

Two options are available within the SWAT model for determining the HRU distribution: single or multiple HRUs for each sub-basin. Winchel *et al,* (2010) have explained that a single HRU for a sub-basin uses the dominant land use category, soil type, and slope class within the sub-basin to simulate the HRU. Multiple HRU option on the other hand allows the user to specify a threshold level for the land use, soil and slope datasets that are used to determine the number of HRUs in each of the sub-basin. These thresholds can be based on a percentage of area or on absolute area.

Multiple HRU option was selected for this study and the percentage area threshold option was adopted on account of its robustness. The purpose of the thresholds is to eliminate minor land uses, soil types, and slopes in each sub-basin. In this study, 5% land use, 20% soil type, and 20% slope class threshold settings were selected to define the HRU in each of the sub-basin in the Sondu catchment area. These thresholds set percentages of the total sub-basin area that land use, soil type and slope class must cover for them to qualify to be included as part of the HRUs in the sub-basin.

2.7.2.3 Main Channels

SWAT associates one main channel with each sub-basin in a watershed area. Runoff from the sub-basin enters the channel network of the watershed in the associated main segment. Flow in a catchment is classified as either overland or channelized. The main channel processes modelled by the SWAT model in a watershed include the movement of water, sediment and other constituents in the stream network, in-stream nutrient cycling and in-stream pesticide transformations (Winchel *et al*, 2010). In this study, focus was mainly on the movement of water in the stream network and how it is impacted on by climate change and land use/land cover change.

2.7.2.4 Canopy Storage

Plant canopy significantly affects infiltration, surface runoff and evapotranspiration. The influence exerted by the plant canopy on these hydrologic processes is a function of the density of the plant cover and therefore any human activity that interferes with this density also impacts on the hydrology of the watershed area (Neitsch *et al*, 2011). During a rainfall event, canopy interception traps a portion of rainfall which therefore does not reach the surface. When SWAT calculates surface runoff using the Soil Conservation Service (SCS) curve number method, canopy interception is lumped in the term for initial abstraction. The maximum amount of water that can be in the canopy storage varies from day to day as a function of Leaf Area Index (LAI).

2.7.2.5 Potential Evapotranspiration

The amount of Potential Evapotranspiration (PET) depends on a combination of several parameters such as solar radiation, condition of the sky, and wind speed among others. Numerous methods of estimating PET have been developed and three of these have been incorporated in the SWAT model; the Penman-Monteith, the Priestly-Taylor and the Hargreaves methods (Neitsch *et al,* 2011). The three methods differ in the number of required inputs necessary for the calculation of PET. Penman-Monteith requires solar radiation, air temperature, relative humidity and wind speed as the necessary inputs for calculation of PET. The other two methods require fewer inputs with the Priestly-Taylor method requiring solar radiation, air temperature and relative humidity while Hargreaves method only requires temperature. Penman-Monteith method (Table 2.1) was used in this study on account of its robustness (Neitsch *et al,* 2011).

Table 2.1: Summary of input variables required by SWAT to calculate PET in a watershed

Variable	**Definition**
IPET	Potential evapotranspiration method
WND_SP	U_z: Daily wind speed (ms^{-1})
CO_2	CO_2: Carbon dioxide concentration (PPmv)
MAX TEMP	T_{mx}: Daily maximum air temperature (^oC)
MIN TEMP	T_{mm}: Daily minimum air temperature (^oC)
GSI	$g_{l,mx}$: Maximum leaf conductance (ms^{-1})
FRGMAX	$fr_{g,mx}$: Fraction of maximum leaf conductance achieved in the vapor pressure deficit specified by Vpd_{fr}
VPDFR	Vpd_{fr}: Vapor pressure deficit corresponding to value given for $fr_{g,mx}$ (kp_a)

(Neitsch et al, 2011)

2.7.2.6 Surface Runoff

Surface runoff, which is a function of many variables including rainfall intensity and duration, soil type, soil moisture content, land use practice, land cover, and slope, occurs whenever the rate of water application to the ground surface exceeds the rate of infiltration. Considering the numerous variables governing the generation of surface runoff, lumped conceptual models are useful approaches of its analysis and prediction. Among the conceptual models developed for the analysis and prediction of surface runoff, the Curve Number (CN) method is one of the most widely accepted (Neitsch *et al,* 2011). SWAT provides two options of estimating runoff; SCS curve number procedure, and the Green and Ampt infiltration method. In this study SCS curve number procedure was adopted on account of its simplicity, predictability, stability, its reliance on only two parameters, and its responsiveness to major runoff producing watershed properties (Neitsch *et al,* 2011; Ponce and Hawkins, 1996).

Table 2.2: Typical SCS curve numbers for moisture condition II

Land use	**Hydrologic Soil Group**			
	A	**B**	**C**	**D**
Fallow	76	85	90	92
Row crops	67	76	82	86
Pasture	52	70	80	84
Woodlands	43	65	77	82
Farmlands	59	74	82	86

(Source: Neitsch et al, 2011)

SCS curve number is a function of the soil's permeability, land use, and antecedent soil moisture conditions (Neitsch *et al,* 2011). Lower values of the curve number indicate low runoff potential while higher values indicate increasing runoff potential. The lower the curve number the more permeable the soil is (Ponce and Hawkins, 1996). For the Sondu catchment area, average moisture condition, normally called moisture condition II was adopted. Typical curve numbers for moisture condition II are listed in Table 2.2 below for various LULC classes and hydrologic soil groups. The LULC classes applicable for this study are Row crops that represent herbaceous rainfed shrub (Tea), Woodlands that represents forests, and farmlands that represents herbaceous rainfed crop (maize).

2.7.2.6 Sub-Surface Flow

Water that enters the soil through infiltration may move in three different pathways that are important in this study; removal from the soil by plant uptake and evaporation, percolation past the bottom of the soil profile to become aquifer recharge, and lateral flow that contributes to stream flow. Of the three pathways, plant uptake of water removes most of the water entering the soil profile (Neitsch *et al*, 2011). Therefore any change in plant cover in a watershed will alter its hydrology. This study investigated the effects of deforestation of the basin whose upper catchment comprises the SWM forest block which has been heavily deforested in the last three decades (Kinyanjui, 2009).

The amount of water held by the soil and made available to traverse the above pathways is a function of the soil structure which determines the drainage characteristics of the soil. The water content of the soil can range from zero when the soil is oven-dried to a maximum value (ϕ_{soil}) when the soil is saturated with water (Neitsch *et al*, 2011). Table 2.3 shows the water content for three soil types as a fraction of the total volume of the soil under different moisture conditions. Water in the soil can flow under saturated or unsaturated conditions. Saturated flow is driven by gravity while unsaturated flow is driven by the gradient arising due to adjacent areas of high and low water content (Neitsch *et al*, 2011). SWAT directly simulates saturated flow only where the model records the water contents of the different soil layers but assumes that the water is uniformly distributed within any given layer.

Table 2.3: Water contents for various soils at different moisture conditions

Texture	**Clay content**	**Water content**		
		Saturation	**Field capacity**	**Permanent wilting point**
Sand	3%	0.40	0.06	0.02
Loam	22%	0.50	0.29	0.05
Clay	47%	0.60	0.41	0.20

(Source: Neitsch et al, 2011)

SWAT models the bypass flow, the vertical movement of free water along macropores and cracks through unsaturated soil horizons, by calculating the crack volume of the soil matrix for each day of simulation. On the days on which rainfall events occur, infiltration and runoff are calculated using the SCS curve number method. If any runoff is generated, it is allowed to enter the cracks and macropores where a volume of water equivalent to the total crack and macropore volume for the soil profile may enter the profile as bypass flow (Neitsch *et al*, 2011).

2.7.7 SWAT Input Data Requirements

Among the data required to run the SWAT model are: the Digital Elevation Model (DEM), land cover, soil types, and climatic data that include: daily precipitation, maximum and minimum temperatures, solar radiation, wind speed, and relative humidity. From the DEM, the catchment and sub-basins are generated automatically as well as the stream network under the ArcGIS environment. The sub-basins, land cover and soils are then used to obtain the HRUs.

Meteorological data at one or more locations in the basin provide sufficient information to run the SWAT model (Droogers *et al,* 2006). A weather generator incorporated within the SWAT model generats a set of daily weather data for each sub-basin. The daily weather data generated by the model may be used to fill in missing data in the observed records or as inputs in simulating stream flow. The precipitation generator component within the SWAT model weather generator uses a first order Markov Chain model to define a day as wet or dry by comparing a random number generated by the model to the monthly wet-dry probabilities input by the user. If a day is classified as wet, the amount of precipitation is generated from a skewed distribution or a modified exponential distribution (Neitsch *et al,* 2011).

Maximum and minimum air temperatures and solar radiation are generated from a normal distribution where a continuity equation is incorporated into the generator to take account of temperature and radiation variations caused by dry and rainy conditions. Here maximum air temperature and solar radiation are adjusted downward when simulating rainy conditions and upwards when simulating dry conditions so that the long term generated values for the average monthly maximum temperature and solar radiation agree with input averages. A modified exponential equation is used to generate daily mean wind speeds given by the mean monthly wind speed data. The relative humidity model uses a triangular distribution to simulate the daily average relative humidity from the monthly means. Just like in the case of temperature and radiation, the mean daily relative humidity is adjusted to account for wet and dry day effects (Neitsch *et al,* 2011).

The outputs from the SWAT model simulations are distinguished into stream flow output and land based results. Stream flow includes the water quality and volume aspects for every stream in the basin. The land based results are extensive and include all the components of the hydrological cycle as well as the erosion, pollutants, nutrients, and crop growth. All this information is available per sub catchment as well as per HRU (Neitsch *et al,* 2011).

No matter what type of problem is being studied using the SWAT model, water balance is the driving force behind all that happens in the watershed. Simulation of the hydrology of a watershed by the SWAT model may be separated into two main divisions namely the land phase and the water routing phase of the hydrologic cycle (Figure 2.14). The land phase mainly controls the water movement into the land and therefore determines the amount of water that is eventually routed in the channel network of the watershed to the outlet (Neitsch *et al*, 2011).

As rainfall descends, it may be intercepted and held in the vegetation canopy or it may fall directly to the soil surface. Once the rain water reaches the soil surface, it infiltrates into the soil profile or flows overland as surface runoff. The surface runoff moves quickly towards the stream channel and contributes to short term stream responses. Infiltrated water is held in the soil profile for some time before making its way back to the atmosphere through evapotranspiration or to the surface water system via underground paths (Figure 2.14).

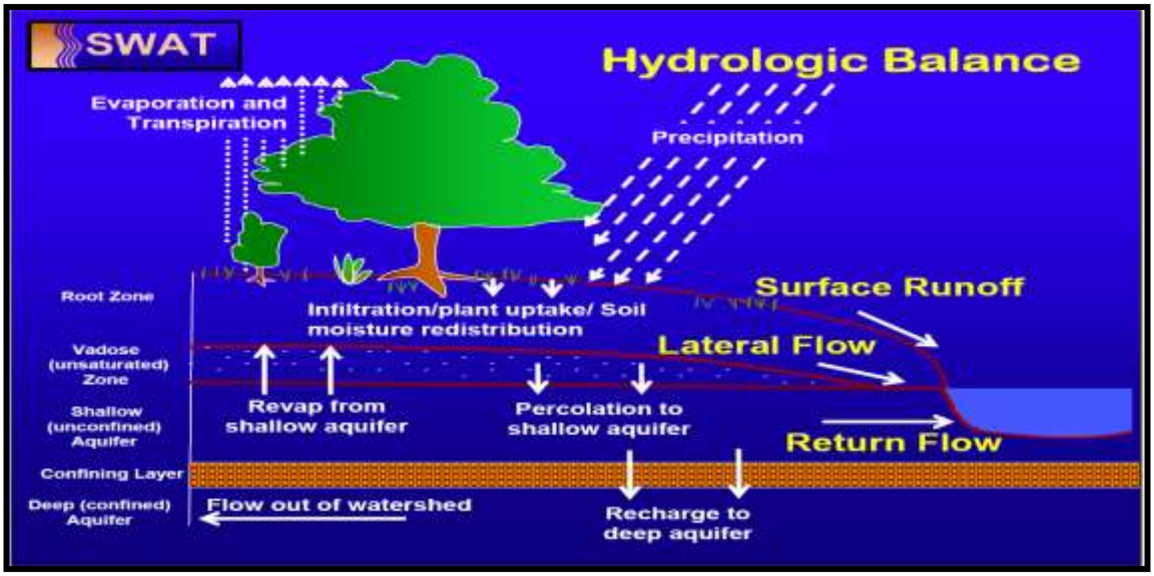

Figure 2.8: Schematic view of the hydrologic cycle (Source: Neitsch et al, 2011)

The land phase of the hydrologic cycle has two main components which control the amount of water that goes into and out of the system. Precipitation, which is a climatic event, controls the amount of water that goes into the system. This water has to be distributed over the land and has to be moved along the land with great accuracy. This greatly depends on the condition of the land surface which is determined by the land cover (Neitsch *et al*, 2011).

The SWAT model has been applied in various basins in different countries and has been calibrated and validated for different conditions (Gassman *et al*, 2007). It is used for modelling basins in the USA and is actively supported by the USDA Agricultural research service (Droogers *et al*, 2006). SWAT model applications are found in various fields in the Nile basin (within which the area of study is located) particularly those that require direct assessments of anthropogenic climate change, and other influences on a wide range of water resources (Ndomba *et al,* 2008; Setegn *et al,* 2009).

In Kenya, SWAT model has been applied in at least three river basins namely Tana Sondu (Jayakrishnan *et al*, 2005), Nyando (Sang, 2005), Tana (Jacobs *et al*, 2007), Nzoia (Githui, 2008) and Mara (Mango *et al,* 2011) basins and found to perform reasonably well. Jayakrishnan and others (2005) used the SWAT model to model the hydrology of river Sondu as part of assessment of the impacts of modern technology on the small holder daily industry. Sang (2005) applied SWAT model to evaluate the impact of changes in landuse, climate and reservoir storage in the Nyando basin. He established that the model performed well in the simulation of streamflow and could also be used to assess the impacts of landuse and climate change on the flooding in the basin. Jacobs and others (2007) used the SWAT model to simulate the environmental implications of reforestation in the higher elevations of the upper Tana basin as part of mitigation of economic damage studies. Githui (2008) applied the SWAT model in the Nzoia river basin as part of the assessment of impacts of environmental change studies. Mango and others (2011) applied the SWAT model to investigate the response of the head water hydrology of the Mara River to scenarios of continued deforestation and projected climate. In the current study, the SWAT model was used to assess the impacts of climate change and deforestation on surface water yields from the Mau forest catchments in Kenya.

2.7.8 SWAT Model Calibration and Validation

Before the model could be applied and used for decision making, it was necessary to first calibrate and validate the model to reduce the uncertainty in the model simulations. This was done following a two-step procedure namely the model sensitivity analysis followed by the model parameter calibration and validation (Winchel *et al,* 2010).

2.7.8.1 Sensitivity Analysis

Hydrologic models such as SWAT usually have a large number of model input parameters which make model calibration a complex and tedious process. It is therefore important that prior to the model calibration and validation exercise, sensitivity analysis be carried out for purposes of identifying and ranking the parameters on the basis of the magnitude of influence on streamflow response in the catchment (Moriasi *et al*, 2007; Gassman *et al*, 2007).

SWAT model has two broad categories of parameter sensitivity analysis namely; local sensitivity analysis, and global sensitivity analysis. The local sensitivity analysis identifies the output responses by sequentially varying each of the model input parameters by a certain fraction while all other parameters are held at their nominal values. This is also referred to as One-factor-at-a-Time (OAT) method. On the other hand the global sensitivity analysis explores the entire range of the model parameters where all the parameters are simultaneously perturbed and their interactions and impacts on the model output are investigated (Glavan and Pintar, 2012; Veith and Ghebremichael, 2009; Griensven, 2005).

The sensitivity analysis method used in SWAT combines both local and global sensitivity analyses by using the Latin Hypercube and One-factor-at-a-Time (LH-OAT) sampling where the LH samples are used as the initial points for an OAT design. The LH generates the distribution of the plausible collections of parameter values from a multidimensional distribution and hence forms the initial points for an OAT design (Liew and Veith, 2010; Griensven, 2005).

The LH simulation is based on Monte Carlo simulation and uses stratified sampling for efficient estimation of the model outputs. The parameter distribution in the LH simulations is divided into N ranges each with a probability of occurrence of $\frac{1}{N}$ where each of the ranges is sampled once for purposes of generating random numbers. The random combinations of the model parameters are used to run the model N times in order to cover the N ranges (Griensven, 2005).

The OAT method integrates local to global sensitivity method. Only one parameter is changed for each model run so that the changes in the output are attributable to the changed input parameter. For n model parameters $n+1$ model runs are necessary in order to obtain the effect of each of the parameters. Since the result of the influence of a parameter may depend on the values chosen for the remaining parameters, the process is repeated for several sets of input parameters. The final effect is the mean of all the partial effects and their variance is used as a measure of the uniformity of the effects (Ghebremichael, 2009; Griensven, 2005).

The combination of LH and OAT methods ensures that the full range of all parameters has been sampled for an OAT design which is a robust and efficient sensitivity analysis method. With m intervals in the LH method and p parameters, a total of m(p+1) model runs are necessary. The SWAT sensitivity analysis tool automatically performs sensitivity analysis both with and without observed data by varying the values of each model parameter within a specified range. Depending on the parameter, changes are made by any of the three methods; multiplying the values by a certain percentage, adding part of the value to the base value, or replacing the base value with a new value (Neitsch *et al*, 2011; Winchel *et al*, 2010; Glavan and Pintar, 2012; Veith and Ghebremichael, 2009; Griensven, 2005). The final results of the sensitivity analysis are parameters arranged in ranks where the parameter with the maximum effect in catchment response is assigned rank 1. A parameter with a global rank of 1 is categorised as "very important", Rank 2-6 as "important" (Glavan and Pintar, 2012).

2.7.8.2 Calibration and Validation

One of the most common uses of the SWAT model is to evaluate the impacts of climate change and different land management practices on stream flow. In order to use the model to perform the impacts studies, it is required that the model first be calibrated and validated for the existing conditions (Arnold *et al,* 2012). Calibration is an effort to better parameterise a model to a given set of local conditions and thereby reducing the model prediction uncertainty. It involves adjustment of model input parameters by comparing model outputs for a given set of assumed conditions with observed data for the same conditions. Validation is the process of demonstrating that a given site specific model is capable of making sufficiently accurate simulations. It involves running the calibrated model using a different set of data other than that used in calibration and comparing outputs to observed data (Arnold *et al,* 2012). Model calibration and validation is normally done following three key steps: (i) selection of a portion of observed data, (ii) running the model at different values of known input parameters and comparing the output with observed data until fit to observation is good, (iii) applying the model with calibrated parameters to the remaining portion of the observed data (Arnold *et al,* 2011).

SWAT has two calibration options: automatic and manual schemes (Arnold *et al,* 2012; Winchel *et al*, 2010). The automated calibration scheme, inbuilt in the SWAT2009, is used to calibrate the model by assigning appropriate lower and upper bounds of parameter values before initiating the process (Moriasi *et al,* 2007, Van Liew *et al*, 2005). The scheme executes up to several thousand model runs to find the optimum parameter values (Gassman *et al*, 2007) under the assumption that all error variance is contained within the simulated values while the observed values are free of error (Moriasi *et al*, 2007). The model input parameters are adjusted within acceptable ranges (Arnold *et al*, 2012; Neitsch *et al*, 2011; Gassman *et al*, 2007) until acceptable agreement between the simulated and observed values of stream flow is achieved (Glavan and Pintar, 2012; Krause *et al*, 2005).

As confirmed by other studies (Van Griensven *et al,* 2012), projected impacts of climate change on streamflow are associated with large uncertainties. These uncertainties arise from the climate model, statistical post processing scheme, and the hydrological model (Bosshard *et al*, 2013). In this respect, using properly distributed datasets for calibration and validation of hydrological models can be a determinant factor in reducing uncertainty (Bosshard *et al,* 2013). Furthermore, a thorough assessment of errors in the data used in the modelling should also deserve more attention. Two main factors currently limiting further improvements in the accuracy of model simulations and predictions are the quality of the data used and the scaling of the information at the resolution required by the particular application (Blasone, 2007).

From the foregoing review, none of the studies has specifically focussed on the water yields at the river catchment area level in relation to climate change and deforestation. PRECIS RCM products were only used to project future climate scenarios but no attempt was made to use the products to determine the impacts of climate change on water yields (Omondi 2010; Sabiiti, 2008). The use of SWAT hydrological model in Nzoia basin (Githui, 2008) did not incorporate products of a regional climate model to assess the impacts of climate change and deforestation on the water yields from the basin. Instead the model used its own self generated climate input data. The present study aims at using the products of PRECIS RCM to drive SWAT hydrological model. The products of SWAT hydrological model were used to determine the impacts of climate change and deforestation on surface water yields from the Sondu River basin in Lake Victoria South Catchment Area (LVSCA).

This study sought to establish how the surface water yields are affected by climate change and deforestation over the Mau forest complex catchments taking 1961 to 1990 as the base line period against which changes in surface water yield levels were computed. The next chapter presents the methods used in this study towards achieving the stated objective.

CHAPTER 3

METHODOLOGIES

3.1 Introduction

In this chapter, methods and principles applied in order to achieve the objective of this study are presented and discussed. The chapter is broken into five sections namely: (i) Data processing and Quality Control (ii) Determination of Trends in Observed Data (iii) Climate Modelling (iv) Hydrologic Modelling, and (v) Analysis of Impacts on Water Yields.

3.2 Data Processing and Quality Control

Data processing and quality control involved sorting, summarising, aggregating, and validating the raw data supplied by the data collection agencies in order to obtain the required information in appropriate formats and to ensure that the data was clean and useful. In this section, the operations performed on observed Hydrometeorological and Spatial data from the area of study and the steps taken to ensure that their quality was not compromised, are discussed.

3.2.1 Hydrometeorological data

Rain-gauge and temperature data collected daily by the Kenya Meteorological Service (KMS) and discharge data computed on a daily time scale by the Water Resources Management Authority (WRMA) were processed to obtain monthly, seasonal, annual and long-term mean values. The summarized data were then sorted into respective time series to enable better description of the climate patterns and the hydrological regime of the area of study.

In order to make valid inferences from the analysis of observed Hydrometeorological data, it was important to first ascertain their quality before they were subjected to further analysis. Data quality control involved the careful scrutiny of the observed datasets in order to establish their completeness and consistency. In this study, estimation of missing data and homogeneity test were used as data quality control checks.

3.2.1.1 Estimation of Missing Data

Continuity of data is a vital requirement in research. Incomplete records of Hydrometeorological data may compromise the integrity of results derived from the data. Estimation of the missing records of Hydrometeorological datasets was important because they were used to drive and calibrate a hydrological model that requires continuous data records. Several methods are available in literature for filling in missing records of Hydrometeorological data. They include spatial correlation, weighted arithmetic mean, double mass curve, linear regression, normal ratio, and inverse distance among others. Details of these methods may be found in Rwigi (2004) and Opere (1998).

In this study, spatial correlation and regression analysis were used in conjunction with weighted arithmetic mean method to fill in the missing records. The weighted arithmetic mean method was used to estimate missing rainfall and temperature data while linear regression was used to estimate missing discharge data. A brief highlight of weighted arithmetic mean and linear regression methods is presented in the following sub-sections.

3.2.1.1.1 Weighted Arithmetic Mean Method

The weighted arithmetic mean is a simple and popular method that is widely used in filling in the missing meteorological records (Opere, 1998). The method estimates the missing record using corresponding records at three stations close and correlated to the station with the missing data record. The ratio of the normal annual precipitation of the station with missing record to that of the station with data corresponding to the missing record is used as the weighting factor. The missing record is therefore estimated using Equation 3.1.

$$P_x = \frac{1}{3}\left(\frac{N_x}{N_A} P_A + \frac{N_x}{N_B} P_B + \frac{N_x}{N_C} P_C \right) \quad \ldots\ldots\ldots\ldots\ldots\ldots\ldots\ldots\ldots\ldots\ldots 3.1$$

P_x is the estimated missing record, N_x is the normal annual rainfall of the station with missing records, N_A is the normal annual rainfall of station A, P_A is the record in station A that corresponds to the missing record in station X, N_B is the normal annual rainfall of station B, P_B is the record in station B that corresponds to the missing record in station X, N_C is the normal annual rainfall of station C, P_C is the record in station C that corresponds to the missing record in station X.

3.2.1.1.2 Linear Regression

Simple linear regression describes the linear relationship between two variables. The method seeks to summarise the relationship between the two variables by a single straight line (Equation 3.2).

The linear relationship is used as a predictive model of a missing record using the corresponding available record in another station. Regression of data from significantly correlated RGSs was performed to obtain the slope coefficient for the relationship which was then tested for significance before the model could be applied to estimate the missing values.

$$\hat{Y}_i = a + bX_i \quad \text{...} 3.2$$

$\hat{Y}_i$ is the estimated random variable of the missing record series, X_i is the available random variable corresponding to the missing record, a is the y-intercept of the regression line, b is the slope of the regression line (Helsel and Hirsch, 2002; Wilks, 2006). The values of a and b are obtained by minimising the least squares equation (Equation 3.3).

$$\sum_{i=1}^{n} \left(Y_i - \hat{Y}_i\right)^2 \quad \text{...} 3.3$$

The significance of the slope was tested at $\alpha = 0.05$ level of significance using student t-statistic computed using Equation 3.4.

$$t_{cal} = \frac{b}{s(b)} \quad \text{...} 3.4$$

t_{cal} is the computed t-statistic, b is the slope of the regression line and $s(b)$ is the standard deviation of the slope. t_{cal} was compared with the corresponding tabulated critical value (t_{crtc}) and slope was considered significant whenever $t_{cal} > t_{crtc}$. This equation was used to determine the significance of trend in observed and simulated time series (Moore and McCabe, 1989).

3.2.1.2 Homogeneity Test

A time series of a climatological variable such as rainfall or temperature, whose variations are caused only by variations of weather and climate are said to be homogeneous. Lack of homogeneity in a data series causes problems in studying a time series since heterogeneity makes data records unsuitable for comparison over long time periods and between different stations. Non-homogeneity may be abrupt or gradual; abrupt non-homogeneity is caused by relocation of instruments, changes in instruments, or changes in observation practices while gradual non-homogeneity is caused by gradual changes in the environment of the observation site such as urbanisation (Hasanean and Basset, 2006). The timing and size of significant non-homogeneities can be estimated using statistical tests. In this study short-cut Bartlett test (Hasanean and Basset,

2006) was used to examine the homogeneity of the surface air temperature, rainfall, and stream flow time series at their designated stations.

3.2.1.2.1 Short Cut Bartlett Test

Short cut Bartlett method tests homogeneity of a dataset by testing whether variability in a time series is constant. A dataset is considered homogeneous if variability in a time series is constant. Bartlett's test is a test of the hypothesis that all factor standard deviations are equal against the alternative hypothesis that the standard deviations are not all equal. The method is applied by dividing the time series into k equal sub periods where $k \geq 2$ (Hasanean and Basset, 2006). Samples of annual Hydrometeorological data were broken into two sub periods of sizes n_1 and n_2 for the purpose of testing homogeneity using the Short cut Bartlett method. In each of these sub periods a sample variance, $s^2{}_k$ (Equation 3.5) was computed.

$$s^2{}_k = \frac{1}{n}\left[\sum x^2{}_i - \frac{1}{n}\left(\sum x_i\right)^2\right] \text{ .... 3.5}$$

Summations range over the n values of the series in the sub period k. $s^2{}_k$ is the sample variance over the period k, n is the sample size, and x_i is the i^{th} random variable. The values of sample variances were used to compute the sample test statistic (Equation 3.6) used to test for homogeneity of the data sample.

$$F_{cal} = \frac{S^2{}_{\max}}{S^2{}_{\min}} \text{ ....3.6}$$

$S^2{}_{\max}$ is the computed larger sample variance, $S^2{}_{\min}$ is the computed smaller sample variance, and F_{cal} is the test statistic used to measure the number of times the variance from one sub period is larger than the other. The resulting ratios from Equation 3.8 will be small if the two sample sub periods have the same variance (Homogeneous) and larger if the two samples have statistically different variances (heterogeneous). The computed F-statistic follows the F-distribution with $n_1 - 1$ and $n_2 - 1$degrees of freedom. By taking the null hypothesis that the two sub periods have the same variance (Equation 3.7), the computed F-values (F_{cal}) were compared to tabulated critical values (F_{tab}) in the F distribution table at $\alpha = 0.05$ level of significance.

$$H_0 : s_1 = s_2 \text{ .... 3.7a}$$

$$H_1 : s_1 \neq s_2 \qquad \text{3.7b}$$

s_1 and s_2 are the standard deviations for the respective sub periods.

The null hypothesis H_0 was rejected if the calculated value of F_{cal} was found to be greater than the tabulated value ($F_{cal} > F_{0.95}$) as this was evidence that the two samples did not have the same variance (Hasanean and Basset, 2006). Since the alternative hypothesis requires the two-sided test, the significance level given in the table was doubled in order to obtain the significance level for the two-sided F-test (Moore and McCabe, 1989).

3.2.1.3 Spatial Data

Spatial data are generally found in form of maps and include Digital Elevation Model (DEM) from which topography is derived; soil types, forest and vegetation, land use, and water resources among others, stored as layers in digital format (Farid, 2008). Spatial data are normally remotely sensed from satellite platforms and therefore need to be processed to make them suit the purpose of the study.

3.2.1.3.1 Digital Elevation Model Data

The DEM was downloaded from the USGS public domain website in geographic coordinate system. In order to apply the DEM in the SWAT model, it was projected to the World Geodetic System of 1984 (WGS84) zone 36S of the Universal Transverse Mercator (UTM) set of coordinate system since this is the UTM zone containing the area of study. To limit the analysis to the area of study, a predefined map of Sondu River basin was used to mask out the area of interest.

3.2.1.3.2 Soil Data

The soil data were provided as a raster layer projected to WGS84 Zone 36N. It was therefore reprojected to WGS84 Zone 36S to make it overlay the DEM layer and therefore make it possible to analyse the two together. The map of Sondu River basin was used to clip the data to the area of interest.

3.2.1.3.3 Satellite Imagery

Figures 3.1 and 3.2 show the false colour composites of LANDSAT MSS (1973), LANDSAT TM (1986), LANDSAT ETM (2000), and LANDSAT ETM+ (2010) Satellite images of the Sondu River basin and South West Mau forest block respectively. The images were taken by sensors aboard LANDSAT satellites. These are a series of Earth observing satellites equipped with sensors that respond to Earth-reflected electromagnetic radiation. The series of satellites is jointly managed by NASA and USGS.

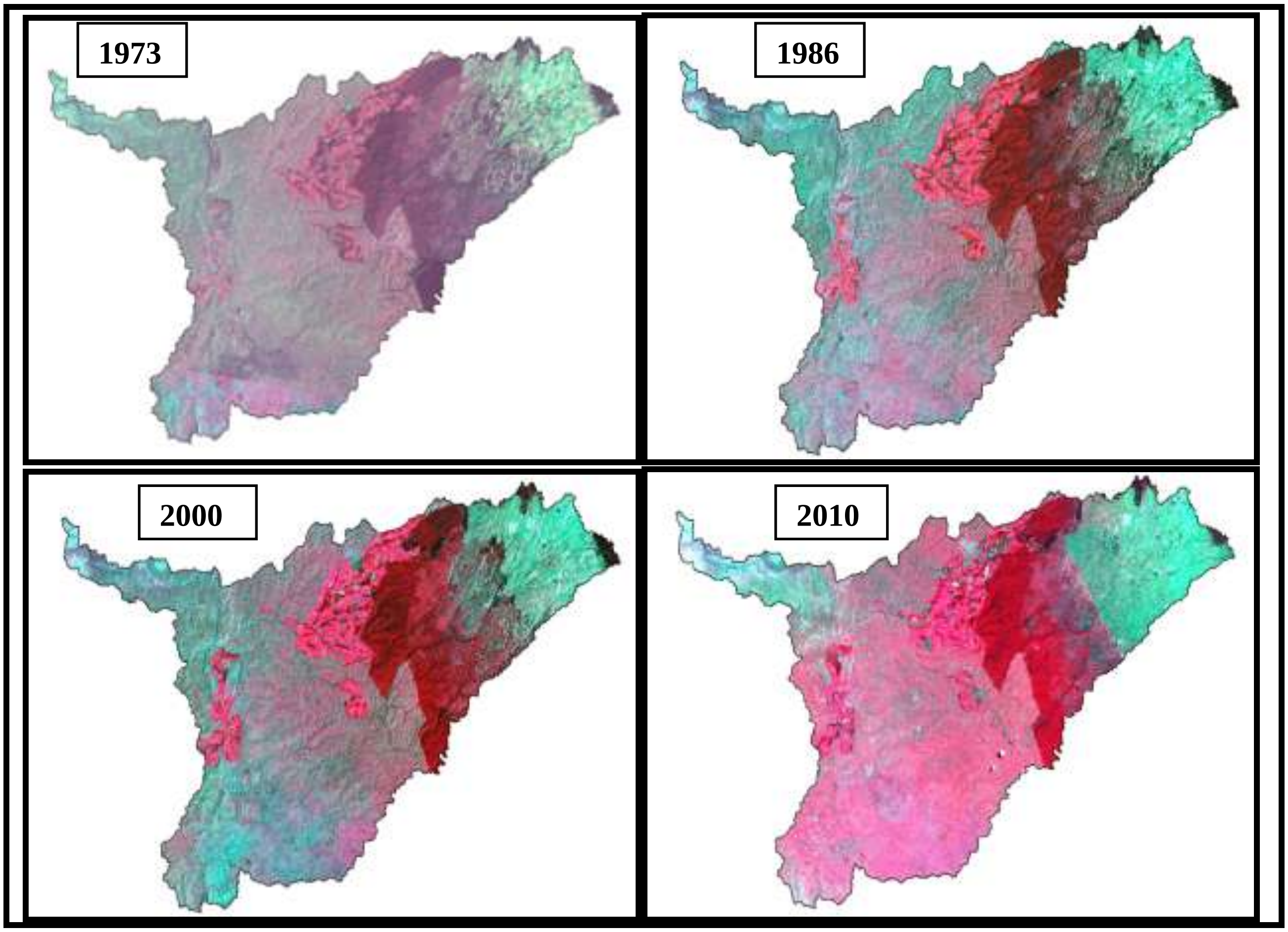

Figure 3.1: Satellite images of Sondu catchment area for 1973, 1986, 2000, and 2010

The 1973 imagery was taken by MSS sensor aboard LANDSAT 1 which has four channels, 2 visible and 2 infrared at 57 m resolution while the 1986 imagery was taken by TM sensor aboard LANDSAT 5 which has seven channels, 3 visible, 2 near infrared, 1 mid infrared and 1 thermal infrared at 30 m resolution. The 2000 imagery was taken by ETM sensor aboard LANDSAT 7, which is similar to the TM sensor but adds an extra 15 m resolution panchromatic band and improved resolution for the thermal infra red band, at 30 m resolution. The 2010 imagery was taken by the ETM+ sensor aboard LANDSAT 7 at 28.5 m resolution. The false colour composite LANDSAT images were interpreted through image classification to obtain LULC thematic maps for the area of study.

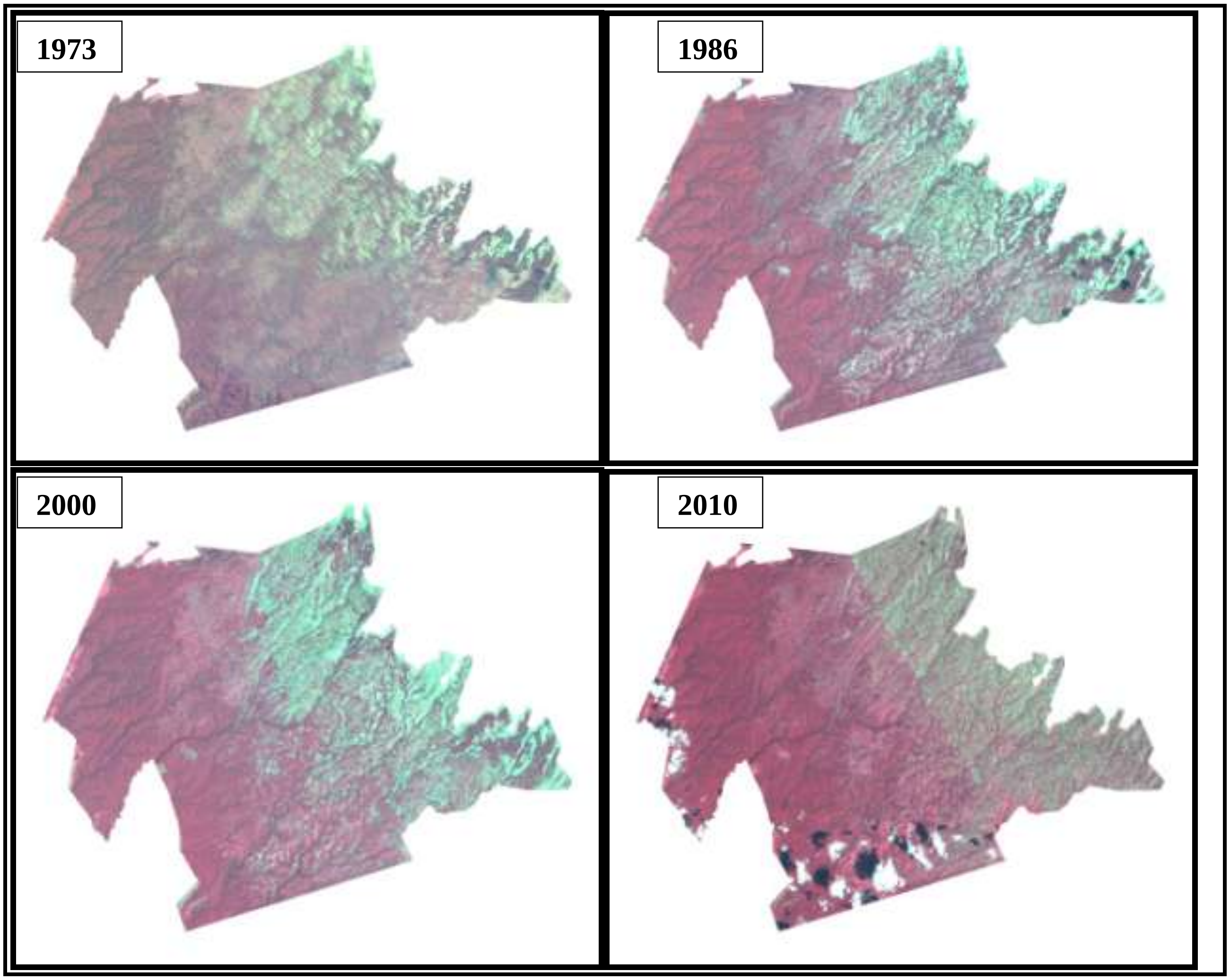

Figure 3.2: Satellite images of South West Mau forest reserve for 1973, 1986, 2000, and 2010

3.2.1.3.3.1 Image Classification

Image classification is the process by which all pixels in a satellite digital image are categorised into one of several classes of LULC in the area of interest using either supervised or unsupervised classification schemes. The classified data are then used to produce thematic maps of LULC that can be analysed in conjunction with other data using GIS technology (Zhou, 1999).

The sensors aboard the LANDSAT satellites cover the complete wavelength bands and hence give grey scale images. During the image processing, individual bands were separated and combined into false colour composite of RGB432 to enhance vegetation visibility (Figures 3.1 and 3.2) since the study partially focussed on the impacts of changes in natural vegetation cover on water yields. The false colours were then interpreted and appropriate colours representing what was actually on the ground surface were assigned.

The false colour composite images provided by DRSRS were interpreted using supervised classification scheme and a total of six LULC classes were delineated; agricultural row crops, evergreen forest, mixed forest, open forest, plantation forest, rainfed herbaceous crop, rangeland, and water. The classified images were converted from raster to vector format and the total area of each class was estimated using geometry tools in ArcGIS 9.3 software. Temporal land use changes between 1973 and 2010 were compared and displayed in map format at a scale of 1:450000.

3.3 Determination of Trends in Observed Data

A brief discussion of methods used to analyse the processed data for purposes of meeting the stated objective are presented in this section. They include: determination of long-term means, variance, and trend analysis of time series of observed rainfall, temperature, stream flow and forest cover between 1961 and 2010.

3.3.1 Time Series Analysis

Time series analysis is a major tool in hydrological analysis. Its main applications include building mathematical models to generate synthetic hydrologic records, forecasting hydrologic events, detecting trends and shifts, cycles and seasonality in hydrologic records, and filling in missing records including extension of short hydrologic records where necessary (Salas, 1993). Time series analysis was used in this study to examine the past, current and future trends of Hydrometeorological data. This subsection presents the methods used to determine the mean, variance and trend sample statistics.

3.3.1.1 Overall Sample Statistics

The overall sample statistics, the mean ($\overline{Y}$) and the variance (S^2) were determined for monthly and annual time series for rainfall, maximum and minimum temperatures, and discharge over the

Sondu catchment area. For a time series denoted by Y_t, the mean $\bar{Y}$ (Equation 3.8) and variance S^2 (Equation 3.9) were determined.

$$\bar{Y} = \left(\frac{1}{N}\right)\sum_{t=1}^{N} Y_t \quad \text{...} 3.8$$

$$S^2 = \frac{1}{N-1}\sum_{t=1}^{N}\left(Y_t - \bar{Y}\right)^2 \quad \text{...} 3.9$$

$\bar{Y}$ is the sample mean, S^2 is the sample variance, N is the sample size, Y_t is the time series variable. These statistics were used to detect trends in observed and simulated data.

3.3.1.2 Trend Analysis

Trends in hydrologic data could be due to long term climatic changes or in the case of streamflow due to changes in a catchment's response to effective rainfall owing to landuse changes that lead to the deforestation of the watershed. There are many parametric and nonparametric methods of detecting trend. One of the most useful parametric methods of detecting trend is the simple linear regression analysis which assumes normality of errors, constant variance and true linearity of relationships. In this study, the trend in time series of different datasets was determined by regression trend lines (Equation 3.10) of the time series.

$$Y_t = b_0 + b_1 t \quad \text{...} 3.10$$

Y_t is the time series variable, b_0 is the initial value of the time series variable, b_1 is the trend of the time series, and t is the time at which Y_t was observed. This equation was used to determine trends in observed and simulated time series datasets. The significance of trend was tested at $\alpha = 0.05$ level of significance using student t-statistic (Equation 3.4).

Trends in LULC data were evaluated by comparing percentage changes (Equation 3.11) in vegetation cover of the area of study at different times with that of the baseline.

$$Deforestation = \left(\frac{LU_B - LU_T}{LU_B}\right) \times 100 \quad \text{...} 3.11$$

LU_B is the baseline forest cover and LU_T is the forest cover at a later date. Positive values of Equation 3.13 indicate increasing trend while negative values indicate decreasing trends.

3.4 Climate Modelling

The regional climate responses were derived from a fully coupled Ocean-Atmosphere model, the third generation of the Hadley Centre Coupled model (HadCM3) which is run at a horizontal resolution of 2.5° latitude and 3.75° longitude (Met Office, 2009). Outputs from the HadCM3 model were used to provide boundary data to the PRECIS regional climate model system which is based on the atmosphere only component (HadAM3P) of the HadCM3 climate model (Wilson *et al*, 2009; Jones *et al,* 2004). In this section the second specific objective was addressed.

3.4.1 PRECIS Modelling

Downscaling of GCM outputs has been used in hydrological studies to translate the projected climate change into hydrological response (Akhtar *et al*, 2009). In this study, dynamical downscaling has been applied with the PRECI RCM using GCM outputs as boundary conditions over the East African region (Figure 3.3)) as the model domain. The domain was set up with a horizontal resolution of 50 km by 50 km and it spans latitudes 12°S to 18°N and longitudes 22°E to 52°E. The domain spans latitudes 12°S to 18°N and longitudes 22°E to 52°E. The domain fully encompasses the area of study lying between latitudes 00°23' S and 01°10' S and longitudes 34°46' E and 35°45′.

3.4.1.1 Regional Climate Scenarios

This subsection describes the techniques used in PRECIS RCM to provide the climate information required to drive the impacts models such as SWAT. The method essentially follows a three-stage process namely; Running the model over the area of interest, in this case, the Sondu River catchment area, to provide climate simulations of the baseline period (1961-1990) and comparing these simulations with the observations to validate the model outputs; Running the model to provide climate projections for future periods (2001-2030) and (2021-2050); Deriving the relevant information from the model projections based on the understanding of the needs of the impacts model (Jones *et al*, 2004).

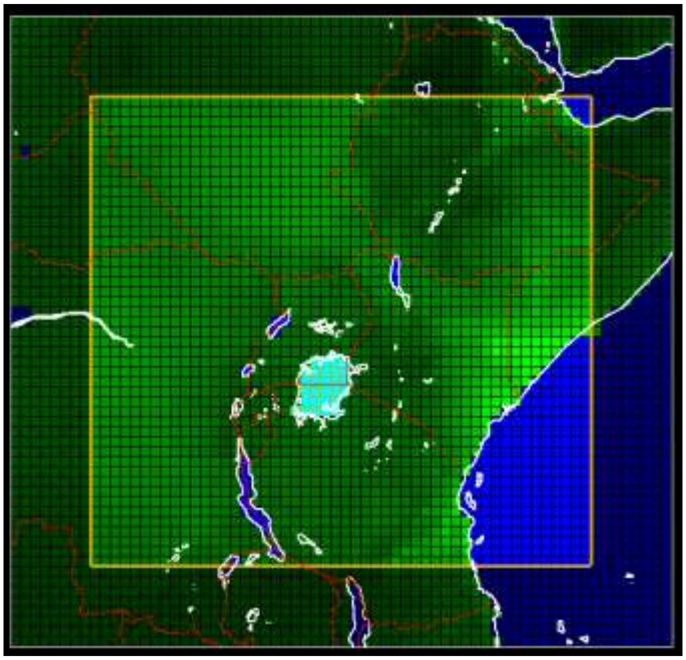

Figure 3.3: Eastern Africa domain used for PRECIS simulations

In order to create regional climate scenarios, PRECIS downscales a recent and a future climate scenario, such as 1961-1990 and 2021-2050 climate periods respectively, which are both functions of local and remote processes with external forcing being provided by solar radiation and atmospheric composition. Atmospheric composition is represented by prescribed concentrations of the most important GHGs derived from scenarios of their emissions (Wilson *et al*, 2009; Jones *et al*, 2004). In this study PRECIS was used to simulate rainfall and temperature for the Sondu River basin using ECHAM4 boundary data under SRES A2 emissions scenarios as the model inputs.

3.4.1.2 Generating Climate Change Scenarios

The coupled ocean atmosphere global climate models (OAGCMs) such as the ECHAM4 used to provide the boundary data for RCMs are usually run in transient modes where they typically run for a long period of time spanning decades to centuries (Jones *et al*, 2004). Such long period transient runs are not practical for RCM such as PRECIS due to the prohibitive computational costs involved. In order to save on these costs, PRECIS is normally run with time slices of between ten to thirty years of OAGCM out put to provide the statistics of climate change of a particular place for a particular period of interest

In this study, the particular place of interest was the entire Sondu River catchment area. To generate climate projections over the area of interest, three time slices (Table 3.1) were selected from ECHAM4 to drive PRECIS; the base period (1961-1990), the present and near future period (2001-2030), and the medium term future period (2021-2050), which targeted Kenya's development blue print, vision 2030 and beyond. The difference between the baseline period climate and those of the near and medium term future periods provided the climate change projections for these periods in the area of study.

The outputs from PRECIS model were used to drive SWAT hydrological model to produce the baseline period and the future surface water yields from the MFC using Sondu River basin as the representative catchment area. The difference between the baseline period and the future surface water yields represent the impacts of climate change on water yields from the MFC.

Table 3.1: PRECIS experiments carried out during the study

Experiment No.	Boundary data code	Scenario	Period	Output diagnostic	Description
1	echja	Baseline	1961-1990	PP daily, monthly and annual data	Nested within ECHAM4 Baseline output
2	echja	SRES A2	2001-2030	PP daily, monthly and annual data	Nested within ECHAM4 A2 GCM output
3	echja	SRES A2	2021-2050	PP daily, monthly and annual data	Nested within ECHAM4 A2 GCM output

3.4.1.3 Simulation Length

Since climates describe statistical distributions of meteorological occurrences which occur at a particular place, reliable simulations of climate should be long enough to sample as wide a range of meteorological phenomena as possible. In order to investigate the state of the regional climate, the minimum simulation length that gives a reasonable idea of the mean changes in climate should be at least ten years. Studies using the Hadley Centre RCM have shown that a ten year simulation captures about half of the variance of the true regional climate change response. To capture over three quarters of the variance of the true signal, a thirty year simulation period is recommended (Jones *et al*, 2004). An integration length of 31 years is however more preferable for the analysis of aspects of climate variability such as distributions of daily rainfall and climate extremes, where a thirty-year period follows a one year spin-up period.

3.4.1.4 Choice of a Domain

The choice of a model domain is crucial when setting up the regional model experiments. The choice is largely governed by the region, the experimental design and the ultimate use of the RCM results. The domain should generally be large enough to allow for the full development of the internal mesoscale circulations and include the relevant regional forcings. It is important that the domain should encompass the inherent dynamics of the region chosen to run the model (Jones *et al*, 2004).

In this study, the model domain stretches over latitudes 12^{o}S to 18^{o}N and longitudes 22^{o}E to 52^{o}E (680 km by 3400 km) at a horizontal resolution of 50 km. The domain is large enough to allow for the full development of internal mesoscale circulations and includes the relevant regional forcings such as the Congo basin air mass, Lake Victoria, and a section of the western side of the Indian Ocean: all of which have a major influence on the climate of the Sondu basin (Akhtar *et al*, 2009; Nyakwanda *et al*, 2009; Christensen *et al*, 2007).

3.4.1.5 Configuring the Region

Although PRECIS RCM can be applied anywhere in the world, it is necessary to reconfigure the model domain in order to reflect the reality. Configuration of the model domain involves the editing of the default characteristics of the underlying surface of the region such as land cover, soil type, and topography in order to reflect what is actually on the ground. In this study, configuration of the region was done through the PRECIS model in-built land-sea mask (Wilson *et al*, 2009).

3.4.1.6 RCM Calendar and Clock

PRECIS uses an artificial calendar consisting of 360 days per year which divides the calendar year into twelve months of thirty days each, and a clock that is always based on the Coordinated Universal Time (UTC) denoted by Z (Wilson *et al*, 2009). The model automatically chooses this calendar when it runs. To ensure that monthly and seasonal mean values diagnosed by the model are compatible with their equivalent observed quantities, the average date of perihelion is shifted from 2.5 to 3.2 days after the beginning of the year, taken as 0Z 1st January (Wilson *et al*, 2009). In this study each PRECIS model run commenced from 0Z 1st January and lasted for a period of 31 years.

3.4.1.7 PRECIS Diagnostic Outputs

All of the model diagnostic outputs are produced and archived during each PRECIS run. The model allows one to output a range of climatic variables on hourly and daily time steps and also always outputs longer timescale averages of these variables. Standard PRECIS diagnostic outputs are climatic means of periods longer than a day together with hourly and daily means, daily maxima and daily minima, which are optional. In this study daily surface, middle, and upper air diagnostics were selected. This was in addition to climatic mean diagnostics which are automatically supplied at 850, 500, and 250 hPa pressure levels (Wilson *et al*, 2009; Met Office, 2009).Time series of monthly and seasonal outputs of rainfall and temperature were used to describe climate scenarios while daily outputs were used as inputs to the SWAT hydrological model to analyse the impacts of climate change on the surface water yields from the Mau forest complex catchments.

3.4.1.8 Baseline Climate

The baseline climate was assumed to belong to the same climatic regime as the present and was therefore used as the control against which future climate changes were measured. There are currently six baseline climates available for use by PRECIS which represent slightly different periods; ECMWF Re-Analysis (ERA) baseline climates consisting of ERA15 (1979-1993), ERA40 (1957-2001), and ERA Interim (1989-2007); National Centre for Environmental Prediction (NCEP) baseline climate consisting of NCEP R2 (1979-2004); the third generation of the Hadley Centre Atmospheric Model (HadAM3P) baseline climates consisting of HadAM3P (1960-1990), and Max Plank Institute of Meteorology baseline climate consisting of ECHAM4 (1960-1990).

The relevant information on the atmospheric composition for the various baseline climates was provided from values of various greenhouse gases for their respective periods as given in Table 3.2 (Wilson *et al*, 2009). The table shows the SRES A2 emissions scenarios mass mixing ratios (kg of gas per kg of air) of carbon dioxide (CO_2), Methane (CH_4), and Nitrous oxide (N_2O).

The World Meteorological Organisation (WMO) has adopted the climate of the period 1961 to 1990 as the current baseline climate against which future climate changes may be assessed. The data for this period may be obtained from ERA40, HadAM3P or ECHAM4. For the purpose of this study, ECHAM4 was selected to provide boundary data since it was the only one available with a transient run. The boundary data were obtained by running 31-year integrations of ECHAM4 (Table 3.2) with one year being used as warm up period. Observed and projected evolutions of GHGs concentrations (Table 3.2) over the entire period of interest; 1950 - 2050 were used to provide the relevant information on atmospheric composition (Wilson *et al*, 2009).

Table 3.2: SRES A2 emissions scenario mass mixing ratios of carbon dioxide, Methane, and Nitrous oxide

Carbon Dioxide (CO_2)		**Methane (CH_4)**		**Nitrous Oxide (N_2O)**	
Year	**Concentration (10^{-4})**	**Year**	**Concentration (10^{-7})**	**Year**	**Concentration (10^{-7})**
1960	4.814	**1957**	6.597	**1950**	4.407
1970	4.948	**1990**	9.514	**1965**	4.471
1980	5.148	**2000**	9.757	**1984**	4.615
1990	5.334	**2010**	10.38	**1990**	4.710
1995	5.440	**2020**	11.14	**2000**	4.832
2000	5.572	**2030**	12.02	**2010**	4.969
2010	5.900	**2040**	13.03	**2020**	5.136
2020	6.310			**2030**	5.334
2030	6.819			**2040**	5.531
2040	7.388				

(Source: Wilson et al, 2009)

3.4.1.9 Transient Climates

To simulate future climates of 2001-2030 and 2021-2050 over the Sondu river basin, PRECIS was run in transient mode. In this mode PRECIS is capable of integrating transient climates continuously from the recent past through the present up to the year 2100 (Wilson *et al*, 2009). Running PRECIS in this mode allows climates of intermediate periods such as 2030s and 2050s to be downscaled directly from the GCMs. There are three main transient runs available that can readily be used in PRECIS. These are HadCM3Qn (1950-2099), ECHAM4 (1990-2100), and ECHAM5 (1950-2100) (Wilson *et al*, 2009).

In this study ECHAM4 was used to provide the necessary boundary conditions to drive PRECIS RCM over the East African domain since it was the only one available with the PRECIS 1.8.2 version that was used for this study (Wilson *et al*, 2009). The external forcing was provided by the SRES A2 emission scenarios (Table 3.2) while the sea surface boundary conditions were taken directly from the GCMs ocean component.

3.4.1.10 Model Output Calibration and Validation

The model-generated values are full of uncertainties arising from the fact that the model is merely a simplification of reality. The model output values therefore need to be calibrated and validated using corresponding observed values in order to bring them closer to the real values before they can be used for impact assessment (CCC, 2009; Islam *et al*, 2008). In order to determine the measure of the confidence to be placed on rainfall, maximum and minimum temperature projections, it was therefore necessary to calibrate and validate PRECIS outputs using corresponding observed data from the area of study.

Calibration of PRECIS-simulated rainfall and temperature was performed over the Sondu basin using surface observed data from KMD for the baseline period (1961-1990) split into two parts: (1961-1980) for calibration and (1981-1990) for validation. Observed data at a particular site are considered as being representative of the location (Islam *et al*, 2008). Grid values of the model data, extracted at the observational site, were compared with the corresponding observed data representing the grid. The model-simulated data of rainfall and temperature were extracted at three observation sites of KMD (Kericho, Keresoi, and Sotik) and were processed to monthly, seasonal, annual and long-term mean values.

There are two calibration methods commonly used to calibrate model-simulated values: bias correction factor, and regression analysis methods (CCC, 2009). Regression analysis method was adopted for this study on account of its robustness compared to the bias correction factor method. PRECIS model-simulated monthly values were regressed on corresponding observed values to calculate regression slopes and constants for rainfall, maximum and minimum temperatures at the three KMD observation stations: Kericho, Keresoi and Sotik. The calibrated parameters obtained through regression analysis were used to validate the PRECIS model projected values (CCC, 2009).

The following regression equations were used to validate projected rainfall (Equation 3.12), maximum temperature (Equation 3.13), and minimum temperature (Equation 3.14).

$$E_{RF} = a_{RF} + b_{RF} \times S_{RF} \quad \text{……………………………………………………….. 3.12}$$

E_{RF} is the estimated projected rainfall, a_{RF} is the rainfall regression constant, b_{RF} is the rainfall regression slope, and S_{RF} is the simulated rainfall scenario.

$$E_{T\max} = a_{T\max} + b_{T\max} \times S_{T\max} \quad \text{…………………………………………..……. 3.13}$$

$E_{T\max}$ is the estimated projected maximum temperature, $a_{T\max}$ is the maximum temperature regression constant, $b_{T\max}$ is the maximum temperature regression slope, and $S_{T\max}$ is the simulated maximum temperature scenario.

$$E_{T\min} = a_{T\min} + b_{T\min} \times S_{T\min} \quad \text{…………………………..…………..…….. 3.14}$$

$E_{T\min}$ is the estimated projected minimum temperature, $a_{T\min}$ is the minimum temperature regression constant, $b_{T\min}$ is the minimum temperature regression slope, and $S_{T\min}$ is the simulated minimum temperature scenario

The model performance was measured by the difference between observed and the model-estimated values which is a measure of whether the model overestimates or underestimates the observed climate variables (Islam *et al*, 2008). In the case of rainfall the model performance was evaluated as the percentage difference between the observed and model-estimated rainfall (Equation 3.15a) while in the case of temperature performance was evaluated as simply the difference between the observed and model-estimated temperatures (Equation 3.15b). Positive performance values indicated model underestimation while negative values indicated model overestimation.

$$Performance_{Rnfl} = \left(\frac{Observed_{Rnfl} - Estimated_{Rnfl}}{Observed_{Rnfl}} \right) \times 100 \quad \text{…………………………3.15a}$$

$$Performance_{Tmp} = \left(Observed_{Tmp} - Estimated_{Tmp} \right) \quad \text{……………….……………..3.15b}$$

$Performance_{Rnfl}$ is the percentage overestimation or underestimation of rainfall by the model, $Observed_{Rnfl}$ is the observed rainfall, $Estimated_{Rnfl}$ is the estimated rainfall from the model-simulated scenarios, $Performance_{Tmp}$ is the overestimation or underestimation of temperature (°C) by the model, $Observed_{Tmp}$ is the observed temperature, and $Estimated_{Tmp}$ is the estimated temperature from the model-simulated scenarios.

3.5 Hydrologic Modelling

This study examineed stream flows, rainfall, and deforestation in the Sondu River basin, whose upper catchment comprises South West Mau forest, the largest of the 22 blocks (Kinyajui, 2009) comprising the MFC in Kenya. The study examined how stream flows and hence surface water yields vary under different climate and forest cover scenarios. The extent of variation in stream flow was quantified in terms of changes in the mean as a central value. In order to achieve this, a physically based hydrological model: the Soil and Watershed Assessment Tool (SWAT) was applied. SWAT is extensively described in Neitsch *et al (*2011), Winchell *et al (*2010), and Arnold *et al* (1998).

In this section the third specific objective, to simulate streamflow for the periods 1961-1990, 2001-2030 and 2021-2050 under different climate and forest cover scenarios and analyse the trends, was addressed. SWAT hydrologic model was used to simulate stream flows, from which water yields from the Sondu catchment area were evaluated, using the baseline and SRES A2 emissions scenarios projected climates under different LULC scenarios over the Sondu catchment area.

3.5.1 SWAT Model Inputs and Setup

This subsection presents the prerequisite requirements for running the SWAT hydrologic model including the operational requirements of input data, data preparation, model set up, model application and the simulation options that were applied in the Sondu basin. Summarised procedures that were followed in the setting up of the model and how it was used to simulate the hydrological characteristics of the area of study are presented.

The model was set up using the digital elevation model (DEM), land use, soil and climate data sets. The model parameterisation was derived using the ArcGIS interface for SWAT (ArcSWAT) which provides a graphical support for the desegregation scheme and hence supports data handling (Schuol *et al*, 2008). The ArcSWAT interface was used to delineate the whole watershed area into sub-basins based on the DEM and the stream network. A drainage area of 10000 ha was selected as the threshold for the delineation of the Sondu river watershed. This threshold was chosen to balance between the resolution of the available data and a practical SWAT project size (Faramarzi *et al*, 2009). This resulted in a total of 17 sub-basins from the main Sondu River basin. The LULC, soil, and slope thematic layers were used to generate the HRUs within each of the sub-basins. Climatic data were used as the main drivers of the model in the respective sub-basins.

The main procedures followed involved: Delineation of the catchment area into different sub-basins; definition of HRUs in each of the sub basins based on land use, soil type and slope datasets; loading of the processed climate datasets; and finally the simulation of streamflow.

3.5.1.1 Data Requirements

Spatial data that include: DEM, LULC, stream network, and soil type maps were projected to the Universal Transverse Mercator (UTM) Zone 36S, which is the transverse Mercator projection zone for this part of Kenya, using ArcGIS 9.3. The DEM was used to delineate the watershed and to analyse the drainage patterns of the land surface terrain. The LULC spatial data were reclassified into SWAT land cover types and a user look up table was created to help in identifying different classes of LULC on the map as per the required SWAT format. The soil map for the area of study was linked with the SWAT soil database.

3.5.1.2 Watershed Delineation

The watershed boundaries of the area of study were derived from the global SRTM 90 m by 90 m DEM using automated procedures within the watershed delineator; an ArcGIS extension within SWAT2009. The key procedures followed in the delineation process included: loading the DEM that was used to calculate sub-basin and reach parameters; Specifying the critical source area which was used to determine the detail of the stream network as well as the size and number of sub-basins in the larger Sondu catchment area; Reviewing and editing the stream network outlet points in order to achieve the optimum number of sub-basins and; Calculating the sub-basin parameters.

The next step after the delineation of the watershed was to input LULC and soil data thematic maps. The thematic maps were input, overlaid, and the characterisation of each sub-basin was automatically performed using the ArcSWAT interface. Having done this, areas with unique soil-landuse-slope combination were differentiated within each sub-basin. These unique areas, called Hydrological response Units (HRUs) were used as the basis of the water balance calculations (Abbaspour *et al*, 2009; Schuol *et al*, 2008). The parameterisation of the stream reaches and the basin geomorphology was automatically done with the help of the ArcSWAT interface (Winchel *et al*, 2010; Schuol *et al*, 2008).

3.5.1.3 Sub-Basin Parameters

Spatial parameterisation of the model was performed by subdividing the Sondu basin into 17 sub-basins based on the surface topography so that the entire Sondu catchment drains through the outlet at Sondu Miriu RGS number IJGO1 (Figure 1.5). The sub-basins were further subdivided into a series of Hydrological response Units (HRUs) based on unique soil, landuse, and slope characteristics (Winchel *et al*, 2010; Faramarzi *et al*, 2009). Parameterisation of the stream reaches and the sub-basin geomorphology was automatically performed using ArcSWAT interface (Schuol *et al*, 2008).

3.5.1.4 HRU Analysis

Land use, soil and slope characterisation for the main catchment area and for each of the respective sub-basins was performed using ArcSWAT interface where the land use and soil data sets were imported and linked to the SWAT databases. Slope classification was performed based on the DEM. Multiple class slopes option was chosen on account of the wide range of slopes in the Sondu catchment area. Landuse, soil types and slope class datasets were used to define at least one HRU for each of the 17 sub-basins.

Land use datasets were defined and reclassified into SWAT land cover types. Since the study area is outside the U.S.A, a user look up table was created by editing the default LULC database in order to reflect the local conditions. The soil dataset was also defined and reclassified. From the digital soil map provided by the Kenya Soil Survey (KSS), the various categories of soils found within the Sondu catchment area were linked to the SWAT soil database.

After land use and soil datasets were successfully reclassified and the slope class chosen, the land use, soil and slope thematic layers were then overlain to the catchment. These layers were used to automatically define the HRUs for each of the 17 sub-basins using preset threshold levels of: 5% land use, 20% soil, and 20% slope.

3.5.1.5 Channel Characteristics

In modelling channel flow in a watershed, SWAT model assumes that the main channels have a trapezoidal shape. The user is then required to define the width and depth of the channel when filled to the top of the bank as well as the channel length, slope along the channel length and the Manning's *n* value for the catchment area. Further, the model assumes the channel sides to have a 2:1 run-to-rise ratio $\left(Z_{ch} = 2\right)$ so that the slope of the channel sides is 0.5. The bottom width of the channel is then calculated (Equation 3.16) from the bank full width (Neitsch *et al*, 2011).

$$W_{btm} = W_{bnkfull} - 2 \cdot Z_{ch} \cdot depth_{bnkfull} \qquad \text{……………………………..3.16}$$

W_{btm} is the bottom width of the channel (m), $W_{bnkfull}$ is the top width of the channel when filled with water (m), Z_{ch} is the inverse of the channel side slope, and $depth_{bnkfull}$ is the depth of water in the channel when filled to the top of the bank (m). By solving Equation 3.17, for a given depth of water in the channel, the width of the channel at the water level was determined.

$$W = W_{btm} + 2 \cdot Z_{ch} \cdot depth \qquad \text{……………………..……………………3.17}$$

W is the width of the channel at the water level (m), W_{btm} is the bottom width of the channel (m), Z_{ch} is the inverse of the channel side slope, $depth$ is the depth of water in the channel (m). The volume of water held in the channel at any one time was evaluated by solving Equation 3.18.

$$V_{ch} = 1000 \cdot L_{ch} . A_{ch} \qquad \text{…………………………..…………….……… 3.18}$$

V_{ch} is the volume of water stored in the channel (m^3), L_{ch} is the channel length (km), A_{ch} is the cross-section area of flow in the channel for a given depth of water (m^2).

3.5.1.6 Climate Component

The climate component of the model was presented in form of weather data gathered from the Sondu catchment area. Climatic input variables required for running the SWAT model consist mainly of daily precipitation, maximum and minimum air temperature, solar radiation, wind speed and relative humidity. The model has an option of using input values of daily weather variables from records of observed or simulated data or use internally generated values using monthly average data summarised over a number of years. Generated climatic data may also be used to fill in gaps in the observed records (Winchel *et al*, 2010).

3.5.1.7 Weather Data

The weather variables that drive the hydrologic water balance are: precipitation, air temperature, solar radiation, wind speed and relative humidity (Arnold *et al,* 1998). Where available, observed daily precipitation, maximum and minimum temperatures can be input directly; otherwise the model can simulate them using the inbuilt weather generator. Solar radiation, wind speed and relative humidity are always internally simulated by the model.

In this study, the weather data used in the catchment simulation of stream flow were imported into the SWAT databases. Weather stations; Kericho, Keresoi, Ndoinet, Sotik, and Timbilil were loaded to the model and used to define the Weather generator datasets which were used to generate various weather parameters for the model. SWAT model weather generator database was created by first creating a location table to provide the location of the local weather generator stations within the Sondu watershed (Winchell *et al*, 2010). Table 3.3 shows the local weather stations used to provide the weather generator data sets for the area of study.

For each of the locations listed in the rain gauge location table (Table 3.3), a daily precipitation data table was made. This table was used to store the daily rainfall records listed in sequential order for each individual rain gauge. The temperature data table used to store the maximum and minimum temperatures for each of the listed temperature station was also made. The table has three columns; date, maximum and minimum temperature columns and can hold a maximum of 150 years of daily temperature data (Winchell *et al*, 2010). The other climate datasets; relative humidity, solar radiation and wind speed were internally generated using the SWAT weather generator. The climate data assigned to a sub-basin was obtained from the closest station.

The weather generator produces synthetic data that have similar statistical properties as the observed data. It is important to note that synthetic data only have similar but not the same statistical properties as the observed data since magnitudes may differ (Brissette *et al,* 2007).

Hence use of synthetic meteorological data introduces uncertainties in SWAT simulations; the best situation would be to use the long term measured data. However, lack of observed time series of adequate length to permit impacts studies and the limited coverage of station networks, and the need for catchment scale response datasets with high spatial and temporal resolutions (Mirus *et al,* 2007), necessitates use of synthetic data in studies such as this one. The quality of this data depends on how well the statistics of the observed data are described (Brissette *et al,* 2007). So long as the statistics of observed data are well described, the use of synthetic time series with physical models such SWAT allows for the direct modelling of future events (Brissette *et al,* 2007).

Table 3.3: Weather stations used by the weather generator component of SWAT model

ID	Name	Code Name	Latitude	Longitude	Elevation (m)
1	Keresoi	Wgnkrsi	-0.2833	35.5333	2682
2	Kericho	Wgnkrch	-0.3667	35.2700	1976
3	Ndoinet	Wgnndnt	-0.4167	35.5500	2438
4	Timbilil	WgnTmbl	-0.3500	35.3500	2073
5	Sotik	Wgnsotk	-0.7000	35.1000	2134

3.5.1.8 Rainfall

Rainfall, the main process through which water enters the land phase component of the hydrological cycle, is one of the most important processes in the land phase of the cycle. Since rainfall controls the water balance, it is important that its amount and distribution, in both space and time, is accurately simulated by the model. Rainfall reaching the earth's surface on a given day (R_{day}) may be read from an input file or be internally generated by the model (Neitsch *et al,* 2011).

The occurrence of rain on any given day has a major impact on relative humidity, temperature and solar radiation reaching the surface for that day. The weather generator component within the SWAT modelling system first generates precipitation for the day independent of the other climatic variables and then computes the distribution of rainfall within the day. Once this is successfully done, maximum and minimum temperatures, solar radiation and relative humidity are then generated based on the presence or absence of rain for the day under consideration. Wind speed is then generated independently (Neitsch *et al*, 2011).

A first order Markov chain-skewed model (Nicks, 1974), inbuilt within the SWAT modelling system, was used to generate (Equation 3.19) daily precipitation for the Sondu basin. The first order Markov chain model was used to define the day as dry or wet by comparing a random number ranging from 0.0 to 1.0, generated by the model, to monthly wet-dry probabilities input by the user (Table 3.4).

Table 3.4: SWAT input variables that appertain to the generation of daily rainfall

Variable name	**Definition**
PCPSIM	Precipitation unit code: 1-measured, 2-generated
PR_W(1,mon)	$P_i(W/D)$: Probability of a wet day following a dry day in a month
PR_W(2,mon)	$P_i(W/W)$: Probability of a wet day following a wet day in a month
IDIST	Rainfall distribution code: O-skewed, 1-exponential
REXP	*rexp*: Value of the exponent. (required if IDIST=1)
PCPMM (mon)	Average monthly precipitation falling in a month (mm H_2O)
PCPDmon	Average number. of days of precipitation in a month (μ_{mon} = PCPMM/PCPD)
PCPSTD (mon)	δ_{mon}: Standard deviation for daily precipitation in a month (mmH_2O)
PCPSKW	g_{mon}: Skew coefficient for daily precipitation in a month

(Source: Neitsch, et al, 2011)

$$R_{day} = \mu_{mon} + 2.\delta_{mon}\left(\frac{\left[\left(SND_{day} - \frac{g_{mon}}{6}\right)\left(\frac{g_{mon}}{6}\right) + 1\right]^3 - 1}{g_{mon}}\right) \quad \text{…..……………….3.19}$$

R_{day} is the amount of rainfall on a given day (mm H_20), μ_{mon} is the mean daily rainfall for the month (mm H_2O), δ_{mon} is the standard deviation of daily rainfall for the month (mm H_2O), SND_{day} is the standard normal deviate calculated for the day, and g_{mon} is the skew coefficient for daily rainfall for the month. Precipitation input parameters include monthly probabilities of receiving precipitation depending on whether the previous day was wet or dry. Given the dry-wet state, the Markov chain-skewed model stochastically determines whether precipitation will occur or not (Arnold *et al*, 1998).

3.5.1.9 Preparation of Rainfall Statistical Parameters

The weather generator component in the SWAT modelling system requires some statistical parameters of daily rainfall as part of the input weather data for use in simulating daily rainfall. These parameters were calculated using the precipitation statistics software (pcpSTAT) written by Liersch (2003). The software uses text files arranged in one column starting with the first day of January of the first year and ending with the last day of December of the last year. Observed and simulated daily rainfall data were arranged in one column and converted to text files to be used as input to pcpSTAT. Observed and simulated data sets were arranged so that the first entry coincided with the first day of January of the first year and the last value with the last day of December of the last year (Liersch, 2003).

The preparation was done for daily rainfall values of observed rainfall in the period 1961-2011 and also for the PRECIS model-simulated daily rainfall for the periods 1961-1990, 2001-2030, and 2021-2050. The outputs from the pcpSTAT included the output file together with two additional files containing a table of total monthly rainfall of each year of the entire period, and a table of average daily rainfall values of each year of the entire period (Liersch, 2003).

3.5.1.10 Solar Radiation and Air Temperature

SWAT internally generates maximum and minimum air temperatures as well as solar radiation using the inbuilt weather generator. A continuity equation is incorporated into the weather generator to account for temperature and radiation variations caused by the dry and wet day conditions. These values were generated from input averages of monthly data (Neitsch *et al*, 2011). The average air temperature was used to determine whether precipitation should be simulated as rainfall or snowfall. Maximum and minimum temperature inputs were used in the calculation of the daily soil and water temperatures which were important in the determination of stream flow rates (Gassman *et al*, 2007). Terrestrial radiation which depends on sunrise, sunset, latitude and solar declination was also calculated (Equation 3.20).

$$H_o = 37.59 E_o \left[\omega T_{SR} \sin\delta \sin\phi + \cos\delta \cos\phi \sin\left(\omega T_{SR}\right) \right] \quad \ldots\ldots\ldots\ldots 3.20$$

H_o is the calculated solar radiation, E_o (dimensionless) is the eccentricity correction factor of the Earth's orbit and is given by evaluating Equation 3.21, ω is the earth's angular velocity (rad/h), T_{SR} is the hour of sunrise, δ is the declination angle (rad), and ϕ is the latitude angle (rad).

$$E_0 = 1.00011 + 0.034221\cos\Gamma + 0.00128\sin\Gamma + 0.000719\cos 2\Gamma + 0.000077\sin 2\Gamma \text{ ....3.21}$$

Γ is the day angle (radians) and is evaluated from Equation 3.22

$$\Gamma = 2\pi\left(\frac{N-1}{365}\right) \text{..3.22}$$

N is the day number of the year and ranges from 1 on January 1 to 365 on December 31 (Wong and Chow, 2001).

Air temperature was calculated using a sinusoidal function (Equation 3.23) within the model oscillating between maximum and minimum daily air temperatures.

$$T_{hr} = \bar{T}_{av} + \frac{(T_{\max} - T_{\min})}{2}\cos(0.2618(hr - 15)) \text{ ....3.23}$$

T_{hr} is the surface air temperature at a given hour (°C), $\bar{T}_{av}$ is the daily average temperature (°C); $T_{\max}$ is the maximum temperature at a given hour (°C); and $T_{\min}$ is the minimum temperature at a given hour (°C). Soil temperature in a given layer was calculated (Equation 3.24) using the previous day's soil temperature, the mean annual air temperature, the current day's soil surface temperature and the depth.

$$T_{soil}(z,d_n) = l.T_{soil}(z,d_n - 1) + [1.0 - l][df\,[\bar{T}_{AAair} - T_{ssurf}] + T_{ssurf}] \text{ ....3.24}$$

$T_{soil}(z,d_n)$ is the soil temperature (°C) at depth *z* (mm) below the surface, and on the day of the year *d_n*; *l* is the lag coefficient that controls the influence of the previous day's temperature and is set to 0.8 in the SWAT model; $T_{soil}(z,d_n - 1)$ is the previous day's soil temperature (°C); *df* is the depth factor which quantifies the influence of the depth below the surface on the soil temperature; $\bar{T}_{AAair}$ is the average annual air temperature (°C); and T_{ssurf} is the soil surface temperature (°C) (Neitsch *et al*, 2011).

3.5.1.11 Wind speed

The SWAT model generated mean daily wind speeds by solving a modified exponential Equation 3.25.

$$\mu_{10m} = \mu wnd_{mon} \cdot \left(-1\mathrm{n}\left(rnd_1\right)\right)^{0.3} \quad \text{……………..……………..……………..... 3.25}$$

μ_{10m} is the mean wind speed for the day at a height of 10 m above the surface (ms^{-1}), μwnd_{mon} is the monthly average wind speed (ms^{-1}), and rnd_1 is a random number between 0.0 and 1.0 (Neitsch *et al*, 2011).

3.5.1.12 Relative humidity

The relative humidity model subcomponent of the SWAT weather generator uses a triangular distribution to simulate the daily average relative humidity from the monthly averages. The triangular distribution used to generate daily relative humidity values requires four inputs namely: mean monthly relative humidity $\left(R_{hmm}\right)$, monthly maximum relative humidity (R_{hUmon}), monthly minimum relative humidity (R_{hLmon}), and a random number between 0.0 and 1.0. Mean monthly relative humidity for the month was calculated by solving Equation 3.26.

$$R_{hmon} = \frac{e_{mon}}{e^0{}_{mon}} \quad \text{……………..……………………..……..………3.26}$$

R_{hmon} is the relative humidity for the month, e_{mon} is the actual vapour pressure at the mean monthly temperature (kPa), and $e^0{}_{mon}$ is the saturation vapour pressure at the mean monthly temperature (kPa). Maximum relative humidity was calculated (Equation 3.27) from the mean monthly relative humidity.

$$R_{hUmon} = R_{hmon} + \left(1 - R_{hmon}\right).\exp\left(R_{hmon} - 1\right) \quad \text{…………………………..…………3.27}$$

R_{hUmon} is the highest relative humidity value that can be generated on a given day in the month, and R_{hmon} is the average relative humidity for the month. Minimum relative humidity value was calculated by solving Equation 3.28.

$$R_{hLmon} = R_{hmon}.\left(1 - \exp\left(-R_{hmon}\right)\right) \quad \text{………..…..……………….………3.28}$$

R_{hLmon} is the lowest relative humidity that can be generated on a given day in the month, and R_{hmon} is the average relative humidity for the month (Neitsch *et al,* 2011).

3.5.1.13 Land Phase Component

The land phase of the hydrologic cycle comprises two main components: hydrology and routing. The hydrology component of the cycle comprises the flow processes occurring on the land phase of the hydrological cycle and is based on the soil water balance equation (Equation 3.29) which forms the basis of hydrological modelling. The main modelling processes of the hydrology component of the SWAT model which are simulated through the soil water balance equation include: surface runoff, infiltration, evaporation, plant water uptake, lateral subsurface flow, percolation to the shallow and deep aquifers, and the base flow (Neitsch *et al,* 2011; Faramarzi *et al,* 2009). In this study the hydrology component was simulated based on the soil water balance equation suggested by Arnold *et al* (1998).

$$SW_t = SW_o + \sum_{i=1}^{t}\left(R_{day} - Q_{surf} - E_a - W_{seep} - Q_{gw}\right) \ldots\ldots 3.29$$

SW_t is the final soil water content (mmH$_2$O), SW_o is the initial soil water content on day *i* (mmH$_2$O), t is the time (days), R_{day} is the amount of rainfall on day *i* (mmH$_2$O), Q_{surf} is the amount of surface runoff on day *i* (mmH$_2$O), E_a is the amount of evapotranspiration on day *i* (mmH$_2$O), W_{seep} is the amount of water entering the vadoze zone from the soil profile on day *i* (mmH$_2$O), and Q_{gw} is the amount of return flow on day *i* (mmH$_2$O).

In this study surface runoff from daily rainfall amounts was modelled using a modified SCS curve number method (Equation 3.30) based on LULC characteristics, soil hydrologic group and antecedent soil moisture content.

$$Q_{surf} = \frac{\left(R_{day} - 0.2\mathrm{S}\right)^2}{R_{day} + 0.8\mathrm{S}} \qquad R_{day} > 0.2S \ldots\ldots 3.30a$$

$$Q_{surf} = 0 \qquad R_{day} \leq 0.2S \ldots\ldots 3.30b$$

Q_{surf} is the accumulated daily surface runoff (mmH$_2$O), R_{day} is the daily rainfall depth (mmH$_2$O), and S is the retention parameter (Abbaspour *et al,* 2009; Schuol *et al,* 2008; Arnold *et al,* 1998).

The retention parameter varies spatially and temporally. The parameter varies spatially among watersheds because soils, land use, management, and slope vary; and temporally because of changes in the soil water content (Arnold *et al*, 1998). The parameter is related to the curve number by the SCS equation (Equation 3.31)

$$S = 254\left(\frac{100}{CN} - 1\right) \qquad 3.31$$

CN is the SCS curve number for the given day and ranges from 30 to 100 (Neitsch *et al*, 2011).

3.5.1.14 Time of concentration

Time of concentration was calculated (Equation 3.32) by summing up the overland flow time and the channel flow time.

$$t_{conc} = t_{ov} + t_{ch} \qquad 3.32$$

t_{conc} is the time of concentration for a sub-basin (hr), t_{ov} is the time of concentration for overland flow (hr) (Equation 3.33), t_{ch} is the time of concentration for channel flow (hr) (Equation 3.34).

$$t_{ov} = \frac{L_{slp}}{3600 \cdot V_{ov}} \qquad 3.33$$

L_{slp} is the sub-basin slope length (m), V_{ov} is the overland flow velocity (ms^{-1}) and 3600 is a unit conversion factor.

$$t_{ch} = \frac{L_c}{3.6 \cdot V_c} \qquad 3.34$$

L_c is the average channel length for the sub-basin (km), V_c is the average channel velocity (ms^{-1}), and *3.6* a unit conversion factor.

3.5.1.15 Canopy Storage

When SWAT calculates surface runoff using SCS curve number method, canopy interception is lumped in the term for initial abstraction. The maximum amount of water that can be in the canopy storage varies from day to day as a function of leaf area index (LAI) and was computed using Equation 3.35.

$$Can_{day} = Can_{mx} \cdot \frac{LAI}{LAI_{mx}} \quad \text{...3.35}$$

Can_{day} is the maximum amount of water that can be trapped in the canopy on a given day (mmH$_2$O), Can_{mx} is the maximum amount of water that can be trapped in the canopy when the canopy is fully developed (mmH$_2$O), LAI is the leaf area index for a given day and LAI_{mx} is the maximum leaf area index for the plant.

3.5.1.16 Sub-Surface Flow

The available soil water capacity (AWC) was calculated (Equation 3.36) by subtracting the fraction of the water present at the permanent wilting point (WP) from the fraction of the water present at field capacity (FC).

$$AWC = FC - WP \quad \text{...3.36}$$

AWC is the available soil water content, FC is the soil water content at field capacity and WP is the soil water content at the permanent wilting point.

3.5.1.17 Routing Component

The model maintains a continuous water balance and hence complex basins have to be sub-divided into sub-basins to reflect the differences in evapotranspiration for various crops and soils. Runoff is thus modelled separately for each sub-basin and then routed to obtain the total runoff for the basin (Arnold *et al,* 1998). This increases accuracy of runoff simulation and gives a better physical description of the water balance. In this study, the modelled runoff from each sub-basin was routed through the river basin to the main basin outlet at RGS 1JG01 using the Muskingum method.

Manning's equation for uniform flow in a channel (Equations 3.37) was used to calculate the rate and velocity of flow in a channel segment for a given time step.

$$q_{ch} = \frac{A_{ch} R_{ch}^{\frac{2}{3}} slp_{ch}^{\frac{1}{2}}}{n} \quad \text{...3.37a}$$

$$v_{ch} = \frac{R_{ch}^{\frac{2}{3}} slp_{ch}^{\frac{1}{2}}}{n} \quad \text{..3.37b}$$

q_{ch} is rate of flow in the channel (m^3/s), A_{ch} is the cross-sectional area of the channel (m^2), R_{ch} is the hydraulic radius for a given depth of flow (m), slp_{ch} is the slope of the channel along the length (m/m), v_{ch} is the flow velocity in the channel (ms^{-1}) and n is the Manning's coefficient for the channel (Neitsch *et al*, 2011).

Muskingum storage method models the storage volume as a combination of wedge and prism storages using Equation 3.38 (Neitsch *et al*, 2011).

$$q_{out,2} = C_1 q_{in,2} + C_2 q_{in,1} + C_3 q_{out,1} \quad \text{...3.38}$$

$q_{out,2}$ is the out flow rate at the beginning of the time step 3; $q_{in,2}$ is the inflow rate at the beginning of the time step 1, $q_{in,1}$ is the inflow rate at the end of the time step 2, $q_{out,1}$ is the outflow rate at the end of the time step 3. Muskingum routing equation (Equation 3.39) was used to route the water in the channel.

$$C_1 = \frac{\Delta t - 2KX}{2K(1-X) + \Delta t} \quad \text{..3.39a}$$

$$C_2 = \frac{\Delta t + 2KX}{2K(1-X) + \Delta t} \quad \text{..3.39b}$$

$$C_3 = \frac{2K(1-X) - \Delta t}{2K(1-X) + \Delta t} \quad \text{..3.39c}$$

C1, C2, and C3 are the routing coefficients and it may always be checked that $C_1 + C_2 + C_3 = 1$, K is the storage time constant for the reach and X is the weighting factor.

The variable storage method is based on the continuity equation for a given channel reach segment. In this method the stored amount of water is basically the difference between the input into and the output out of the segment. In this method, one of the options provided for in the SWAT model storage for a given channel segment is based on the continuity Equation 3.40.

$$V_{in} - V_{out} = \Delta V_{stored} \quad \text{……..……………………………………..……..… 3.40}$$

V_{in} is the volume of inflow (m^3H_2O), V_{out} is the volume of outflow (m^3H_2O), ΔV_{stored} is the change in the volume of storage during the time-step (m^3H_2O).

3.5.2 SWAT Model Simulations

Having loaded all the necessary data into the SWAT model, initial model runs at two selected gauging stations, Sondu and Kiptiget, were performed to establish whether the data were correctly loaded. The initial runs were also used to assess the suitability of the model for the catchment before moving on to the model calibration and validation stage (Winchel *et al*, 2010).

3.5.2.1 Model Calibration and Validation

After successfully setting up the model, the next important and challenging step was the calibration and validation procedure. Before the model could be applied and used for decision making, it was necessary to first calibrate and validate the model input parameters to reduce the uncertainty in the model simulations. In this study the model was calibrated and validated at the sub-basin level based on monthly observed discharge values at Kiptiget RGS following a three-step procedure; the model sensitivity analysis followed by the model parameter calibration and validation (Winchel *et al*, 2010; Abbaspour *et al*, 2009; Schuol *et al*, 2008).

3.5.2.2 Sensitivity Analysis

Automated sensitivity analysis of 21 SWAT model input parameters (Gassman *et al*, 2007) for the 188 km^2 Kiptiget sub-catchment was performed. The model was run for the period between 1969 and 1990 using Kiptiget RGS observed discharge data. During each model run, the objective function was calculated as the sum of the squared errors between the observed and simulated streamflows. The effect of a change of a parameter value on this objective function was then calculated and the parameters ranked with decreasing sensitivity (Veith and Ghebremichael, 2009).

3.5.2.3 Calibration and Validation

The model was calibrated and validated at the sub-basin level based on monthly observed discharge at Kiptiget RGS. Calibration was done manually using split sample approach following the procedure recommended by Arnold *et al* (2011). Model-simulated and corresponding observed monthly discharges from 1983 to 1987 were used to calibrate the model input parameters while those observed from 1988 to 1990 were used to validate the model. The sum of squares method was used as the optimisation scheme accompanied by visual inspection of monthly hydrographs (Van Liew *et al*, 2005). Results of model validation were used to accept or reject the model results based on the criteria set in the next section (Moriasi *et al*, 2007).

3.5.2.4 Assessment of Model Performance

The appropriateness of a hydrologic model in a catchment area can be evaluated based on three criteria: fit-to-observations, fit-to-reality, and fit-to-purpose (Van Griensven, *et al*, 2012). The fit-to-observations involves the evaluation of performance indicators where the error between the model outputs and observed values for the same variable is computed, fit-to-reality involves the evaluation of the extent to which the hydrological processes in the catchment area are realistically represented by means of parameter and mass balance evaluations, and fit-to-purpose involves evaluation of the extent to which the model is able to tackle the problem.

In this study, the fit-to-observations criterion, which computes the accuracy of simulations compare observations, was adopted. This is the most typical evaluation criterion used to evaluate the performance of hydrologic models on account of its objectivity and affordability (Van Liew *et al*, 2005; Krause *et al,* 2005; Moriasi *et al*, 2007; Van Griensven, *et al*, 2012).

Based on this criterion, Moriasi *et al* (2007) have recommended the following quantitative statistics for model evaluation: Coefficient of determination (R^2), Nash-Sutcllife Efficiency (NSE), Percentage Bias (PBIAS), and the ratio of root-mean-square error (RSR) to the standard deviation of the observation data. This is in addition to graphical assessment through hydrographs and percent exceedance probability curves (Krause *et al*, 2005; Moriasi *et al*, 2007; Sexton *et al,* 2010; Van Griensven, *et al*, 2012). The following subsections present a brief highlight of the quantitative statistics used for model assessment in this study.

3.5.2.4.1 Coefficient of Determination (R^2)

The coefficient of determination is a number between 0 and 1 that reveals how closely the model-predicted values correspond to the actual observed values as reflected by the values estimated by the trend line (Muthama *et al,* 2008). The R-squared value is usually computed as a measure of how well the observed values are replicated by the model as a proportion of total variations explained by the model (Moriasi *et al,* 2007). The R-squared statistic is computed as a comparison of the variability of the estimation error (SS_E) with the variability of the original value (SS_T) using Equation 3.41.

$$R^2 = 1 - \frac{SS_E}{SS_T} \quad \ldots\ldots\ldots\ldots\ldots\ldots\ldots\ldots\ldots\ldots\ldots\ldots\ldots\ldots 3.41$$

SS_E is the sum of squared errors and SS_T is the total sum of squares.

The smaller the SS_E, the higher the values of R^2 and the more reliable the predictions obtained from the model. Values of R^2 close to 1 indicate less variance and values of $R^2 > 0.5$ are considered acceptable. This statistic however has short comings that make it necessary to use other statistics to assess the model performance. It is highly sensitive to outliers and insensitive to additive and proportional differences between model predictions and observed data (Moriasi *et al,* 2007).

3.5.2.4.2 Nash–Sutcliffe Efficiency (NSE)

This efficiency criterion was proposed by Nash and Sutcliffe (1970) and is the most frequently used indicator in hydrological modelling to assess the accuracy of model simulations based on observations. It is a normalised index (Equation 3.42) that measures the fraction of the observed flow variance that is reproduced by the model (Van Griensven, 2005; Glavan and Pintar, 2012; Moriasi *et al,* 2007; Van Liew *et al,* 2005)

$$NSE = 1 - \frac{\sum_{i=1}^{n} \left(O_i - P_i\right)^2}{\sum_{i=1}^{n} \left(O_i - \overline{O}\right)^2} \quad \ldots\ldots\ldots\ldots\ldots\ldots\ldots\ldots\ldots\ldots 3.42$$

NSE is the model efficiency, O_i is the observed discharge series, P_i is the predicted discharge series, $\overline{O}$ is the mean of the observed discharge series, and n is the total number of observations. Values of NSE range between $-\infty$ and 1. Values of NSE between 0 and 1 are considered acceptable while those that are less than 0 are considered unacceptable (Moriasi *et al,* 2007).

Minimisation of the difference between observed (O_i) and simulated (P_i) values through calibration results in maximising the NSE index for a given series that is calibrated. The differences between simulated and observed values may be due to either data deficiencies or model deficiencies (Van Liew *et al,* 2005). Moriasi *et al* (2007) recommended the following NSE criteria for evaluation of model performance: $0.5 < NSE \leq 0.65$ (Satisfactory performance), $0.65 < NSE \leq 0.75$ (Good performance), and $0.75 < NSE \leq 1.0$ (Very good performance).

3.5.2.4.3 Percentage Bias (PBIAS)

Percentage Bias (*PBIAS*), evaluated using Equation 3.43, is a measure of the average tendency of the simulated values to be larger or smaller than the corresponding observed values and has ability to clearly indicate the level of model performance (Moriasi *et al*, 2007). The optimal value of PBIAS is 0, indicating a perfect model. Positive and negative values of PBIAS indicate model bias towards underestimation and overestimation respectively (Galvan and Pintar, 2012; Van Griensven, *et al*, 2012).

$$PBIAS = \left(\frac{\sum_{i=1}^{n} (O_i - Pi)}{\sum_{i=1}^{n} O_i} \right) \times 100 \quad \text{...3.43}$$

O_i is the observed stream flow (m^3s^{-1}), P_i is the simulated streamflow (m^3s^{-1}), and $PBIAS$ is the deviation of stream flow discharge expressed as a percentage. Moriasi *et al* (2007) recommended the following $PBIAS$ criteria for evaluation of model performance: $\pm 15\% \leq PBIAS < 25\%$ (Satisfactory performance), $\pm 10\% \leq PBIAS < \pm 25\%$ (Good performance), and $PBIAS < \pm 10\%$ (Very good performance).

3.5.2.4.4 Ratio of Root-Mean-Square Error to Standard Deviation of Observations (RSR)

The Root Mean Square Error (RMSE) is one of the error index statistics commonly used to evaluate model performance. The lower the RMSE values (Equation 3.44a) the better the model performance. During model evaluation, RMSE values less than half of the standard deviation of observed (STDEVobs) data, as given in Equation 3.44b, are considered low enough to accept the model performance (Moriasi *et al,* 2007; Van Griensven, *et al*, 2012).

$$RMSE = \sqrt{\sum_{i=1}^{n} (O_i - P_i)^2} \quad \text{...3.44a}$$

$$STDEVobs = \sqrt{\sum_{i=1}^{n} (O_i - \overline{O})^2} \quad \text{...3.44b}$$

O_i is the observed stream flow (m^3s^{-1}), P_i is the simulated streamflow (m^3s^{-1}), and $\overline{O}$ is the mean observed streamflow (m^3s^{-1}).

RMSE-Observations standard deviation ratio (RSR) standardises RMSE using the standard deviation of observed data (Equation 3.45).

$$RSR = \frac{\left[\sqrt{\sum_{i=1}^{n}(O_i - P_i)^2}\right]}{\left[\sqrt{\sum_{i=1}^{n}(O_i - \overline{O})^2}\right]} \quad \ldots\ldots\ldots\ldots 3.45$$

RSR values range from 0, for a perfect model simulation, to large positive values. Lower RMSE values lead to lower RSR values and hence to better model performance. Values of $RSR \leq 0.7$ are considered satisfactory indicators of model performance (Van Griensven, *et al*, 2012).

3.6 Impacts Assessment

In this section the fourth specific objective, to conduct sensitivity analysis using rainfall and forest cover changes on the hydrological regime of the catchment to determine their impacts on surface water yields, was addressed. This was done by simulating projected water yields using projected temperature and rainfall as inputs under two main forest cover scenarios: deforestation scenario and forest conservation scenario (Figure 3.4). The impacts of climate change and deforestation on water yields from the Mau forest complex were evaluated by getting the percentage difference between simulated water yields under baseline climate and forest cover scenario, and simulated water yields under changed climate and forest cover scenario.

For the purpose of this study, landuse scenarios are defined as the extent of percentage forest cover based on the LANDSAT satellite imageries of the area of study taken in 1973 (LU73), 1986 (LU86), 2000 (LU00), and 2010 (LU10). The impacts on water yields were evaluated at three levels: (A) impacts of deforestation only, (B) impacts of climate change only, and (C) impacts of climate change and deforestation.

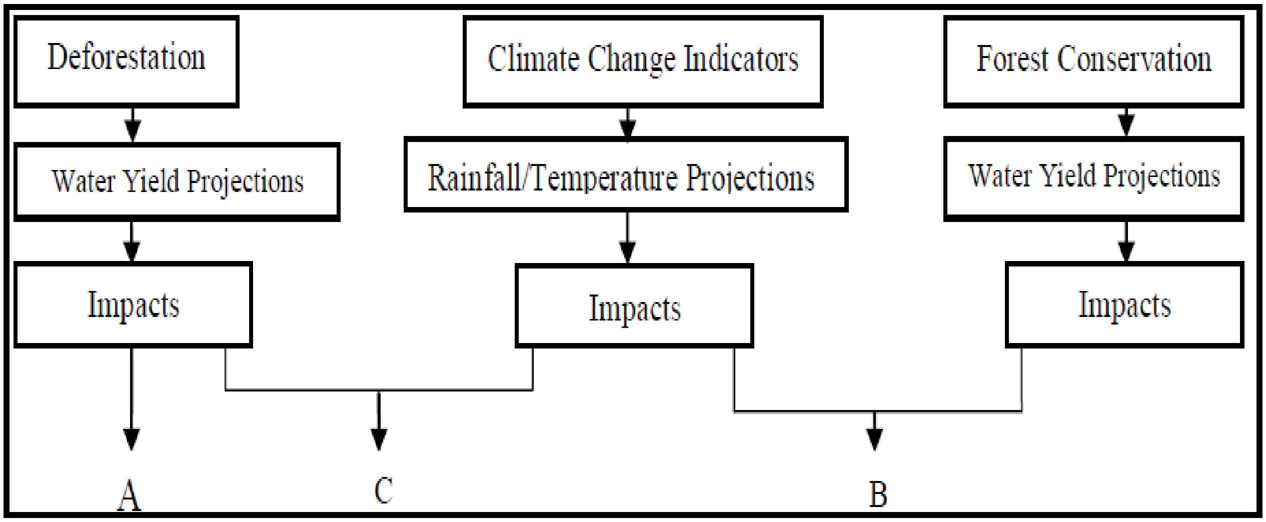

Figure 3.4: Flow chart of how the fourth specific objective was achieved

3.6.1 Impacts of Climate Change on Water Yields

The impacts of climate change on water yields from the Mau forest complex were assessed by simulating water yields at the baseline forest cover (LU73) and allowing the climate to change. Water yields were therefore simulated under baseline climate (1970s) and projected climates in 2010s and 2030s. The impacts of climate change were evaluated as the percentage difference between the projected and the baseline water yields (Equation 3.46). Any changes in the simulated water yields were attributed to climate change.

$$impacts = \left(\frac{WYLD_{CC} - WYLD_{BF}}{WYLD_{BF}} \right) \times 100 \quad \ldots\ldots\ldots\ldots\ldots\ldots\ldots\ldots\ldots 3.46$$

$WYLD_{CC}$ is the water yields under changing climate, $WYLD_{BF}$ is the water yields under the baseline forest cover scenario

3.6.2 Impacts of Deforestation on Water Yields

The impacts of deforestation on water yields from the Mau forest complex were assessed by simulating water yields at the baseline climate (1970s) and allowing the forest cover to change. Water yields were therefore simulated under baseline forest cover (LU73) and under changed land cover scenarios LU86, LU00, and LU10. The impacts of deforestation were evaluated as the percentage difference between the simulated water yields under changed forest cover scenarios and the baseline water yields (Equation 3.47). Any changes in the simulated water yields were attributed to deforestation.

$$impacts = \left(\frac{WYLD_{DF} - WYLD_{BC}}{WYLD_{BC}} \right) \times 100 \quad \ldots\ldots\ldots\ldots\ldots\ldots\ldots\ldots\ldots\ldots..3.47$$

$WYLD_{DF}$ is the water yields under deforestation, $WYLD_{BC}$ is the water yields under the baseline climate.

3.6.3 Impacts of Climate Change and Deforestation on Water Yields

The impacts of climate change and deforestation on water yields from the Mau forest complex were assessed by simulating water yields at the baseline climate (1970s) for all the forest cover scenarios: LU73, LU86, LU00, and LU10 to obtain baseline water yields. To obtain projected water yields under changing climate and deforestation, climates of 2010s and 2030s were used to simulate water yields under all the forest cover scenarios. The impacts of climate change and deforestation on water yields were evaluated as the percentage difference between the projected water yields under changed climate and forest cover scenarios and the baseline water yields (Equation 3.48). Any changes in the simulated water yields were attributed to both climate change and deforestation.

$$impacts = \left(\frac{WYLD_{CC,DF} - WYLD_{BC,BF}}{WYLD_{BC,BF}} \right) \times 100 \ldots\ldots\ldots\ldots\ldots\ldots\ldots\ldots\ldots.3.48$$

$WYLD_{CC,DF}$ is the water yields under climate change and deforestation, $WYLD_{BC,BF}$ is the water yields under baseline climate and forest cover scenarios. Results of these computations are presented and discussed in detail in the next chapter.

CHAPTER 4

RESULTS AND DISCUSSION

4.1 Introduction

The results of this study and their discussion are presented in this chapter in five sections namely: (i) Data Quality Control, (ii) Trends of Observed Climate, Discharge, and Forest Cover, (iii) Climate Simulations, (iv) Stream Flow Simulations, and (v) Impacts on Water Yields.

4.2 Data Quality Control

In this section, results of data quality control are presented and their suitability for the study established. Specifically this section presents results homogeneity tests.

4.2.1 Homogeneity Test

Once the problem of missing data records was sorted out, it was then necessary to establish the consistency of data from each of the stations by testing their homogeneity. Results of Bartlett test of homogeneity (Tables 4.1 to 4.3) revealed that most of the data from the basin were homogenous. Table 4.1 shows results of rainfall data homogeneity test using Bartlett method. The table shows values of computed F-statistic $\left(F_{cal}\right)$ and the tabulated critical F-values $\left(F_{2\alpha}\right)$ for the two-sided test required for this study. $S^2{}_{\max}$ is the maximum sample variance, $S^2{}_{\min}$ is the minimum sample variance, $F_{2\alpha=0.1}$ is the critical value for a two-sided test. From the results, any values of F_{cal} greater than $F_{2\alpha}$ show inconsistency of the whole data set and hence the sample data is not homogeneous. In this case, rainfall data from Bomet, Chagaik, and Kaisugu were found to be inconsistent while data from the other stations were found to be homogeneous according to this test.

The stations with inconsistent data were all found to be located outside the catchment area boundary and therefore data from them were left out of any further analysis and only data from those stations that showed consistency (Kericho, Keresoi, Ndoinet, Sotik and Timbilil) were considered for further analyses for the purpose of this study.

Table 4.1: Results of Barttlet homogeneity test for rainfall data collected at stations in and around Sondu basin

S/No	Station	Numerator		Denominator		$F_{cal} = \frac{S^2_{\max}}{S^2_{\min}}$	$F_{2\alpha=0.1}$	Conclusion
		$S^2_{\max}$	Sample size	$S^2_{\min}$	Sample size			
1	Bomet	72436	21	25575	22	2.83	1.78	Inconsistent
2	Chagaik	157370	25	86699	22	1.82	1.73	Inconsistent
3	Kaisugu	68598	25	36273	25	1.89	1.70	Inconsistent
4	Kericho	96613	21	56823	18	1.70	1.86	Homogeneous
5	Keresoi	117828	21	74078	29	1.59	1.69	Homogeneous
6	Ndoinet	97761	16	62170	21	1.57	1.86	Homogeneous
7	Sotik	64758	21	49094	21	1.32	1.79	Homogeneous
8	Timbiril	124001	21	78410	26	1.58	1.72	Homogeneous

Table 4.3 shows results of discharge data homogeneity test using Bartlett method. From the results, all the RGSs had homogeneous data and could therefore therefore be used further analyses. Table 4.3 shows results of homogeneity test for maximum and minimum temperatures using Bartlett test.

Table 4.2: Results of Barttlet homogeneity test for discharge data collected at stations within Sondu basinn

S/No	Station	Numerator		Denominator		$F_{cal} = \frac{S^2_{\max}}{S^2_{\min}}$	$F_{2\alpha=0.1}$	Conclusion
		$S^2_{\max}$	Sample size	$S^2_{\min}$	Sample size			
1	Kiptiget	0.6552	15	0.6364	13	1.25	2.03	Homogeneous
2	Ndoinet	0.0418	13	0.0271	15	1.54	2.05	Homogeneous
3	Sondu	318.7	13	210.9	15	1.51	2.05	Homogeneous
4	Sambret1	0.0018	13	0.0015	15	1.23	2.05	Homogeneous
5	Sambret2	0.000349	13	0.000257	15	1.36	2.05	Homogeneous
6	Sambret3	0.00302	15	0.00269	13	1.15	2.17	Homogeneous

Only two stations, Kericho and Timbilil, had temperature data within the area of study. Kericho had data records spanning 36 years (1975–2010) while Timbilil had records spanning 43 years (1968–2010). From the tabulated results of maximum and minimum temperatures F_{cal} values were all found to be less than the $F_{2\alpha}$ critical values indicating that temperature data were homogeneous. From the results of homogeneity tests, it was established that temperature data from the Sondu basin were homogeneous and therefore fit for further analysis.

Table 4.3: Results of Barttlet homogeneity test for mean maximum and minimum temperatures (°C)

Station Name	**Temperature**	**Numerator**		**Denominator**		$F_{cal} = \frac{S^2_{\max}}{S^2_{\min}}$	$F_{2\alpha=0.1}$	**Conclusion**
		$S^2_{\max}$	n	$S^2_{\min}$	n			
Kericho	Maximum	0.9620	16	0.0863	19	1.06	1.89	Homogeneous
	Minimum	0.4236	16	0.1034	19	1.84	1.89	Homogeneous
Timbilil	Maximum	0.2388	21	0.2087	19	1.14	1.84	Homogeneous
	Minimum	0.3839	21	0.2370	19	1.62	1.84	Homogeneous

4.3 Trends of Observed Climate, Discharge, and Forest Cover

In this section, results of temperature, rainfall, discharge variations and trends together with the trends in forest cover, are presented and discussed.

4.3.1 Temperature

Results of mean monthly annual cycle and trends of temperature showing temporal variation within the year and over longer term periods are presented in this section. The annual cycle of mean monthly temperature (Figure 4.1) shows the seasonal variation of maximum and minimum temperatures averaged over three 30-year climate regimes updated every ten years: 1961-1990, 1971-2000, and 1981-2010 which are centred in the 1970s, 1980s, and 1990s decades respectively. Results indicated that February has the warmest days while July has the coolest. The warmest nights occur in April while the coolest are in September.

Mean maximum temperatures vary from about 23°C in July to about 26°C in February while mean minimum temperatures vary from about 11°C in September to about 12°C in April. It was noted that both maximum and minimum temperatures have progressively been increasing since the 1970s (Figure 4.6). Temperatures in the 1990s are higher than those of 1980s which are in turn higher than those of 1970s except maximum temperatures in October indicating that the month of October has been cooling unlike the other months. The changes in temperature in subsequent decades after the 1970s could be a manifestation of climate change in the region where days and nights are becoming warmer compared to the baseline decade.

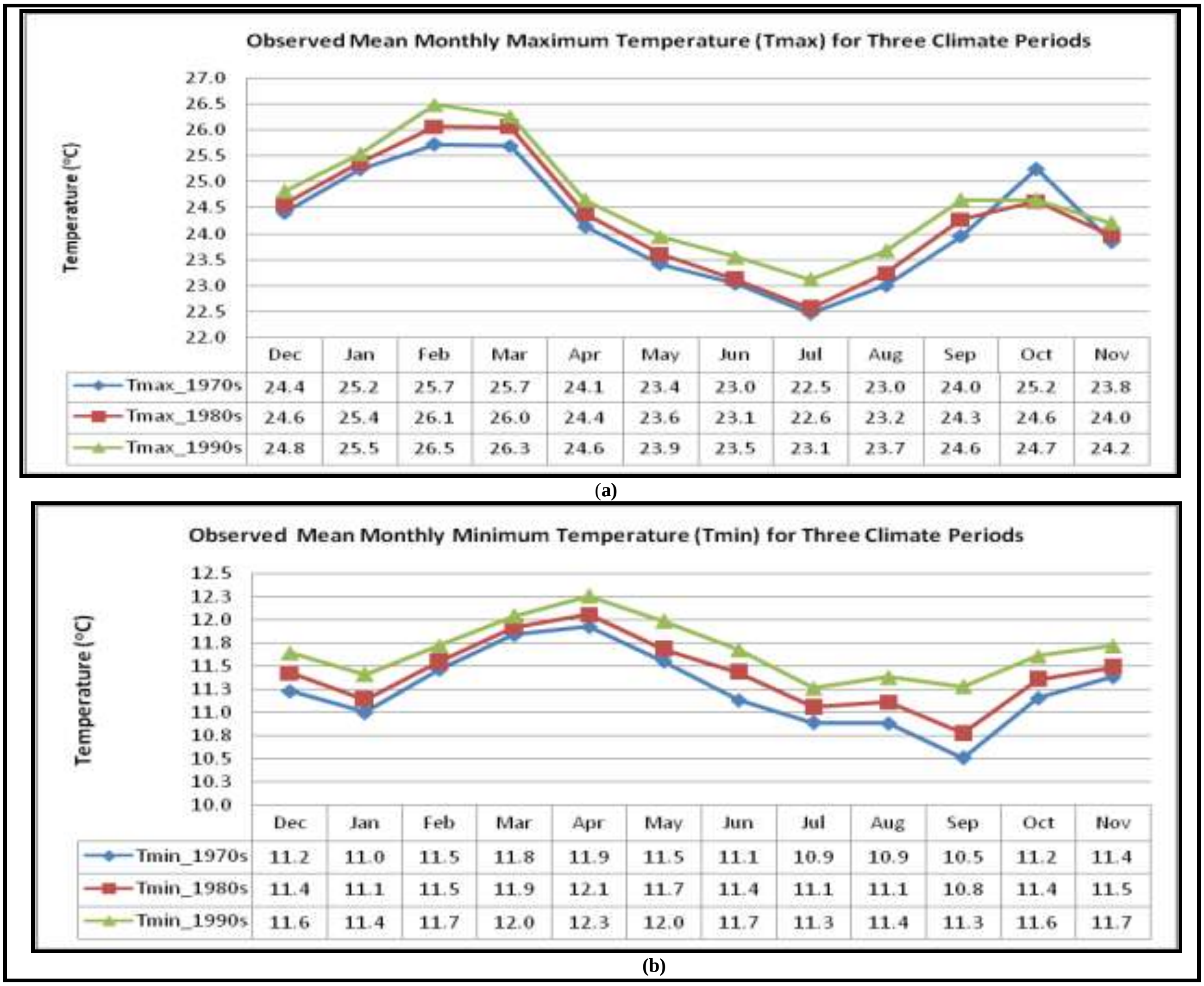

Observed Mean Monthly Maximum Temperature (Tmax) for Three Climate Periods

	Dec	Jan	Feb	Mar	Apr	May	Jun	Jul	Aug	Sep	Oct	Nov
Tmax_1970s	24.4	25.2	25.7	25.7	24.1	23.4	23.0	22.5	23.0	24.0	25.2	23.8
Tmax_1980s	24.6	25.4	26.1	26.0	24.4	23.6	23.1	22.6	23.2	24.3	24.6	24.0
Tmax_1990s	24.8	25.5	26.5	26.3	24.6	23.9	23.5	23.1	23.7	24.6	24.7	24.2

(a)

Observed Mean Monthly Minimum Temperature (Tmin) for Three Climate Periods

	Dec	Jan	Feb	Mar	Apr	May	Jun	Jul	Aug	Sep	Oct	Nov
Tmin_1970s	11.2	11.0	11.5	11.8	11.9	11.5	11.1	10.9	10.9	10.5	11.2	11.4
Tmin_1980s	11.4	11.1	11.5	11.9	12.1	11.7	11.4	11.1	11.1	10.8	11.4	11.5
Tmin_1990s	11.6	11.4	11.7	12.0	12.3	12.0	11.7	11.3	11.4	11.3	11.6	11.7

(b)

Figure 4.1: Observed mean (a) monthly maximum air Temperature (Tmax), and (b) minimum air temperature (Tmin) distribution for three climate periods over the Sondu basin

Figure 4.2 shows the changes in maximum and minimum temperatures in the 1980s and 1990s from the 1970s decade. From the figure it was observed that there was an increasing trend in both maximum and minimum temperatures in all months except in the month of October where the maximum temperature decreased by about 0.6 °C below the baseline average . The increase during

1980s decade ranged from 0.1°C in January , June and November to 0.4°C in March for maximum temperatures and from 0.1°C to 0.3°C for minimum temperatures.

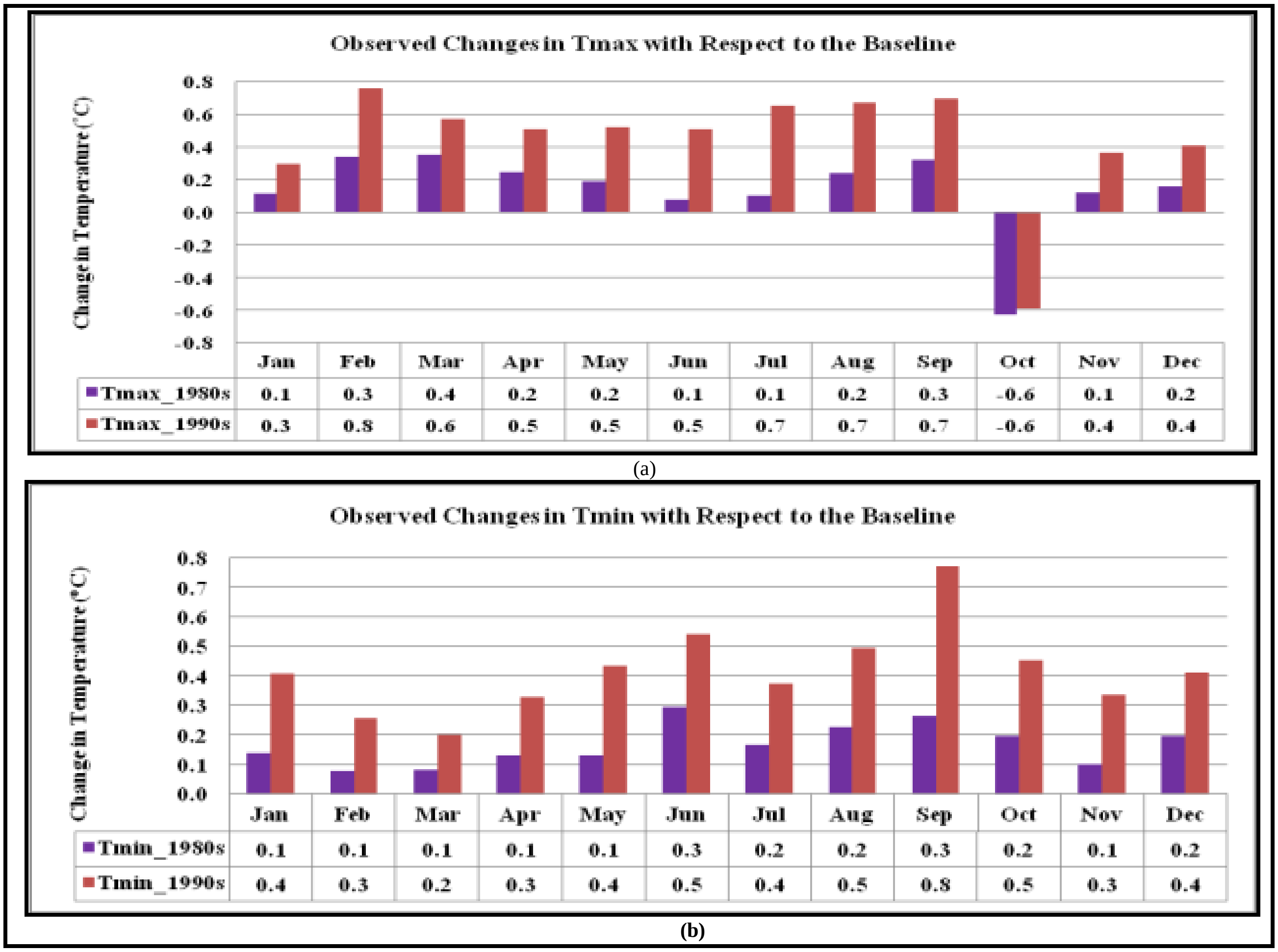

Figure 4.2: Changes in 1980s and 1990s of mean monthly (a) maximum air Temperature (Tmax), and (b) minimum air temperature (Tmin) from the baseline period over the Sondu basin

Changes in the 1990s from the 1970s were noted to follow the same patterns as those of the 1980s except that the changes were higher in the 1990s. The changes ranged from about 0.3˚C in January to 0.8˚C in February for maximum temperatures and from 0.2˚C in March to about 0.8˚C in September for minimum temperatures. While all the months indicated an increase in maximum temperature, the month of October indicated a decrease of about 0.6˚C, similar to the 1980s (Figure 4.2a).

The annual mean maximum and minimum temperature anomalies based on the baseline mean are presented in Figure 4.3 which shows the time series of normalised anomalies for both maximum and minimum temperatures over the Sondu basin. Both mean annual maximum and minimum observed temperature anomaly values show increasing trends for the fifty year period which is an indication of warming days and nights respectively. However the trends were found not to be significant (Tables 4.4 and 4.5).

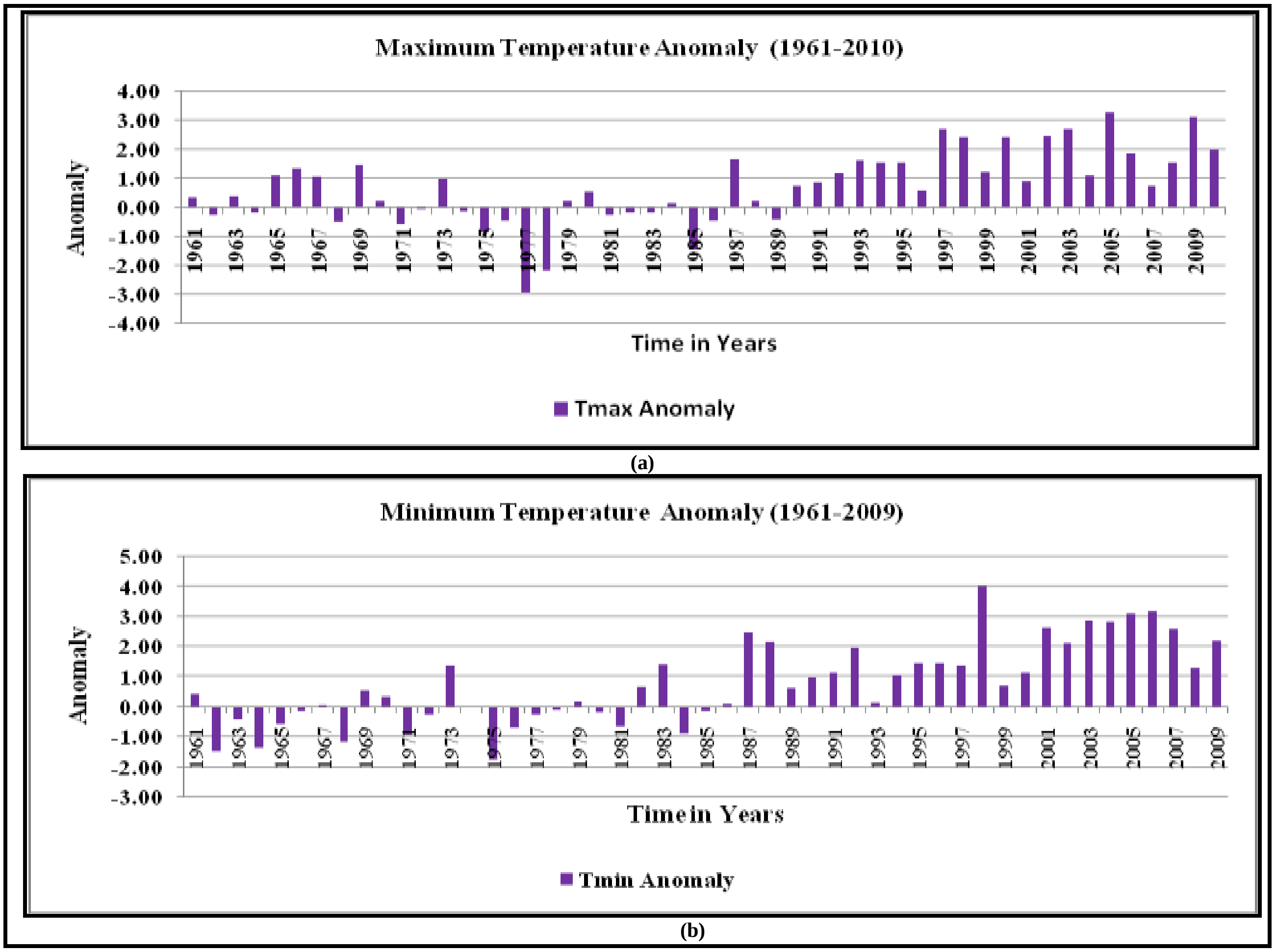

(a)

(b)

Figure 4.3: Time series of observed mean annual (a) maximum and (b) minimum temperature anomalies over the Sondu basin based on the 1961-1990 average

From the figure, 1977 had the lowest while 2005 had the highest recorded maximum temperatures respectively over the 50-year period of available data. This could be attributed to the fact that 1977 was one of the wettest years in the area while 2005 was one of the driest over the last five decades (Figure 4.8). The decade between 1971 and 1980 was the coolest with maximum temperatures falling below the baseline mean except in 1973. During the decade between 1981 and 1990 the maximum temperatures were also mainly below the baseline mean except in 1987. From 1991 onwards maximum temperatures have largely remained above the baseline mean and they have continued to increase. It is during this period that the highest temperatures in 50 years were recorded (maximum temperature in 2005 and minimum temperature in 1998)

It was observed from Figure 4.3 that from 1961 to 2010 the decades between 1971 and 2010 progressively became warmer with 1971-1980 being the coolest and 2001-2010 being the warmest. 1987 was the warmest year between 1971 and 1990 while 1997 was the warmest between 1991 and 2000; and 2005 was the warmest year between 2001 and 2010.

Trends of annual mean maximum and minimum temperatures at Kericho, Timbilil, Kisumu and Kisii stations were tested for significance against the hypothesis that they are not significantly different from zero (H_o: $b_1 = 0$) using the student's t-statistic at $\alpha = 0.05$ level of significance. The computed t-statistic t_{cal} was less than the tabulated critical value ($t_{\frac{\alpha}{2}} = 2.021$) in all the stations (Tables 4.4 and 4.5).

Table 4.4: Annual mean maximum air temperature trends (b), standard error [s(b)], and the computed t-statistic (t_{cal})

Station	**Trend (b)**	**Standard Error [s(b)]**	$\mathbf{t_{cal}} = \frac{b}{s(b)}$	**Remarks**
Kericho	0.078	0.932	0.455	Trend not significant
Timbilil	0.30	0.519	0.177	Trend not significant
Kisumu	0.019	0.418	0.111	Trend not significant
Kisii	0.011	1.041	0.064	Trend not significant

Hence the null hypothesis was accepted and it was concluded that although both maximum and minimum temperatures show positive trends in this area, the changes are not statistically significant. However these small changes in temperature can bring about significant changes in the water cycle which could impact on the water yields in the catchment.

Analysis of patterns and trends of temperature has established that the climate of this part of Kenya has become warmer since the 1970s decade. Between 1970s and 1990s, maximum temperature has increased by about 0.5°C while minimum temperature has increased by about 0.4°C at Kericho station (Figure 4.2). Taking the 1970s as the baseline decade, updates of 30-year climate after every ten years show that subsequent decades are becoming warmer in line with the global trends, where 1997 has also been documented as the warmest year globally in the last 100 years (Ahrens, 2007). Since 2005 and 2009 were warmer than 1997, it could also be concluded that the three years were the warmest in the catchment for the last 100 years.

Table 4.5: Annual mean minimum air temperature trends (b), standard error [s(b)], and the computed t-statistic (t_{cal})

Station	**Trend (b)**	**Standard Error [s(b)]**	$\mathbf{t_{cal}} = \frac{b}{s(b)}$	**Remarks**
Kericho	0.055	0.697	0.321	Trend not significant
Timbilil	0.015	0.578	0.089	Trend not significant
Kisumu	0.019	0.300	0.111	Trend not significant
Kisii	0.009	0.169	0.053	Trend not significant

4.3.2 Rainfall

Results of the analysis of observed rainfall showing the monthly annual cycle, long-term changes within the annual cycle in terms of: percentage changes in monthly rainfall, changes in the probabilities of a wet day following a dry day (PR_W1) and of a wet day following a wet day (PR_W2), changes in the number of days of rainfall in a month, and the time series anomaly of annual rainfall are presented in this section.

4.3.2.1 Monthly Rainfall Characteristics

This sub-section presents results of the analysis annual cycle of mean monthly total rainfall and their trends showing temporal variation within the year and over longer term periods. The annual cycle of mean monthly rainfall totals (Figure 4.4) shows the seasonal variation of rainfall, together with the corresponding percentage changes from the baseline rainfall climatology, averaged over three 30-year climate regimes updated every decade: 1970s, 1980s, and 1990s. This confirms the three rainfall seasons in this part of Kenya with the main rainfall season in March-April-May (MAM) where peak rainfall is centred in May followed by a minor peak in June-July-August (JJA) centred in August. These are followed by another minor rainfall peak in September-October-November (SON) centred in October. The period from December to February (DJF) is relatively dry compared to the other seasons.

This trimodal pattern of rainfall is attributed to the geographical location of the catchment, lying on the high plateau between the Rift Valley and Lake Victoria. The area is under the influence of the easterly air stream of the Indian Ocean monsoons and the large scale thermal winds of Lake

Victoria which together with low level westerly winds from the Atlantic Ocean bring in the Congo air mass which tends to enhance the JJA rainfall in the area (Nyakwanda *et al*, 2009).

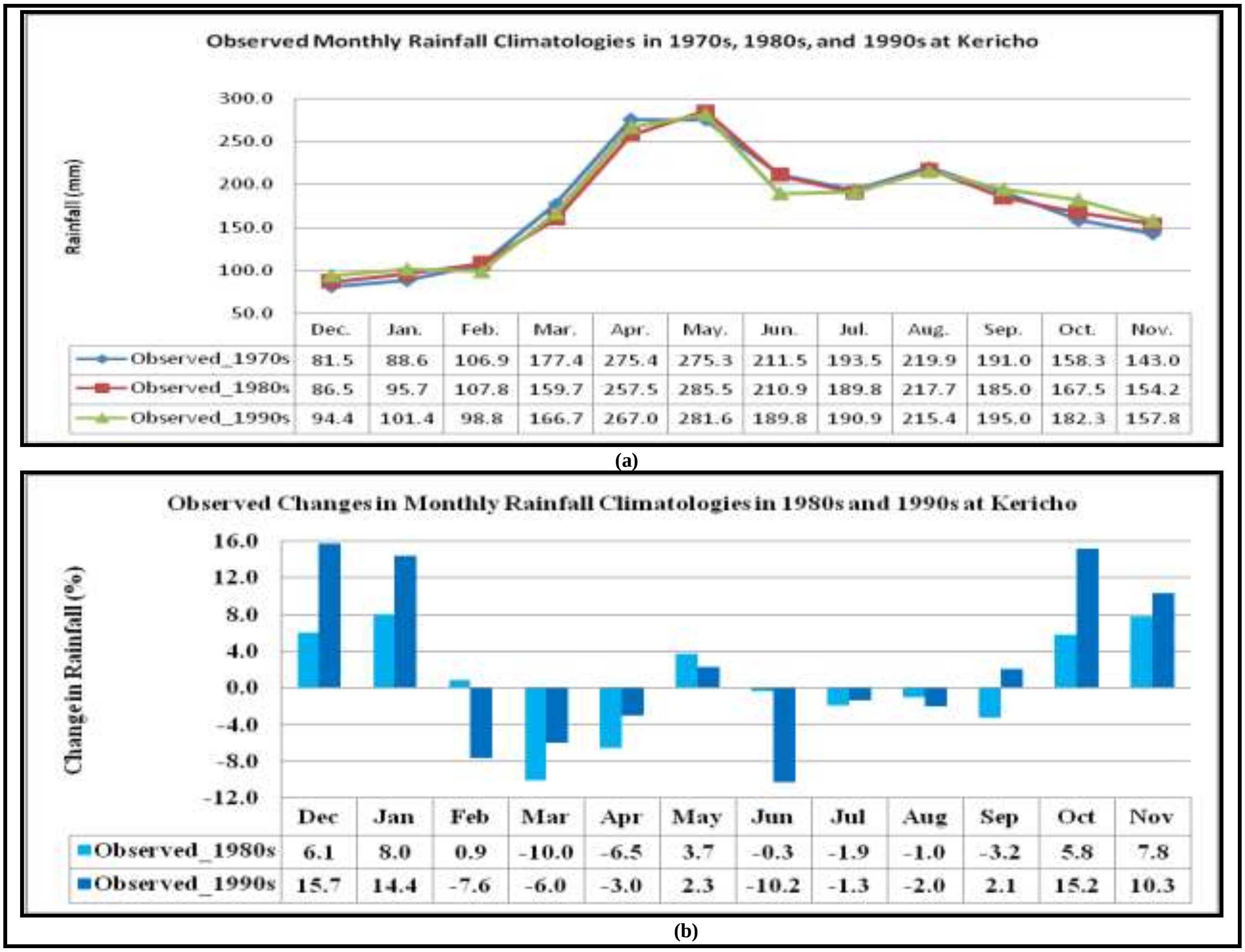

	Dec.	Jan.	Feb.	Mar.	Apr.	May.	Jun.	Jul.	Aug.	Sep.	Oct.	Nov.
Observed_1970s	81.5	88.6	106.9	177.4	275.4	275.3	211.5	193.5	219.9	191.0	158.3	143.0
Observed_1980s	86.5	95.7	107.8	159.7	257.5	285.5	210.9	189.8	217.7	185.0	167.5	154.2
Observed_1990s	94.4	101.4	98.8	166.7	267.0	281.6	189.8	190.9	215.4	195.0	182.3	157.8

	Dec	Jan	Feb	Mar	Apr	May	Jun	Jul	Aug	Sep	Oct	Nov
Observed_1980s	6.1	8.0	0.9	-10.0	-6.5	3.7	-0.3	-1.9	-1.0	-3.2	5.8	7.8
Observed_1990s	15.7	14.4	-7.6	-6.0	-3.0	2.3	-10.2	-1.3	-2.0	2.1	15.2	10.3

Figure 4.4: Observed (a) monthly rainfall distribution for three climate periods and (b) corresponding percentage changes from the baseline period at Kericho Met. Station

The difference between the baseline rainfall and the 1980s and 1990s rainfall, expressed as a percentage of the baseline rainfall, was used as an indicator of changes in rainfall patterns in this part of Kenya (Figure 4.2b). It was noted that there was a progressive increase in monthly rainfall from the baseline period (1970s) to 1990s during DJF and SON seasons. The increases in monthly rainfall ranged between 1% and 8% in the 1980s and between 10% and 16% in 1990s of the baseline rainfall. The largest increase from the baseline rainfall in the 1980s was noted in the month of January (8%) and in the 1990s in the month of December (16%). During MAM and JJA months, there was a progressive decline in monthly rainfall from the baseline to the 1990s. The largest decrease from the baseline in the 1980s was noted in the month of March (10%) while in 1990s it was in the month of June (10%).

From the results of analysis of monthly rainfall climatology, it was established that the overall observed seasonal changes in rainfall indicate a likely shift in rainfall patterns where the relatively dry DJF and SON seasons are becoming relatively wet and the relatively wet MAM and JJA seasons are becoming relatively dry (Figure 4.2b). The overall change in DJF and SON seasons is positive, +5.1% in 1980s and +7.5% in1990s for DJF and +3.5% in 1980s and +9.2% in 1990s for SON. Hence the two seasons are becoming wetter with time. On the other hand the overall changes in MAM and JJA seasons are negative: -4.3% in 1980s and -2.2% in 1990s for MAM and -1.1% in 1980s and -4.5% in 1990s for JJA. These observed changes in monthly rainfall across the three climate regimes have a direct impact on the water yields from the catchment area.

4.3.2.2 Probabilities of Rainfall Days in a Month

Figure 4.5 shows the probabilities of a wet day following a dry day in a month (PR_W1) in the three climate periods: 1970s, 1980s, and 1990s and their corresponding percentage changes from the baseline period probabilities. PR_W1 shows progressive changes from the baseline period to the 1990s where it increased in some months but decreased in others (Figure 4.5b). PR_W1 in the 1970s, 1980s, and 1990s shows a decrease in two of the three months during DJF (December and February) and MAM (March and May) seasons. JJA and SON show relatively smaller changes in PR_W1 but the changes do not follow any particular pattern (Figure 4.5b).

The increases in the probability of a wet day following a dry day range from 3% to 8% in 1980s and from 1% to 11% in 1990s while decreases range from 1% to 7% in 1980s and from 1% to 20% in 1990s. There are more months showing a decrease in PR_W1 than those showing an increase (Figure 4.5b) while the probability of a wet day following a wet day in a month (PR_W2) is less than that of the baseline period in all the months by between 1% and 6% in 1980s and between 1% and 7% in 1990s (Figure 4.6).

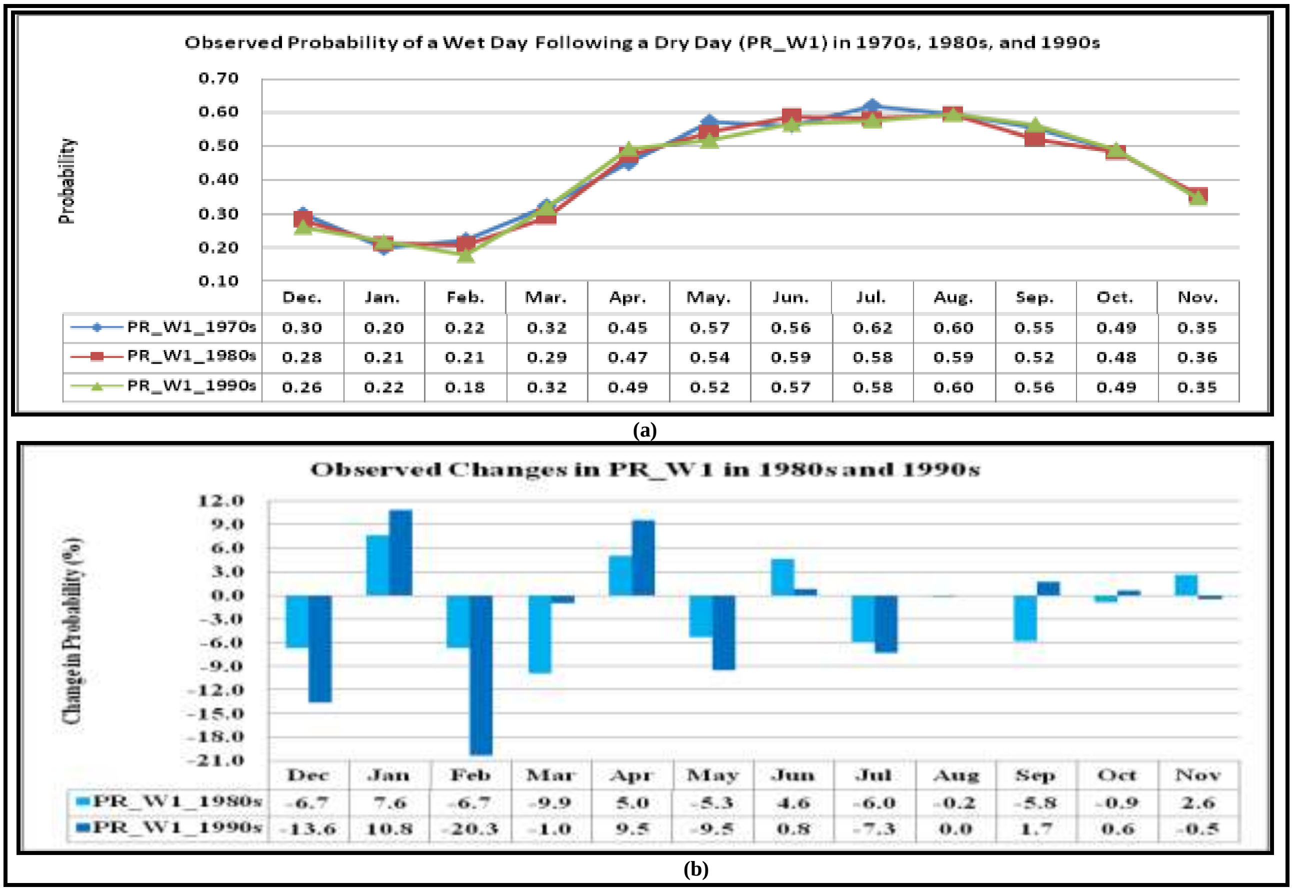

Figure 4.5: Observed (a) Probability of a wet day following a dry day in a month (PR_W1) and (b) corresponding changes from the baseline period at Kericho Met. Station

Results of the analysis of the probabilities of a wet day following a dry day (PR_W1) and a of a wet day following a wet day (PR_W2) have established that the observed changes in PR_W1 and PR_W2 indicate that there has been a tendency towards water stress from the baseline period to the 1990s resulting in declining water yields from the catchment.

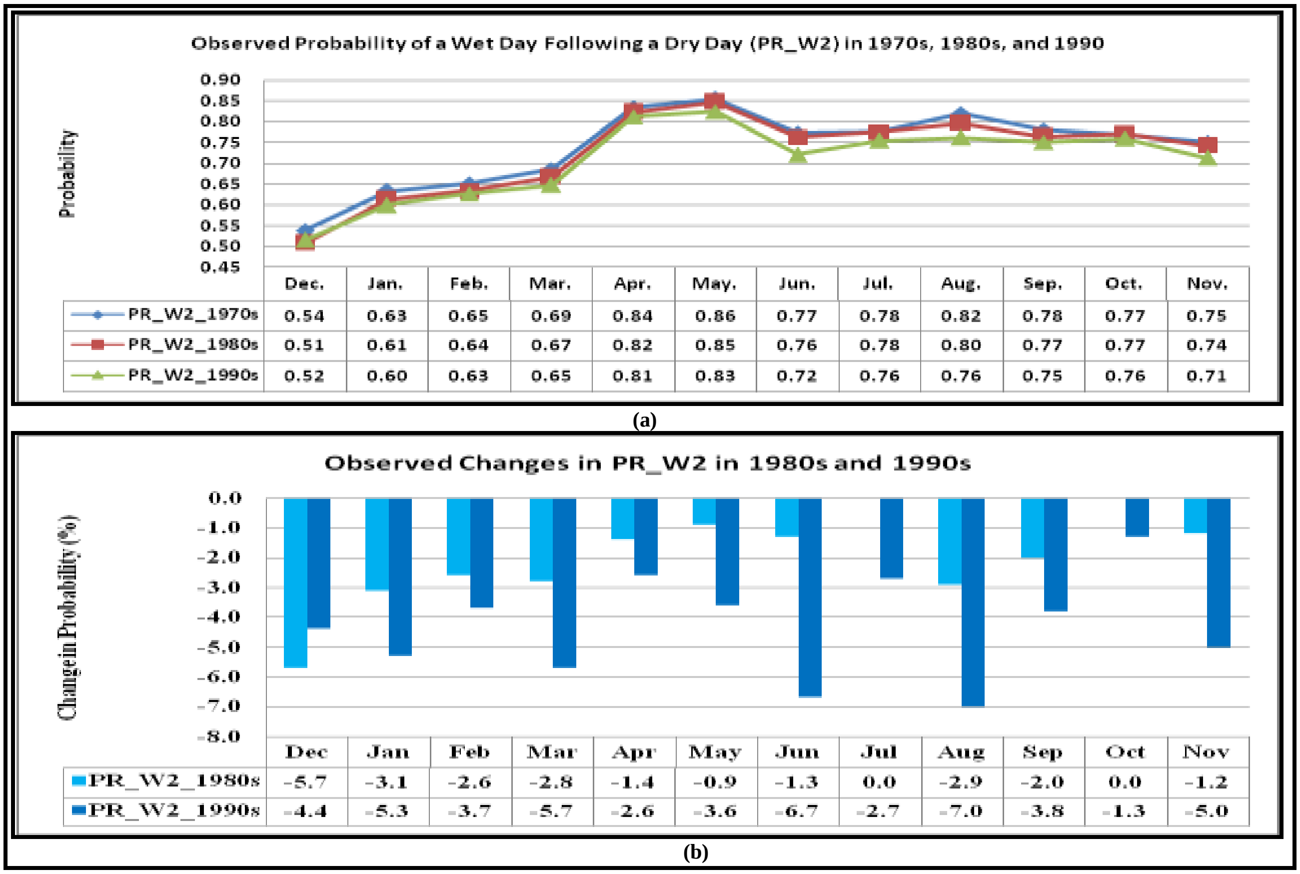

Figure 4.6: Observed (a) Probability of a wet day following a wet day in a month (PR_W2) and (b) corresponding changes from the baseline period at Kericho Met. Station

4.3.2.3 Average Number of Days of Rainfall in a Month

The average number of days with rainfall in a month shows a progressively decreasing trend from the 1970s to 1990s (Figure 4.7a). Except the month of January, all the other months have had fewer days with rainfall in the 1980s and 1990s compared to the baseline period. The largest decrease in the number of days of rainfall is found in the month of February. The decreases range between 1% and 8% in 1980s and between 2% and 18% in 1990s (Figure 4.7b). The observed changes in the number of days of rainfall are in line with the changes in PR_W1 and PR_W2 which further affirms the observed declining water yields from the catchment area.

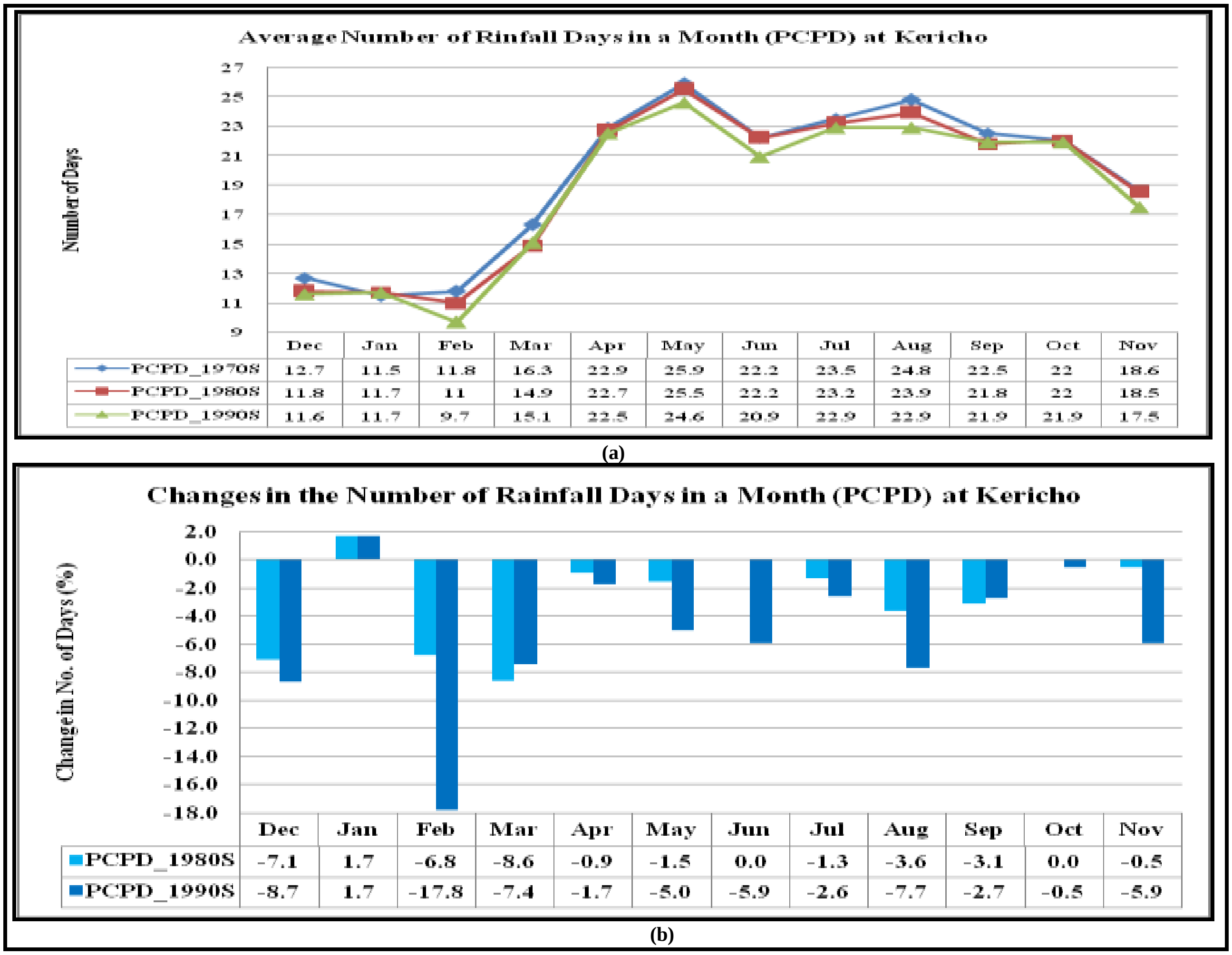

(a)

(b)

Figure 4.7: Observed (a) average number of days of rainfall in a month (PCPD) and (b) corresponding changes from the baseline at Kericho Met. Station

4.3.2.4 Annual Rainfall Trends

Figure 4.8 shows the annual rainfall time series and trends for Keresoi and Kericho stations. A decreasing trend in annual rainfall was noted at Keresoi while Kericho indicated an increasing trend. Trends of annual rainfall at Keresoi and Kericho were tested for significance against the hypothesis that they are not significantly different from zero (H_o: $b_1 = 0$) using the students t-statistic at $\alpha = 0.05$ level of significance. The computed t-statistic (t_{cal}) was compared to the tabulated critical values ($t_{\alpha=0.05}$) and the annual rainfall trends were found to be significant (Table 46). The null hypothesis was therefore rejected and it was concluded that the annual rainfall trends are significantly different from zero. The annual rainfall trends show that there is a progressive change in annual rainfall in this area which is likely to impact on water yields from the catchment area.

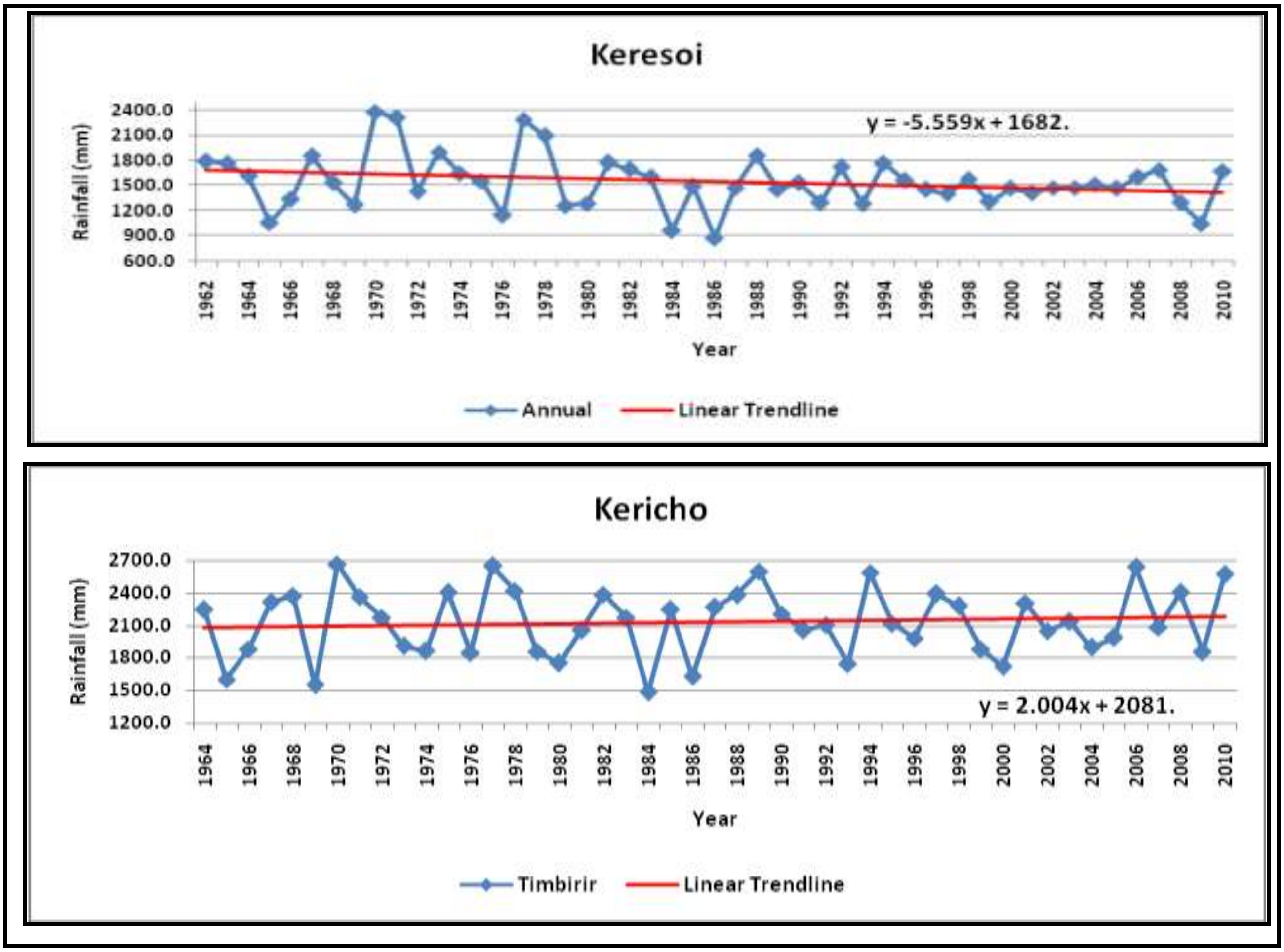

Figure 4.8: Time series of observed total annual rainfall at Keresoi and Kericho stations

Table 4.6: Annual rainfall trends (b), standard error [s(b)], and the computed t-statistic (t_{cal})

Station	**Trend (b)**	**Standard Error [s(b)]**	$\mathbf{t_{cal}} = \frac{b}{s(b)}$	**Remarks**
Keresoi	-5.559	0.144	-38.6	Significant trend
Kericho	2.004	0.147	13.6	Significant trend

4.3.3 Discharge

Figure 4.9 shows time series of mean seasonal discharge at Kiptiget and Sondu RGSs. Corresponding seasons at both stations follow similar patterns of high and low flows. January-February-March (JFM) flow season has the least seasonal discharge at both stations. The season is particularly important for this study since being the season with lowest mean discharge it can be used to assess water yields and availability in the catchment for planning purposes. It was noted from the figure that 1967 had the least while 1978 had the highest flows in JFM season. Between 1980 and 1986 the flows recorded at both stations were generally low compared to other periods.

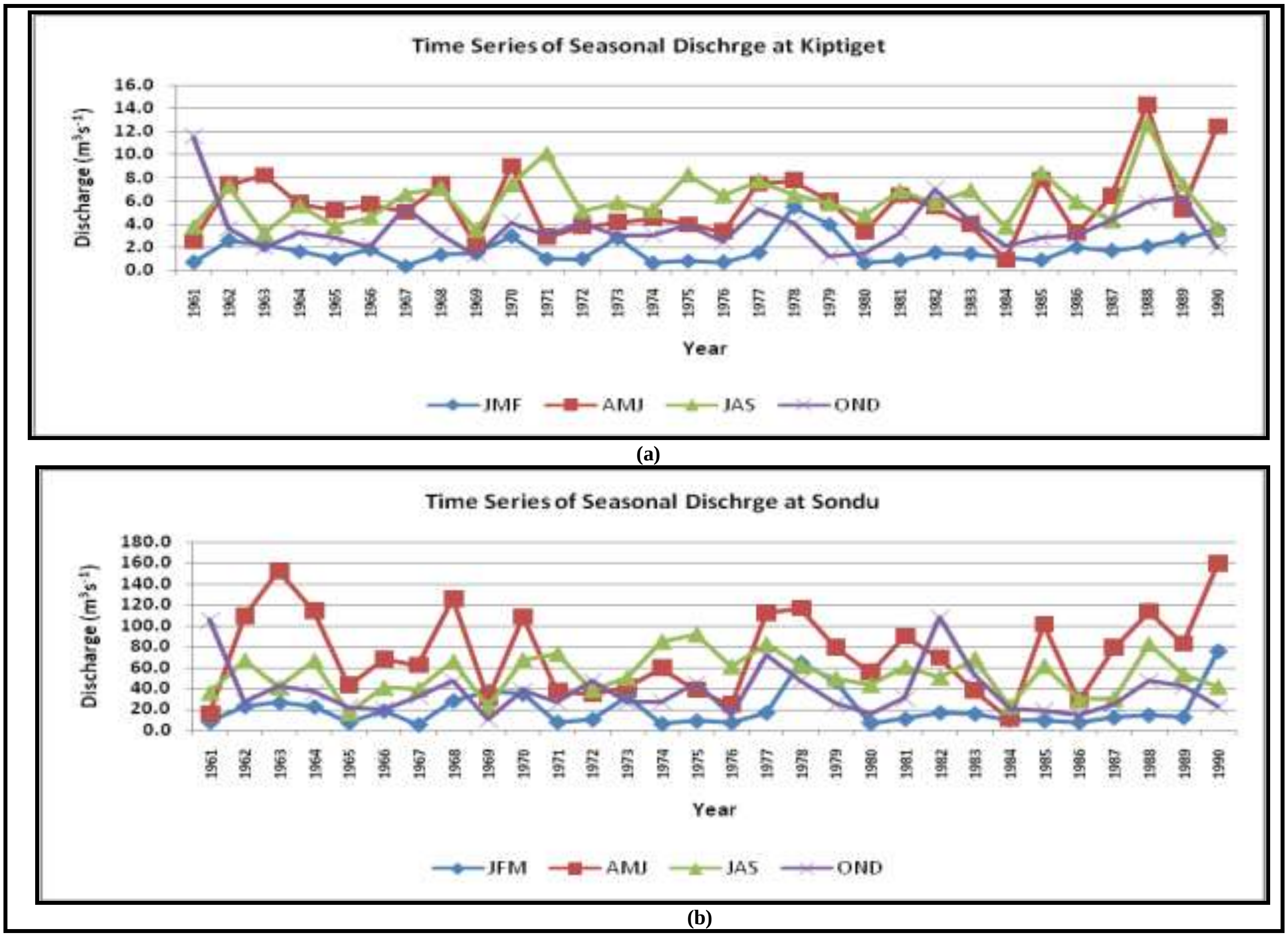

Figure 4.9: Time series of observed seasonal discharge (m^3s^{-1}) at (a) Kiptiget and (b) Sondu RGSs

Kiptiget RGS is located upstream of Sondu RGS and therefore has lower discharge values than Sondu. The upstream area drained at Kiptiget is about 189 km^2 which is about 5% of the total Sondu catchment area while the upstream area drained at Sondu is about 3287 km^2 which is about 94% of the total catchment area. Sondu is therefore an important RGS for this study since the seasonal hydrograph represents the hydrological response of almost the entire catchment area. However Kiptiget occupies a more central part of this study since most of the upstream area drained at the station comprises the South West Mau Forest, the largest of the 22 blocks that make up the Mau forest complex. The station was therefore found to be the best placed for assessing the impacts of deforestation changes on water yields

Figure 4.10 shows a time series of observed normalised annual discharge anomalies at Kiptiget and Sondu stations. From the figure, it was observed that Sondu station recorded more discharge extremes than Kiptiget between 1961 and 1987. This could be attributed to the fact that the catchment area drained at Kiptiget RGS is much less and hence more homogeneous in terms of hydrologic responses compared to area drained at Sondu RGS. The highest recorded annual discharge value at Sondu was in 1978 followed by 1977 while the lowest recorded values in the same station were in 1984 followed by 1986. At Kiptiget, the highest recorded values were in 1970 followed by 1985 while the lowest values were recorded in 1984 followed by 1969. From the available rainfall records, the low annual discharge years correspond to dry years while the high annual discharge years correspond to wet years (Figure 4.8). From the rainfall analysis, 1984 was the driest year in the basin for the last 50 years and hence reduced water yields into the streams and rivers.

Figure 4.10 shows a generally decreasing trend in annual average discharge values between 1961 and 1987. The decreasing trends are in line with the observed annual rainfall trends in the area. Trends of annual mean discharge were tested for significance at $\alpha = 0.1$ level against the null hypothesis that they were not significantly different from zero (H_o: $b_1 = 0$). The computed t-statistic (t_{cal}) was greater than the tabulated critical value ($t_{\frac{\alpha}{2}} = 1.708$) at Sondu but less at Kiptiget (Table 4.7). Hence based on the available data, it was concluded that the decreasing trend at Sondu was significant while that at Kiptiget was not.

From the analysis of discharge data at Sondu and Kiptiget RGSs, it was established that the decreasing trend in annual discharge values is an indicator that there is less surface water available with time for abstraction, and hence decreasing yields, from the Sondu catchment area. The cause of this decline could be attributed to climate change, deforestation of the upper catchment areas which mainly comprise the South West Mau forest or a combination of both.

Table 4.7: Annual discharge trends (b), their standard error [s(b)], and computed t-statistic (t_{cal}) at Kiptiget and Sondu

Station	**RGS Code**	**Trend (b)**	**Standard Error [s(b)]**	$\mathbf{t_{cal}} = \frac{b}{s(b)}$	**Remarks**
Kiptiget	1JA02	-0.019	0.196	0.097	no significant trend
Sondu	1JG01	-0.368	0.196	1.876	significant trend

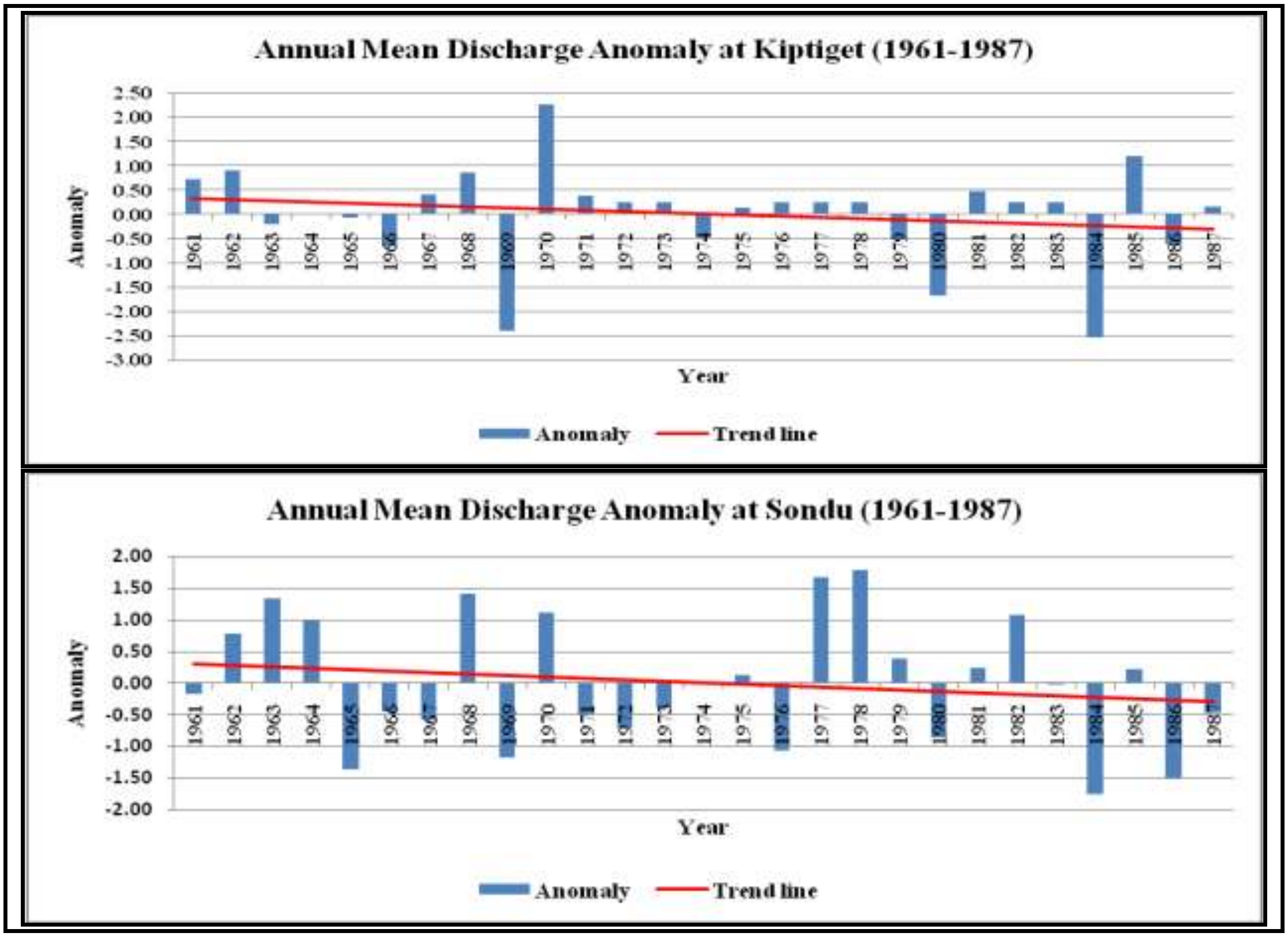

Figure 4.10: Time series of normalised annual mean discharge anomalies at Kiptiget and Sondu RGSs

4.4 Trends of Land Use/Land Cover

The landuse/landcover (LULC) changes over the Sondu catchment area in the last four decades are analyzed and discussed in this section at three levels: catchment, forest, and sub-basin levels.

4.4.1 Sondu Catchment Area

Figure 4.11 presents the land cover scenario maps over the Sondu catchment area created from the classified satellite images of the area of study for the years 1973, 1986, 2000, and 2010 and defined as LU73, LU86, LU00, and LU10 respectively, for the purpose of this study. The figure shows that the basin has four main land cover types that include agriculture, closed forest, open forest, and rainfed shrub crop (tea). In all the four land cover types, land under agriculture occupies the largest area, over 60% of the total catchment area while the land area under forest started off at about 27% in 1973 but reduced to about 21% in 2010 (Table 4.8).

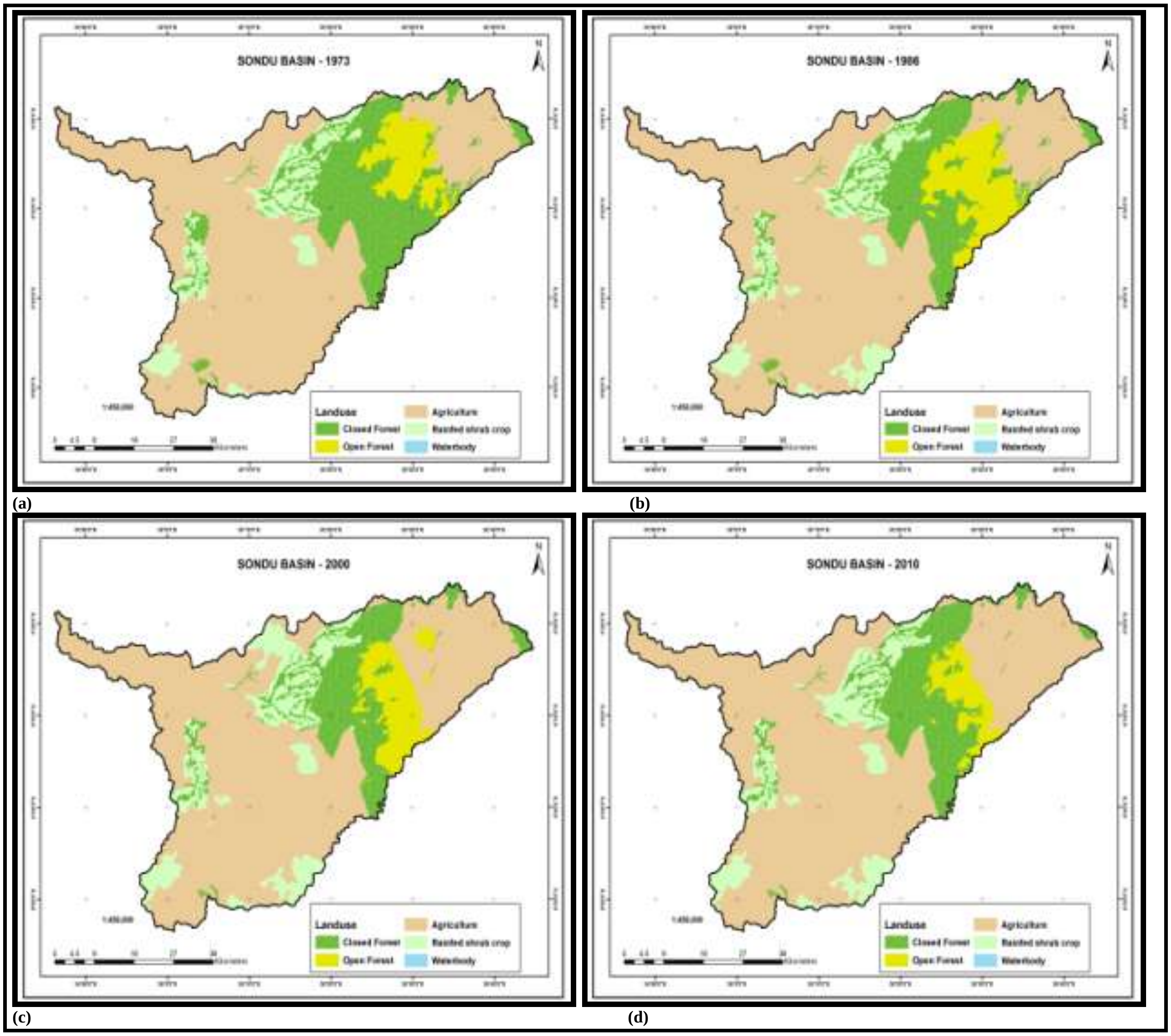

Figure 4.11: LULC maps of Sondu basin derived from Satellite images for (a) 1973, (b) 1986, (c) 2000, and (d) 2010

Table 4.8 shows the evolution of LULC over the Sondu basin between 1973 and 2010. From the table, the area under combined forest cover decreased from about 27% in 1973 to about 21% in 2010 while the land area under combined agriculture increased from about 73% to about 79% in the same period. Since part of the main objective of this study was to assess the impacts of deforestation on the water yields from the MFC, South West Mau forest block, which traverses the upper parts of the Sondu catchment area and the largest of all the MFC blocks, was chosen as the focus of the study.

Table 4.8: Evolution of land cover over Sondu basin from 1973 to 2010

LULC	LU1973 (%)	LU1986 (%)	LU2000 (%)	LU2010 (%)
Closed Forest (FRSE)	20.91	17.17	14.79	16.34
Open Forest (FRSD)	6.34	9.18	7.04	4.46
Agriculture (AGRR)	64.42	63.30	66.00	68.06
Rainfed Shrub Crop (AGRC)	8.33	10.34	12.17	11.13

4.4.2 South West Mau Forest

The main LULC types within the South West Mau (SWM) forest reserve include closed forest (FRSE), open forest (FRSD), rainfed herbaceous crop (AGRR), and rainfed shrub crop (AGRC) (Figure 4.12). Table 4.9 shows the areal distribution of the different types of vegetation found within the SWM forest and the corresponding percentage changes, based on the 1973 status, between 1973 and 2010. Positive values of percentage changes indicate growth while negative changes indicate decline in the areal coverage of the respective vegetation types relative to the baseline status as shown in columns 4, 6, 8, and 10 of Table 4.9. Figure 4.12a and column 2 of Table 4.9 show the status of the different types of vegetation cover within the forest reserve as of 1973 when the first satellite image of the area was available. This status was treated as the baseline against which changes in forest coverage with time were evaluated.

The predominant vegetation cover in the forest reserve as of 1973 was closed forest which covered about 55000 ha out of a total of 84000 ha of the forest reserve. This represents about 65% of the total area of the forest reserve. The other important vegetation covers in the forest reserve as of 1973 included rainfed herbaceous crop and the open forest type which occupied about 13000 ha and 10000 ha of the total area of the forest reserve respectively (Table 4.9 column 2). The others were regenerating forest and plantation forest which occupied about 4000 ha and 1000 ha of the total area respectively.

Between 1973 and 1986, there were tremendous changes in the extent of the area of the forest reserve covered by each type of vegetation (Figure 4.12b and Table 4.9 column 3). By 1986 closed forest cover had reduced from about 55000 ha in 1973 to about 37900 ha. About 17000 ha (20%) of the natural forest cover had been cleared. The redistribution of the other vegetation types within the forest reserve was as shown in Figure 4.12b and Table 4.9 column 3. The open forest type increased from about 10300 ha in 1973 to about 37800 ha in 1986. This tremendous growth of about 27500 ha was accounted for mainly by the decrease in the natural forest cover (17000 ha) and in rainfed herbaceous crop (11900 ha).

By 1986 closed forest type occupied about 45% of the total forest cover compared to 65% in 1973 while the open forest type occupied about 44% compared to 12% in 1973. The percentage changes in areal coverage of the other vegetation types are as shown in Table 4.9 column 4. These changes indicate evidence of deforestation as a result of logging or charcoal burning since the acreage occupied by the crops reduced while that occupied by open and regenerating forests increased during this period. Indeed the area covered by closed forest type reduced by about 31% of the total while that of open forest overwhelmingly increased by 260% (Table 4.9 column 4).

Table 4.9: Evolution of land cover within the South West Mau forest reserve between 1973 and 2010 relative to 1973

	1973	**1986**		**1995**		**2000**		**2010**	
	2	**3**	**4**	**5**	**6**	**7**	**8**	**9**	**10**
LULC	**Ha**	**Ha**	**% Change**	**Ha**	**% Change**	**Ha**	**% Change**	**Ha**	**% Change**
Closed Forest	55,060	37,912	-31.1	38,299	-30.4	22,477	-59.2	32,304	-41.3
Open forest	10,287	37,012	+260	36,344	+253.3	15,468	+50.4	16,278	+58.2
Plantation forest	1,324	1,324	0.0	1,324	0.0	1,324	0.0	214	-83.8
Rain-fed herbaceous	13,597	1,695	-87.5	1,566	-88.5	29,233	+115.0	27,432	+101.7
Rain-fed shrub crop	52	226	+334.6	242	+365.4	5,078	+9665	6496	+12392
Regenerating forest	3,679	6,179	+68.0	6,224	+69.2	10,418	+183.2	2,275	-38.2
Grand Total	**83,999**	**83,999**		**83,999**		**83,999**		**83,999**	

Between 1986 and 1995 there was not much change in the areal coverage of the different vegetation types from the 1986 status (Table 4.9 column 5). There was a minor increase in the area covered by the closed forest vegetation that corresponded to a slight decrease in the open forest.

By 1995 the closed forest type covered about 38300 ha which was slightly over 1% growth compared to the 1986 status. The open forest type occupied about 36300 ha which was about 2% decline compared to the 1986 status. Rainfed shrub crop, which is mainly tea occupying part of the original closed forest vegetation, grew by about 7% while rainfed herbaceous crop, which is mainly maize declined by about 8% respectively as of the 1986 areal coverage statistics. Percentage changes of areal coverage of the different vegetation types are as shown in Table 4.9 column 6.

Between 1995 and 2000 there was tremendous reduction in closed forest vegetation cover which by then occupied only about 22500 ha compared to 55000 ha in 1973 (Figure 4.12c and Table 4.9 column 7). This was about 27% of forest coverage compared to the 65% coverage in 1973 and represented the worst case of the natural forest cover ever witnessed in this forest reserve since 1973 (Table 4.9 column 7). The open forest coverage had also declined significantly and was replaced with the cultivation of rainfed herbaceous crop. The open forest occupied about 15500 ha by 2000 compared to 36300 ha in 1995. This was a decline of over 57% in only eight years. The decline in the open forest coverage was matched by a significant increase in the coverage of maize crop on the upper sides of the forest (Figure 4.12c) which by 2000 occupied about 29200 ha compared to 1600 ha in 1995. This was an overwhelming increase of over 1760%. Percentage changes in the coverage of different vegetation types by 2000 relative to the baseline are shown in Table 4.9 column 8.

Between 2000 and 2010 there was tremendous improvement in the area covered by closed forest vegetation which by 2010 had recovered to just about the 1986 level (Figure 4.12d and Table 4.9 column 9). The closed forest areal coverage had grown from about 22500 ha in 2000 to about 32300 ha with a corresponding change in the regenerating forest type which declined from about 10400 ha to 2300 Ha in the same period (Figure 4.12d and Table 4.9 column 9). This was a growth of over 43% in the natural forest cover in less than ten years. This impressive growth in the natural forest cover could be attributed to the government efforts towards conservation of the original forest coverage in the Mau forest complex. Changes in the other types of vegetation by 2010 relative to the baseline are shown in Table 4.9 column 10).

Figure 4.13 shows a summary of the three dominant vegetation cover types: closed forest (FRSE), open forest (FRSD), and rainfed agriculture (AGRR). The figure shows that the most dominant vegetation cover within the SWM forest reserve as of 1973 was the closed forest type with a coverage of over 65%. The decline in the area covered by the closed forest vegetation type between 1973 and 1986 is matched by the increase in the open forest vegetation type.

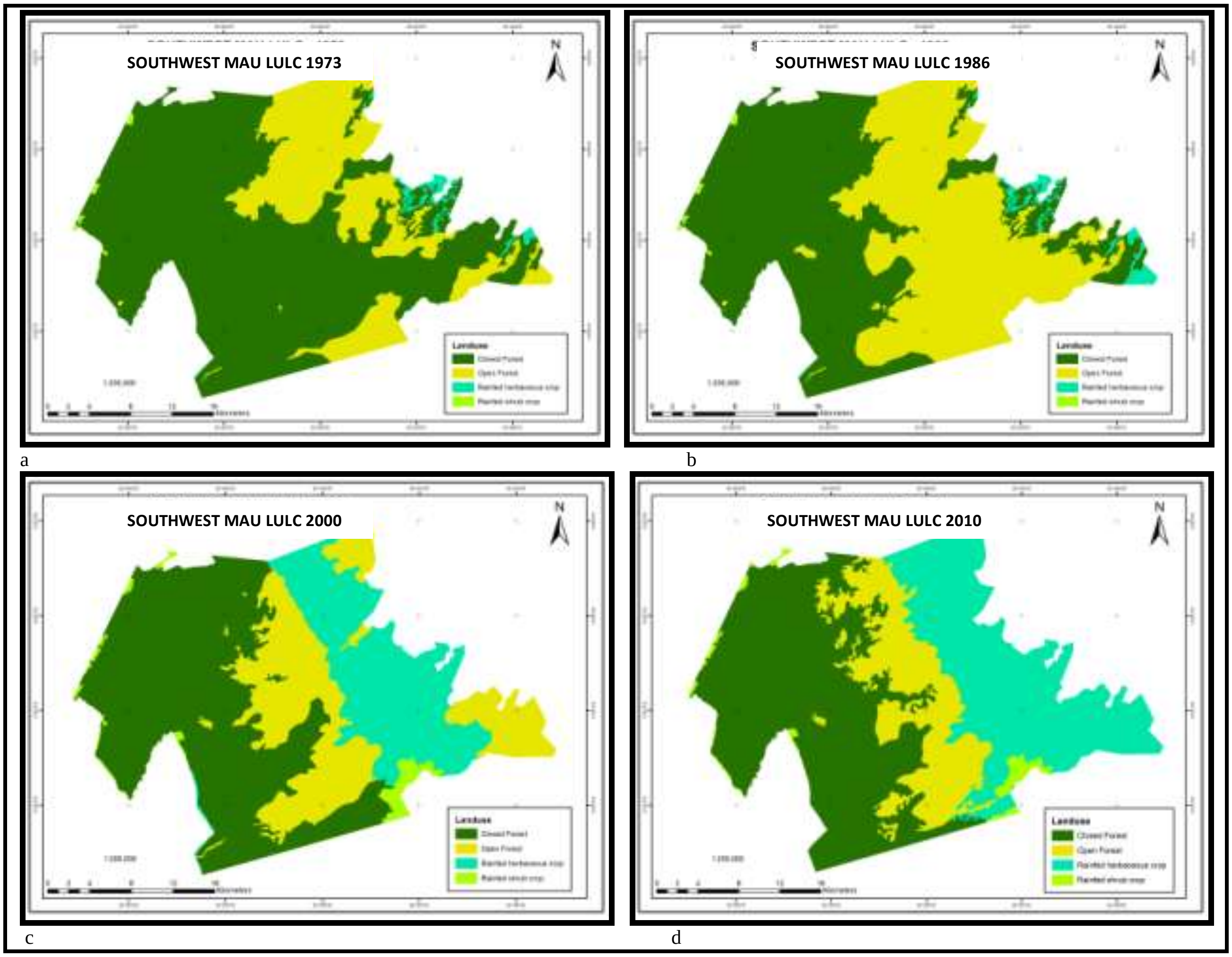

Figure 4.12: LULC *maps of South West Mau forest derived from Satellite images*

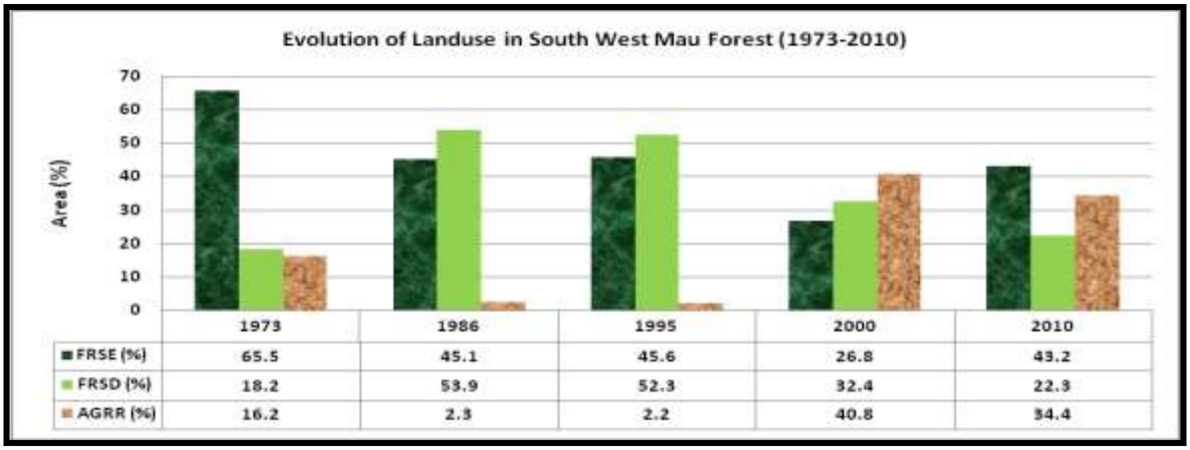

Figure 4.13: Evolution of percentage areal coverage by dominant land covers in south West Mau forest between 1973 and 2010

Between 1995 and 2000 closed and open forests declined to 26% and 32% respectively representing the worst forest coverage in the entire reserve for the last four decades. The decline in the area covered by both closed and open forest types in this period was matched by a tremendous growth in land area under agriculture whose coverage rose from a meagre 2% coverage in 1995 to over 40% in 2000 and only declined slightly by 2010 to settle at 34%. This is evidence of deforestation where previously forested land was replaced by cultivated land.

4.4.3 Kiptiget Sub-Basin

Figure 4.14 shows the evolution of the two dominant land cover classes namely the combined forest cover (Forest) and rainfed agriculture (AGRR) over Kiptiget sub-basin which was selected as the focus of this study. The sub-basin is in the heart of SWM forest reserve and is traversed by Kiptiget River which is gauged at the outlet of the sub-basin.

Between 1973 and 2010, there was a decreasing trend in the land area under forest cover while there was an increasing trend in the land area under rainfed agriculture. The land area under forest cover progressively decreased at a rate of 8% per decade from about 84% in 1973 to about 62% in 2010 while that under rainfed agriculture increased at a rate of 8% from about 16% in 1973 to about 38% in 2010 as shown by the slopes of trend lines (Figure 4.14).

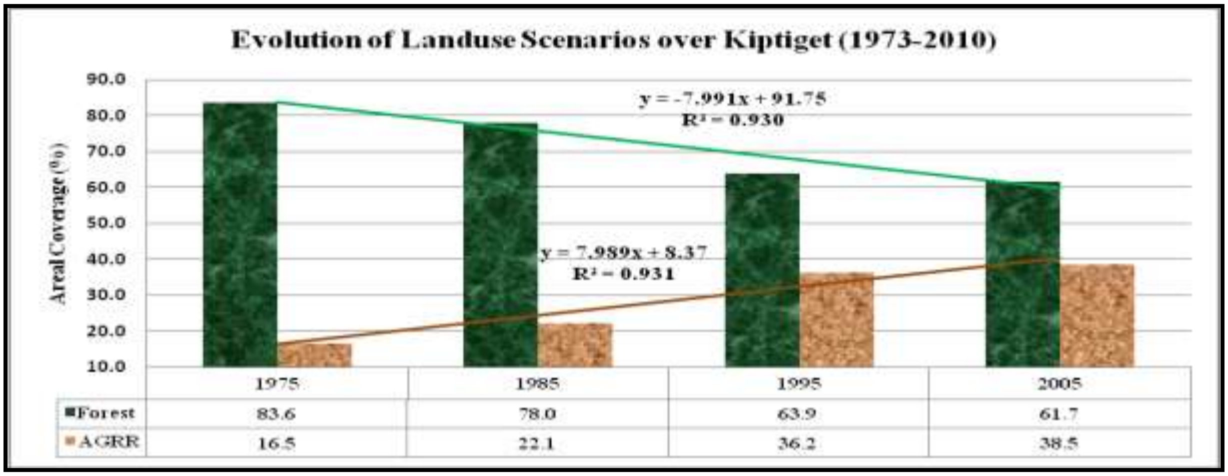

Figure 4.14: Evolution of percentage areal coverage of forest and rainfed agriculture (AGRR) over Kiptiget sub-basin

When tested for significance at $\alpha = 0.05$ level of significance using the student's t-test, the slopes were found to be significant. The computed t-statistics values, t_{cal} = 13.841 and t_{cal} = 13.838 for forest and rainfed agriculture respectively were found to be less than the tabulated value (t_{cal}=

2.920). Over 93% of the variability in LULC change over this sub-basin can be explained by the independent variable (time). Hence if no interventions are made, deforestation of this sub-basin and that of the Mau forest complex in general will continue. This may have negative effects on the hydrology of the catchment properties of the sub-basin.

The analysis of changes in the different types of vegetation cover found within the Sondu catchment area has established that there is evidence of deforestation in this watershed as demonstrated by the decline in the natural forest cover and the growth in the agricultural land cover at the three levels considered: catchment level (Table 4.8), forest level (Figure 4.13), and sub-basin level (Figure 4.14).

These changes in LULC have an influence on the hydrology and therefore the water yields into the streams and rivers of the basin. The general decrease in the area covered by the natural forest and the corresponding general increase in the cultivated area has influenced the hydrology negatively as shown by the decreasing trends in stream flows within this period (Figure 4.10).

The decreasing trend in the amount of water in rivers and streams in the watershed could be attributed to the changes in LULC where natural forest coverage has been on the decline. This has influenced infiltration and therefore recharge of soil and groundwater in the basin resulting in reductions in discharge during dry spells. Unless the trends are reversed, projections indicate that by 2030 the land area under forest cover will decrease by up to about 40% while that under cultivation and other uses will increase by up to about 60% of the 1973 coverage. This will further worsen the water yields from the catchment and there is therefore need for the concerned authorities to make every effort to ensure that the trends are reversed.

4.5 Climate Simulations

The results obtained from PRECIS Regional Climate Model simulations are presented and discussed in this section. The model results are divided into two main parts; baseline and projected climates. The key climate elements discussed are rainfall, maximum and minimum temperatures.

4.5.1 Baseline Climate

In this section, calibration and validation of the model-simulated results using observed data from the area of study are presented. Comparison of simulated and observed climatology of total monthly rainfall, mean monthly maximum and minimum temperatures averaged over the period 1961–1990 are presented in both graphical and tabular formats.

4.5.1.1 Calibration and Validation of Model-Simulated Outputs

Using model-simulated and the corresponding observed data at Kericho, Keresoi, and Sotik stations, calibration parameters (Table 4.10) obtained through regression analysis were used to calibrate PRECIS model-simulated outputs. The table shows the regression constants (a_{RF}), (a_{TMX}), and (a_{TMN}); Regression slopes (b_{RF}), (b_{TMX}), and (b_{TMN}) for rainfall, maximum and minimum temperatures, respectively; coefficients of determination (R^2), and correlation coefficients between observed and simulated values (r_{os}), for rainfall (RF), maximum temperature (TMX), and minimum temperature (TMN) respectively.

Table 4.10: Regression parameters for rainfall and temperature used to calibrate PRECIS model outputs

Station	Rainfall (RF)				Maximum Temperature (TMX)				Minimum Temperature (TMN)			
	a_{RF}	b_{RF}	R^2	r_{os}	a_{TMX}	b_{TMX}	R^2	r_{os}	a_{TMN}	b_{TMN}	R^2	r_{os}
Kericho	45.5	1.03	0.86	0.93	14.3	0.325	0.91	0.96	3.6	0.485	0.82	0.91
Keresoi	15.5	0.495	0.81	0.90	14.3	0.459	0.82	0.90	4.8	0.534	0.95	0.98
Sotik	45.5	0.368	0.56	0.75	17.7	0.330	0.85	0.92	6.8	0.408	0.77	0.88

Correlation coefficients between observed and simulated rainfall, maximum and minimum temperatures which range between 0.75 and 0.98 were tested for significance using student t-statistic at $\alpha = 0.05$ level of significance. In all the cases the computed t-statistic was found to be greater than the tabulated critical value ($t_{\alpha=0.05} = 1.812$). Hence it was established that the correlation between the observed and model-simulated rainfall and temperature were significant.

4.5.1.2 Temperature

Figure 4.15 shows a comparison of estimated mean monthly maximum temperature (Tmax_Sim) obtained from the model simulations using the slope (b_{TMX}) and constant (a_{TMX}) given in Table 4.10 with corresponding observed values (Tmax_Obs) during calibration (1983-1987) and validation (1988-1990) periods at Kericho Met Station.

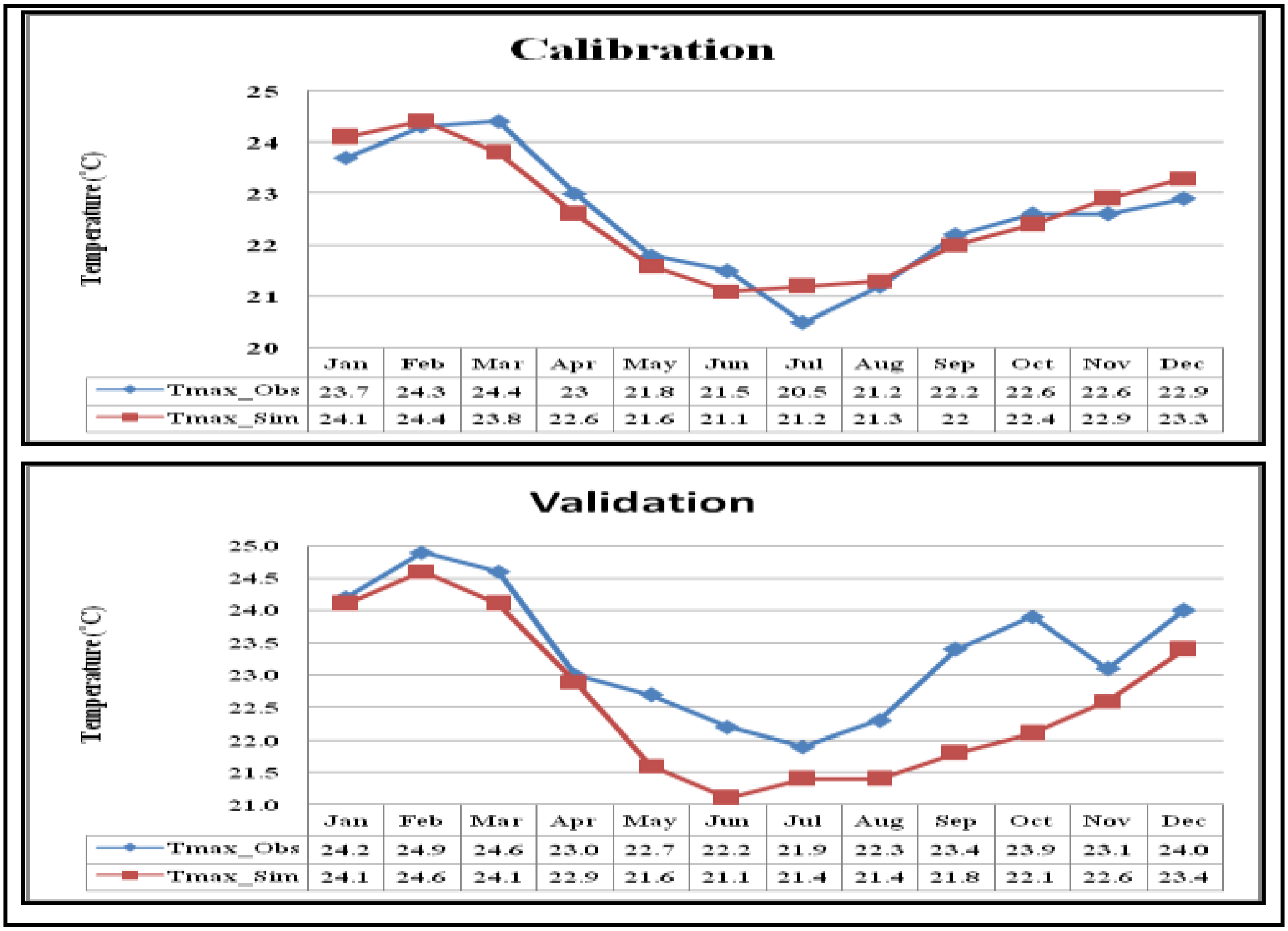

Calibration

	Jan	Feb	Mar	Apr	May	Jun	Jul	Aug	Sep	Oct	Nov	Dec
Tmax_Obs	23.7	24.3	24.4	23	21.8	21.5	20.5	21.2	22.2	22.6	22.6	22.9
Tmax_Sim	24.1	24.4	23.8	22.6	21.6	21.1	21.2	21.3	22	22.4	22.9	23.3

Validation

	Jan	Feb	Mar	Apr	May	Jun	Jul	Aug	Sep	Oct	Nov	Dec
Tmax_Obs	24.2	24.9	24.6	23.0	22.7	22.2	21.9	22.3	23.4	23.9	23.1	24.0
Tmax_Sim	24.1	24.6	24.1	22.9	21.6	21.1	21.4	21.4	21.8	22.1	22.6	23.4

Figure 4.15: Annual cycles of observed and model-simulated mean monthly maximum temperature (Tmax) during calibration and validation at Kericho Met. Station

On a month-by-month scale, the deviation between observed and model-simulated maximum temperature ranges between -0.6°C and 0.6°C and between 0.0°C and 1.8°C during calibration and validation periods respectively. On average, the model underestimates maximum temperatures by about 0.8°C. However, the model captures the seasonal patterns of maximum temperature in the region quite well with the model-estimated high and low temperatures matching the observed high and low temperatures.

The model-simulated (Tmax_Sim) and observed (Tmax_Obs) mean monthly maximum temperatures were found to be significantly correlated at $\alpha = 0.05$ level of significance with coefficients of correlation of $r = 0.952$ and $r = 0.890$ during calibration and validation periods respectively. The percentage variability in the estimated mean monthly maximum temperature that can be explained by the corresponding observed values were 91% and 79% during calibration and validation periods respectively (Figure 4.16). This means that the model was able to simulate the catchment's maximum temperature climatology. Therefore, by carefully calibrating the model outputs, it is possible to use the model to project future maximum temperature climatology in the area.

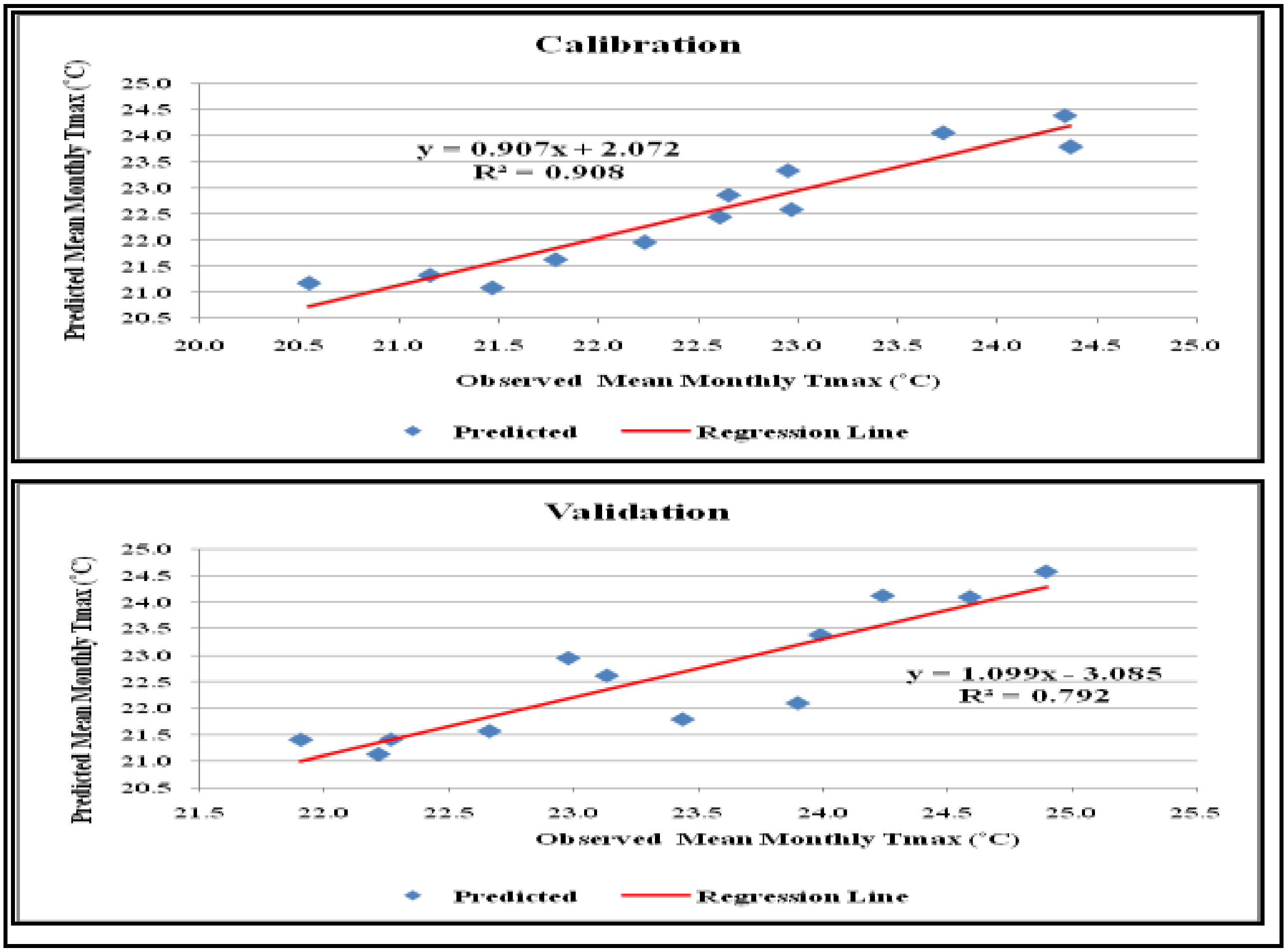

Figure 4.16: Regression of mean monthly model-simulated on corresponding observed maximum air temperature (Tmax) during calibration and validation at Kericho Met. Station

Observed (Tmin_Obs) and model-estimated (Tmin_Sim) mean monthly minimum temperatures are presented in Figure 4.17. The figure shows a comparison of estimated mean monthly minimum temperature obtained from the model simulations using the slope (b_{TMN}) and constant (a_{TMN}) given in Table 4.10 with corresponding observed values during calibration and validation periods at Kericho Met Station. From these results, it was observed that on a month-by-month scale, the deviation between observed and model-estimated minimum temperature ranges between -0.2°C and 0.3°C and between 0.2°C and 0.9°C during calibration and validation periods respectively. On average, the model underestimates minimum temperatures by about 0.6°C.

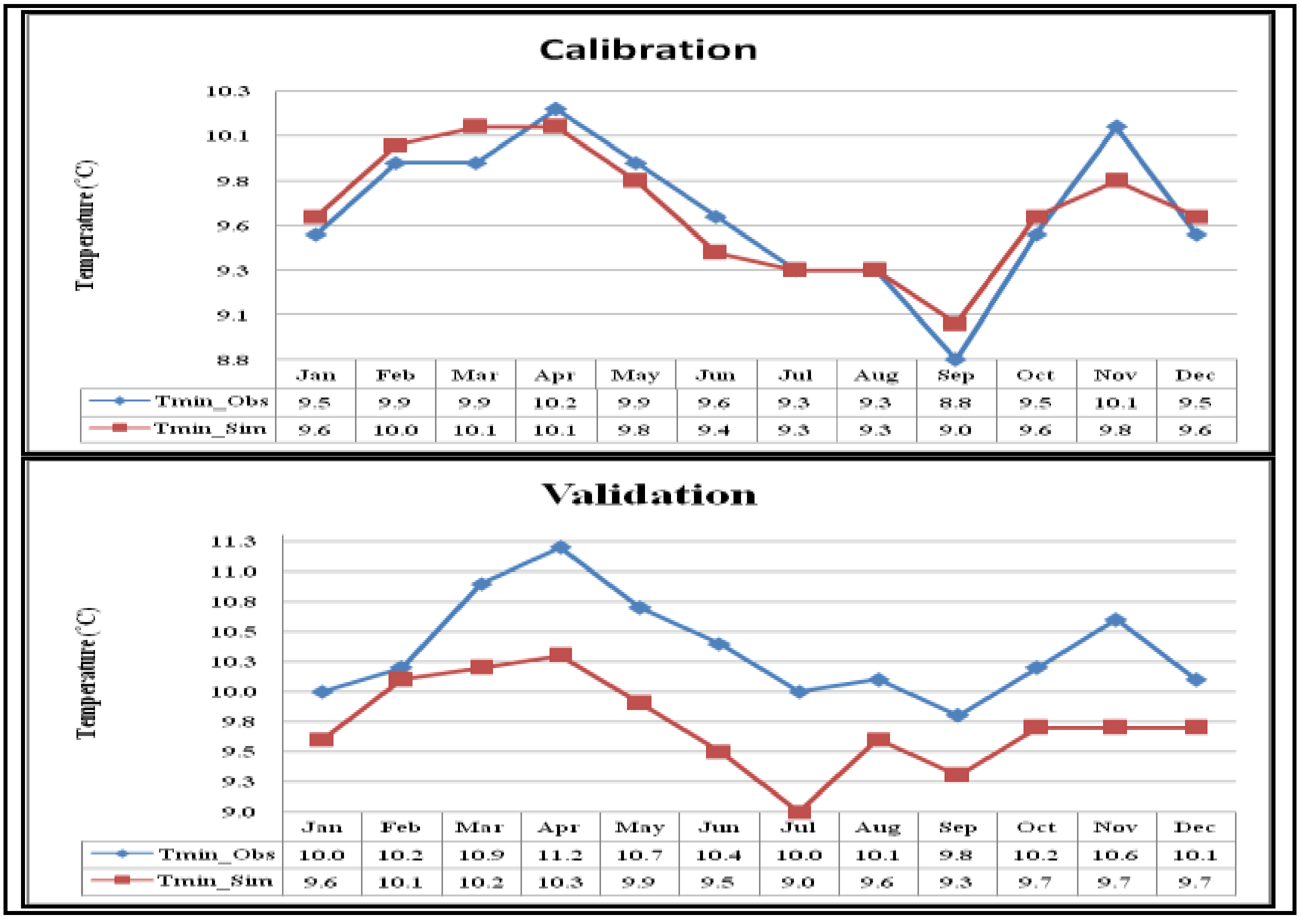

Figure 4.17: Annual cycles of observed and model-simulated mean monthly minimum temperature (Tmin) during calibration and validation at Kericho Met. Station

Estimated and observed mean monthly minimum temperatures were found to be significantly correlated at $\alpha = 0.05$ level of significance with coefficients of correlation of $r = 0.906$ and $r = 0.817$ during calibration and validation periods respectively. The percentage variability in the estimated mean monthly minimum temperature that can be explained by the corresponding observed values were 82% and 67% during calibration and validation periods respectively (Figure

4.18). The model could therefore be used to project future minimum temperature patterns in the catchment area subject to calibration of the model-simulated values.

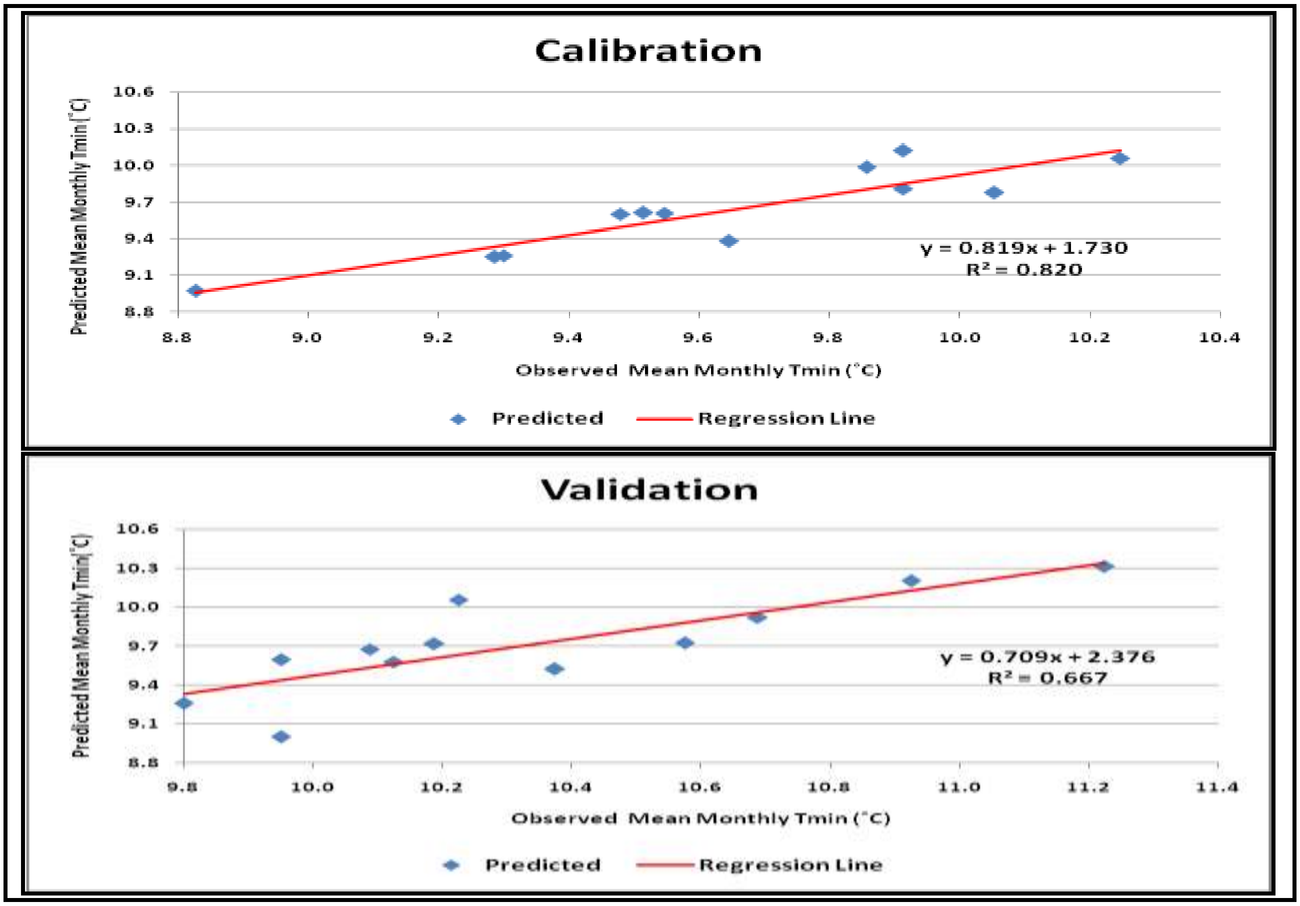

Figure 4.18: Regression of mean monthly model-simulated on corresponding observed minimum air temperature (°C) during calibration and validation at Kericho Met. Station

4.5.1.3 Rainfall

Figure 4.19 shows a comparison of estimated mean monthly rainfall obtained from model simulations using the slope (b_{RF}) and constant (a_{RF}) given in Table 4.10 with corresponding observed values during calibration and validation periods at Kericho Met Station. The observed rainfall peaks in May, August, and November are fairly well replicated by the model in both calibration and validation periods. The model results are consistent with observed values. However, the model was found to overestimate monthly rainfall between the months of June and December in both calibration and validation.

Figure 4.20 presents the regression of model-estimated on corresponding observed mean monthly rainfall in both calibration and validation periods. Estimated and observed mean monthly rainfall was found to be significantly correlated at $\alpha = 0.05$ level of significance with coefficients of correlation of $r = 0.926$ and $r = 0.846$ during calibration and validation periods respectively. The percentage variability in the model-estimated mean monthly rainfall that could be explained by the corresponding observed rainfall was 86% and 72% during both calibration and validation periods respectively. It was therefore concluded that the model could be used to project monthly rainfall climatology of the basin subject to calibration of the model-simulated outputs using observed values.

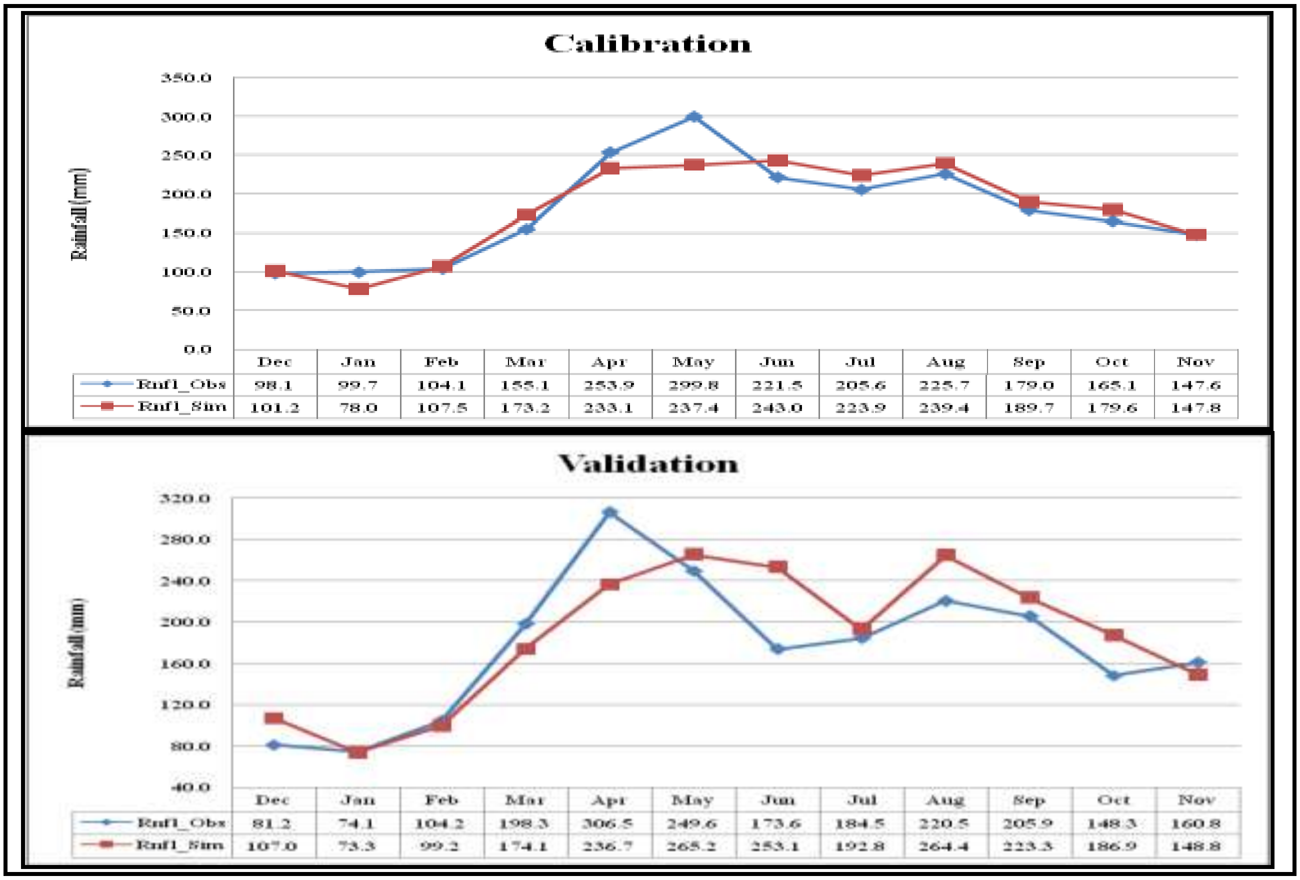

Figure 4.19: Annual cycles of observed and model-simulated mean monthly rainfall (mm) during calibration and validation at Kericho Met. Station

Table 4.11 presents a comparison of observed and model-estimated mean monthly rainfall and the model performance as a percentage difference between model-simulated and corresponding observed rainfall in the calibration and validation periods. Positive values in the model performance columns indicate under estimation while negative values indicate over estimation of monthly rainfall.

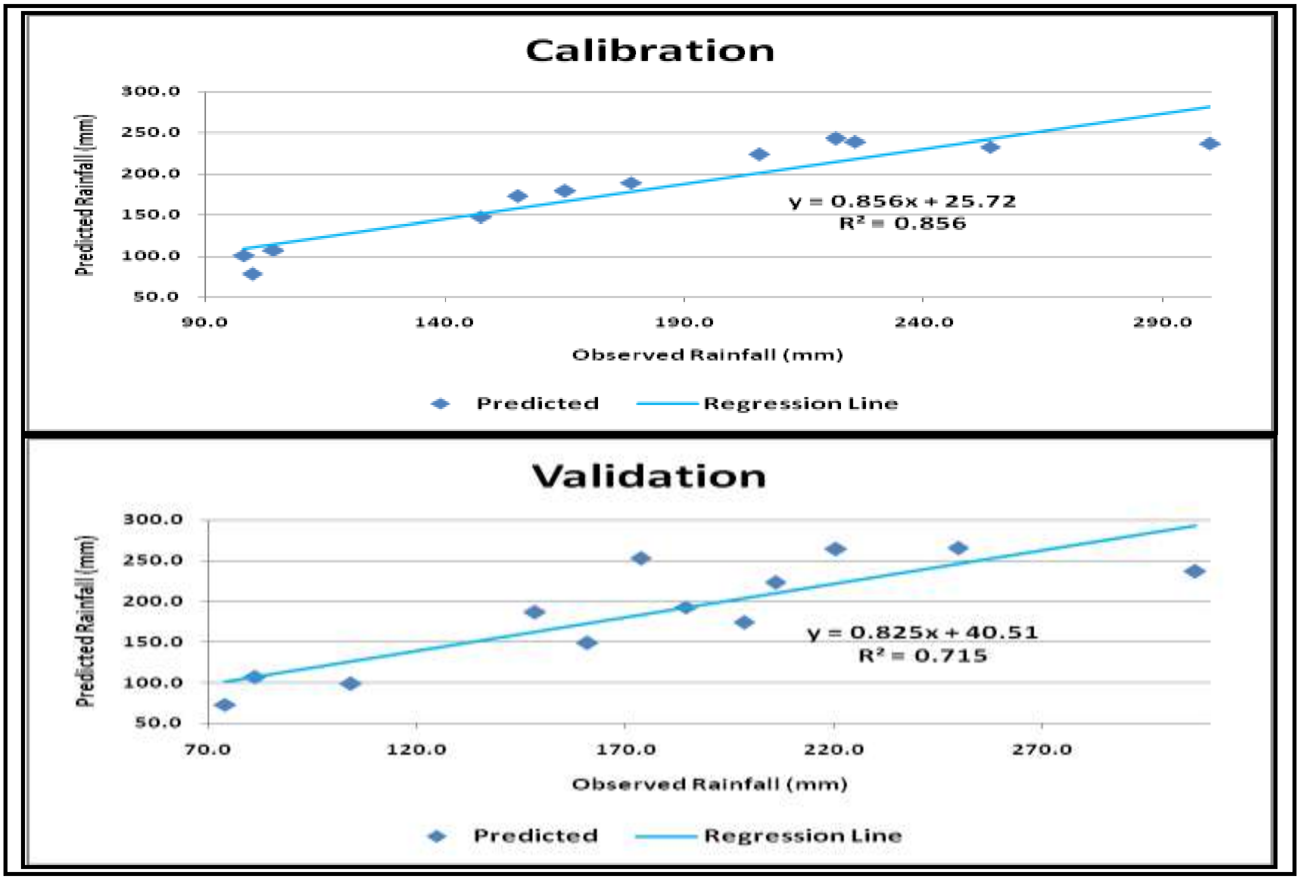

Figure 4.20: Regression of mean monthly model-simulated on corresponding observed rainfall (mm) during calibration and validation at Kericho Met. Station

On a month-by-month scale, the percentage deviation between observed and model-estimated rainfall ranges between -11% and 22% and between -45% and 23% during calibration and validation periods respectively. On a season-by-season scale the model underestimates DJF and MAM rainfall by about 5% and 6% respectively and overestimates JJA and SON rainfall by about 8% and 5% respectively. On average, the model overestimates mean annual rainfall by about 0.6% and 7.9% during calibration and validation periods respectively. Performance of PRECIS model on the Sondu basin is therefore quite reasonable on the seasonal and annual scales since the less than 10% average deviation is small enough to be considered acceptable.

From the calibration and validation results of the PRECIS model outputs using observed values, it was established that the model captures the baseline climate of the area of study quite well as shown by the regression statistics (Table 4.10) and the model performance statistics in both calibration and validation periods (Table 4.10). Hence subject to calibration of the model outputs using observed values, the model was found suitable for simulating the climate of this part of Kenya.

Table 4.11: Predicted and observed mean monthly rainfall and model performance in calibration and validation periods

Month	Calibration Period (1983-1987)			Validation Period (1988-1990)		
	Observed (mm)	**Predicted (mm)**	**Model Performance (%)**	**Observed (mm)**	**Predicted (mm)**	**Model Performance (%)**
Jan	99.7	78.0	21.7	74.1	73.3	1.1
Feb	104.1	107.5	-3.3	104.2	99.2	4.8
Mar	155.1	173.2	-11.7	198.3	174.1	12.2
Apr	253.9	233.1	8.2	306.5	236.7	22.8
May	299.8	237.4	20.8	249.6	265.2	-6.2
Jun	221.5	243.0	-9.7	173.6	253.1	-45.8
Jul	205.6	223.9	-8.9	184.5	192.8	-4.5
Aug	225.7	239.4	-6.0	220.5	264.4	-19.9
Sep	179.0	189.7	-5.9	205.9	223.3	-8.5
Oct	165.1	179.6	-8.8	148.3	186.9	-26.0
Nov	147.6	147.8	-0.2	160.8	148.8	7.4
Dec	98.1	101.2	-3.1	81.2	107.0	-31.7

4.5.2 Projected Climates of 2010s and 2030s

In this section, model-simulated projections of rainfall, maximum, and minimum temperature climatology under SRES A2 scenario for the periods 2001-2030 and 2021-2050, centred in the 2010s and 2030s decades respectively, are presented together with the corresponding changes from the baseline climatology. The model results are presented and discussed in the next sub-sections.

4.5.2.1 Projected Temperature in 2010s and 2030s

Figure 4.21 shows a time series anomalies of observed (1964-2010) and projected (2011-2050) annual average land-surface air temperature anomalies relative to the 1961-1990 average over the Sondu catchment area. It is evident from the figure that between 1961 and mid 1980s, most of the temperatures were below the baseline normal but thereafter the values have largely been above normal and progressively continue to rise with 2011 so far recorded as the warmest year in the last 50 years in the region and the rise is expected to continue to 2050 following a polynomial trend curve of the third order.

These results are consistent with global and regional observations where anomalies are also largely above the baseline values after the mid 1980s and progressively increase with 2005 being recorded as the warmest year in the last 100 years by 2006 (IPCC, 2007). The frequency of the number of years with temperatures above that of 2005 has also increased since then with 2011 and 2012 recording the highest temperatures in the basin. Model projections show that henceforth the temperatures will largely be above the 2005 value (Figure 4.21).

An increasing rate in warming (Figure 4.22 and Table 4.12 column 3) has taken place over the Sondu catchment area which is in line with the global observations. Globally, the decades of 1990s and 2000s have been the warmest in the last 100 years with more than ten out of the twelve warmest years recorded in the last 100 years occurring within this period (IPCC, 2007). Figure 4.21 shows that 2011 was the warmest year in the Sondu basin followed by 2012 and 2005 in the last 50 years.

Figure 4.22 shows the 30-year average temperatures between 1961 and 2050 updated after every 10 years from the baseline period. The linear trend across the entire data set and has a slope of about 0.88°C per decade which was found to be significant at $\alpha = 0.05$ significance level. Over 97% of the variability in the 30-year mean annual temperature can be explained by the independent variable (time) and it was therefore concluded that climate of this area is becoming warmer with time.

However, the 30-year average values appear to be following a regular pattern where they oscillate about the trend line in a third order polynomial curve indicating accelerated warming between 1985 and 2015. In order to establish how the rate of warming was changing with time, five shorter trend lines were fitted using three data points each and the resulting slopes of the trend lines assigned to the end of the decades listed in Table 4.12 column 1.

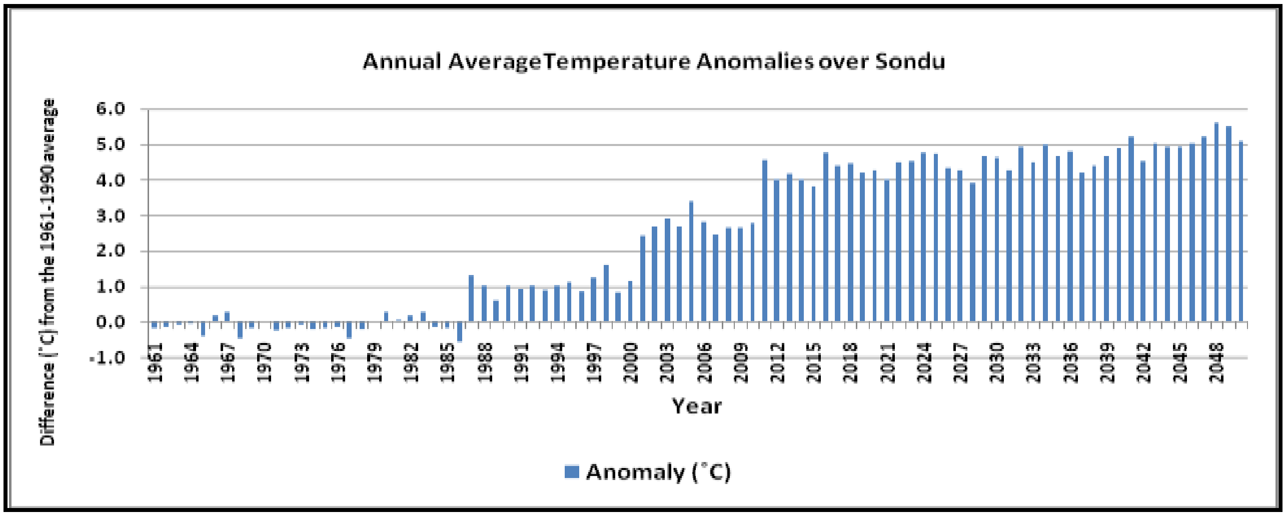

Figure 4.21: Time series of annual average land-surface air temperature anomalies (˚C) relative to the 1961-1990 baseline average over Sondu basin

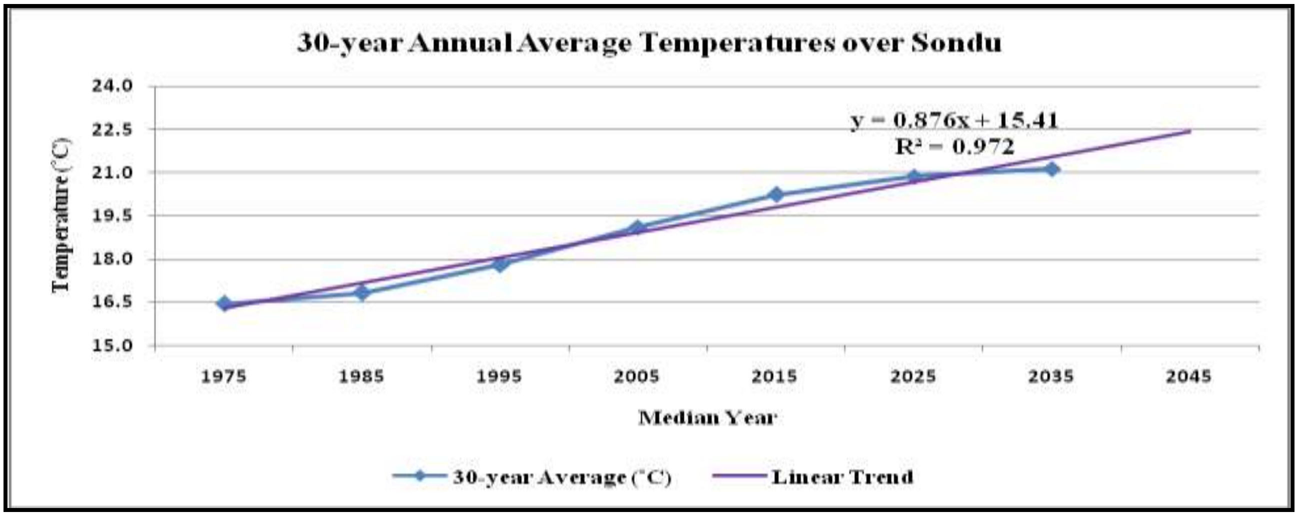

Figure 4.22: Time series of 30-year annual average air temperature (°C) updated every ten years from 1961 to 2050

Table 4.12 shows the equations of trend lines, from where slopes were extracted to represent rates of warming over different decades centred in the years shown in column 1 together with the corresponding coefficients of determination. It is clear from the table that although the rate of warming will fall, temperatures will continue to rise as indicated by the positive slopes of the linear equations and the progressively increasing values of the y-intercepts.

Table 4.12: Linear equations of 30-year averages of air temperatures and the corresponding R^2 values over Sondu basin

Target Year	**Linear Equation**	**Rate of Warming (slope) °C/decade**	**R^2**
1990	$y = 0.667t + 15.7$	0.67	0.943
2000	$y = 1.135t + 15.6$	1.14	0.992
2010	$y = 1.213t + 16.6$	1.21	0.998
2020	$y = 0.876t + 18.8$	0.88	0.974
2030	$y = 0.455t + 19.8$	0.46	0.951

Figure 4.23 presents observed and projected rates of warming over the Sondu catchment area between 1961 and 2050. It is evident from the results that the rates of warming, extracted from the slopes of the linear equations in Table 4.12, have been on the rise since the baseline period rising from about 0.67°C to about 1.14°C per decade and are projected to reach a maximum of 1.21°C per decade by 2020 and begin falling thereafter. By 2050, the rates will have fallen to about 0.46°C per decade. It is therefore evident that although the temperatures will continue to rise in this region, the rates of increase will slow down after 2010s.

Figure 4.24 presents the projected mean monthly maximum temperature patterns (Figure 4.24a) and changes (Figure 4.24b) in the 2010s and 2030s. Projected mean monthly maximum temperatures in 2010s and 2030s show that daytime temperatures will be higher than the baseline temperatures between the months of April and December by between 0.3°C and 2°C, and between 0.2°C and 2.4°C in 2010s and 2030s respectively (Figure 4.24b). Between the months of January and March, mean monthly maximum temperatures are projected to be lower than the baseline temperatures by between 0.1°C and 0.4°C, and between 0.2°C and 0.6°C in 2010s and 2030s respectively (Figure 4.24b)

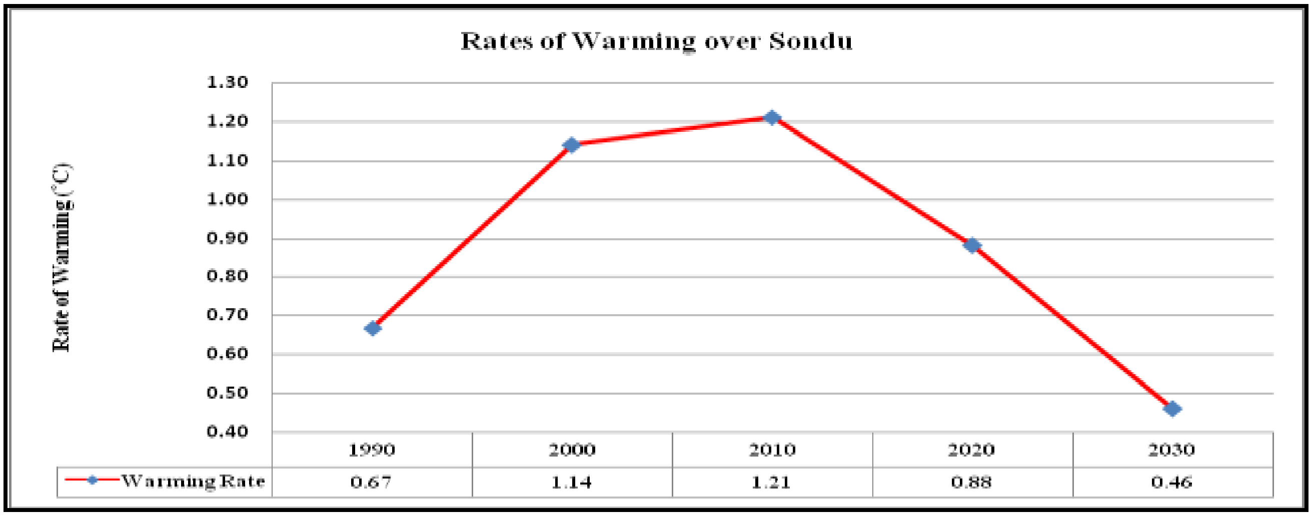

	1990	2000	2010	2020	2030
Warming Rate	0.67	1.14	1.21	0.88	0.46

Figure 4.23: Time series of observed and projected rates of warming over the Sondu basin

Projected mean minimum temperature patterns for 2010s and 2030s are presented in Figure 4.25 together with the corresponding changes from the baseline temperatures. Results show that the projected mean monthly minimum temperatures will be higher than the baseline temperatures in all the months of the year in 2010s and 2030s except March and April in 2010s. The month of April is projected to have the warmest nights while July is projected to have the coolest in both 2010s and 2030s. The projected month with warmest nights (April) corresponds to what has been observed but the projected month with coldest nights (July) deviates from the observed month with the coolest nights (September) (Figure 4.25a).

From the analysis of projected temperatures, it was established that temperatures in and around the Sondu catchment area have risen to above the baseline level in the last 50 years and they progressively continue to rise. In the years after the mid 1980s, the temperatures are all above the baseline normal. This is evidence that the region has become warmer with time and subsequent decades are becoming warmer with the highest temperatures in the area being reported in the most recent decades in line with the global and regional trends (IPCC, 2007).

Although the area is becoming warmer, the rate of warming is not uniform, rising from about 0.67°C per decade in 1990 to an all time high of about 1.21°C per decade in 2010 (Figure 4.23). Warming rates are projected to decrease to about 0.46°C per decade by 2030. Temperatures will however continue to rise since the reduced rates of warming are starting from already higher temperatures (Table 4.12).

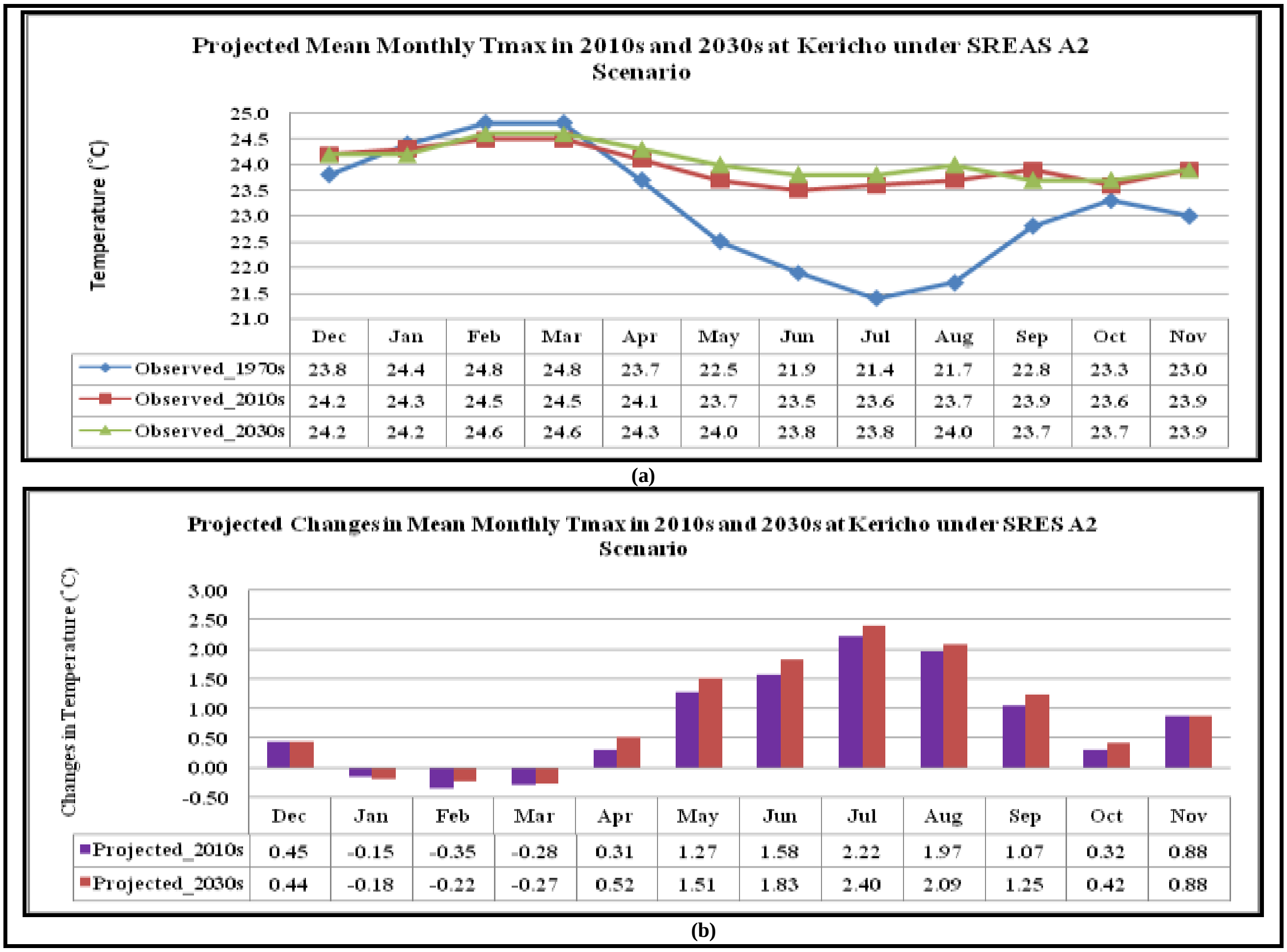

	Dec	Jan	Feb	Mar	Apr	May	Jun	Jul	Aug	Sep	Oct	Nov
Observed_1970s	23.8	24.4	24.8	24.8	23.7	22.5	21.9	21.4	21.7	22.8	23.3	23.0
Observed_2010s	24.2	24.3	24.5	24.5	24.1	23.7	23.5	23.6	23.7	23.9	23.6	23.9
Observed_2030s	24.2	24.2	24.6	24.6	24.3	24.0	23.8	23.8	24.0	23.7	23.7	23.9

(a)

	Dec	Jan	Feb	Mar	Apr	May	Jun	Jul	Aug	Sep	Oct	Nov
Projected_2010s	0.45	-0.15	-0.35	-0.28	0.31	1.27	1.58	2.22	1.97	1.07	0.32	0.88
Projected_2030s	0.44	-0.18	-0.22	-0.27	0.52	1.51	1.83	2.40	2.09	1.25	0.42	0.88

(b)

Figure 4.24: Projected (a) Mean monthly maximum air temperature scenarios (Tmax) and (b) Corresponding changes from the baseline at Kericho Met. Station

Seasonally, the months of April to December will have warmer days while the months of January to March will have cooler days than the baseline normal. However the general pattern of mean monthly maximum temperature will still be maintained where February and March will remain the warmest while June and July will remain the coolest months during the day (Figure 4.24). Nights are projected to be warmer between the months of May and February. March and April will have cooler nights by 2010s but warmer by 2050s compared to the baseline values (Figure 4.25). The progressive warming of the Sondu catchment and the surrounding areas are likely to result into increased rates of evapotranspiration which is likely to influence water yields from the catchment.

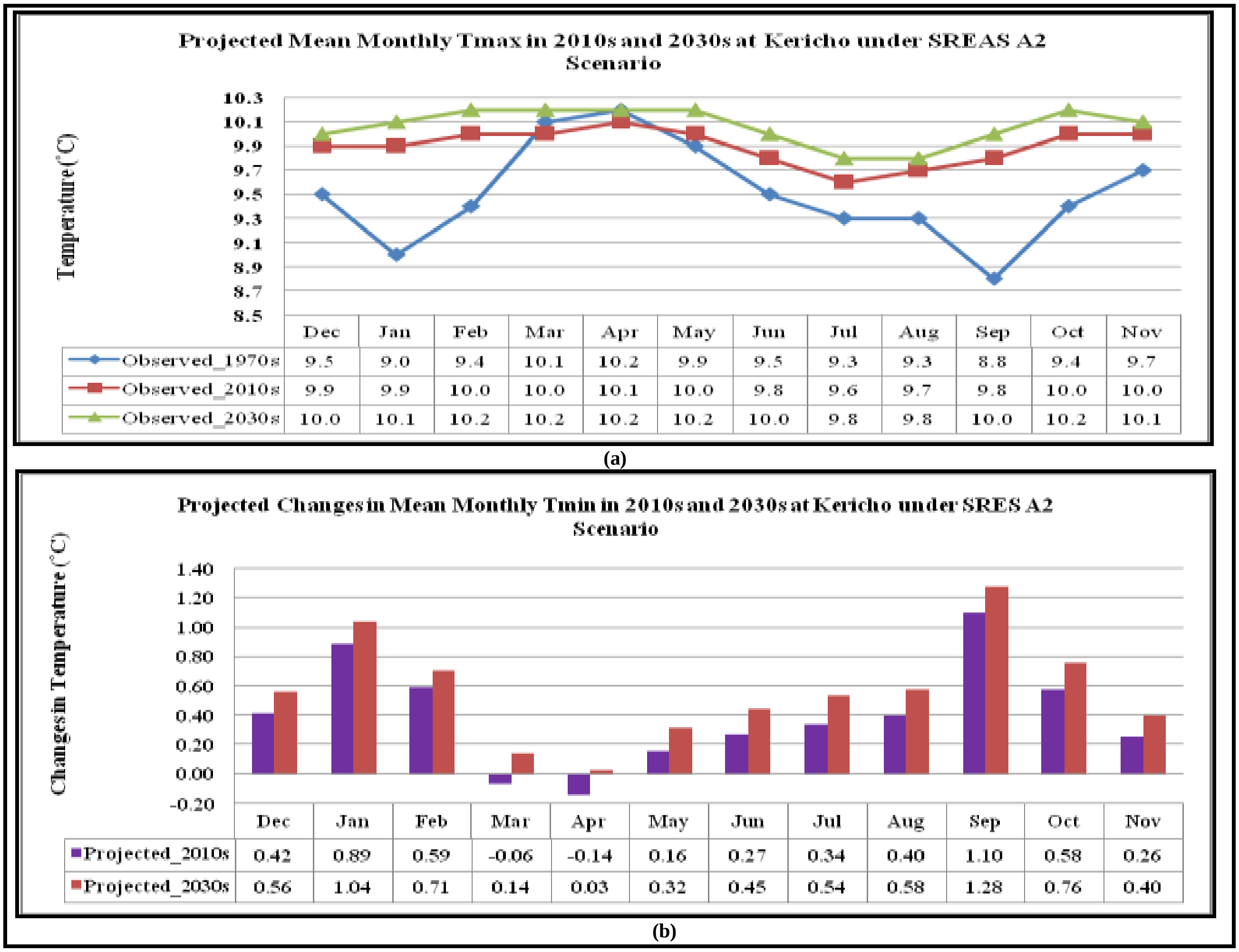

Figure 4.25: Projected (a) Mean monthly minimum air temperature scenarios (Tmin) and (b) Corresponding changes from the baseline at Kericho Met. Station

4.5.2.2 Projected Rainfall in 2010s and 2030s

Figure 4.26 shows a time series of observed (1964-2010) and projected (2011-2050) annual rainfall anomaly over the Sondu catchment area as a percentage of the 1961-1990 baseline period. It was noted from the figure that between 1961 and 2030 the anomalies in annual rainfall over the area range between -24% and +24% of the baseline mean annual rainfall with only a few years going beyond this threshold. The percentages are within the global annual precipitation anomalies that range between -40% and +40% in the period between 1960 and 2005 (IPCC, 2007).

For purposes of this study any values beyond the ±24% thresholds were considered extreme and the years with anomalies beyond this threshold labelled extremely dry or wet depending on the direction of change. From the observed annual rainfall, 1970 was therefore the wettest while 1984 was the driest in the past fifty years. The model predicted that 2013 would be wetter than 1970 and the next year projected to be wetter than 1970 will be 2036 (Figure 4.26).

The frequency of the number of years with rainfall below that of the baseline period decreased from an average of about once every two years between 1990 and 2000 to once every five years between 2000 and 2010 with 2016 projected to be the next dry year in this area. The model projects a further decrease in the occurrence of dry years to about once every fifteen years between 2010 and 2030 and once every thirty years between 2030 and 2050. The frequency and severity of the number of years with rainfall below that of the baseline period decreased sharply after 2000 and the projected rainfall shows only three years (2016, 2019, and 2032) that will have rainfall below that of the baseline period (Figure 4.26).

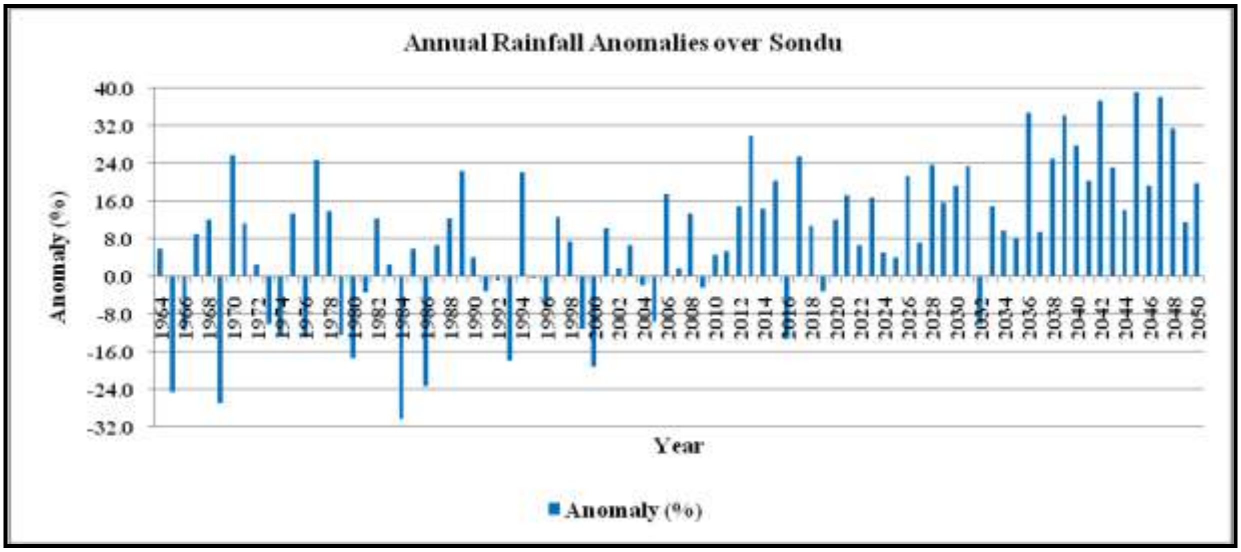

Figure 4.26: ***Time series of annual rainfall anomalies over Sondu basin relative to the 1961-1990 baseline average***

Figure 4.27 shows the 30-year average rainfall between 1961 and 2050 updated after every 10 years from the baseline period. It is evident from the results that there was an increasing trend in the mean annual rainfall in the area. The trend is not linear since it is modelled better by the 3rd degree order polynomial ($R^2 = 0.999$) compared to the linear model ($R^2 = 0.927$). The mean trend across the entire data set as given by the slope of the trend line (72 mm per decade) was found to be significant at $\alpha = 0.05$ significance level. Over 92% of the 30-year mean annual rainfall variability could be explained by the independent variable (time) and it was therefore concluded that climate of this area is becoming wetter with time.

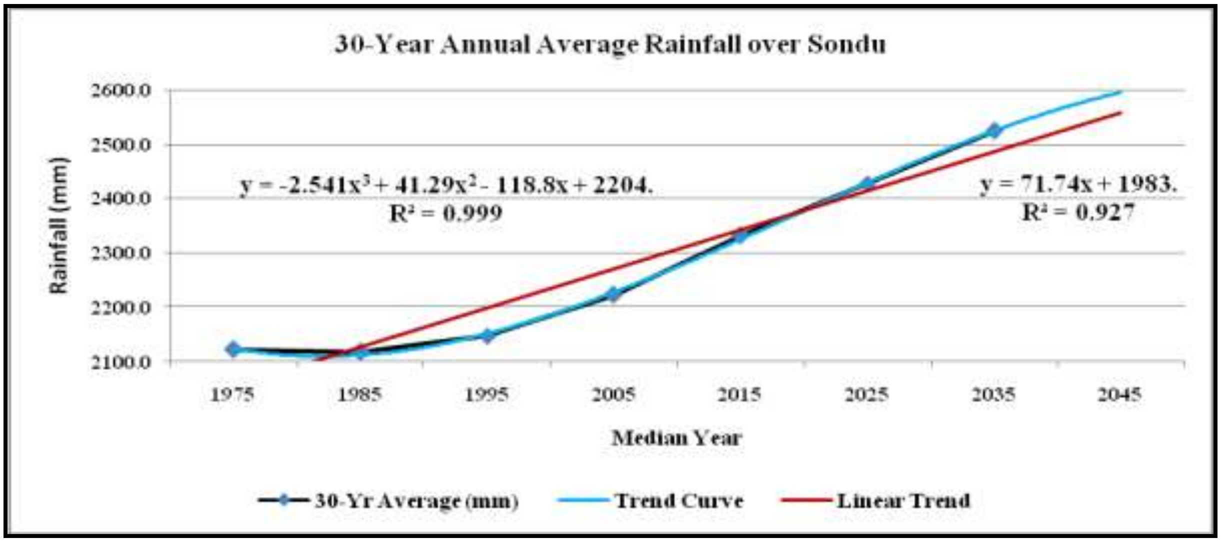

Figure 4.27: Time series of 30-year annual average rainfall (mm) updated every ten years from 1961 to 2050

Figure 4.28 shows the baseline climatology and projected monthly rainfall climatology together with projected changes in 2010s and 2030s. From the results, it is apparent that there will be substantial increases in monthly rainfall during the DJF and SON seasons by 2030 and 2050. The relatively dry DJF and SON seasons are projected to become relatively wet under the SRES A2 scenario in this part of Kenya.

During the DJF season, the month of January, which has the lowest rainfall during the baseline period, is projected to have peak rainfall for the season by 2030 and 2050 under the SRES A2 scenario. Under SRES A2 scenario, rainfall in the month of January is projected to increase by over 434% and 489% of the baseline rainfall by 2030 and 2050 respectively making January the wettest month in the season (Figure 4.33b). This represents a shift from the observed climatology where the month of December is the wettest in the season and the month of January is the driest (Figure 4.28a).

This finding is consistent with observations so far made (Figure 4.4) only that they are alarmingly higher under SRES A2 scenario. They are also consistent with the findings of another study conducted in Nzoia basin (Githui, 2008) which concluded that rainfall will substantially increase during the drier months and slightly decrease in the wetter months which is comparable with the results obtained in this study (Figure 4.28).

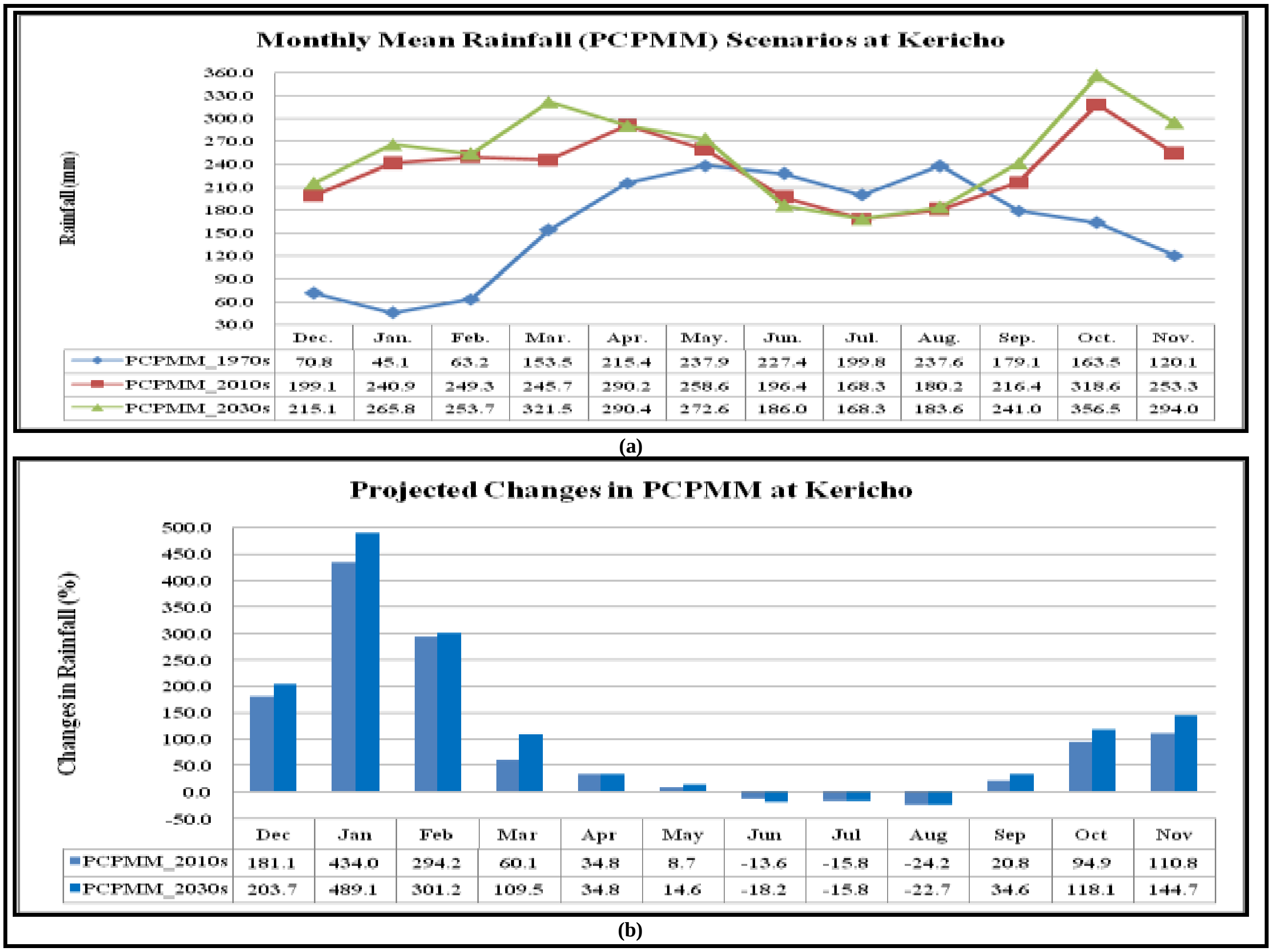

	Dec.	Jan.	Feb.	Mar.	Apr.	May.	Jun.	Jul.	Aug.	Sep.	Oct.	Nov.
PCPMM_1970s	70.8	45.1	63.2	153.5	215.4	237.9	227.4	199.8	237.6	179.1	163.5	120.1
PCPMM_2010s	199.1	240.9	249.3	245.7	290.2	258.6	196.4	168.3	180.2	216.4	318.6	253.3
PCPMM_2030s	215.1	265.8	253.7	321.5	290.4	272.6	186.0	168.3	183.6	241.0	356.5	294.0

(a)

	Dec	Jan	Feb	Mar	Apr	May	Jun	Jul	Aug	Sep	Oct	Nov
PCPMM_2010s	181.1	434.0	294.2	60.1	34.8	8.7	-13.6	-15.8	-24.2	20.8	94.9	110.8
PCPMM_2030s	203.7	489.1	301.2	109.5	34.8	14.6	-18.2	-15.8	-22.7	34.6	118.1	144.7

(b)

Figure 4.28: Projected (a) Mean monthly rainfall scenarios (PCPMM), and (b) Percentage change in PCPMM from the baseline at Kericho Met. Station

SRES A2 emissions scenario represents the worst case scenario of business as usual with no envisaged change in policy and the findings of this study are taken to represent the extremes of projected rainfall in the area of study by 2030 and 2050 if nothing is done to reverse or slow down the global and regional warming rates. The scenario may however not be realistic for the Kenyan case. The country now has a new constitution in which many policy guidelines have changed, (GOK, 2010b) with county governments now in place, which were not factored in the SRES A2 scenario.

Although SRES A2 scenario has not been updated since 2000, it was still used in this study as it was the one in place for practical applications at the time of this study. It may therefore not be realistic but only represents guidelines for the extreme cases. The extremely high rainfall projected for DJF is good for the area as it means that the area will have more water available for various uses. However the higher amounts of water are likely to cause an increase in flooding incidents unless efforts to conserve the upper parts of the water catchment areas, that include the South West Mau forest, are stepped up and sustained.

The MAM season, the wettest during the baseline period, is projected to have a shift in the monthly rainfall distribution. The peak monthly rainfall in the season is projected to shift from the month of May to the month of April by 2030 and to the month of March by 2050 (Figure 4.28a). During this season, March will experience the largest increase in rainfall amount of about 60% and 110% of the baseline rainfall by 2030 and 2050 respectively (Figure 4.28b) which will make it the wettest month in the season.

The JJA season, which is the second wettest season in this area during the baseline period, is projected to become the relatively dry season in 2010s and 2030s. Rainfall amounts in this season are projected to decrease by between 14% and 24% and between 16% and 23% of the baseline rainfall in 2010s and 2030s respectively (Figure 4.28b). This is the only season where monthly rainfall is expected to decrease. In addition, the rainfall patterns will radically change during this season. The observed peak in August during the baseline period is projected to shift to October (Figure 4.28a). A similar study by Githui (2008) in Nzoia basin in Kenya has shown similar results where JJA rainfall is projected to decrease by about 40% under the SRES A2 scenario.

Rainfall in the SON season, the second driest season in this area during the baseline period, is projected to increase by between 21% and 110% and between 35% and 145% of the baseline rainfall in 2010s and 2030s respectively (Figure 4.28b). The peak rainfall in this season is projected to occur in the month of October in both 2010s and 2030s.

The probability of a wet day following a dry day (PR_W1) is projected to increase during the DJF and SON months and to decrease during the MAM and JJA months except month of August in 2030s (Figure 4.29a). During the DJF months, chances of a wet day following a dry day are projected to be higher by between 5% and 114% and by between 22% and 163% of the baseline probabilities in 2010s and 2030s respectively (Figure 4.29b).

During the SON months, chances of a wet day following a dry day are projected to be higher by between 47% and 156% and by between 47% and 160% of the baseline probabilities in 2010s and 2030s respectively. On the other hand, PR_W1 is projected to decrease during MAM and JJA months by between 3% and 38% and by between 5% and 35% of the baseline probabilities in

2010s and 2030s respectively (Figure 4.29b) which is consistent with the projected decreases in rainfall during these seasons.

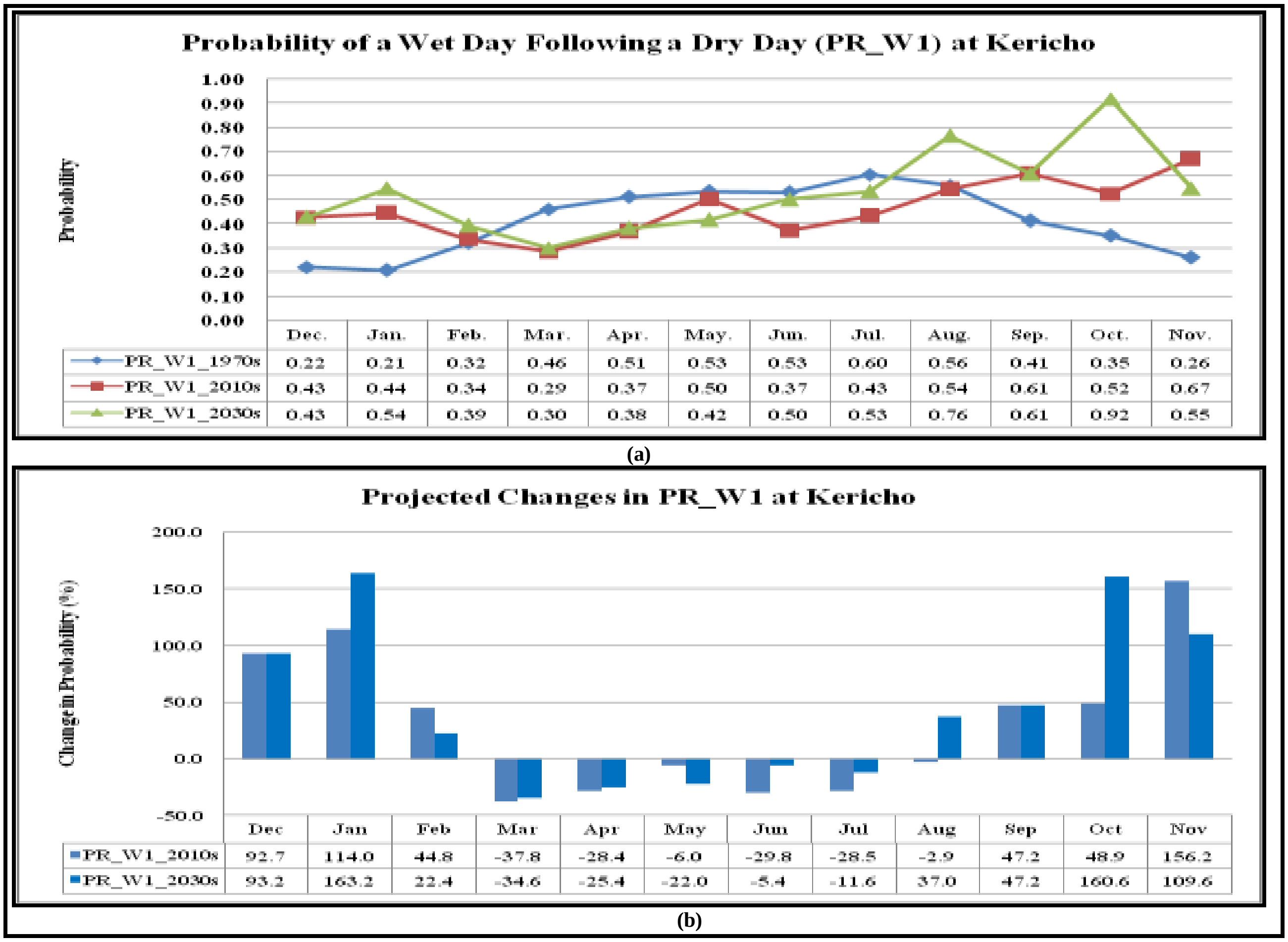

Figure 4.29: Projected (a) Probability of a wet day following a dry day (PR_W1), and (b) Percentage changes in the PR_W1 relative to the baseline at Kericho Met. Station

The probability of a wet day following a wet day (PR_W2) is projected to increase in all the months of the year by between 7% and 65% and by between 6% and 67% of the baseline probabilities in 2010s and 2030s respectively (Figure 4.30). The highest increase is in the month of November while the lowest is in the month of April.

The number of rainfall days in a month (PCPD) in all the months of the year is projected to increase by between 3% and 138% and by between 3% and 148% of the baseline numbers in 2010s and 2030s respectively (Figure 4.31). The highest increase is found between the months of November and January where the number of days of rainfall in a month is projected to increase by between 130% and 138% and by between 134% and 148% of the baseline numbers in 2010s and

203s respectively (Figure 4.31b). The lowest changes are found in the months of March and April with changes ranging from 3% to 5% and from 3% to 15% of the baseline numbers in 2010s and 2030s respectively. The changes in the number of days of rainfall in a month indicate an increase in the period that the soil will remain moist and hence a possible increase in the water yields from the catchment area.

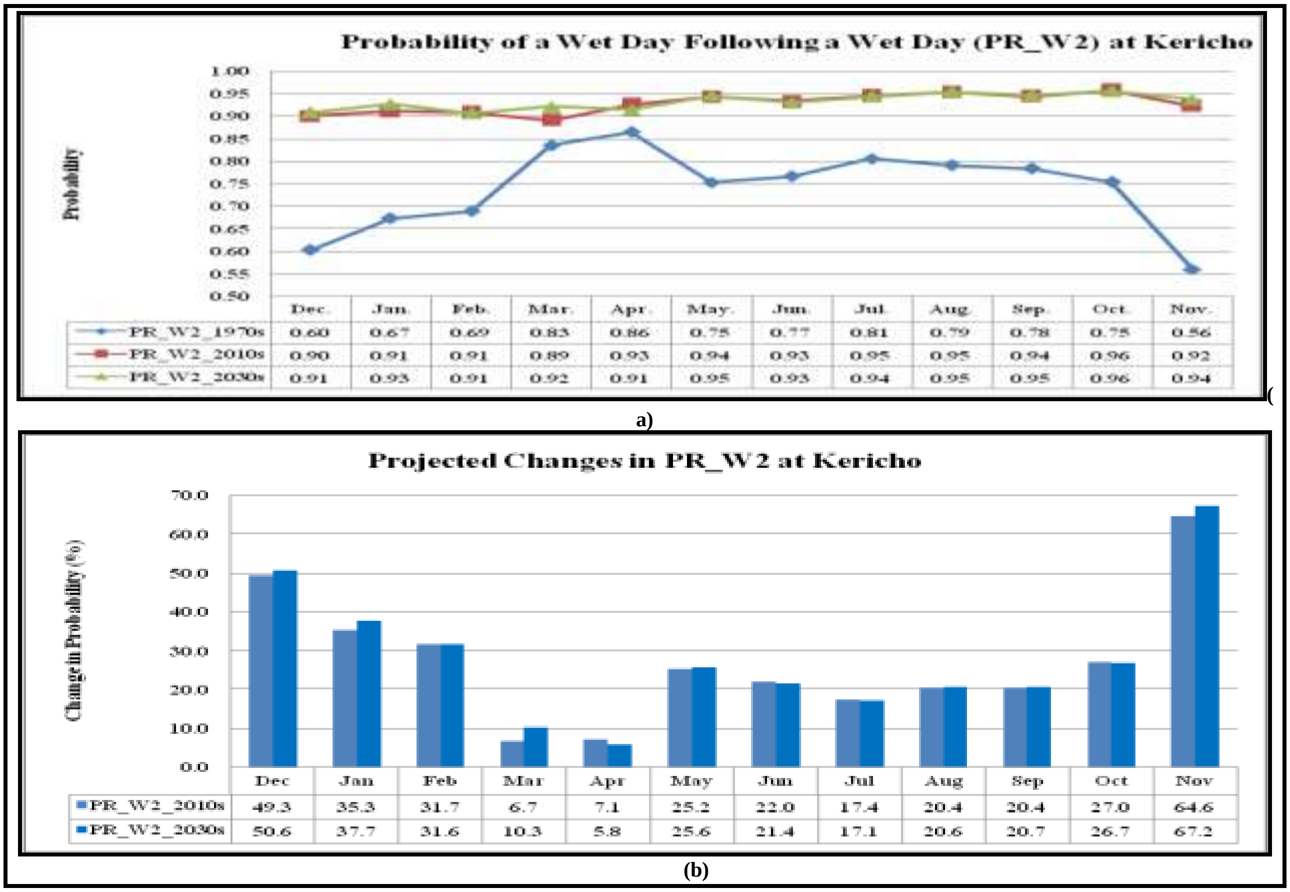

a)

(b)

Figure 4.30: Projected (a) Probability of a wet day following a wet day (PR_W2), and (b) Percentage changes in PR_W2 relative to the baseline at Kericho Met. Station

From the analysis of projected rainfall, it was established that there will be more rainfall in the 2010s and 2030s than in the baseline period. The annual rainfall is projected to be largely above the baseline average and will progressively increase up to 2050. The projected extremes are higher and more frequent than the baseline values. The highest annual rainfall in the area for the last 50 years was observed in 1970 and this was predicted to be surpassed in 2013. However rainfall data for 2013 was not immediately available to confirm this by the time writing this report. The frequency of the extreme annual rainfall is also projected to increase from about 1 in15 years during the baseline period to about 1 in 10 years by 2030 and about 1 in 3 years by 2050 (Figure 4.26).

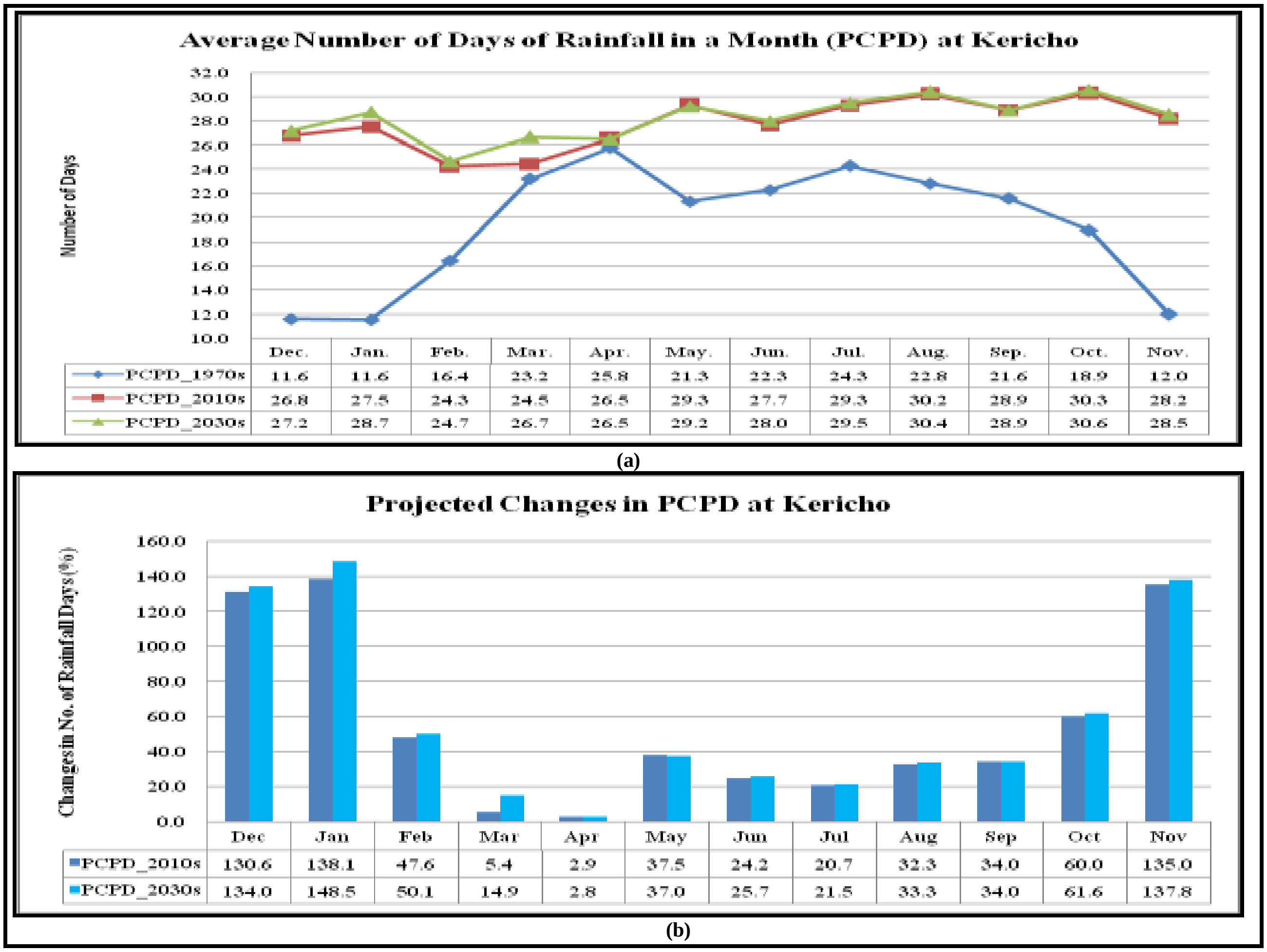

(a)

(b)

Figure 4.31: Projected (a) average number of days of rainfall in a month (PCPD) and (b) percentage changes in PCPD relative to the baseline at Kericho Met. Station

From the projected monthly rainfall patterns, October will receive the highest rainfall while July will receive the lowest in the 2010s and 2030s. This is in contrast to the baseline period where the highest rainfall is received in April and the lowest in January. Therefore apart from the projected increase in annual rainfall amounts in the 2010s and 2030s, seasonal rainfall patterns will also change and this will influence the water yields from the Sondu catchment area. The projected increase in rainfall amounts in DJF and SON coupled with a relatively small decrease in MAM and JJA rainfall amounts imply that under the SRES A2 scenario the basin will receive more water from rainfall by the years 2030 and 2050 than is currently available (Figure 4.26).

4.5.3 Climate Change

Figure 4.32 shows trends of the 30-year annual average temperature and rainfall over the Sondu catchment area for three climate periods: the observed baseline period (1961-1990), projected periods (1991-2020) and (2021-2050). These periods are centred in the 1970s, 2000s and 2030s decades respectively. Both temperature and rainfall show increasing trends of the 30-year averages between 1970s and 2030s with temperature changing at a rate of about 2.3°C and rainfall changing at a rate of about 201mm every 30 years.

The significance of the slopes was tested by computing the t-statistic (t_{cal}) and comparing it to the tabulated critical value ($t_{(2,0.05)} = 2.92$). The computed t-statistic values were $t_{tmp} = 3.328$ and $t_{rnf} = 295.9$ for temperature and rainfall respectively (Table 4.13). Since the values were both greater than the critical value, it was concluded that based on the available data the rate of change of the climate of the area of study between 1970s and 2030s is significant.

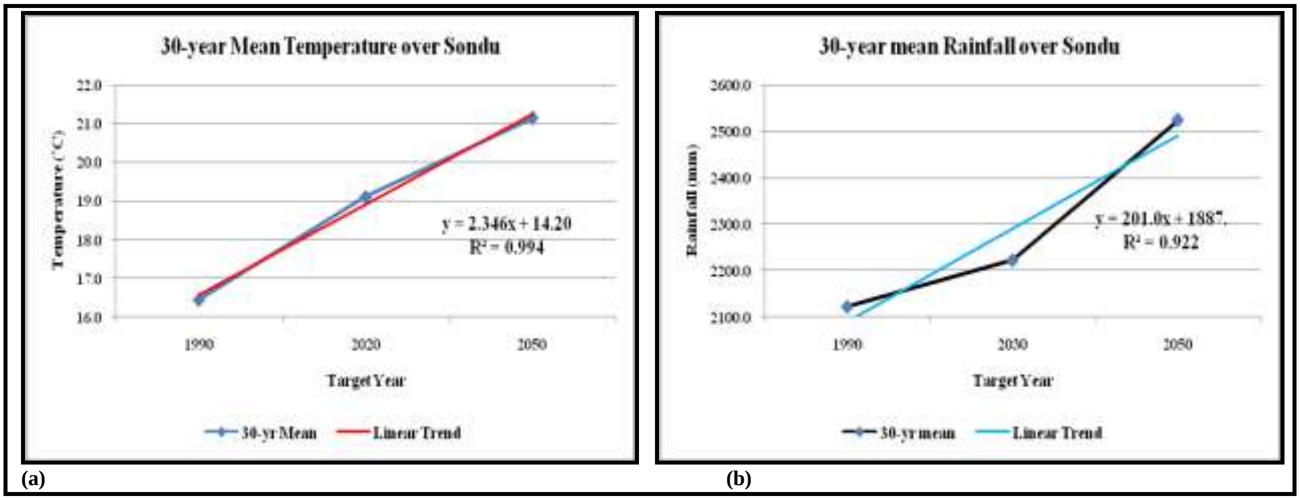

(a) (b)

Figure 4.32: Time series of 30-yr averages of temperature and rainfall over the Sondu catchment area

Table 4.13: Table of trends in 30-year average annual air temperature and rainfall (1970s-2030s) over Sondu basin

Climate Element	Equation of Trend line	R^2	t_{cal}	Remarks
Temperature	$y = 2.346t + 14.2$	0.994	3.328	change in temperature is significant
Rainfall	$y = 201t + 1887$	0.922	295.9	change in rainfall is significant

Table 4.14 shows the 30-year annual average temperature, rainfall, and the corresponding changes from the baseline period. The averages were calculated to give an overview of the general differences in climate by the end of 2000s and 2030s compared to that of the baseline period. On average, there were notable changes in both temperature and rainfall from the baseline values (Table 4.15 columns 3 and 6).

The two sample t-statistic (t_{cal}) was computed to test for significance in the differences in the mean values of temperature and rainfall in 2000s and 2030s respectively compared to the baseline mean values (Table 4.15). The t_{cal} values were compared to the tabulated critical value ($t_{0.025} = 2.045$). The t_{cal} values were all greater than the critical value except for the rainfall in the 2000s. On the basis of this data, changes from the baseline values for both temperature and rainfall were therefore found to be statistically significant except for the rainfall in the 2000s.

Table 4.14: 30-year average annual temperature and rainfall and the corresponding standard deviations (Stdev) together with changes relative to the baseline period

Climate Period	**Temperature**			**Rainfall**		
	1	**2**	**3**	**4**	**5**	**6**
	Mean (°C)	**Stdev (°C)**	**Change (°C)**	**Mean (mm)**	**Stdev (mm)**	**Change (%)**
1970s	16.4	0.44	0	2122.3	341.9	0
2000s	19.1	1.35	2.7	2222.6	264.4	4.7
2030s	21.1	0.40	4.7	2524.3	245.3	18.9

Table 4.15: Computed values of t-statistic (t_{cal}) for differences in the means for air temperature and rainfall for 30-year periods

Climate Period	**Temperature**		**Rainfall**	
	t_{cal}	**Remarks**	**t_{cal}**	**Remarks**
2000s	10.4	significant change	1.23	no significant change
2030s	42.7	significant change	5.05	significant change

From the analyses of 30-year averages of temperature and rainfall, it was established that the climate of Sondu and that of the surrounding areas has undergone statistically significant changes since the baseline period and the changes are projected to continue up to 2050 and beyond. The annual average temperature and rainfall are expected to change from the baseline values by about 2.7°C and 4.7% respectively by the end of 2010s, and by about 4.7°C and 18.9% respectively by the end of 2030s (Table 4.15). The changes in climate are expected to influence the hydrology of the catchment area through changes in evapotranspiration and water yields.

4.6 Hydrologic Simulations

This section presents the results obtained from the SWAT Hydrological Model. The model results are divided into six areas namely: Climate Data Processing, Catchment Delineation, Hydrologic Response Units (HRU), Default Simulations, Model Calibration and Validation, and Model Projections. The results are presented and discussed in the subsequent subsections in tabular and graphical formats.

4.6.1 Climate Data Processing

Results of the average monthly statistical parameters of rainfall and temperature, which were used by the weather generator component of the SWAT model to calculate the daily values of rainfall, maximum and minimum temperature, solar radiation, relative humidity, and wind speed, are presented in Tables 4.16 to 4.25.

The input variables used to generate daily rainfall include: mean monthly rainfall (PCPMM) in Table 4.16, standard deviation of daily rainfall in a month (PCPSTD) in Table 4.17, probability of a wet day following a dry day in a month (PR_W1) in Table 4.18, probability of a wet day following a wet day in a month (PR_W2) in Table 4.19, skew coefficient of daily rainfall in a month (PCPSKW) in Table 4.20, and the average number of days of rainfall in a month (PCPD) in Table 4.21.

The input variables that appertain to the generation of daily temperature and solar radiation include: mean monthly maximum air temperature (TMPMX) Table 4.22, standard deviation of daily maximum air temperature in a month (TMPSTDMX) in Table 4.23, mean monthly minimum air temperature in a month (TMPMN) in Table 4.24, and standard deviation of daily minimum air temperature in a month (TMPSTDMN) in Table 4.25.

Table 4.16: Mean monthly rainfall (PCPMM) used to generate daily rainfall in three climate periods

Month	**Kericho**			**Ndoinet**			**Sotik**		
	PCPMM (mmH_2O)			**PCPMM (mmH_2O)**			**PCPMM (mmH_2O)**		
	1970s	**2010s**	**2030s**	**1970s**	**2010s**	**2030s**	**1970s**	**2010s**	**2030s**
Jan	99.0	240.9	265.8	65.1	140.1	192.4	84.6	174.6	192.4
Feb	108.6	249.3	253.7	80.6	137.8	168.4	105.0	166.6	166.4
Mar	179.8	245.7	321.5	96.6	132.2	152.6	143.2	137.2	161.9
Apr	253.1	290.2	290.4	181.9	177.9	139.5	209.2	144.2	135.2
May	276.9	258.6	272.6	198.2	146.9	125.9	141.5	119.3	123.9
Jun	181.0	196.4	186.0	171.7	136.6	93.3	92.6	102.0	90.2
Jul	187.6	168.3	168.3	188.0	122.6	86.3	84.7	90.6	89.1
Aug	221.9	180.2	183.6	235.3	125.8	97.8	106.5	95.5	102.5
Sep	198.0	216.4	241.0	140.9	136.2	137.5	86.5	120.5	128.6
Oct	146.7	318.6	356.5	80.4	196.2	194.0	76.7	179.4	198.2
Nov	143.3	253.3	294.0	84.5	142.5	198.9	118.4	178.8	196.1
Dec	75.3	199.1	215.1	69.8	104.6	176.4	82.7	151.2	162.5

The skew coefficient (PCPSKW) in Table 4.26 were used by the Markov chain-skewed model in the weather generator component of the SWAT model to generate rainfall amounts in a day for a particular month after the model has determined the probability of rain on a given day.

Tables 4.24 and 4.25 show the probabilities of rainfall on a given day in a month which is conditioned to the wet or dry status of the previous day (Neitsh *et al*, 2011). These probabilities were used by the SWAT model to generate daily rainfall for the month.

Table 4.17: Standard deviation of daily rainfall (PCPSTD) used to generate daily rainfall in three climate periods

Month	**Kericho**			**Ndoinet**			**Sotik**		
	PCPSTD (mmH_2O)			**PCPSTD (mmH_2O)**			**PCPSTD (mmH_2O)**		
	1970s	**2010s**	**2030s**	**1970s**	**2010s**	**2030s**	**1970s**	**2010s**	**2030s**
Jan	8.38	9.59	9.81	6.24	6.75	6.26	6.96	5.82	6.14
Feb	8.32	11.38	11.37	13.84	7.19	6.65	8.41	6.62	6.58
Mar	10.76	9.79	13.22	7.58	6.28	6.04	10.10	5.09	6.12
Apr	11.31	9.88	10.61	10.78	7.35	4.76	11.89	5.00	4.61
May	10.42	8.01	7.54	10.13	5.34	4.21	9.12	4.17	3.99
Jun	9.14	5.54	5.25	9.75	4.44	2.99	7.03	3.28	2.78
Jul	9.02	4.58	4.58	8.60	3.99	2.91	6.51	2.75	2.63
Aug	9.49	4.20	4.34	10.61	3.54	2.59	7.60	2.33	2.58
Sep	9.59	6.41	8.10	9.22	4.46	4.29	6.23	3.32	3.87
Oct	8.60	8.49	8.80	6.04	6.29	4.69	5.32	4.70	4.35
Nov	7.84	10.40	10.11	6.74	7.07	6.57	7.84	6.28	5.91
Dec	5.81	8.97	8.82	10.70	6.33	6.29	6.01	5.20	5.48

Table 4.18: Probability of a wet day following a dry day (PR_W1) for different months in three climate periods

Month	**Kericho**			**Ndoinet**			**Sotik**		
	PR_W1			**PR_W1**			**PR_W1**		
	1970s	**2010s**	**2030s**	**1970s**	**2010s**	**2030s**	**1970s**	**2010s**	**2030s**
Jan	0.22	0.44	0.54	0.10	0.39	0.36	0.18	0.45	0.63
Feb	0.21	0.34	0.39	0.15	0.29	0.38	0.23	0.36	0.46
Mar	0.32	0.29	0.30	0.18	0.28	0.34	0.29	0.41	0.39
Apr	0.46	0.37	0.38	0.30	0.32	0.41	0.38	0.40	0.38
May	0.51	0.50	0.42	0.32	0.48	0.28	0.33	0.49	0.44
Jun	0.53	0.37	0.50	0.32	0.38	0.47	0.27	0.38	0.49
Jul	0.53	0.43	0.53	0.38	0.43	0.38	0.24	0.48	0.56
Aug	0.60	0.54	0.76	0.43	0.60	0.41	0.27	0.58	0.76
Sep	0.56	0.61	0.61	0.25	0.44	0.66	0.25	0.63	0.66
Oct	0.41	0.52	0.92	0.16	0.57	0.22	0.26	0.62	0.79
Nov	0.35	0.67	0.55	0.17	0.62	0.83	0.33	0.70	0.67
Dec	0.26	0.43	0.43	0.10	0.38	0.33	0.21	0.50	0.51

Table 4.19: Probability of a wet day following a wet day (PR_W2) for different months in three climate periods

Month	**Kericho**			**Ndoinet**			**Sotik**		
		PR_W2			**PR_W2**			**PR_W2**	
	1970s	**2010s**	**2030s**	**1970s**	**2010s**	**2030s**	**1970s**	**2010s**	**2030s**
Jan	0.60	0.91	0.93	0.60	0.88	0.94	0.54	0.93	0.94
Feb	0.67	0.91	0.91	0.47	0.87	0.92	0.54	0.92	0.92
Mar	0.69	0.89	0.92	0.50	0.85	0.91	0.63	0.89	0.92
Apr	0.83	0.93	0.91	0.65	0.90	0.91	0.70	0.92	0.91
May	0.86	0.94	0.95	0.67	0.92	0.93	0.56	0.93	0.93
Jun	0.75	0.93	0.93	0.62	0.93	0.91	0.52	0.92	0.91
Jul	0.77	0.95	0.94	0.67	0.93	0.93	0.52	0.94	0.93
Aug	0.81	0.95	0.95	0.69	0.95	0.94	0.48	0.94	0.94
Sep	0.79	0.94	0.95	0.64	0.93	0.94	0.58	0.94	0.94
Oct	0.78	0.96	0.96	0.54	0.94	0.95	0.48	0.95	0.96
Nov	0.75	0.92	0.94	0.52	0.89	0.95	0.57	0.94	0.95
Dec	0.56	0.90	0.91	0.50	0.85	0.93	0.60	0.92	0.92

Table 4.20:* Skewness *coefficient of daily rainfall in a month (PCPSKW) for different months in three climate periods

Month	**Kericho**			**Ndoinet**			**Sotik**		
	PCPSKW			**PCPSKW**			**PCPSKW**		
	1970s	**2010s**	**2030s**	**1970s**	**2010s**	**2030s**	**1970s**	**2010s**	**2030s**
Jan	4.35	3.17	3.04	4.66	2.37	3.11	4.00	2.61	3.23
Feb	2.71	3.62	2.96	18.14	2.52	2.96	3.68	2.82	2.77
Mar	2.61	2.66	3.82	3.46	2.16	4.74	5.49	2.68	4.24
Apr	2.15	2.23	2.90	3.19	2.33	1.81	3.39	2.28	2.18
May	1.56	5.02	2.88	2.60	3.08	4.32	3.43	4.67	4.36
Jun	2.25	1.74	2.05	2.44	1.83	1.36	4.33	1.82	1.43
Jul	2.66	2.25	2.45	1.89	2.72	3.50	4.45	2.77	2.61
Aug	2.00	1.35	1.49	2.18	2.26	1.19	3.57	1.13	1.14
Sep	2.34	4.35	4.70	4.40	2.34	3.62	4.27	2.00	2.98
Oct	5.84	2.44	3.08	3.15	2.14	2.24	3.18	2.69	2.17
Nov	2.72	4.61	2.96	3.46	2.81	3.09	3.35	3.70	2.83
Dec	3.61	4.32	3.36	14.53	4.51	2.59	4.07	2.55	2.68

***Table 4.21:* Average number of days of rainfall in a month (PCPD) for different months in three climate periods**

Month	**Kericho**			**Ndoinet**			**Sotik**		
	PCPD			**PCPD**			**PCPD**		
	1970s	**2010s**	**2030s**	**1970s**	**2010s**	**2030s**	**1970s**	**2010s**	**2030s**
Jan	11.6	27.5	28.7	6.7	24.8	28.8	9.5	28.8	29.6
Feb	11.6	24.3	24.7	6.4	21.4	25.3	9.7	25.4	25.5
Mar	16.4	24.5	26.7	8.4	21.6	26.6	14.0	26.3	27.4
Apr	23.2	26.5	26.5	14.3	24.5	26.1	17.3	26.6	26.4
May	25.8	29.3	29.2	16.3	28.3	27.6	14.1	28.8	28.6
Jun	21.3	27.7	28.0	14.0	27.2	26.7	11.3	26.9	27.2
Jul	22.3	29.3	29.5	17.2	28.5	28.0	10.8	28.9	29.0
Aug	24.3	30.2	30.4	19.0	29.8	28.9	10.9	29.7	29.9
Sep	22.8	28.9	28.9	13.1	27.7	29.0	11.8	28.9	28.9
Oct	21.6	30.3	30.6	8.5	29.6	29.6	10.8	30.3	30.5
Nov	18.9	28.2	28.5	8.3	26.7	29.2	13.6	28.8	29.2
Dec	12.0	26.8	27.2	5.4	24.0	27.7	11.4	28.5	28.6

Table 4.22: Mean monthly maximum air temperatures (TMPMX) used to generate daily values in three climate periods

Month	**Kericho**			**Ndoinet**			**Sotik**		
	TMPMX (˚C)			**TMPMX (˚C)**			**TMPMX (˚C)**		
	1970s	**2010s**	**2030s**	**1970s**	**2010s**	**2030s**	**1970s**	**2010s**	**2030s**
Jan	24.1	23.4	23.4	24.9	24.7	26.0	26.3	25.4	26.1
Feb	24.6	23.6	23.7	25.5	25.0	26.4	26.7	25.6	26.4
Mar	24.9	23.7	23.7	25.4	25.1	26.4	26.7	25.8	26.4
Apr	23.0	23.3	23.4	23.9	24.5	26.0	25.1	25.4	26.1
May	22.3	23.0	23.2	23.3	24.1	25.7	24.5	25.2	25.9
Jun	21.9	22.8	23.0	22.9	23.8	25.5	24.2	25.0	25.7
Jul	21.3	22.9	23.0	22.3	23.8	25.5	23.8	25.1	25.7
Aug	21.7	23.0	23.1	22.9	23.8	25.6	24.3	25.1	25.8
Sep	23.0	23.1	23.2	23.8	24.1	25.8	25.2	25.3	26.0
Oct	23.3	22.9	23.0	24.9	24.0	25.5	26.3	25.0	25.7
Nov	22.6	23.2	23.2	23.6	24.4	25.7	25.1	25.2	25.9
Dec	23.3	23.4	23.4	24.1	24.7	26.0	25.5	25.4	26.1

Table 4.23: Standard deviation of daily maximum air temperature (TMPSTDMX) in three climate periods

Month	**Kericho**			**Ndoinet**			**Sotik**		
	TMPSTDMX (˚C)			**TMPSTDMX (˚C)**			**TMPSTDMX (˚C)**		
	1970s	**2010s**	**2030s**	**1970s**	**2010s**	**2030s**	**1970s**	**2010s**	**2030s**
Jan	1.66	1.39	1.17	1.66	1.32	1.17	1.61	1.31	1.17
Feb	1.70	1.82	1.03	1.70	1.70	1.03	2.08	1.60	1.03
Mar	1.88	1.52	1.14	1.88	1.62	1.14	1.91	1.39	1.14
Apr	1.76	1.37	1.29	1.76	1.47	1.29	1.14	1.29	1.29
May	1.41	0.90	1.29	1.41	1.08	1.29	0.76	1.01	1.29
Jun	1.17	0.85	0.84	1.17	1.09	0.84	0.74	0.92	0.84
Jul	1.30	1.26	0.71	1.30	1.38	0.71	0.73	1.20	0.71
Aug	1.04	1.12	0.89	1.04	1.21	0.89	0.87	1.10	0.89
Sep	1.21	0.80	1.05	1.21	1.14	1.05	1.13	0.79	1.05
Oct	1.32	0.82	0.78	1.32	1.03	0.78	1.10	0.87	0.78
Nov	1.62	0.94	0.83	1.62	1.09	0.83	1.06	1.09	0.83
Dec	1.37	1.28	1.34	1.37	1.31	1.34	0.99	1.26	1.34

Table 4.24: Mean monthly minimum air temperatures (TMPMN) used to generate daily values in three climate periods

Month	**Kericho**			**Ndoinet**			**Sotik**		
	TMPMN (˚C)			**TMPMN (˚C)**			**TMPMN (˚C)**		
	1970s	**2010s**	**2030s**	**1970s**	**2010s**	**2030s**	**1970s**	**2010s**	**2030s**
Jan	9.8	9.9	10.1	10.2	10.3	10.6	12.7	13.3	13.5
Feb	10.1	10.0	10.2	10.6	10.5	10.7	13.1	13.4	13.6
Mar	10.5	10.0	10.2	10.1	10.5	11.0	13.4	13.4	13.7
Apr	10.8	10.1	10.2	10.2	10.8	11.0	13.5	13.4	13.6
May	10.3	10.0	10.2	9.9	10.7	11.0	13.1	13.3	13.5
Jun	10.0	9.8	10.0	9.5	10.3	10.6	12.6	13.0	13.2
Jul	9.6	9.6	9.8	9.3	10.1	10.5	12.3	12.8	13.1
Aug	9.7	9.7	9.8	9.3	10.2	10.6	12.3	12.9	13.1
Sep	9.5	9.8	10.0	8.8	10.4	10.8	12.1	13.2	13.4
Oct	9.9	10.0	10.2	9.4	10.6	11.0	12.7	13.3	13.6
Nov	10.3	10.0	10.1	9.7	10.4	10.6	12.9	13.3	13.5
Dec	10.2	9.9	10.0	9.9	10.2	10.4	12.8	13.3	13.5

Table 4.25: Standard deviation of daily minimum air temperature (TMPSTDMN) in three climate periods

Month	Kericho			Ndoinet			Sotik		
		TMPSTDMN (˚C)		TMPSTDMN (˚C)			TMPSTDMN (˚C)		
	1970s	2010s	2030s	1970s	2010s	2030s	1970s	2010s	2030s
Jan	1.55	0.58	0.67	0.50	0.74	0.68	0.65	0.48	0.60
Feb	1.65	0.66	0.63	0.55	0.74	0.84	0.82	0.54	0.63
Mar	1.68	0.76	0.69	0.65	0.92	0.81	0.91	0.74	0.70
Apr	1.38	0.52	0.63	0.58	0.62	0.71	0.60	0.58	0.64
May	1.35	0.53	0.62	0.59	0.63	0.68	0.49	0.62	0.68
Jun	1.43	0.42	0.56	0.54	0.57	0.56	0.50	0.52	0.56
Jul	1.30	0.50	0.49	0.55	0.48	0.55	0.57	0.45	0.50
Aug	1.25	0.66	0.56	0.60	0.67	0.55	0.53	0.64	0.56
Sep	1.53	0.73	0.64	0.79	0.71	0.58	0.70	0.69	0.58
Oct	1.47	0.43	0.58	0.50	0.50	0.56	0.48	0.41	0.51
Nov	1.45	0.35	0.47	0.42	0.43	0.60	0.47	0.36	0.44
Dec	1.46	0.53	0.55	0.52	0.62	0.51	0.52	0.52	0.57

4.6.2 Catchment Delineation

Results of the catchment delineation include topographic characteristics and the generation of the sub-basins in the Sondu catchment area. Using the ArcSWAT interface, the SWAT model delineated a total area of 344837 hectares divided into seventeen sub-basins based on the topographic information provided in the Digital Elevation Model (DEM). The seventeen sub-basins were further sub divided into 94 Hydrologic Response Units (HRUs) depending on the heterogeneity of the land use, soil types, and slope (Figures 4.33). The figure shows the maps of the delineated catchment area that include: (a) seventeen sub-basins, (b) land use map, (c) soil class map, and (d) land slope map.

Table 4.26 and Figure 4.34 show the West-East cross-section of the basin from the lowest point (1137 m) at the level of Lake Victoria in sub-basin number 8, to the highest point (2934 m) at Keresoi forest station in sub-basin number 14. The mean elevation of the catchment as calculated by the ArcSWAT interface is about 2039 m with a standard deviation of 310 m. The change in elevation from the lowest to the highest point in the catchment is about 1795 m. Hence elevation increases eastwards from the eastern shores of Lake Victoria causing rivers in this catchment area to generally flow westwards. Sub-basin number 8 has the lowest mean elevation (1585 m) while number 12 has the highest (2410 m)

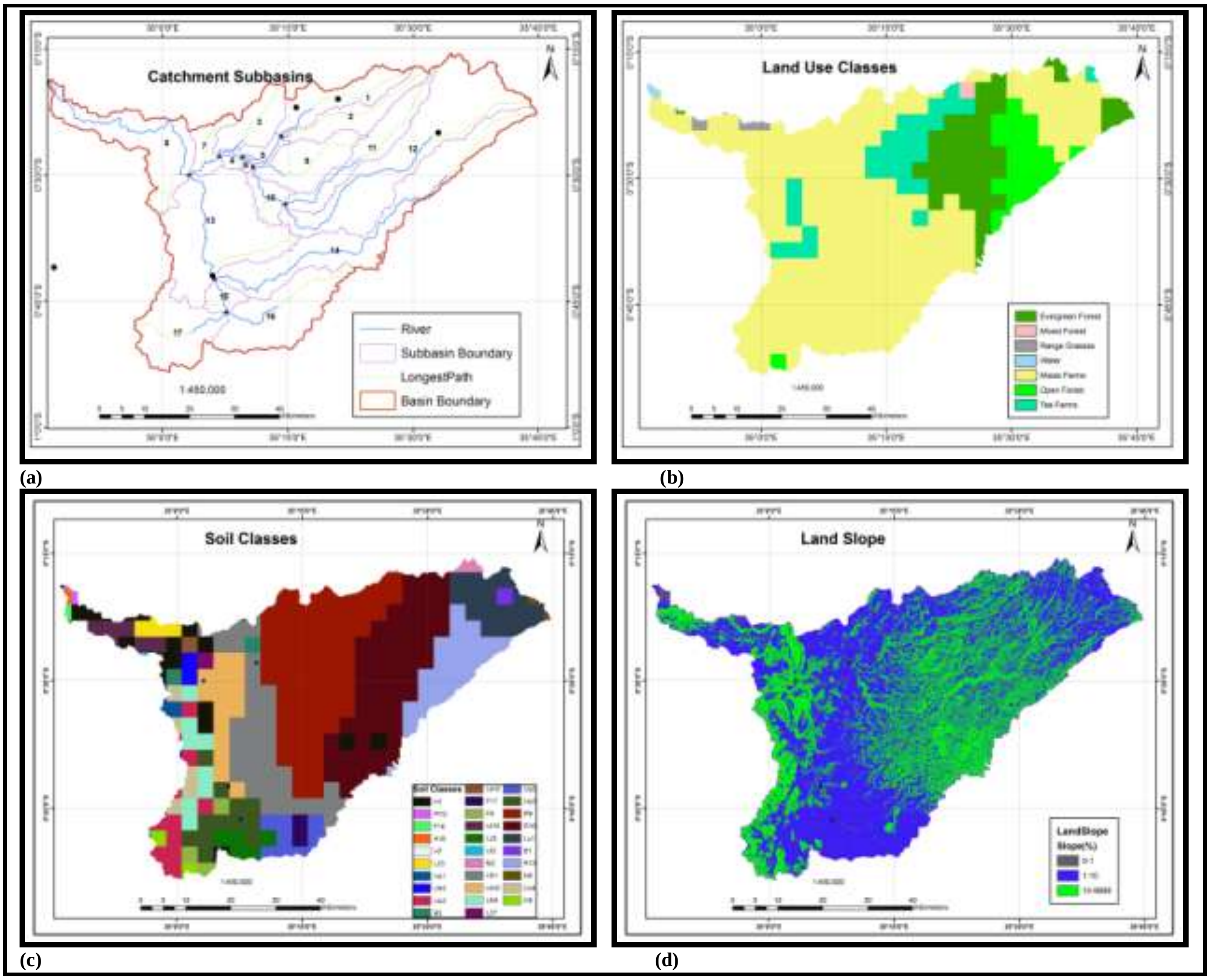

(a) (b) (c) (d)

Figure 4.33: Sondu catchment area maps showing the (a) seventeen sub basins, (b) distribution of the different landuse classes, (c) distribution of the different soil classes, and (d) distribution of slope, over the Sondu catchment area as created by the ArcSWAT interface

.

Table 4.26 Sub basins of the Sondu catchment area delineated by ArcSWAT

Sub Basin No.	Minimum Elevation (m)	Maximum Elevation (m)	Mean Elevation (m)	Area (ha)	% Area
1	1837	2566	2141	16494	4.8
2	1837	2616	2253	14135	4.1
3	1657	2056	1866	12977	3.8
4	1657	1791	1722	1747	0.5
5	1689	2006	1818	3355	1.0
6	1690	1824	1753	732	0.2
7	1582	1914	1749	6651	1.9
8	1137	2152	1585	30306	8.8
9	1718	2382	2012	17887	5.2
10	1719	2003	1890	6669	1.9
11	1854	2684	2283	18886	5.5
12	1852	2931	2410	58441	17.0
13	1583	2214	1852	50539	14.7
14	1729	2934	2203	48182	14.0
15	1727	1913	1800	4580	1.3
16	1763	2162	1891	30231	8.8
17	1762	2190	1910	23028	6.7

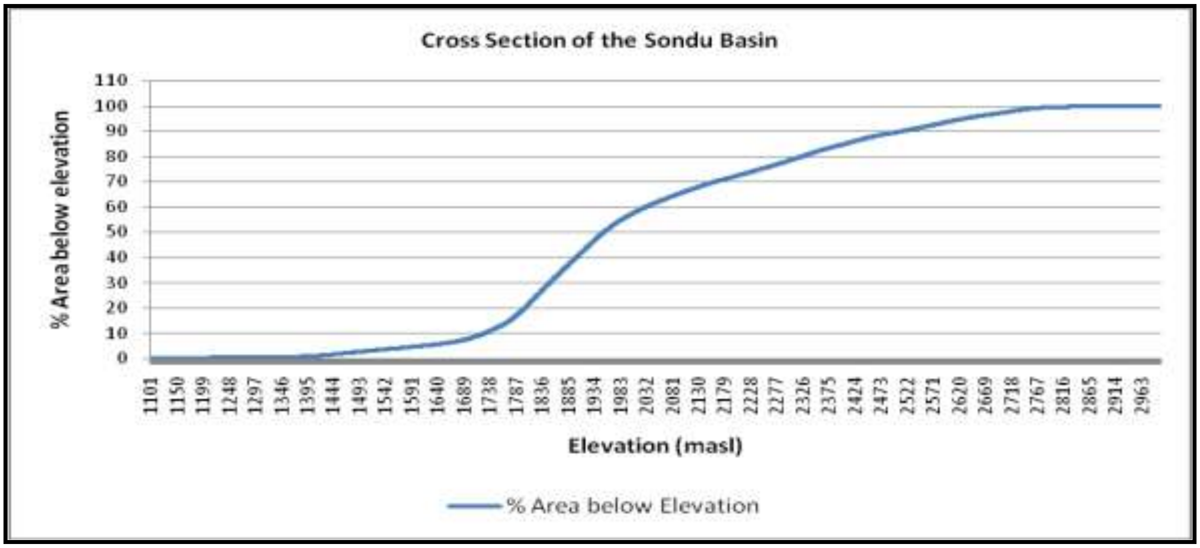

Figure 4.34: Cross section of the Sondu catchment area from Lake Victoria eastwards to the watershed boundary near Keresoi forest station

4.6.3 Hydrologic Response Units

As already pointed out, seventeen sub-basins were created during the delineation process. From the sub-basins, a total of 101 Hydrologic Response Units **(**HRUs) were created using the ArcSWAT interface by applying a threshold of 5%, 20%, and 20% for landuse, soil class, and slope respectively. Using these threshold levels and the classified satellite raster image of the Sondu basin, the model picked four landcover types within the Sondu catchment area: Rainfed herbaceous crop (Maize) (75.0%), closed forest (13.4%), Rainfed herbaceous with shrub (Tea) (7.6%), and open forest (4.0%) (Table 4.27). Figure 5.38b shows the distribution of these landuse activities across the entire catchment.

Table 4.27: The main landcover types distributed across the entire Sondu catchment by area

Landuse/Landcover	**Area (Ha)**	**% Area**
Rainfed herbaceous crop (Maize)	258366	75.0
Closed Forest	114437	13.4
Rainfed herbaceous with shrub (Tea)	26776	7.6
Open Forest	13884	4.0

Table 4.28 presents the seventeen sub basins of the larger Sondu catchment area together with the landuse, number of HRUs, major soil class and slope. From the table it was noted that forestry and rainfed herbaceous crop with shrub activities are confined to elevations above 2000 m and are mainly found in sub-basin Numbers 1, 2, 9, 12, and 14 whose mean elevations are all above 2000 m (Table 4.26). Most of the tributaries of the main Sondu River originate from these sub-basins. It was noted from the table and Figure 4.33b that the most dominant landuse activity in the area is rainfed herbaceous crop (maize) since it is practiced in all the seventeen sub-basins delineated by ArcSWAT interface.

The three most common soil classes in the basin, delineated by the ArcSWAT interface from the raster images obtained from the Kenya Soil Survey, are ando-humic nitisols (R10), humic cambisols (R9), and humic nitisols (Uh1) which collectively cover about 66% of the total catchment area and dominate in seven out of the seventeen sub basins (Figure 4.33c and Table 4.29).

Table 4.28: Sub basins and HRUs created using the ArcSWAT interface in the Sondu catchment area showing the landuse, dominant soil class and slope for each of the sub basins

Sub Basin No.	**Landuse**	**No. of HRUs**	**Major Soil Class**	**Slope (%)**	
				0 - 8	**8 - 30**
1	Closed forest, mixed forest, maize farms, tea	10	R9	49.2	50.8
2	Closed forest, maize farms, tea farms	8	R9	33.6	66.5
3	maize farms, tea farms	1	R9	63.6	36.5
4	maize farms	3	Uh1	62.9	37.2
5	maize farms, tea farms	4	R9	55.2	44.8
6	maize farms	3	R9	63.7	36.3
7	maize farms, tea farms	3	Uh1	71.6	28.4
8	maize farms, tea, Closed forest, range grasses	6	H1	43.7	54.7
9	maize farms, tea farms, Evergreen forest	8	R9	30	70
10	maize farms	4	R9	48.1	52.0
11	maize farms, tea farms, Closed forest, open forest	10	R10	32.8	67.3
12	maize farms, tea farms, Closed forest, open forest	10	R10	39.6	60.5
13	maize farms, tea farms	3	Uh1	57.1	43.0
14	maize farms, Closed forest, open forest	11	R10	33.6	66.4
15	maize farms	1	Up2	88.5	11.6
16	maize farms	2	UP2	88.2	11.9
17	maize farms, open forest	7	Uu2	62.1	37.9

The three most dominant soils have properties that range from moderately to extremely deep, are all well drained, and mostly found on valley sides. They therefore allow higher infiltration rates, recharge of ground water and movement of water as interflow to the rivers in the catchment area. This allows rivers within the area to have water long after rainfall has ceased. Forestry and tea farming are mainly concentrated in the sub basins dominated by R9, R10 and Uh1 soil classes which are mainly found between altitudes 1718m and 2410m (Figure 4.33b and Table 4.29).

Table 4.29: Major soil types, their properties and distribution within the Sondu catchment area as identified by the ArcSWAT interface during the catchment delineation process

Mapping Code	Soil Class	Soil Properties	Area (Ha)	%Area
R10	ando-humic nitisols	Shallow to moderately deep, well drained	76581	22.2
R9	humic cambisols	Extremely deep, well drained	72785	21.1
Uh1	humic nitisols	Extremely deep, well drained	79220	23.0
L23	niti-rhodic ferrasols	Very deep, well drained	1271	0.4
Ul10	chromic luvisols	Moderately deep to deep, well drained	919	0.3
H1	humic cambisols	Shallow to moderately deep, excessively drained	27651	8.0
Lu1	humic andosols	Deep to very deep, well drained	17349	5.0
R13	ando-eutric cambisols	Shallow to moderately deep, well drained	16981	4.9
Um5	humic nitisols	Extremely deep, well drained	8598	2.5
Up3	chromo-luvic phaeozems	Moderately deep to deep, well drained	15162	4.4
Uu2	ando-luvic phaeozems	Deep to very deep, well drained	11330	3.3
F6	gleyic phaeozems	Deep, moderately well to imperfectly drained	563	0.2
H8	lithosols	Shallow, somewhat excessively drained	594	0.2
Up2	chromic vertisols	deep, imperfectly drained	15832	4.6

Figure 4.33d shows that the Sondu catchment area is dominated by two land slope categories; 0-8% and 8-30%. Higher slopes are mainly found on the eastern side of the catchment area and are mainly confined to the river valleys. The western side of the catchment also has higher slopes but are mainly confined next to the catchment boundary. The area between 35°0'0"E and 35°15'0"E has generally low slopes ranging from 0 to 8%. The slope distribution explains why majority of the soils found on the eastern side of longitude 35°15'0"E are generally well drained.

4.6.3.1 Kiptiget Sub-basin

Out of the seventeen sub-basins delineated by the model, Kiptiget, which is drained by River Kiptiget, was the sub-basin most representative for this study. Kiptiget sub-basin is over 83% forest covered (Figure 4.14) and therefore a good representation of the SWM forest, the largest block of the Mau forest complex system. Kiptiget River, which originates from the heart of the SWM forest, is gauged at the outlet of the sub-basin and is therefore ideal for comparison of the simulated and observed water yields from the sub-basin.

Kiptiget is an upstream sub-basin and a larger portion of the main drainage channel passes through the forest before reaching outlet. Water withdraws from the river channels, which requires more resources to quantify, are therefore much less compared to the RGSs which are located at points further downstream. Therefore, calibration and validation of the model and the subsequent water yield predictions were based on Kiptiget sub-basin which was taken to represent the larger Mau forest catchment area.

4.6.4. SWAT Model Default Simulations

Figure 4.35 shows a comparison of mean monthly water yields simulated before model calibration with observed values between 1971 and 1990 at the outlet of the Sondu catchment. The simulated water yields closely follow the observed patterns with a near perfect match for the peaks and troughs. The observed and simulated peaks fall in May with two minor peak yields in September and November (Figure 4.35a). A regression of simulated on observed mean monthly water yields (Figure 4.35b) revealed a strong linear relationship between the observed and model-simulated stream flows ($R^2 = 0.867$). The high coefficient of determination shows that about 87% of the variability in the simulated mean monthly water yields could be explained by the variability in the observed mean monthly water yields.

Simulated (*sim*) and observed (*ob*) mean monthly water yields were significantly correlated at $\alpha = 0.05$ level of significance. The computed t-statistic for the slope of the regression line $(t_{cal} = 3.69)$ was compared with the tabulated critical value $(t_{crtc} = 1.81)$ and found to be significant. This was an indication that SWAT model can suitably be applied to the Sondu catchment area.

However, the model substantially overestimates mean monthly water yields at the catchment's outlet in all the months of the year (Figure 4.35a). In order to bridge the gap between simulated and the observed values, it was found necessary to calibrate the model before it could be used to simulate future water yields. The calibration would tune the model to the dominant characteristics of the catchment and therefore make it more suitable for use in predicting future water yields in the basin.

Figure 4.36 shows the comparison of simulated and observed mean monthly water yields at Kiptiget station which is located at the immediate neighbourhood of the downstream side of South West Mau forest block. Just like the Sondu station there was good agreement between observed and simulated mean monthly water yield patterns. The observed values show two peak flows centred in May and September which are also captured by the model in addition to a third peak in November (Figure 4.36a)

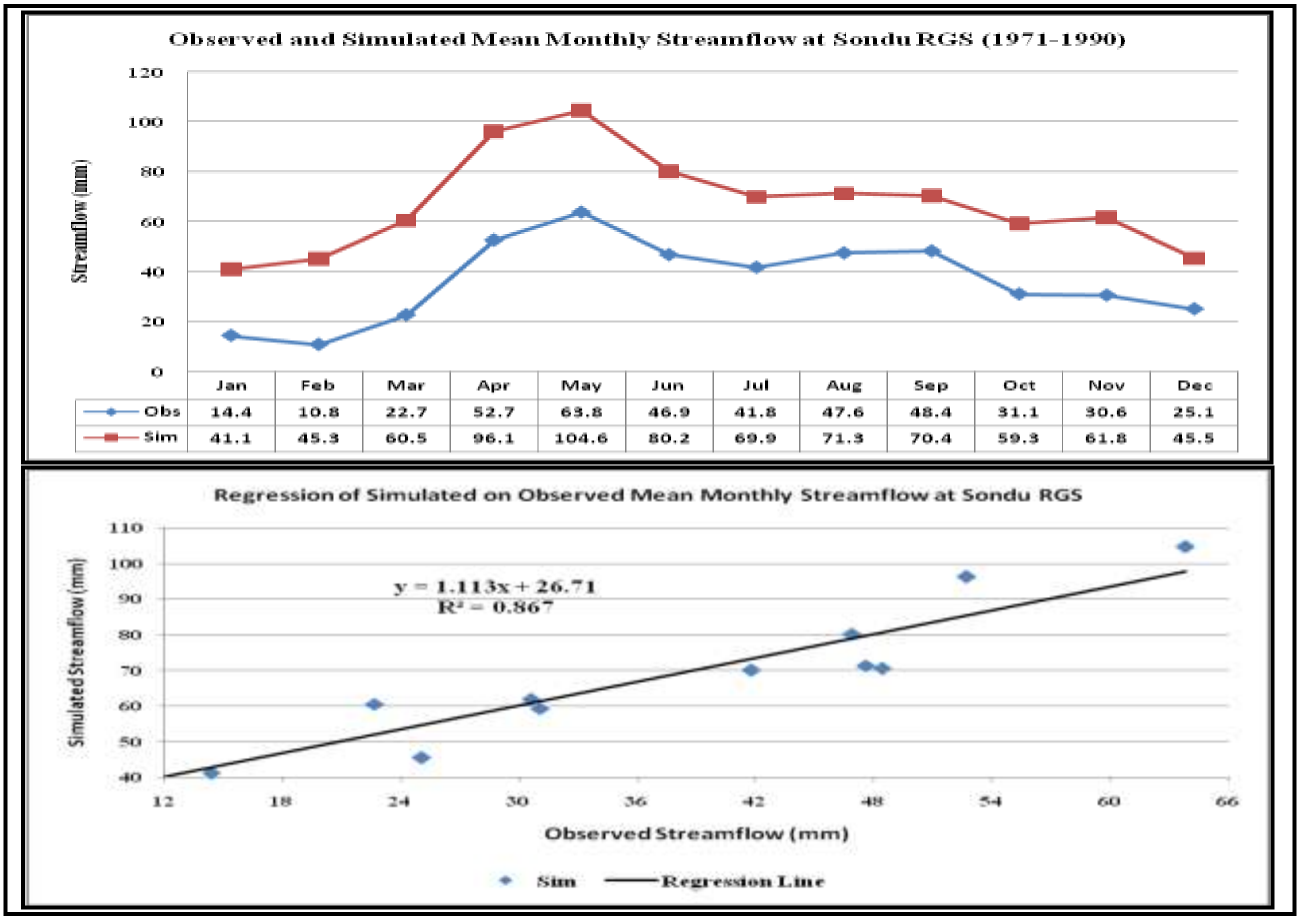

	Jan	Feb	Mar	Apr	May	Jun	Jul	Aug	Sep	Oct	Nov	Dec
Obs	14.4	10.8	22.7	52.7	63.8	46.9	41.8	47.6	48.4	31.1	30.6	25.1
Sim	41.1	45.3	60.5	96.1	104.6	80.2	69.9	71.3	70.4	59.3	61.8	45.5

Figure 4.35: Comparison of mean monthly simulated and corresponding observed water yields during default SWAT model simulation at Sondu RGS

The model substantially overestimated mean monthly water yields between November and May and underestimated between August and September at Kiptiget RGS. Regression of simulated on observed water yields revealed that there was a fairly strong linear relationship between the SWAT model-simulated and observed mean monthly water yields at Kiptiget RGS (Figure 4.36b) with $\left(R^2 = 0.606\right)$.

Simulated (sim) and observed (ob) mean monthly water yields at Kiptiget RGS were found to be significantly correlated at $\alpha = 0.05$ level of significance. The computed t-statistic for the slope of the regression line $\left(t_{cal} = 2.06\right)$ was compared with the tabulated critical value $\left(t_{crtc} = 1.81\right)$ and found to be significant. From the results of default model simulation at Sondu and Kiptiget RGSs, it was found necessary to calibrate the model in order to make it more reduce the uncertainty between the simulated and observed water yields.

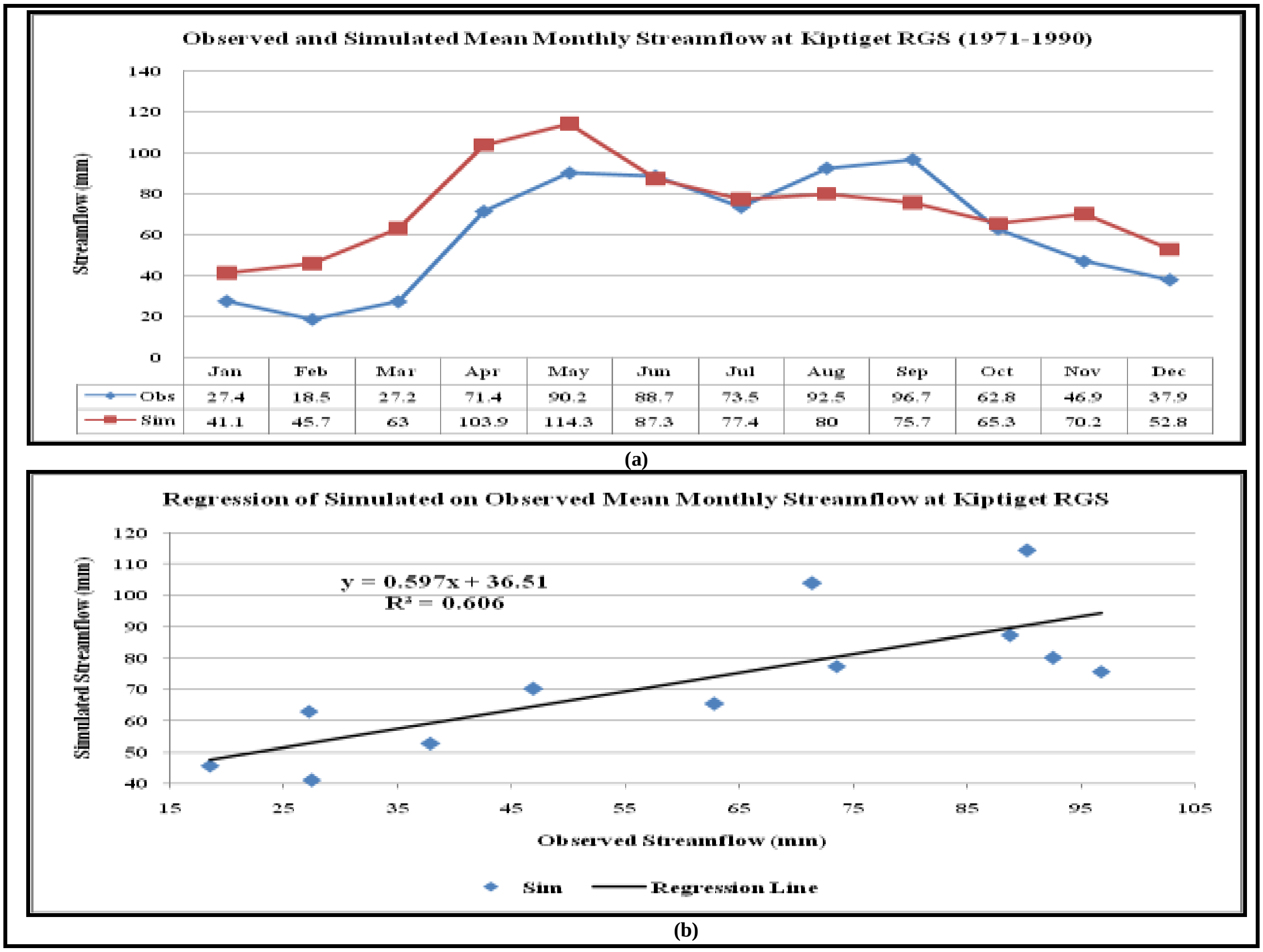

Figure 4.36: Comparison of mean monthly simulated and corresponding observed water yields during default SWAT model simulation at Kiptiget RGS

4.6.5 SWAT Model Calibration and Validation

The model calibration procedure involved sensitivity analysis to determine the most appropriate parameters to calibrate, followed by manual calibration where the ten most sensitive parameters (Table 4.30) were manually perturbed one at a time. The criteria used to calibrate the model were to minimise the difference between simulated and observed values by manually manipulating the sensitive parameters within the allowable ranges (Table 4.30).

4.6.5.1 Model Sensitivity Analysis

The sensitivity analysis ranked the hydrological input parameters that are responsive to streamflow generation in the Sondu catchment area in the order of decreasing sensitivity. Table 4.36 presents the first ten SWAT model hydrological input parameters that have notable impacts on the model output when they are changed. These results were obtained using the sensitivity analysis tool in the SWAT model and manual calibration for flow input parameters. The results of the sensitivity analysis indicated that the most important parameter for streamflow generation was the Soil Evaporation Coefficient (Esco) and was assigned a global rank 1.

Table 4.30: Results of sensitivity analysis (columns I and 2) and for calibration (column 5)

Rank	Code	Parameter Description	Default value	Calibrated value 1971-1990	Range
1	**Esco**	Soil evaporation compensation factor	0.95	0.008	0.01-1.0
2	**Cn2**	initial SCS runoff curve number for moisture condition II	70	60.88	±25%
3	**Sol_Z**	Depth from soil surface to to the bottom of layer (mm)	120	default	
4	**Canmx**	Maximum canopy storage (mm)	1	100	1-100
5	**Blai**	Maximum potential leaf area index		default	
6	**Revapmn**	Threshold water level in shallow aquifer for “revap” to occur (mm)	1	0.725	0-500
7	**Sol_Awc**	Available soil water capacity (mm H_2O/mm soil)	0.17	0.269	0-1.0
8	**Ch_K2**	Effective hydraulic conductivity in the main channel (mm/hr)	0	0.36	0-5
9	**Alpha_Bf**	Baseflow recession factor (days)	0.025	0.022	0.1-1.0
10	**GW_Revap**	Delay time for aquifer recharge (days)	0.02	0.2	0.02-0.2

Other parameters that are assigned global ranks between 2 and 6 and categorised as important are; SCS runoff curve number for moisture condition II (CN2), the depth from soil surface to the bottom of layer (Sol_Z), maximum canopy storage (Canmx), maximum potential leaf area index (Blai), and threshold water level in shallow aquifer for ‘revap’ to occur (Revapmn). The other parameters are less important and are assigned global ranks between 7 and 42 (Glavan and Pintar, 2012; Ndomba *et al*, 2008**)**

4.6.5.2 Model Calibration and Validation

In this section, the results of model calibration and validation are presented in both graphical and tabular form. Graphical results include a time series and an annual cycle together with their respective regression lines of monthly water yields during calibration and validation periods (Figures 4.37, 4.38, 4.39. and 4.40). Graphical comparison between SWAT model-simulated and observed water yields after model calibration for six years (1982 to 1987) and validation using an independent data set of three years (1988 to 1990) indicated that there was good agreement between model-simulated and observed water yields (Figures 4.37 and 4.39).

Figure 4.37 presents a comparison between time series of model simulated and corresponding observed monthly between 1982 and 1987 (calibration) and 1988 and 1990 (validation). Graphical comparison of simulated and observed water yields at the Kiptiget RGS shows that the model simulates water yields from the landscapes of Kiptiget sub-catchment in ways that capture the dynamics of the watershed response fairly well (Figures 4.37). Except in 1986 and 1987, the model slightly over estimates the peak yield values during calibration period (Figure 4.37a). However, the flow patterns are fairly well captured by the model especially in 1982 and 1983 in some cases overestimating by up to about 9% (Table 4.31). During the validation period, the model also captured the patterns fairly well but with a slight over-estimation of about 7% (Table 4.31).

Figure 4.38 presents the regression of simulated on corresponding observed monthly water yields during calibration (1982-1987) and validation (1988-1990) periods respectively at Kiptiget RGS. Monthly simulated and observed water yields at Kiptiget RGS were found to be significantly correlated at $\alpha = 0.05$ level of significance in both calibration and validation periods. The computed t-statistics for the slopes of the regression lines during calibration $(t_{cal} = 9.55)$ and validation $(t_{cal} = 4.61)$ periods were compared with the tabulated critical value $(t_{crtc} = 1.81)$ and found to be significant. The percentage variation in simulated water yields that could be explained by variations in the observed water yields was about 80% and 55% during calibration and validation periods respectively. Based on these results, it was concluded that the model could be used to predict water yields on a monthly basis subject to adequate calibration.

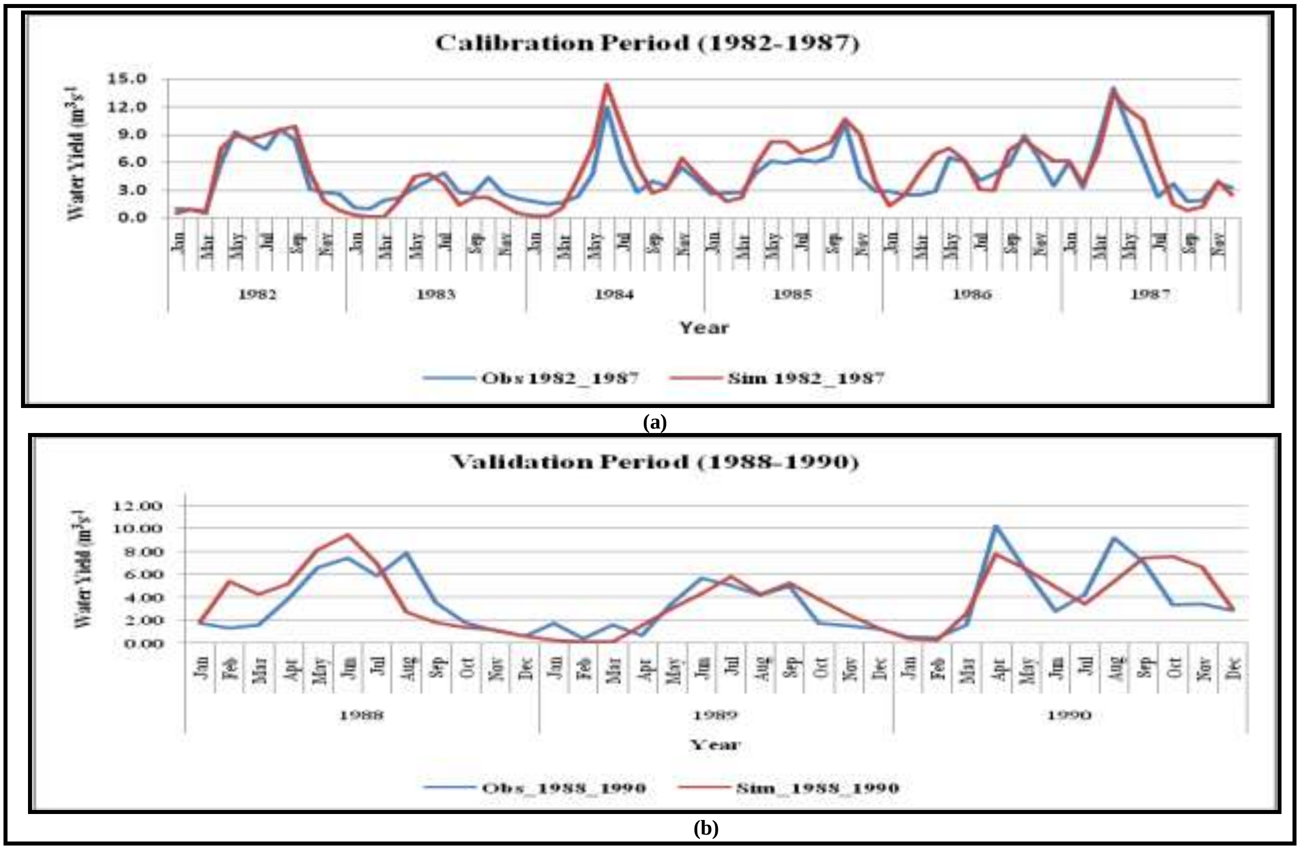

Figure 4.37: Time series of observed and model-simulated monthly water yields (m^3s^{-1}) during calibration and validation at Kiptiget RGS

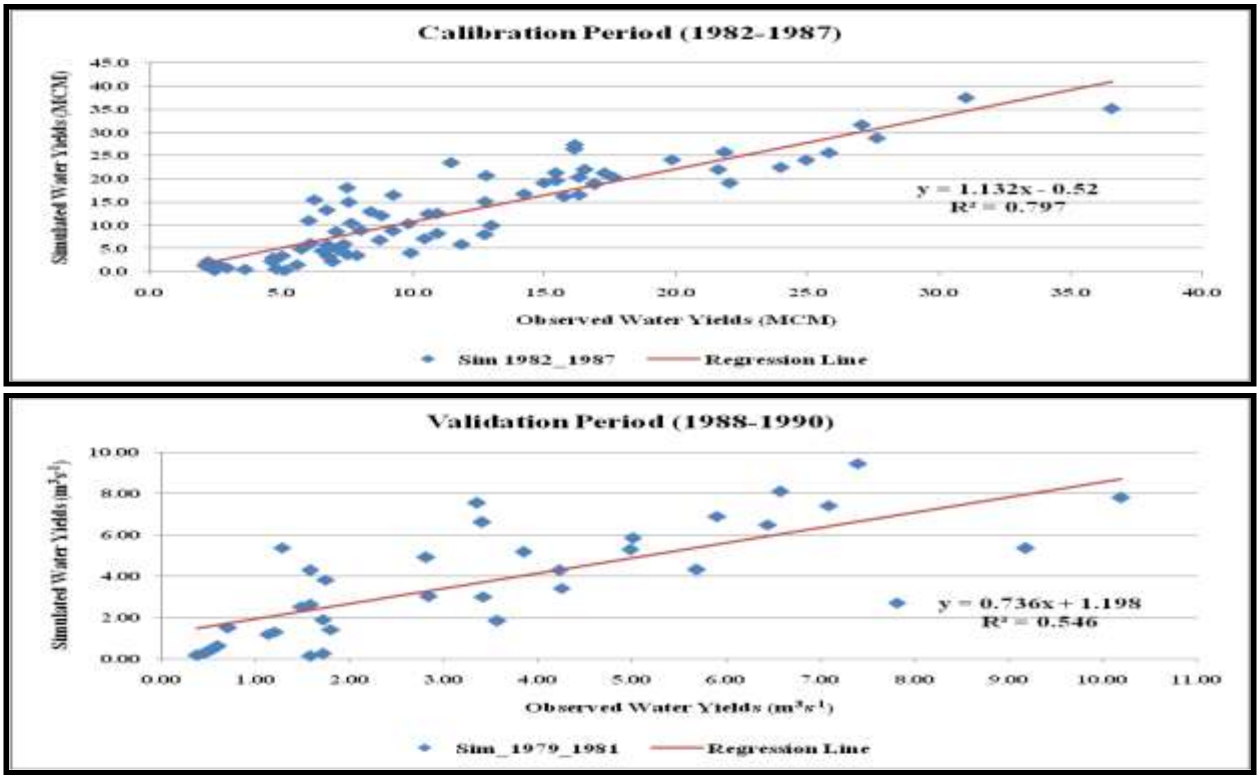

Figure 4.38: Regression of SWAT model-simulated on observed monthly water yields (MCM) at Kiptiget RGS during (a) calibration and (b) validation

Figure 4.39 presents a comparison of hydrographs of simulated and observed mean monthly water yields averaged calibration (1982-1987) and validation (1988-1990) periods respectively. It is evident from the figure that during calibration, the model captures the monthly distribution of water yields from the catchment quite well but overestimates between April and July. During validation period monthly distribution of water yields are fairly well captured but the model generally overestimates water yields in all the months except August.

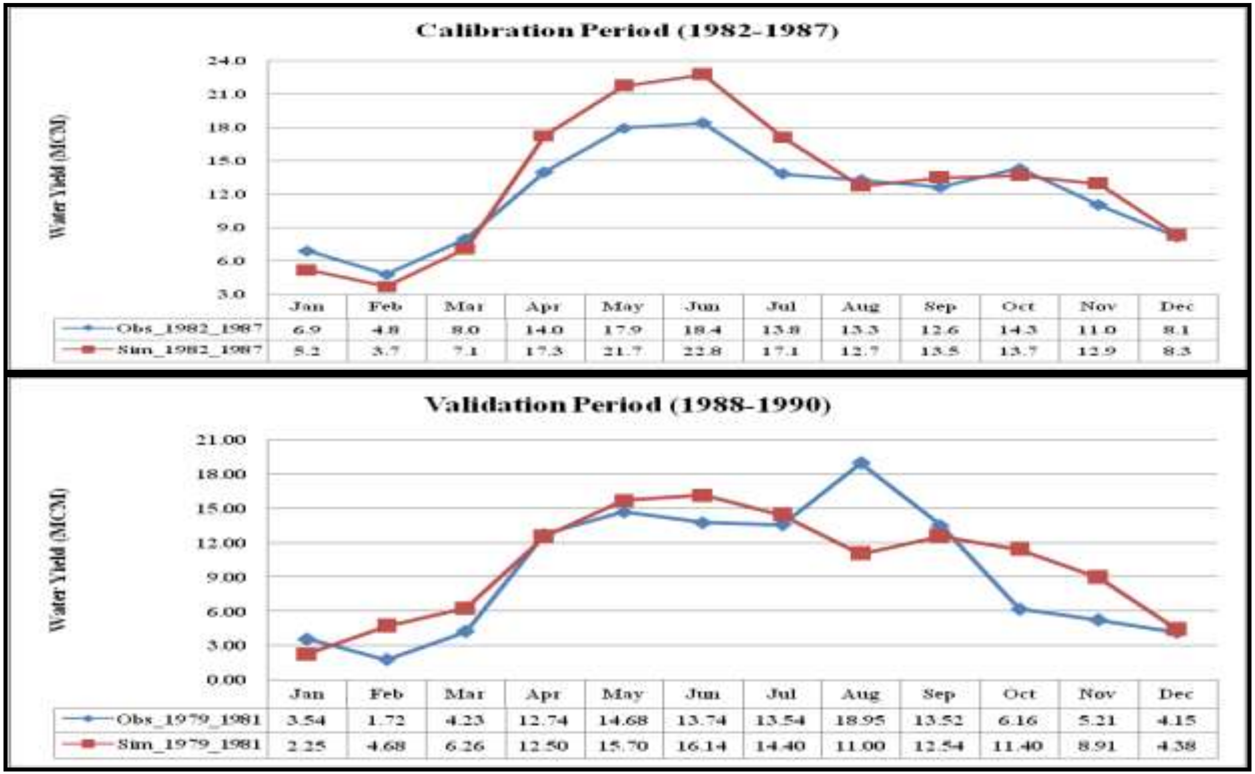

Figure 4.39: Hydrographs of observed and SWAT model-simulated mean monthly water yields (MCM) during calibration and validation at Kiptiget RGS

Figure 4.40 presents regression of simulated mean monthly on corresponding observed water yields averaged over the calibration (1982-1987) and validation (1988-1990) periods respectively. Simulated mean monthly and observed water yields at Kiptiget RGS were found to be significantly correlated at $\alpha = 0.05$ level of significance in both calibration and validation periods. The computed t-statistics for the slopes of the regression lines during calibration $\left(t_{cal} = 43.2\right)$ and validation $\left(t_{cal} = 28.3\right)$ periods were compared with the tabulated critical value $\left(t_{crtc} = 1.81\right)$ and found to be significant. The percentage variation in mean monthly simulated water yields that could be explained by variations in the observed water yields was about 95% and 66% during calibration and validation periods respectively. Hence based these results these results the model is recommended for use in predicting monthly water yields in the catchment area subject to adequate calibration.

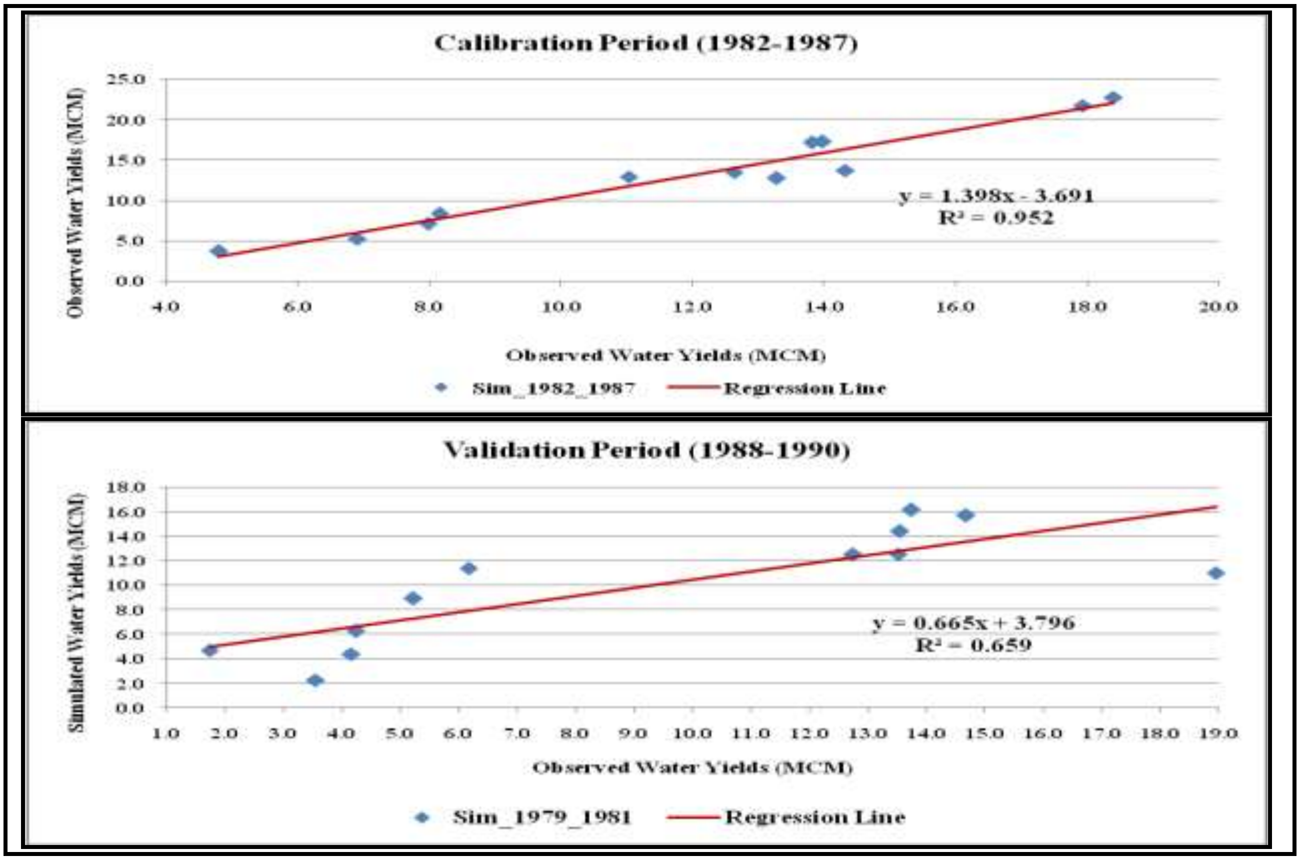

Figure 4.40: Regression of mean monthly SWAT model-simulated on observed water yields (MCM) during calibration and validation at Kiptiget RGS

The goodness of fit of the SWAT model was quantified using four statistics: coefficient of determination (R^2), percentage bias (PBIAS), Nash-Sutcliffe efficiency (NSE), and the ratio of root mean square error to the standard deviation of observed values (RSR) (Table 4.31). The statistics indicated that SWAT model performed generally well in the Sondu catchment area. There was good correlation between observed and model-simulated values during calibration and validation periods. The coefficient of determination R^2, during calibration and validation periods surpassed the threshold of acceptability ($R^2 > 0.5$) as proposed by Moriasi *et al*, (2007). The R-squared values were $R^2 = 0.797$ and $R^2 = 0.952$ for monthly and mean monthly water yields during calibration and $R^2 = 0.546$ and $R^2 = 0.659$ for monthly and mean monthly water yields during validation (Figures 4.38 and 4.40).

The percentage bias (PBIAS) in both calibration and validation periods shows very good performance $(PBIAS < 10\%)$ of the model in the simulation of average magnitudes of water yields. The simulated magnitudes of water yields fall within the "very good" band of model performance criteria (PBIAS $\leq \pm 10\%$) as suggested by Moriasi et al, (2007) in both calibration and validation periods respectively. In the simulation of trends and residual variations as exemplified by NSE and RSR, the model performance was good during calibration since the yield values fall within the "good" band of model performance criteria $(0.54 < NSE \leq 0.65)$and$(0.6 < RSR \leq 0.7)$ and satisfactory during validation period since the yield values fall within the "satisfactory" band of model performance criteria $(0.5 < NSE \leq 0.54)$ and $(0.6 < RSR \leq 0.7)$ as suggested by Moriasi et al (2007) and as shown in Table 4.31.

The simulated average monthly water yields during the calibration and validation periods were 13.0 MCM and 10.0 MCM with standard deviations of 9.4 MCM and 6.9 MCM respectively while the corresponding observed values were 11.9 MCM and 9.4 MCM with standard deviations of 7.4 MCM and 7.0 MCM respectively (Table 4.31). Even though the model does not capture all the peak flows, the model performance is acceptable since the hydrological processes and streamflow dynamics were realistically simulated based on the results in Table 4.31.

Based on the varied performance rating supported by the different performance indices that range from very good (PBIAS) to satisfactory (NSE and RSR) during calibration, and from very good (PBIAS) to acceptable (NSE and RSR) performance during validation periods, the overall model performance in the basin was rated satisfactory. Results of these hydrological analyses can therefore be used to provide essential information for water resources management and planning in the catchment.

Table 4.31: Statistics of observed and SWAT model-simulated monthly water yields during calibration and validation

Period	**Observed (MCM)**		**Simulated (MCM)**		**Evaluation Statistics**			
	Mean	Stdev	Mean	Stdev	R^2	PBIAS	NSE	RSR
Calibration (1982-1987)	11.93	7.41	13.0	9.40	0.80	-8.94	0.63	0.60
Validation (1988-1990)	9.35	7.00	10.01	6.93	0.55	-7.43	0.48	0.72

4.6.6 Model Simulations and Projections

Results of the calibrated model simulations (1971-2010) and projections (2001-2050) of water yields are presented in this section. The results are presented in three parts: i. simulated water yields under changing landuse scenarios, ii. Projected water yields under climate change, and iii. Projected water yields under changing landuse scenarios.

4.6.6.1 Simulated Water Yields under Deforestation Scenario (1971-2010)

Figure 4.41 presents mean monthly and annual water yields at Kiptiget RGS averaged over the period 1971-2010 under deforestation scenario while holding climate of the area constant at the baseline level. It is evident from the figure that under the deforestation scenarios and using the baseline climate to drive the SWAT model, water yields Kiptiget RGS indicated an increasing trend the forest cover decreased from an all time high of about 84% in 1973 (LU73) to a low of about 62% in 2010 (LU10).

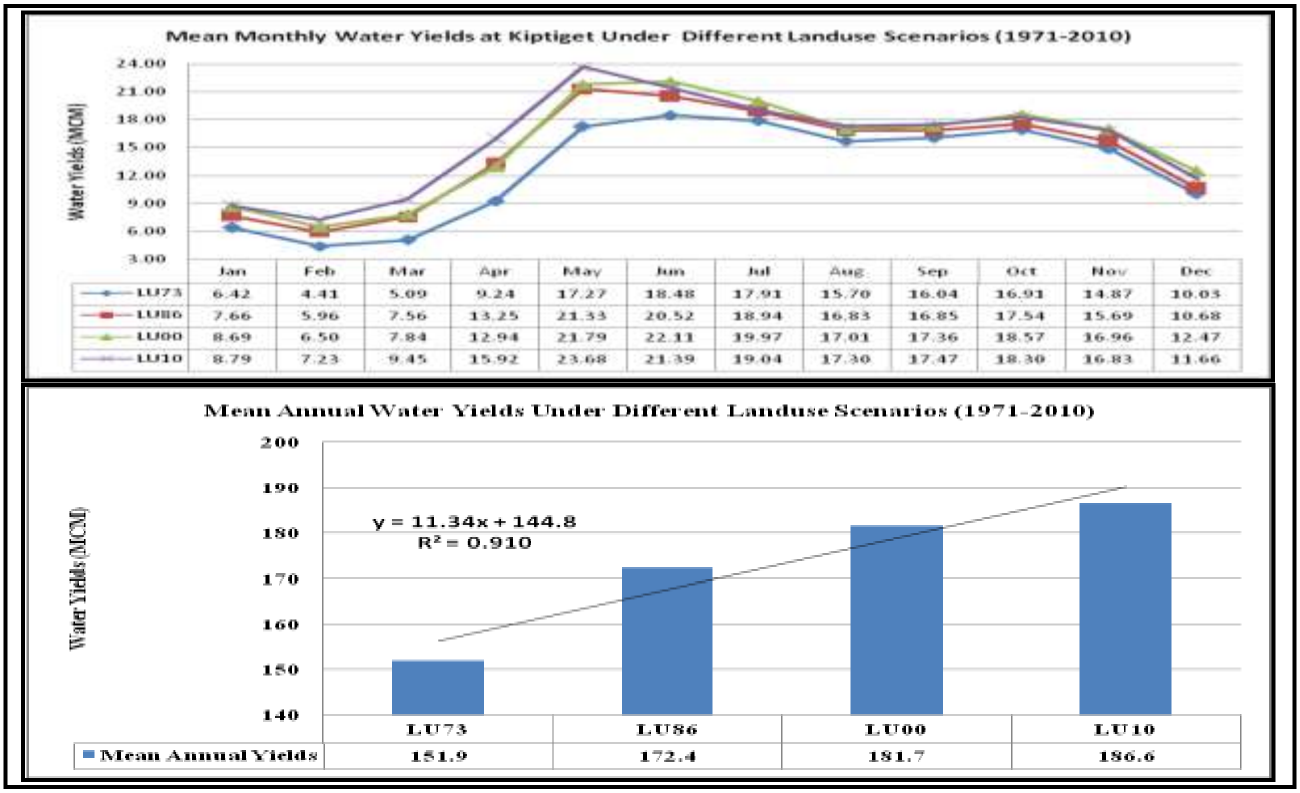

Mean Monthly Water Yields at Kiptiget Under Different Landuse Scenarios (1971-2010)

	Jan	Feb	Mar	Apr	May	Jun	Jul	Aug	Sep	Oct	Nov	Dec
LU73	6.42	4.41	5.09	9.24	17.27	18.48	17.91	15.70	16.04	16.91	14.87	10.03
LU86	7.66	5.96	7.56	13.25	21.33	20.52	18.94	16.83	16.85	17.54	15.69	10.68
LU00	8.69	6.50	7.84	12.94	21.79	22.11	19.97	17.01	17.36	18.57	16.96	12.47
LU10	8.79	7.23	9.45	15.92	23.68	21.39	19.04	17.30	17.47	18.30	16.83	11.66

Mean Annual Water Yields Under Different Landuse Scenarios (1971-2010)

	LU73	LU86	LU00	LU10
■ Mean Annual Yields	151.9	172.4	181.7	186.6

Figure 4.41: Simulated mean monthly and annual water yields under deforestation scenarios using the baseline climate

The possible cause of this observation is that reduction in the extent of forest cover reduces infiltration rates in the sub-basin which leads to more water from rainfall events reaching the river system as surface runoff. In such circumstances the water in the rivers would not be sustainable in the long run since the groundwater flow component would be reduced. Since the region experiences rainfall in all the months of the year, the catchment can sustain the flow in the river system under reduced forest cover each month and subsequently each year (Figures 4.41).

In the last four decades the forest cover in the sub-basin has been decreasing at a rate of about 8% every decade (Figure 4.14). In the same period, the mean annual water yields have been increasing at a rate of about 11 MCM every decade (Figure 4.41). Hence deforestation alone would lead to higher water yields from the sub-basin if climate were to remain at the 1970s level.

4.6.6.2 Projected Water Yields under Climate Change

Results of projected water yields using different climate scenarios to drive the SWAT model under the baseline landuse scenario (LU73) are presented in this section. Figure 4.42 shows a comparison of the baseline (1961-1990) and the projections for (2001-2030 and 2021-2050) 30-year average monthly and annual water yields under SRES A2 scenario at Kiptiget RGS. In the figure, WYLD1970s, WYLD2010s, and WYLD2030s stand for the 30-year average monthly water yields in the periods 1961-1990, 2001-2030, and 2021-2050 respectively.

Comparison between the baseline and projected water yields indicates that projected mean monthly water yields would experience increasing trends between October and June but decreasing trends between July and September(Figure 4.42). The months currently experiencing relatively low water yields (December, January, February, and March) would experience relatively higher water yields while those currently experiencing relatively high water yields (August and September) would experience relatively lower water yields under this kind of a scenario. This is consistent with the projected changes in monthly rainfall under SRES A2 scenario (Figure 4.28).

From the 1970s through 2010s to 2030s, the mean annual water yields averaged over the thirty-year periods: 1961-1990, 2001-2030, and 2021-2030, would increase at a rate of about 105 MCM every 30 years under this kind of a scenario (Figure 4.42). This increase in the annual water yields can be attributed to climate change as it is supported by increased rainfall in the same periods projected by PRECIS climate model (Figure 4.27). Hence climate change would lead to higher water yields from the sub-basin if land cover characteristics were to remain at the 1973 level.

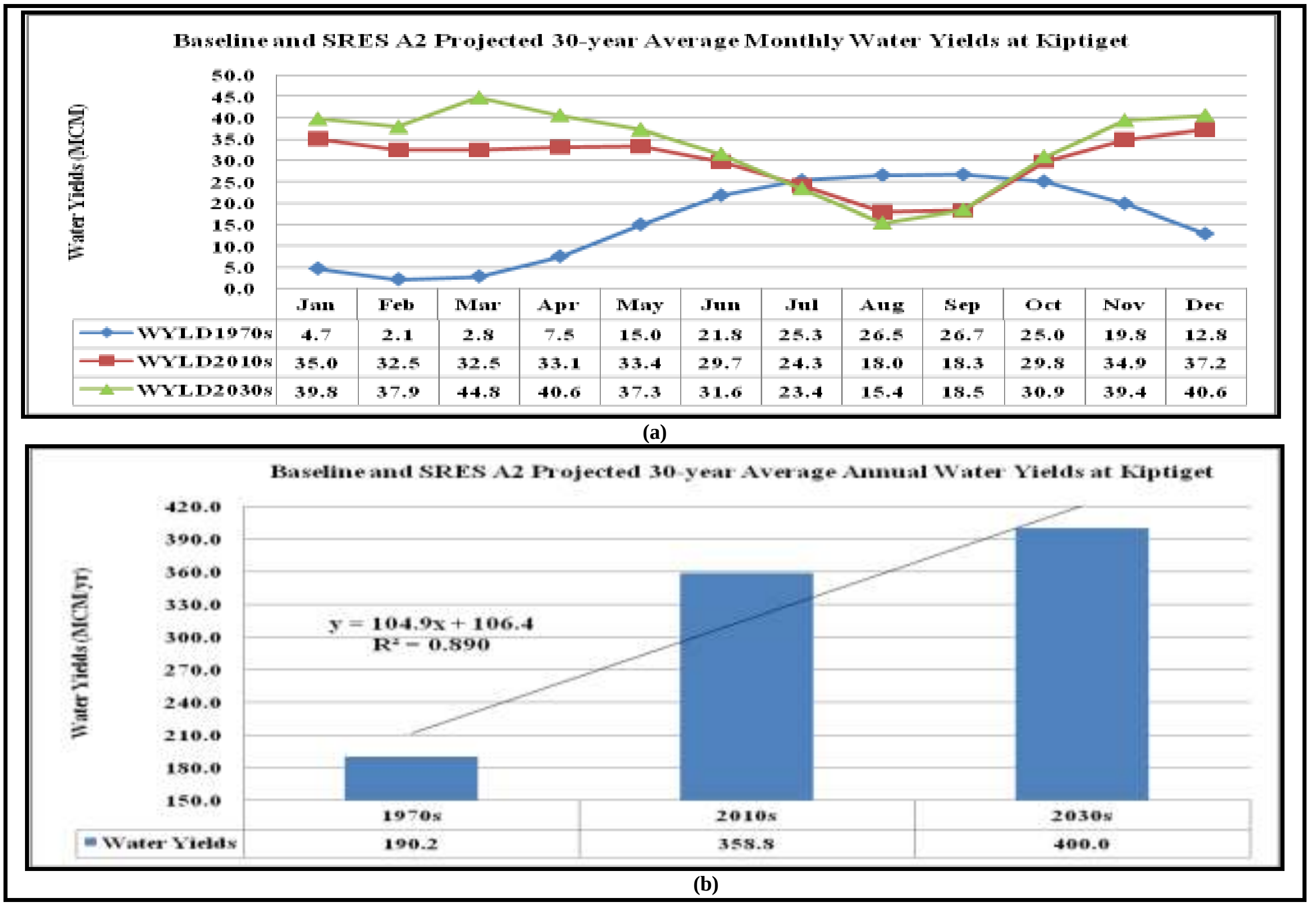

(a)

(b)

Figure 4.42: Baseline and SRES A2 scenario projected mean monthly and annual water yields under the (LU73) scenario

4.6.6.3 Projected Water Yields under Deforestation Scenarios

In this section, monthly and annual water yields under changing landuse scenarios for the periods 2001-2030 and 2021-2050 are presented. Since the projections under deforestation scenarios are under different climate regimes from that of the baseline, any changes in the in the projected water yields are attributed to both climate change and deforestation.

4.6.6.4 Projected Water Yields (2001-2030)

Figure 4.43 presents projected 30-year mean monthly and annual water yields at Kiptiget RGS averaged over the period 2011-2030. The mean monthly hydrograph for the period 2001-2030 shows an increasing trend in mean monthly water yields between September and April while between May and August the trend is decreasing under the four landuse scenarios (LU73, LU86, LU00, and LU10). While consecutive mean monthly changes in water yields are progressively noticeable from LU73 through to LU00 landuse scenarios, changes from LU00 to LU10 landuse scenarios are not obvious. This can be explained by the recovery of forest cover between mid 2000s and 2010 (Figure 4.13).

The 30-year mean annual water yields from the sub-basin in the same period indicate a decreasing trend of about 0.70 MCM per year as deforestation increases. This will lead to less annual water yields from the catchment in future. The possible explanation for this is that the higher temperatures of 2010s and 2030s (Figures 4.24 and 4.25) will lead to increased rates of evaporation. A ground surface that is under natural forest conditions experiences less evaporation, improved recharge of ground water and hence ensures more water is available during prolonged dry spells (Hynes, 1975).

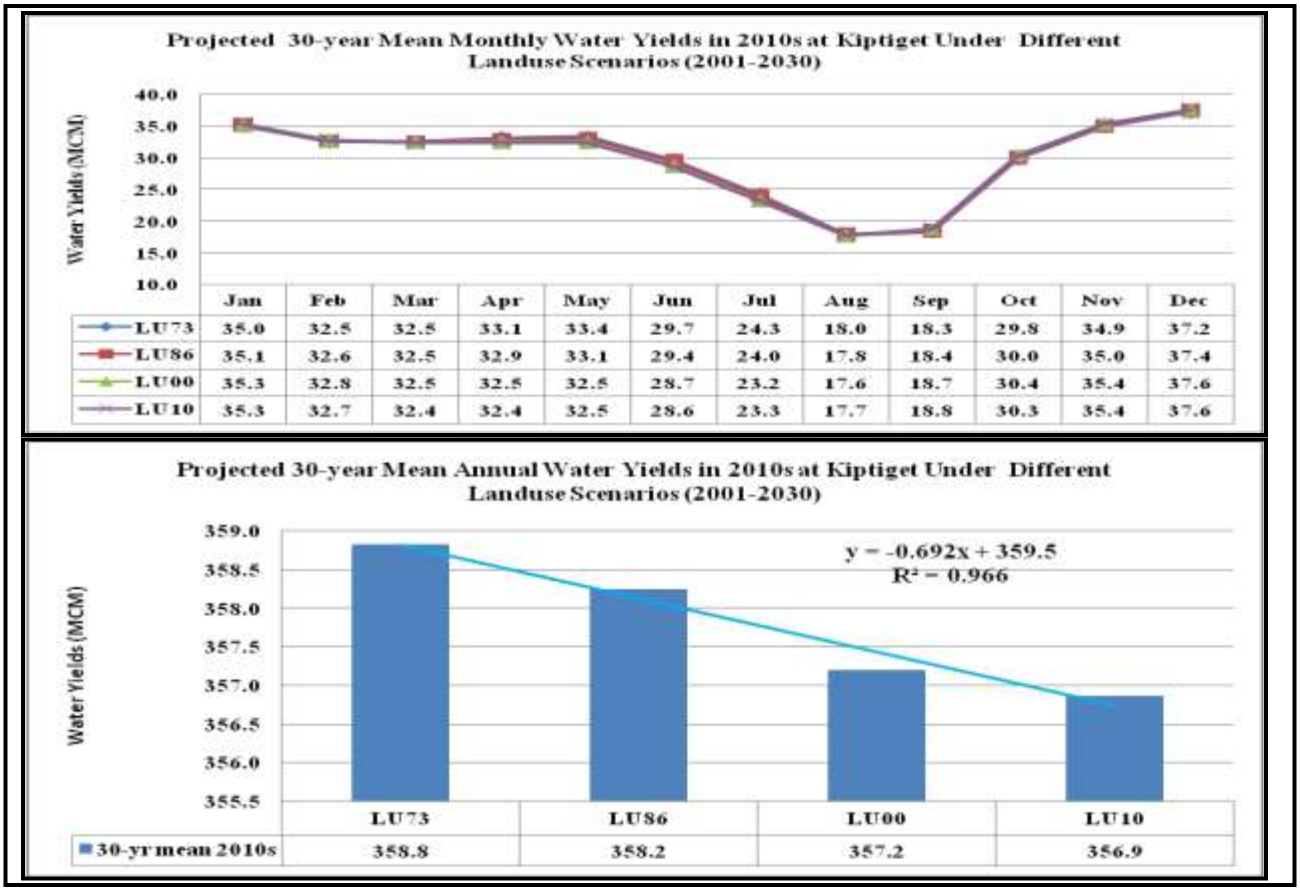

	Jan	Feb	Mar	Apr	May	Jun	Jul	Aug	Sep	Oct	Nov	Dec
LU73	35.0	32.5	32.5	33.1	33.4	29.7	24.3	18.0	18.3	29.8	34.9	37.2
LU86	35.1	32.6	32.5	32.9	33.1	29.4	24.0	17.8	18.4	30.0	35.0	37.4
LU00	35.3	32.8	32.5	32.5	32.5	28.7	23.2	17.6	18.7	30.4	35.4	37.6
LU10	35.3	32.7	32.4	32.4	32.5	28.6	23.3	17.7	18.8	30.3	35.4	37.6

	LU73	LU86	LU00	LU10
■ 30-yr mean 2010s	358.8	358.2	357.2	356.9

Figure 4.43: Projected 30-year mean monthly and annual water yields under climate change and deforestation (2010s)

4.6.6.5 Projected Water Yields (2021-2050)

Figure 4.43 presents projected 30-year mean monthly and annual water yields at Kiptiget RGS averaged over the period 2021-2050. It is evident from the figure that by the 2050, mean monthly water yields will be higher than those of 2010 but will follow similar patterns to the 2010s projected yields. The 30-year mean annual water yields averaged over period 2021-2050 show a decreasing trend of about 0.71 MCM per year as the extent of deforestation increases. There is, however a slight improvement in the mean annual water yields simulated under LU10 landuse scenario from that of 2001-2030.

The possible explanation for this improvement is that in the decade between 2000 and 2010 the government and other stake holders spearheaded a spirited campaign to conserve the Mau Forest complex which resulted in the slowing down of the rate of deforestation in this sub-basin. This means that the current efforts towards conservation of the Mau forest complex are expected to bear fruits between 2021 and 2050 (Figure 4.13).

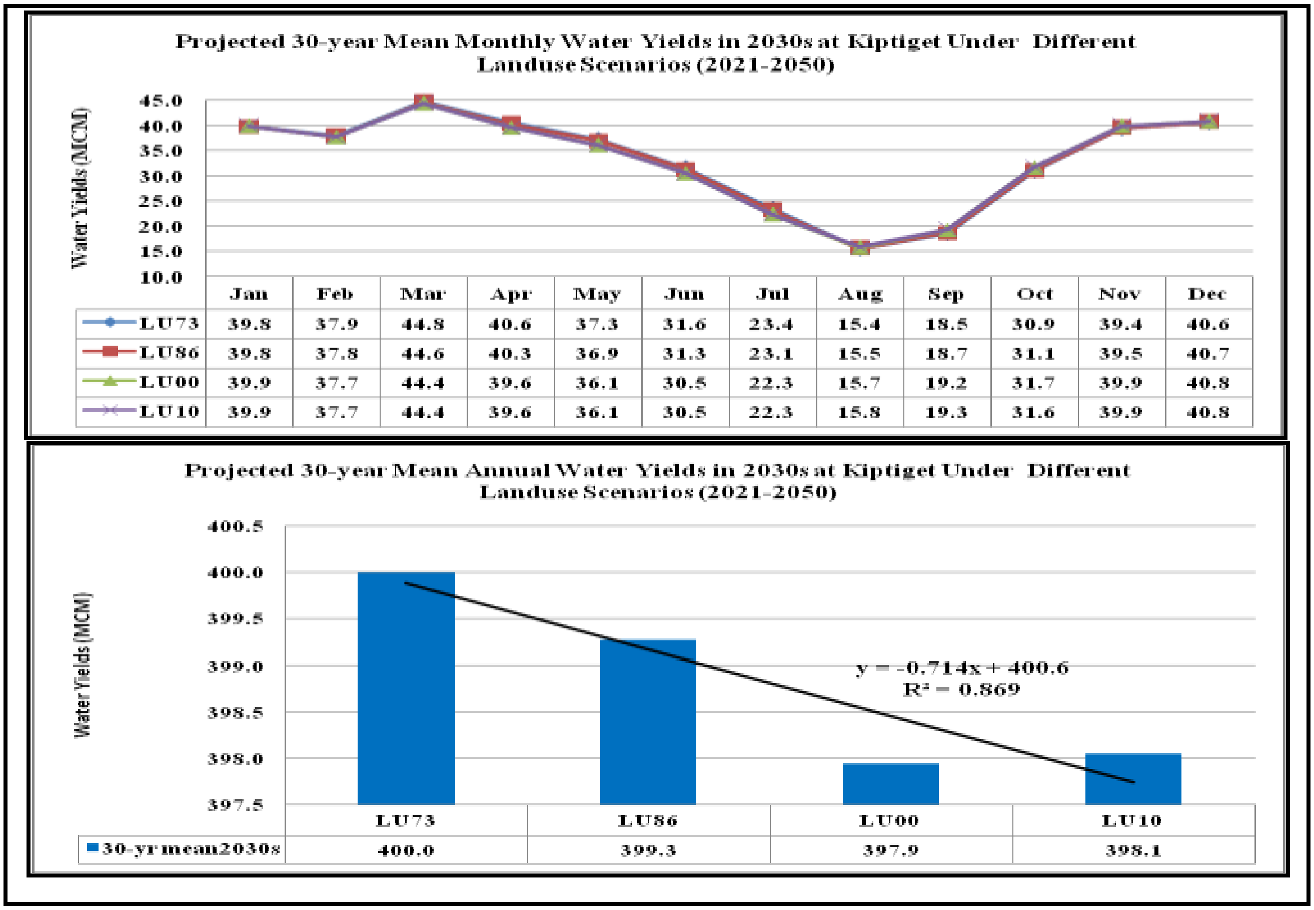

	Jan	Feb	Mar	Apr	May	Jun	Jul	Aug	Sep	Oct	Nov	Dec
LU73	39.8	37.9	44.8	40.6	37.3	31.6	23.4	15.4	18.5	30.9	39.4	40.6
LU86	39.8	37.8	44.6	40.3	36.9	31.3	23.1	15.5	18.7	31.1	39.5	40.7
LU00	39.9	37.7	44.4	39.6	36.1	30.5	22.3	15.7	19.2	31.7	39.9	40.8
LU10	39.9	37.7	44.4	39.6	36.1	30.5	22.3	15.8	19.3	31.6	39.9	40.8

	LU73	LU86	LU00	LU10
30-yr mean2030s	400.0	399.3	397.9	398.1

Figure 4.44: Projected 30-year mean monthly and annual water yields under climate change and deforestation (2030s)

4.7 Impacts on Water Yields

Results of analyses of impacts of climate change and deforestation on water yields are presented in this section. The results are presented in three parts: (i) Impacts of climate change on water yields under the baseline landuse scenario, (ii) Impacts of deforestation (changing landuse scenarios) on water yields under the baseline climate, and (iii) Impacts of climate change and deforestation on water yields.

4.7.1 Impacts of Climate Change on Water Yields

Results of impacts of climate change under the baseline landuse scenario (LU73) on water yields from the Mau forest complex indicate that on average, the catchment would be expected to yield more water annually by about 89% and 110% of the baseline yields in 2010s and 2030s respectively assuming that the baseline landuse scenario were to be maintained (Figure 4.45). Annual water yields under climate change only would increase at a rate of about 55% of the baseline yields every 30 years as shown by the equation of the trend line. The R-squared ($R^2 = 0.890$) shows that 89% of water yield information under climate change alone is explained by the independent (time) variable. Since the ground cover, as represented by LU73, was assumed not to have changed on the basis of sustained catchment conservation policy, the observed changes in simulated annual water yields from the sub-basin were therefore attributed to climate change. Hence climate change under the SRES A2 scenario would result in more water in the basin over time.

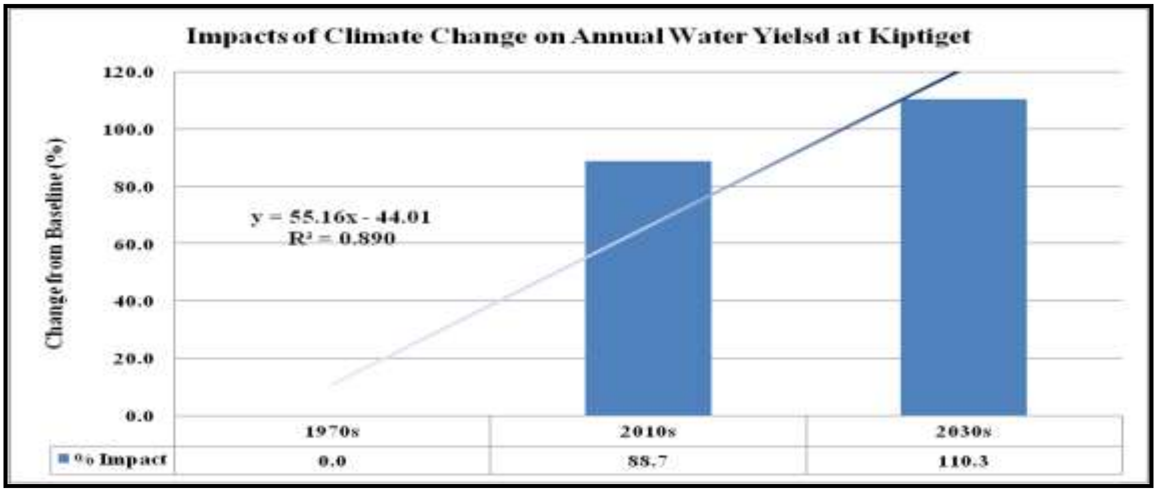

Figure 4.45: 30-year average annual percentage changes in water yields from the baseline under LU73 landuse scenario

Figure 4.46 shows a regression of 30-year mean annual water yields (%) on rainfall (%) changes at Kiptiget RGS. The figure shows that changes in rainfall between the baseline period, 2010s and 2030s under the baseline forest cover scenario will significantly influence water yields from this catchment.

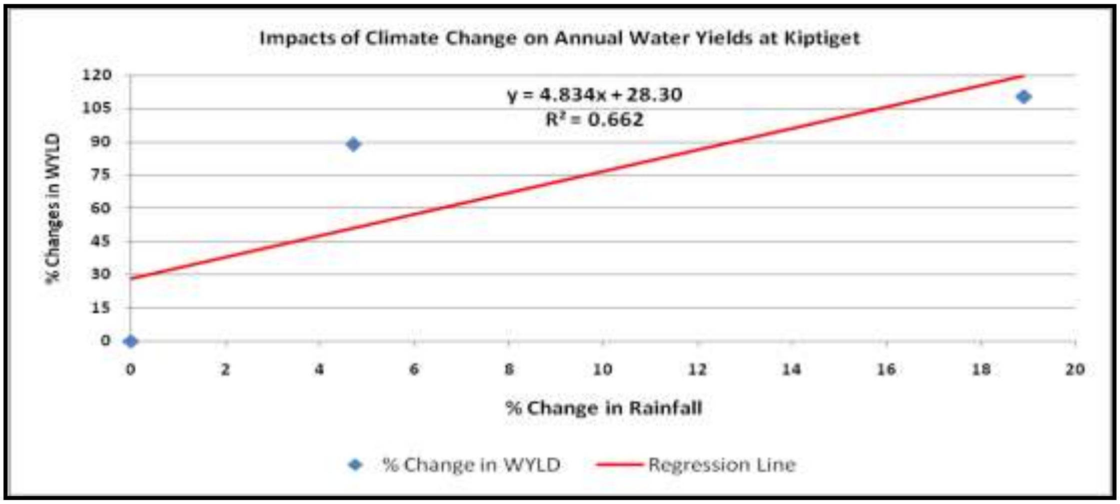

Figure 4.46: Regression of 30-year mean annual percentage changes in water yields on rainfall under the LU73 landuse scenario

This is supported by the regression slope (4.8%), which was found to be significant at $\alpha = 0.05$ level of significance. The computed t-statistic ($t_{cal} = 6.83$) was compared to the tabulated critical value ($t_{crtc} = 6.31$) and the slope was declared significant ($t_{cal} > t_{crtc}$). The coefficient of determination ($R^2 = 0.66$) indicates that over 66% of the variability in projected water yield under climate change only would be explained by the variability in rainfall. Hence climate change under the 1973 landuse scenario would lead to an increase in water yields from the basin at a rate of about 4.8 percentage points for every 1 percentage point change in rainfall.

4.7.2 Impacts of Deforestation on Water Yields

Monthly and annual water yields were simulated for the period 1971-2010 under different landuse scenarios (LU73, LU86, LU00, and LU10), which represent progressive deforestation using observed baseline climate data (1961-1990). Since the climate was assumed to remain constant at the baseline level, any changes in simulated water yields were attributed to deforestation of the watershed.

Simulated mean monthly and annual water yields under deforestation scenarios were analysed and compared to the baseline landuse scenario (LU73) simulation. Percentage changes in water yields from the baseline (100%) were evaluated and the results given in Figures 4.47. It was noted that there was a positive change in mean monthly water yields in all the months ranging from about 3.6% to about 86% of the baseline scenario values (Figure 4.47a). The annual water yields also indicated positive changes of between 13.5% and 22.9% from the baseline landuse scenario (LU73) to the 2010 landuse scenario (LU10) as shown in Figure 4.47b.

Since climate was assumed to remain constant at the baseline level during the simulations, and the only variable was landuse scenario, the observed changes in monthly and annual water yields were attributed to deforestation which altered the hydrological response of the catchment to rainfall. Since scenario LU73 represents the highest and scenario LU10 the lowest percentage forest cover in the sub-basin and in the Mau forest complex (Table 4.9 and Figure 4.13), it was concluded that assuming that climate does not change, the impact of deforestation would be to increase the water yields at a rate of about 7.5% of the baseline yields to between 14% and 23% for annual water yields while monthly yields would increase by between 4% and 86%. The R - squared computed for this scenario ($R^2 = 0.910$) shows that 91% of variability in the simulated annual water yields could be explained by variations in deforestation, the independent variable in this case.

However, increases in water yields with deforestation may not sustainable in the long run since the reduced rates of infiltration will deny the catchment the much needed subsurface and groundwater flow components that sustain water yields during the dry seasons. Further there are indications that the climate of the region has been changing since the 1970s (Figure 4.4) and therefore the assumption that the climate remains constant at the baseline level may not apply.

Regression of changes in mean annual water yields on different forest cover scenarios to determine the change in annual water yields for a unit change in the forest cover (Figure 4.48) indicated a high dependence of annual water yields on the extent of the forest cover. The slope of the regression equation as shown in the figure represents the rate of change of water yields with forest cover from the sub-basin. A unit percentage change in forest coverage changes the annual water yields by about 0.88% and about 87% of variability in simulated water yields from this sub-basin can be explained by deforestation ($R^2 = 0.869$). The negative relationship between annual water yields and deforestation (Figure 4.47) can be attributed to the fact that reduction in forest cover tends to reduce the rates of infiltration and thus allow more water from effective rainfall to reach the stream channels annually via direct runoff.

The test of significance at $\alpha = 0.05$ level revealed that the slope of the regression line was not significantly different from zero. The computed t-statistic $(t_{cal} = 1.525)$ was less than the critical value $(t_{crtc} = 2.92)$. It was therefore concluded that although there was an increasing trend in simulated annual water yields, the influence of the rate of deforestation on annual water yields was not statistically significant.

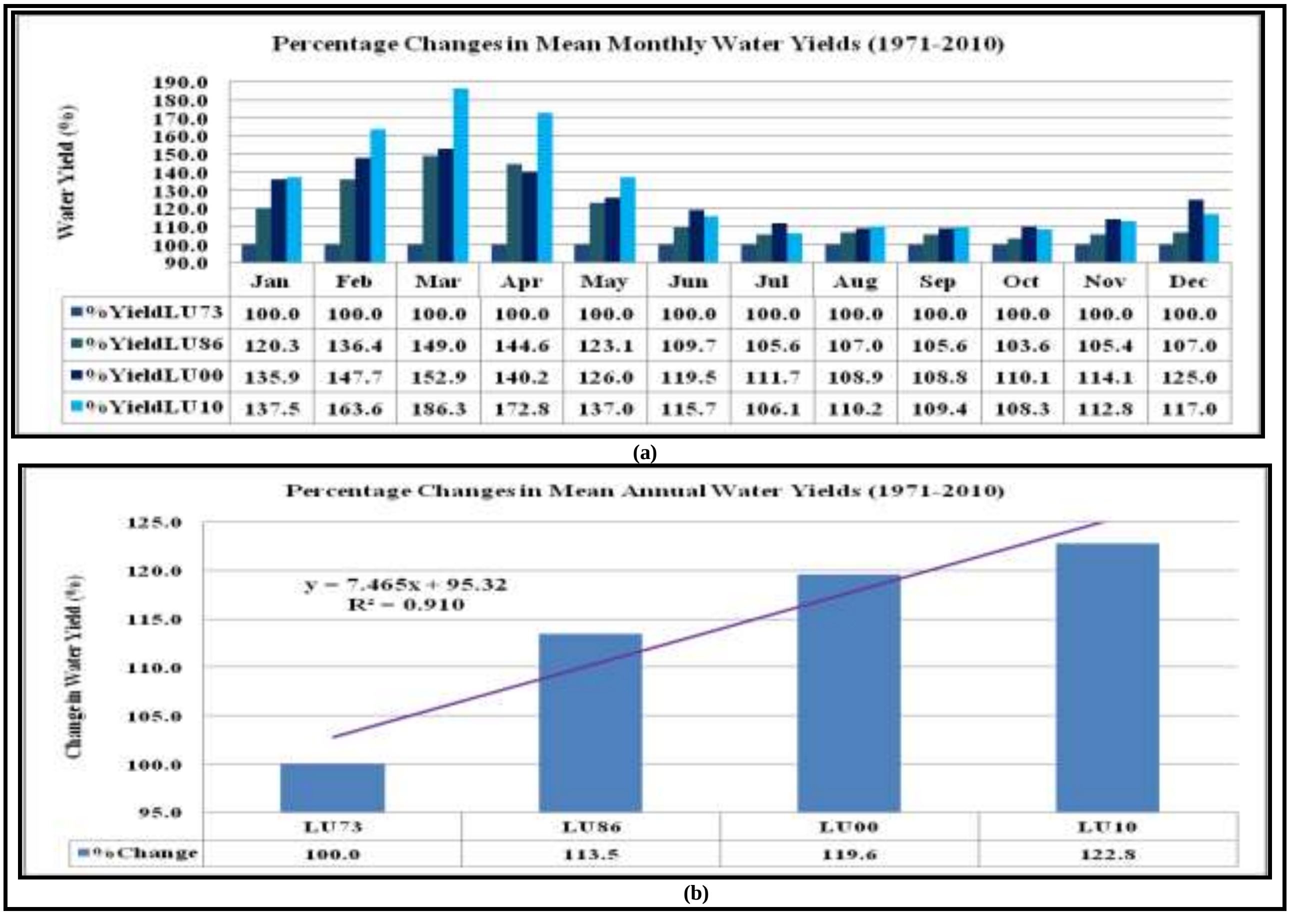

(a)

(b)

Figure 4.47: Percentage changes in mean monthly and annual water yields with deforestation under the baseline climate

Table 4.32 which was used to determine the relationship between water yields and deforestation (Figure 4.48) shows the changes in forest cover and the corresponding changes in mean annual water yields at Kiptiget RGS. For purposes of this study water yields under the LU73 landuse scenario were assumed to be at 100%. Subsequent landuse scenarios resulted in water yields higher than 100% indicating that deforestation under the baseline climate leads to higher annual water yields.

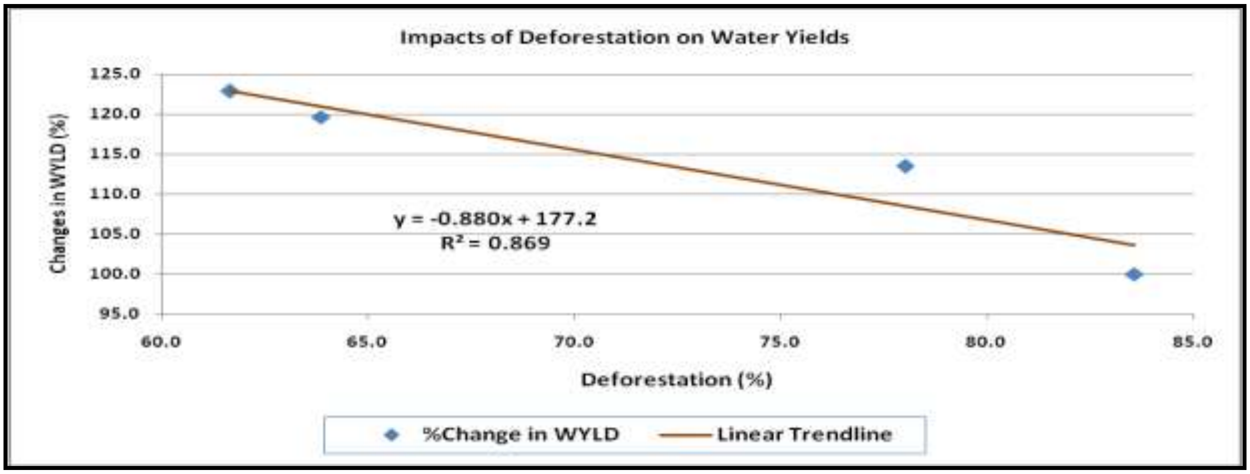

Figure 4.48: Regression of changes in annual water yields on deforestation under the baseline climate

Table 4.32: Percentage forest cover under different landuse scenarios and the corresponding mean annual water yields

Landuse	**LU73**	**LU86**	**LU00**	**LU10**
Deforestation (%)	83.6	78.0	63.9	61.7
Water Yields (%)	100	113.5	119.6	122.8

4.7.3 Impacts of Climate Change and Deforestation on Water Yields

Projected water yields in 2010s and 2030s under changing landuse scenarios (LU73, LU86, LU00, and LU10) were analysed and compared to the baseline (1970s) simulations under similar landuse scenarios (Figure 4.49a). Percentage changes from the baseline values under similar landuse scenarios were evaluated to determine the impacts of climate change and deforestation on water yields (Figure 4.49b). From the comparison of annual water yields (Figure 4.49a) it is evident that annual water yields are progressively increasing from the baseline climate regime (1970s) through 2010s to 2030s projected climate regimes under all the landuse scenarios. However, while water yields show an increasing trend from the baseline landuse scenario (LU73) through to the LU10 scenario, decreasing trends are evident under projected climate regimes in 2010s and 2030s (Figure 4.49a).

In general, it was observed that 30-year annual average water yields increased with increased rainfalls in 2010s and 2030s (Figure 4.49a and Table 4.33). However, proportional changes in annual water yields were much higher than those of rainfall in both 2010s and 2030s. The changes in annual rainfall ranged between 51% and 64% compared to between 215% and 264% of annual water yields in 2010s and 2030s respectively (Table 4.33). This was an indication that other factors such as antecedent soil moisture conditions and ground water storage, which are functions of ground vegetation cover, could have influenced water yields from the sub-basin.

Table 4.33: Percentage changes in 30-year average annual rainfall and water yields in 2010s and 2030s

Changes in annual rainfall (%)		**Changes in annual water yields in 2010s (%)**				**Changes in annual water yields in 2030s (%)**			
2010s	**2030s**	**LU73**	**LU86**	**LU00**	**LU10**	**LU73**	**LU86**	**LU00**	**LU10**
50.7	63.9	215.2	215.1	214.8	214.4	265.0	264.4	263.3	263.4

Projected changes in 30-year annual average water yields from the baseline landuse scenario (LU73) through to the LU10 scenario show progressively decreasing trends at rates of about 15% and 16% per decade in 2010s and 2030s respectively under all the landuse scenarios (Figure 4.49b). It is therefore evident that though climate change from the 1970s baseline through 2010s to 2030s will result in higher water yields from the catchment, the potential yields will decrease with deforestation from about 136% to about 91% and from about 163% to about 113% of the baseline yields in 2010s and 2030s respectively. This is supported by the high values of R-squared ($R^2 > 0.88$) in both 2010s and 2030s (Figure 4.49b) showing that over 88% of water yields information is explained by variations in forest cover under climate change.

It is evident from Figure 4.49a that while annual water yields progressively increase with deforestation from 152.4 MCM/yr (LU73) to 187.4 MCM/yr (LU10) in the 1970s, the trend is different in the 2010s and 2030s. In the 2010s, annual water yields progressively decrease with deforestation from 358.8 MCM/yr (LU73) to 356.7 MCM/yr (LU10). In the 2030s, annual water yields progressively decrease with deforestation from 400.0 MCM/yr (LU73) to 397.9 MCM/yr (LU00). This translates into a potential loss of between 0.6 MCM/yr and 1.9 MCM/yr and 0.7 MCM/yr and 2.1 MCM/yr in 2010s and 2030s respectively. This is about 0.2% and 0.5% in 2010s and 2030s respectively. Hence climate change and deforestation will lead to potential loss in water yields from the forest complex.

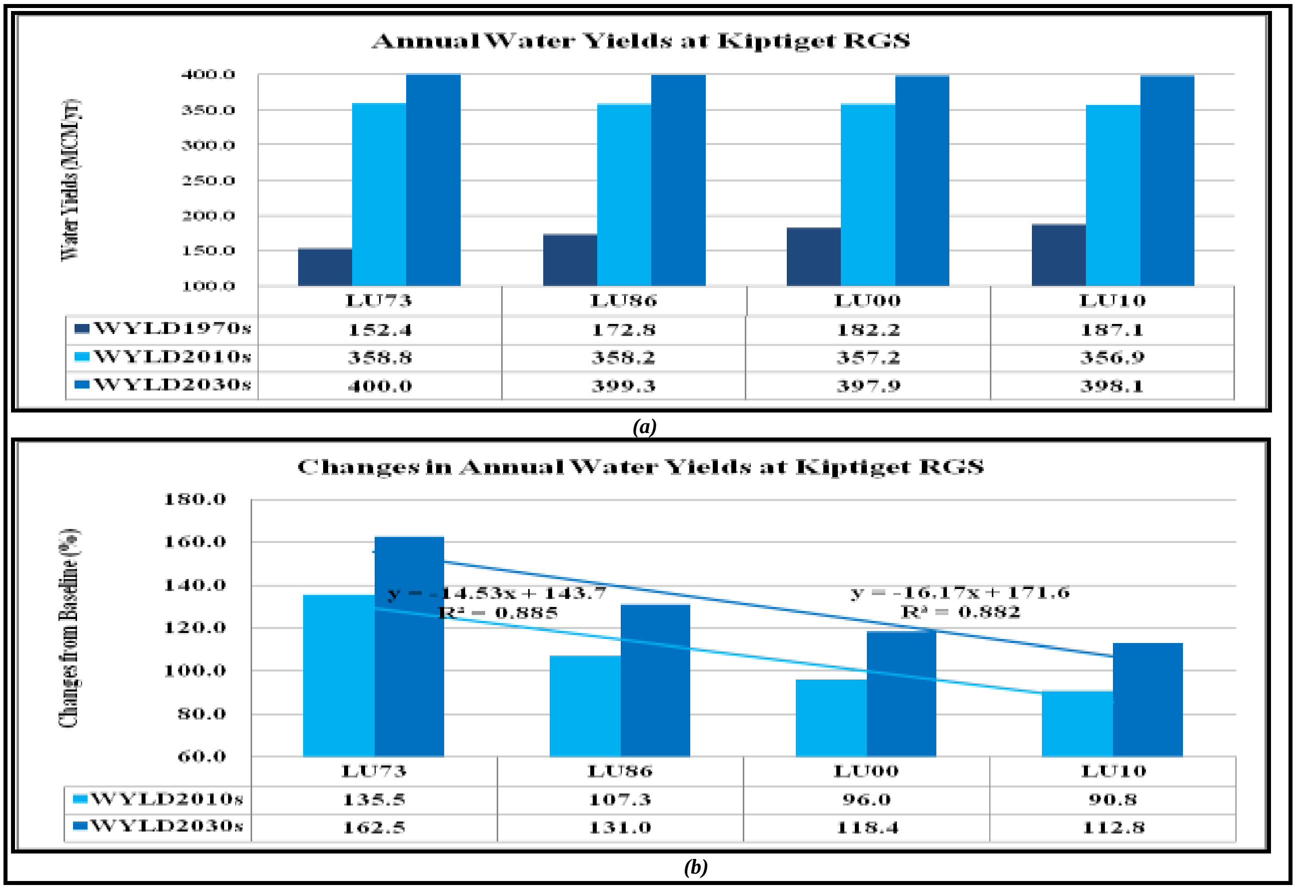

Figure 4.49: Mean annual 30-year average (a) baseline and projected water yields (MCM/yr), and (b) projected percentage changes in water yields under climate change and deforestation

Regression of changes in 30-year mean annual water yields on different forest cover scenarios in 2010s and 2030s (Figure 4.50) indicated a high dependence of annual water yields on deforestation as supported by the slopes of the regression equations which represent the rate of change of water yields with deforestation. The test of significance at $\alpha = 0.05$ level revealed that under climate change the slopes of the regression lines were significantly different from zero. The computed t-statistics (t_{cal}) were beyond the critical value of $t_{crt} = 2.92$ (Table 4.34). The high values of R-squared ($R^2 > 0.97$) indicate that under climate change, over 97% of the variability in simulated water yields is explained by deforestation rates. It was therefore concluded from the results that annual water yields are significantly dependent on climate change and the rate of deforestation.

Table 4.34: Linear equations, coefficients of determination (R^2) and the calculated student's t-statistic (t_{cal})

Climate Regime	Regression equation	R^2	computed t-statistic for slope (t_{cal})	Remarks
1970s	$y = -0.880x + 177.2$	0.869	1.525	slope not significant
2010s	$y = 2.339x - 96.69$	0.993	4.051	significant slope
2030s	$y = 2.294x - 94.16$	0.978	3.976	significant slope

It was noted that a unit percentage increase in deforestation will reduce the annual water yields by about 2.34% and 2.30% in 2010s and 2030s respectively. The slightly lower rate of decrease in annual water yields in 2030s than that of 2010s was attributed to forest recovery between 2000 and 2010 indicating that if the Mau forest complex were to recover to the 1973 baseline level (LU73) potential water yields from this water tower would be higher than currently projected. The reduction in annual water yields with deforestation under climate change can be attributed to the fact that deforestation exposes more of the ground surface to the vagaries of weather under the changed climate leading to enhanced erosion and loss of water to the atmosphere through evaporation.

Table 4.35, which was used to determine the relationship between water yields and climate change under deforestation (Figure 4.50), shows the changes in forest cover and the corresponding changes in mean annual water yields from the baseline in 2010s and 2030s. For purposes of this study water yields under the LU73 landuse scenario were assumed to be at 100%. Subsequent landuse scenarios under climate change in 2010s and 2030s resulted in water yields that are lower than the 100% baseline yields.

Hence it was concluded from the results of impacts assessment that impacts of deforestation on water yields under climate change will be a reduction in the potential annual water yields from the catchment by between 28% and 45% in 2010s and between 31% and 50% in 2030s (Figure 4.49b). It is therefore important to rehabilitate and conserve the forests in the catchment in order to ensure sustainable availability of water in this area as supported by the slight improvement in water yields under LU10 landuse scenario in 2030s (Table 4.35)

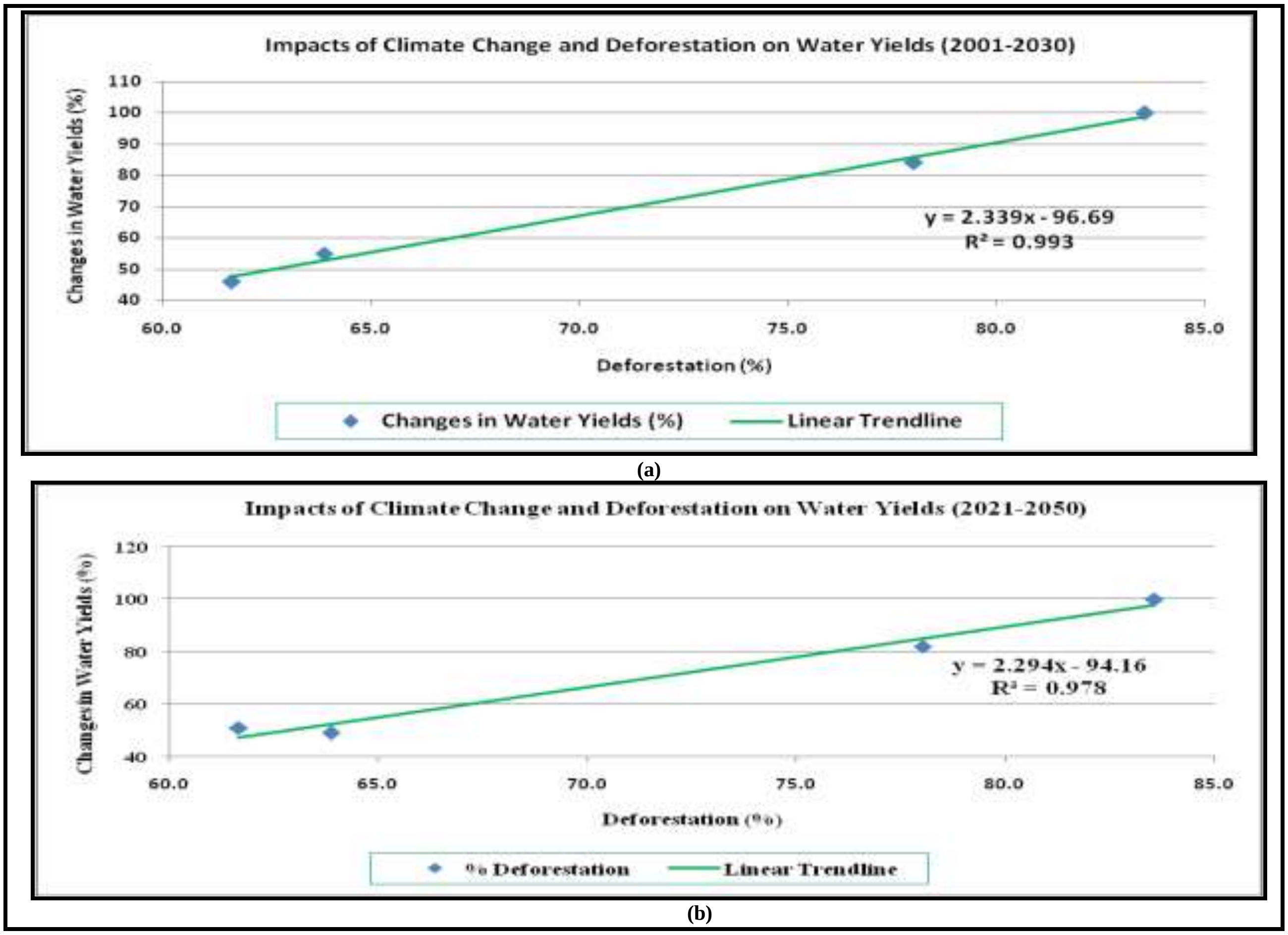

Figure 4.50: Regression of percentage changes in annual water yields on deforestation under climate change and deforestation over Kiptiget sub-basin in (a) 2010s and (b) 2030s

Table 4.35: Percentage deforestation under different landuse scenarios and the corresponding mean annual water yields

Landuse	LU73	LU86	LU00	LU10
Deforestation (%)	83.6	78.0	63.9	61.7
2010s Water Yields (%)	100	84	55	46
2030s Water Yields (%)	100	82	49	51

CHAPTER 5

CONCLUSIONS AND RECOMMENDATIONS

5.1 Conclusions

The study has shown that between 1961 and 2010 the climate of the basin has been changing. Days and nights have become warmer by about 0.5°C and 0.4°C respectively. Over the same period monthly rainfall patterns indicated a shifting tendency where the relatively dry DJF and SON seasons became relatively wetter by about 7.5% and 9.2% respectively by 1990s while the relatively wet MAM and JJA became relatively drier by about 2.2% and 4.5% respectively by 1990s. In the same period, annual rainfall indicated a slightly increasing trend. It was also established from the observed landuse patterns that indeed Mau forest complex experienced deforestation ranging from about 18% to 25% between 1973 and 2010 with the peak deforestation rate witnessed in the early years of 2000s but the trend has since been reversed. It was therefore concluded from the results of the observed data that besides being deforested, the Mau forest catchments have become warmer and wetter during this period with stream flows showing decreasing trends.

Projected temperatures and rainfall in 2010s and 2030s show increasing trends thus indicating that the climate of the area is changing. The annual average temperatures and rainfall are projected to change from the baseline values by about 2.7°C and 4.7% respectively by 2030 and by 4.7°C and 18.9% respectively by 2050. The area is therefore projected to progressively become warmer and wetter. This will impact on the water yielding properties of the area. Monthly rainfall patterns are projected to shift with the relatively dry seasons becoming relatively wetter and the relatively wet seasons becoming relatively drier. This affirms results of a similar study in Nzoia River basin by Githui (2008).

From the SWAT simulation results between 1961 and 1990, it was concluded that holding the climate constant at the baseline level (1970s), deforestation alone would tend to increase the amount of surface water flowing in the rivers due to increased water yields from the basin. This is however, contrary to the observation suggesting that another factor, such as climate change, could be influencing water yields from the basin. From the results of simulations under the baseline landuse scenario (LU73) but under changing climates, it was concluded that in the absence of deforestation, the amount of water flowing in the rivers would progressively increase from about

201 MCM/yr in the 1970s through 305 MCM/yr in the 2010s to 420 MCM/yr in the 2030s as a result of increased surface water yields from the basin. But the basin has been deforested since 1973. This may therefore not be viable and suggested a need to take both deforestation and climate change into consideration. From the results of simulated water yields in the 1970s and 2010s, under deforestation scenarios, it was concluded that climate change coupled with deforestation of Mau forest complex has contributed to the dwindling water levels in rivers emanating from this water tower. Results of the projected water yields in 2030s under similar conditions indicate that the trend is projected to continue to 2030 and beyond if nothing is done to curb deforestation of this critical water tower. Rehabilitation of the Mau forest complex would therefore lead to increased water yields as it was noted between 2000 and 2010.

The overall impacts of climate change and deforestation on water yields from the Mau forest complex is a reduction in the potential annual water yields by between 0.2% and 0.5%. Continued deforestation of this critical water tower will therefore result in less water than expected coming from this important water tower since climate change is a reality

This study has provided useful insights into the sensitivity of Mau forest complex water towers to deforestation and climate change. The results obtained in this study will contribute to the scientific community’s understanding of the impacts of climate change and deforestation on water resources in Lake Victoria south catchment area in general and Sondu River catchment area in particular. Further, as a result of this study, a great amount of Hydrometeorological data in and around the area of study spanning the period 1961-2050 has been acquired. This forms significant contribution researchers wishing to advance the science of Hydrometeology. The results of this study could also be used to provide information to inform policy in the strategic planning and management of water resources in Lake Victoria south catchment area as set out in the National water Master Plan 2030 in various sectors such as agriculture, hydropower generation, and water supply.

5.2 Recommendations

Arising from the results of this study and the challenges encountered therein, the author wishes to make the following general recommendations to policy makers and researchers in the water resources sector.

5.2.1 Recommendations to Policy Makers

i. Results of this study have provided useful methods and products that can broadly be used to inform medium and long term planning of water resources management in this part of Kenya. They should therefore be put in the mainstream economic development strategies and be integrated in the implementation of the National Water Master Plan 2030.
ii. Operational use of SWAT model should be encouraged by those working in the water sector particularly in the design of flood control and water supply structures.
iii. Results of this study have shown that a combination of both climate change and deforestation leads reduced water yields in this part of Kenya. Efforts must therefore be made to conserve this critical forest complex.

5.3.2 Recommendations to Researchers

i. PRECIS has shown itself to have potential to provide fine resolution data needed for climate change impacts studies. Performance of PRECIS RCM at finer resolutions should be explored further given that river basin scale studies require much finer resolutions.
ii. SWAT hydrologic model has shown its potential in modelling water yields in this area under different climate and forest cover scenarios. Performance of other hydrologic models on impacts studies should also be explored.

REFERENCES

Abbaspour, K.C., M. Framarzi, S. Ghasemi, H. Yang (2009): Assessing the Impact of Climate Change on Water Resources in Iran. *Water Resour. Res., 45, W10434, doi: 10.1029/2008WR007615*

Ahrens C. D., (2009): Meteorology Today, an introduction to weather, climate and the environment, Ninth Edition, *Brooks/Cole 10 Davis Drive, Belmont CA94002, USA, 439-499*

Akhtar, M., Ahmad N, and Booij M.J, (2008): The impact of climate change on the water Resources of Hindukush-Karakorum-Himalaya region under different glacier coverage scenarios, *Journal of Hydrology, 355: 148-163*

Akhtar, M., N. Ahmad, and M. J. Booij (2009): Use of regional climate model simulations as input for hydrological models for the Hindukush-Karakorum-Himalaya region. *Hydrol. Earth Syst. Sci., 13, 1075–1089*

Albinus, M.P., Makalle, J. Obando and Y. Bamataze (2008): Effects of Land use practices on livelihoods in the transboundary sub catchments of the Lake Victoria basin, *African Journal of Environmental Science and Technology, Vol. 2 (10), 309 – 317, October, 2008*

Arnold, J.G., R. Srinivasan, R. S. Muttiah, J. R. Williams (1998): Large Area Hydrologic Modelling and Assessment-Part 1: Model Development. *J. Am. Water Resour. Assoc. 34 (1), 73-89*

Arnold, J. G., J. R. Kiniry, R. Srinivasan, J. R. Williams, E. B. Haney, S. L. Neitsch (2011): Soil and Water Assessment Tool Input/Output File Documentation Version 2009, *Grassland, Soil and Water Research Laboratory – Agricultural Research Service, Blackland Research Centre – Texas Agrilife Research.* T*exas Water Resources Institute Technical Report No. 365, September 2011.*

Arnold, ,J. G., D. N. Moriasi, P. W. Gassman, K. C. Abbaspour, M. J. White, R. Srinivasan, C. Santhi, R. D. Harmel, A. van Griensven, M. W. Van Liew, N. Kannan, M. K. Jha (2012): SWAT: MODEL USE, CALIBRATION, AND VALIDATION, *Transactions of the ASABE, Vol. 55(4): 1491-1508 2012 American Society of Agricultural and Biological Engineers ISSN 2151-0032*

Baldyga, T.J., S.N. Miller, K.L. Driese and C.M. Gichamba (2007): Assessing land cover change in Kenya's Mau forest region using remotely sensed data, *Afr. J. Ecol. 46, 46-54*

Bates, B.C., Kundzewicz, Z.W., Wu, S. and Palutikof, J.P, Eds., (2008): Climate Change and Water, *Technical Paper of the Intergovernmental Panel on Climate Change, IPCC Secretariat, Geneva, 210pp*

Blasone, (2007): Parameter Estimation and Uncertainty Assessment in Hydrological Modelling, *PhD Thesis, Institute of Environment & Resources, Technical University of Denmark*

Bosshard, T., M. Carambia, K. Goergen, S. Kotlarski, P. Krahe, M. Zappa, and C. Schar (2013): Quantifying uncertainty sources in an ensemble of hydrological climate-impact projections, *Water Resour. Res., 49, doi: 10.1029/2011WR011533*

Brissette, F. P., M. Khalili, R. Leconte (2007): Efficient stochastic generation of multi-site synthetic precipitation data, *Journal of Hydrology (2007) 345, 121– 133*

Bubb, P., May, I., Miles, L. Sayer, J. (2004): Cloud Forest Agenda. *UNEP-WCMC, Cambridge, UK, 36*

CCC, (2009): Generation of PRECIS scenarios for Bangladesh (Validation and Parameterization), *Climate Change Cell, DoE, MoEF; Component 4b, CDMP, MoFDM. Month 2009, Dhaka, 84*

Comber, A.J., (2007): The Identification of Data Primitives to Separate the Concepts and Semantics of Land Cover and Land Use: The Example of 'Forest'. In *Proceedings of 5th International Symposium of Spatial Data Quality (ed. Alfred Stein), 13th-15th June, Enschede, 7*

Creed, I. F, A. T. Spargo, J. A. Jones, J. M. Buttle, M. B. Adams, F. D. Beall, E. G. Booth, J. L. Campbell, D. Clow, K. Elder, M. B. Green, N. B. Grimm, C. Miniat, P. Ramlal, A. Saha , S. Sebestyen, D. Spittlehouse, S. Sterling, M. W. Williams, R. Winkler and H. Yao (2014): Changing Forest Water Yields in Response to Climate Warming: Results from Long-Term Experimental Watershed Sites Across North America, *Global Change Biology (2014), doi: 10.1111/gcb.12615, 18*

Christensen, J.H., B. Hewitson, A. Busuioc, A. Chen, X. Gao, I. Held, R. Jones, R.K. Kolli, W.-T. Kwon, R. Laprise, V. Magaña Rueda, L. Mearns, C.G. Menéndez, J. Räisänen, A. Rinke, A. Sarr and P. Whetton, (2007): Regional Climate Projections. In: *Climate Change 2007: The Physical Science Basis. Contribution of Working Group I to the Fourth Assessment Report of the Intergovernmental Panel on Climate Change* [Solomon, S., D. Qin, M. Manning, Z. Chen, M. Marquis, K.B. Averyt, M. Tignor and H.L. Miller (eds.)]. Cambridge University Press, Cambridge, United Kingdom and New York, NY, USA, *847-871*

Di Baldassarre, G., M. Elshamy, A. van Griensven, E. Soliman, M. Kigobe, P. Ndomba, J. Mutemi, F. Mutua, S. Moges, Y. Xuan, D. S. and S. Uhlenbrook (2011): Future Hydrology and Climate in the River Nile Basin: A Review, *Hydrological Sciences Journal, 56: 199-211*

DRSRS/KFWG (2006): Changes in forest cover in Kenya's Five Water Towers: 2003–2005; a presentation by the Department of Resource Surveys and Remote sensing, and Kenya forests Working Group with support from the Royal Netherlands Embassy, November 2006, *1-28.*

Droogers, P, Mantel, S. Kauffman, S. (2006): River Basin Models to support Green Water Credit Assessments, (DRAFT): Sponsored by: *IFAD, World Soil Informat, SEI–Stockholm Environment, Institute, Future Water Science for Solutions, 25*

Edwards, K.A and J.R. Blackie (1979): The Kericho Tea Research Project. *East African Agricultural and Forestry Journal, Special Issue, 1979, 44-50*

FAO, (2008): Forests and Water; A Thematic Study Prepared in the Framework of the Global Forest Resources Assessment 2005; *Forestry Paper 155, Rome, 92*

FAO, (2006): Global Forest Resources Assessment 2005; Progress towards Sustainable Forest Management, Food and Agriculture Organisation of the United Nations *Forestry Paper 147, Rome, 350*

Farid, R. (2008): GIS, Remote Sensing and Image Processing in Studying Urban Systems, *http://rashidfaridi.com/2008/02/09/gis-remote-sensing-and-image-processing-in-studying-urban-systems/ (29/03/2014*

Forster, P., V. Ramaswamy, P. Artaxo, T. Berntsen, R. Betts, D.W. Fahey, J. Haywood, J. Lean, D.C. Lowe, G. Myhre, J. Nganga, R. Prinn, G. Raga, M. Schulz and R. Van Dorland, (2007): Changes in Atmospheric Constituents and in Radiative Forcing. *In: Climate Change 2007: The Physical Science Basis. Contribution of Working Group I to the Fourth Assessment Report of the Intergovernmental Panel on Climate Change [Solomon, S., D. Qin, M. Manning, Z. Chen, M. Marquis, K.B. Averyt, M.Tignor and H.L. Miller (eds.)]. Cambridge University Press, Cambridge, United Kingdom and New York, NY, US, 129-234*

Gasman P. W., M. R. Reyes, C. H. Green, J. G. Arnold (2007): The Soil and Water Assessment Tool: Historical Development, Applications, and Future Research Directions. *American Society of Agricultural and Biological Engineers, vol. 50 (4): 1211-1250*

Gereta, E.J., E. Wolanski and E.A.T. Chiombala (2003): Assessment of the Environmental, Social and Economic Impacts on the Serengeti Ecosystem of the Developments in the Mara River in Kenya, *Frankfurt Zoological society, January, 2003, 59*

Githui, F.W., (2008): Assessing the Impacts of Environmental change on the Hydrology of the Nzoia Catchment in the Lake Victoria Basin, *PhD Thesis, Vrije Universiteit – Brussels, 1-142*

Glavan, M. and Pintar M. (2012): Strengths, Weaknesses Opportunities and Threats of Catchment Modelling With Soil and Water Assessment Tool (SWAT) Model, *Water Resources Management and Modelling, Dr. Purna Nayak (Ed.), ISBN: 978-953-51-0246-5, InTech, Available from http:www.intechopen.com/books/water-resources-management-and–modeling/strengths-weaknesses-opportunities-and-threats-of–catchment-modeling-with-soil-and-water-assessment*

GOK, (2010a): Rehabilitation of the Mau Forest Ecosystem Programme; *Prepared by the Interim Co-ordinating Secretariat, Office of the Prime Minister, on Behave of the Government of Kenya, with Support from the United Nations Environment Programme, April 2010, 260*

GOK, (2010b): The Constitution of Kenya (2010), *Published by the National Council for Law reporting with the authority of the Attorney General, 47*

GOK, (2007): Kenya Vision 2030; Vision 2030, a competitive and prosperous Kenya. Government printers, Nairobi, *20*

GOK, (2005): Kenya Gazette Supplement, Acts, 2005; The Forest Act (2005), Kenya Gazette Supplement No. 88 (Acts No. 7), Special Issue, Government printers, *234 - 279*

GOK, (2002): Kenya Gazette Supplement, Acts, 2002; The Water Act (2002), Kenya Gazette Supplement No. 107 (Acts No. 9), Special Issue, Government printers, *940 – 976*

GOK, (2000): The environmental Management and Co-ordination Act. 1999 No. 8 of 1999, *Government Printers 15-19*

GOK, (1999): Sessional Paper Number 1 of 1999 on National Policy on Water Resources Management and Development, *Ministry of Water Resources, 64*

Hasanean, H. M., and H. A. Basset (2006): Variability of summer temperature over Egypt. *Int. J. Climatol. 26: 1619-1634 (2006)*

Helsel, D.R and R.M. Hirsch (2002): Statistical Methods in Water Resources; Techniques of Water-Resources Investigations of the United States Geological Survey, Book 4, Hydrologic Analysis and Interpretation, *209-291*

Hewlett, J. D. and Helvey, J. D. (1970): Effects of forest clear-felling on the storm hydrograph: Forest Hydrology; commentary by: DeWalle, D. R. (2011), *Benchmark Papers in Hydrology, (7), 104-115*

Hoover, M. D. and Hursh, C. R. (1943): Influence of topography and soil-depth on runoff from forest land: Streamflow Generation Processes; commentary by: Beven, K. J (2006), *Benchmark Papers in Hydrology, (1), 43-48*

Hynes, H. B. N (1975): The stream and its valley: Riparian Zone Hydrology and Biogeochemistry; commentary by: Burt, T. P, Pinay G. , Sabaster S (2010), *Benchmark Papers in Hydrology, (5) 26-41*

Ininda J.M (1995): Simulations of the Impact of Sea Surface Temperature Anomalies on the Short Rains over East Africa. *J. African Meteo. Soc., 3, 1, 127-140*

IPCC, (2000): IPCC Special report: Emissions' Scenarios, summary to policy makers: *A special report of IPCC working group III; Published for the Intergovernmental Panel on Climate Change, 27*

IPCC, (2007): Climate Change 2007: The Physical Science Basis. Contribution of Working Group I to the Fourth Assessment Report of the Intergovernmental Panel on Climate Change (Solomon et al). *Cambridge University Press, Cambridge, United Kingdom and New York, NY, 93-217*

Islam, M. N., M. Rafiuddin, A. U. Ahmed and R. K. Kolli (2008): Calibration of PRECIS in Employing Future Scenarios in Bangladesh *Int. J. Climatol. Vol. 28 (5) 617-628*

Jacobs, J.H., Angerer, J., Srinivasan, R., and Kaitho, R. (2007): Mitigating Economic Damage in Kenya's Upper Tana River Basin: An Application of Arc-View SWAT. *Journal of Spatial Hydrology, Vol. 7, No. 1, Spring 2007, 23-46*

Jayakrishnan, J., Srinivasan, R., Santhi, C., and Anald, J.G. (2005): Advances in the Application of the SWAT Model for Water Resources Management, *Hydrological Processes.19, 749-762 (2005), Wiley Interscience, John Wiley and Sons Limited*

JICA, (2013): The Project on the Development of the National Water Master Plan 2030, *Final Report Volume –I, Executive Summary, October 2013, Ex-46-Ex-65*

JICA, (1987): Water resources /transportation / Energy. The study of integrated Regional Development master plan for the Lake Basin Development area, *Final report Vol. 5, sector report 3, (7-1) – (7-113)*

JICA, (1992): Sectoral Report (B) Hydrology: The Study on the National Water Master Plan, January 1992, *(B-1) – (B-49)*

Jones, R.G., Noguer, M., Hassle, G.G., Hudson, D., Wilson, S.S., Jenkins, G.J. Mitchell, J.F.B., (2004): Generating High Resolution Climate Change Scenarios Using PREIS, *Met Office Hadley Centre, Exeter, UK, 44pp, April 2004*

Kiangi, P.M.R., M.M. Kavishe, and J.K. Patnaik (1981): Some Aspects of the Mean Tropospheric Motion Field in East Africa during the Long Rains Season. *Kenya J. of Sci. and Tech. (A), 2, 91-103*

Kienzle, S.W. and Mueller M. (2013): Mapping Alberta's Surface Water Resources for the period 1971-2000. The Canadian Geographer, Volume 57, Issue 4, 506–518

KIFCON, (1994): Forest inventory report No. 1_South Western Mau and Transmara, *Karura Forest station, Nairobi, 50*

Kilavi, M.K (2008): Assessing the Temporal Characteristics of Extreme Temperature Events over ASALS and the Coastal Regions of Kenya as an Indicator of Climate Change. *MSc. Dissertation, University of Nairobi, Kenya, 20-21*

Kinyanjui, J.M., (2009): The effect of human encroachment on the forest cover, composition and structure in the western blocks of the Mau forest complex, *PhD thesis, Egerton University, Kenya, 128*

Kinyanjui, J.M., (2010): NDVI-based vegetation monitoring in Mau forest complex, Kenya. *Afr. J. Ecol., 49, 165-174*

Krause P., D.P. Boyle and F. Base (2005): Comparison of Different Efficiency Criteria for Hydrological Model Assessment *Advances in Geosciences, 5, 89-97.*

KTWA, (2013): Rapid Assessment of the Mau forest water tower, a report of the Kenya Water Towers Agency (KWTA) detailing the status of the land cover, land cover change and associated hydrological trends in the Mau forest water tower in the period 1990-2013***, 51***

Kumi-Boateng, B. and I. Yakubu (2010): Assessing the Quality of Spatial Data. E*uropean journal of scientific research, ISSN1450-216X Vol.43 No.4 (2010), 507-515*

Kundzewicz, Z.W., L.J. Mata, N.W. Arnell, P. Döll, P. Kabat, B. Jiménez, K.A. Miller, T. Oki, Z. Sen and I.A. Shiklomanov, (2007): Freshwater resources and their management. Climate Change 2007: Impacts, Adaptation and Vulnerability. Contribution of Working Group II to the Fourth Assessment Report of the Intergovernmental Panel on Climate Change, M.L. Parry, O.F. Canziani, J.P. Palutikof, P.J. van der Linden and C.E. Hanson, Eds., *Cambridge University Press, Cambridge, UK, 173-210*

Le Treut, H., R. Somerville, U. Cubasch, Y. Ding, C. Mauritzen, A. Mokssit, T. Peterson and M. Prather, (2007): Historical Overview of Climate Change. In: *Climate Change 2007: The Physical Science Basis. Contribution of Working Group I to the Fourth Assessment Report of the Intergovernmental Panel on Climate Change* [Solomon, S., D. Qin, M. Manning, Z. Chen, M. Marquis, K.B. Averyt, M. Tignor and H.L. Miller (eds.)]. *Cambridge University Press, Cambridge, United Kingdom and New York, NY, USA, 93-127*

Liebscher, H. J. (2009): The Role of Hydrology in Water Resources Management (Proceedings of a Symposium Held on the Island of Capri, Italy, October 2008) *IAHS Publ. 327, 2009. 1-6*

Liersch, S. (2003): The Program pcpSTAT, User's Manual, *Berlin, August 2003, 5*

Maidment, D.R (1993): A Handbook of Hydrology. *McGraw-Hill Inc., New York.*

Mango, L. M., A. M. Melesse, M. E. McClain, D. Gann, and S. G. Setegn (2011): Land use and climate change impacts on the hydrology of the upper Mara River Basin, Kenya: results of a modeling study to support better resource management, *Hydrol. Earth Syst. Sci., 15, 2245–2258*

Mauser, W. and T. Marke (2009): Climate Change and Water Resources: Scenarios of Low-Flow Conditions in the Upper Danube River Basin; *The role of hydrology in water resources management (proceedings of a symposium held on the island of Capri, Italy, October 2008). IAHS Publ. 327, 2009, 225 - 236*

McBean, E. and H. Motiee (2008): Assessing the Impacts of Climate Change on Water Resources: a long term analysis of the Great Lakes of North America, *Journal of Hydrology and Earth System Sciences, 12, 239-258*

Melesse A. (2006): Soil Water Assessment Tool (SWAT) model input. *Caribbean Coastal Scenarios Project Meeting, Miami, FL, Jan 30 – 31, 2006 17*

Met Office, (2007b): Climate Research at the Met Office Hadley Centre; *Informing Government policy into the future; FitzRoy Road, Exeter, Devon, EX1 3PB, United Kingdom, 15*

Met Office, (2008): Regional climate prediction (PRECIS), *Met office, FitzRoy Road, Exeter, Devon, EX1 3PB, United Kingdom, 2*

Met Office, (2009): Designing and Evaluating Regional Climate Model Experiments; *PRECIS workshop, Vietnam, 28th September-1st October 2009, 41*

Met Office, (2002): The Hadley Centre Regional Climate Modelling System: PRECIS–Update 2002; Providing Regional Climate for Impacts Studies, *20*

Miller, K. and D. Yates (2005): Climate Change and Water Resources: A Primer for Municipal Water Providers, jointly sponsored by AWWA and UCAR, *94*

Miller, S.N., D.J. Semmens, D.C. Goodrich, M. Hernandez, R.C. Miller, W.G. Kepner and D.P. Guertin (2007): The Automated Geospatial Watershed Assessment Tool, *Environmental modelling and software 22 (2007) 365-377*

Mirus, B. B., K. Loague, N. C. Cristea, S. J. Burges, S. K. Kampf (2011): A synthetic hydrologic-response dataset, J. *Hydrol. Process, (2011)*

Mitchell, J.F.B., T.C. Johns, M. Eagles, W.J. Ingram and R.A. Davis (1999): Towards the Construction of Climate Change Scenarios. Climate Change, 41, 547-581, *Kluwer academic publishers, Printed in the Netherlands*

Mogaka, H., Gichere, S., Davis, R. and Hirji, R. (2006): Climate Variability and Water Resources Degradation in Kenya: Improving water resources development and Management: *World Bank Working paper No. 69, Washington, D.C, 130*

Moore, D. S., and G. P MaCabe (1989): Introduction to the Practice of Statistics, *W. H. Freeman snd Company, New York, 653-684*

Moriasi, D.N., J.G. Arnold, M.W. Van Liew, R.L. Bingner, R.D. Harnel, T.L. Veith (2007): Model Evaluation Guidelines for Systematic Quantification of Accuracy in Watershed Simulations, *Transactions of the ASABE, 2007 American Society of Agricultural and Biological Engineers ISSN 0001-2351, Vol. 50(3): 885-900*

Muhati, D. F., Ininda, J.M., Opijah F.J., (2008): Simulation of impacts of deforestation on the rainfall in Lake Victoria basin. *Journal of the Kenya Meteorological Society 2(2) 125 – 131*

Muthama, N.J., Manene, M.M., Ndetei, C.J. (2008): Simulation of Decadal Precipitation over Nairobi in Kenya. *SQU Journal for Science, 13 (2008) 43-54*

Mutua, F.M. (1986): On the Identification of Optimum Flood Frequency Model, PhD. Thesis, University of Nairobi, *1-52*

Nam, W. H, Choi, J. Y, Hong, E.M. Kim H. K. (2010): Development of web-GIS based SWAT data generation system. 2010 international SWAT conference and workshops, Aug 4-6, 2010, Seoul Korea

Ndomba, P., F. Mtalo, and A. Killingtveit (2008): SWAT model application in a data scarce tropical complex catchment in Tanzania, Journal of *Physics and Chemistry of the Earth, 33, 626–632*

Neitsch S. L., J. G. Arnold, J. R. Kiniry, J. R. Williams (2011): Soil and Water Assessment Tool Theoretical Documentation Version 2009. *Grassland Soil and Water Research Laboratory – Agriculture Research Service Blackland Research Centre – Texas AgriLife Research, 596*

Nicks, A. D., (1974): Stochastic Generation of the Occurrence, Pattern, and Location of Maximum Amount of Daily Rainfall. *In: Proc. Symp. Statistical Hydrology, Aug-Sept. 1971, Tucson, Arizona, U.S. Dept. Agri, Misc. Publ. No. 1275, 154-171*

Nyakwanda W., Ogallo L. A, and Okoola R. E (2009): The Atlantic-Indian Ocean Dipole and its influence on East african seasonal rainfall, *Journal of Meteorology and Related Sciences, Kenya Meteorological Society, J. Meteorol. Rel., 3 3-12*

Nyangaga J. M., (2008): The Effects of Environmental Degradation on the Stream Flow, Volume and Turbidity in the Itare Sub-Catchment within the Lake Victoria Drainage Basin in Kenya. *Ph.D Thesis, University Of Nairobi, 110*

Okoola, R.E (1996): Space-Time Characteristics of the ITCZ over Equatorial Eastern Africa during Anomalous Years. *Phd Thesis, Department of Meteorology, University of Nairobi*

Omeny, P.A., L. Ogallo, R. Okoola, H. Hendon and M. Wheeler, (2008): East African Rainfall Variability Associated with the Madden-Julian Oscillation, *Journal of Kenya Meteorological Society, A Journal in Meteorology and Related Sciences, Volume 2, Numbers 1-2, October 2008, 105-114*

Omondi, P.A., (2010): Teleconnections between Decadal Rainfall Variability and Global Sea Surface Temperatures and Simulations of Future Climate Scenarios Over East Africa. *PhD Thesis, University of Nairobi Kenya: 1-23*

Opere, A.O, (1998): Space-Time characteristics of stream flow in Kenya. *PhD Thesis, University of Nairobi Kenya: 1-23.*

Ponce, V. M. and R. H. Hawkins (1996): Runoff curve number: Has it reached maturity? *Journal of Hydrologic Engineering 1(1):11-19*

Pryde, J. K., J. Osorio1, M.L. Wolfe1, C. Heatwole1, B. Benham, A. Cardenas (2007): Comparison of watershed boundaries derived from SRTM and ASTER digital elevation datasets and from a digitized topographic map, *An ASABE Meeting Presentation, Paper Number: 072093, Written for presentation at the 2007 ASABE Annual International Meeting Sponsored by ASABE Minneapolis Convention Center Minneapolis, Minnesota 17 - 20 June 2007*

Rummukainen, M. (2010): State –of-the-art with regional climate models; *Advanced Review, WIREs Climate Change 2010 I, 82-96*

Rwigi, S.K, (2004): Comparative Case Study of Rainfall - Runoff Models over the Nyando River Basin. *MSc Thesis, University of Nairobi, Kenya: 18 – 22.*

Sabiiti, G. (2008): Simulation of Climate Scenarios over the Lake Victoria Basin Using the PRECIS Regional Climate Model. *MSc Dissertation, University of Nairobi, Kenya: 29-46*

Sang, (2005): Modelling the Impact of Changes in Landuse, Climate and Reservoir Storage on Flooding in the Nyando Basin, *Msc Thesis, Jomo Kenyatta University of Science and Technology*

Salas J.D (1993): Analysis and Modelling of Hydrologic Time Series. *Handbook of Hydrology, maidment d.r, editor in chief, McGraw-Hill, inc. 19.1-19.72*

Schuol, J., R. C. Abbaspour, R. Srinivasan, H. Yang (2008): Estimation of Fresh Water Availability in the West African Sub-Continent Using the SWAT Hydrologic Model, *Journal of hydrology (2008) 352, 30-39*

Setegn, S.G., R. Srinivasan, B. Dargahi (2008): Hydrological Modelling in Lake Tana Basin, Ethiopia Using SWAT Model. *Open Hydrology Journal, 2008, 2, 49-62*

Sexton, A. M., A. M. Sadeghi, X. Zhang, R. Srinivasan, A. Shirmohammadi (2010): Using Nexrad and Rain Gauge Precipitation Data for Hydrologic Calibration of Swat in a Northeastern Watershed, *Transactions of the ASABE Vol. 53(5): 1501-1510 2010, American Society of Agricultural and Biological Engineers ISSN 2151-0032*

Thompson, J.A., J. C. Bell, C. A. Butler (2001): Digital elevation model resolution: effects on terrain attribute calculation and quantitative soil-landscape modelling, *Geoderma 100 (2001). 67–89, Elsevier Science B.V*

Trenberth, K.E., P.D. Jones, P. Ambenje, R. Bojariu, D. Easterling, A. Klein Tank, D. Parker, F. Rahimzadeh, J.A. Renwick, M. Rusticucci, B. Soden and P. Zhai, (2007): Observations: Surface and Atmospheric Climate Change. In: *Climate Change 2007: The Physical Science Basis. Contribution of Working Group I to the Fourth Assessment Report of the Intergovernmental Panel* *on Climate Change [Solomon, S., D. Qin, M. Manning, Z. Chen, M. Marquis, K.B. Averyt, M. Tignor and H.L. Miller (eds.)]. Cambridge University Press, Cambridge, United Kingdom and New York, NY, US, 102*

Tucker C.J., J.R.G. Townshend, T.E. Goff (1985): African Land Cover Classification Using Satellite Data, *SCIENCE, Vol. 227, No. 4685, Jan. 1985, 369-375*

UNEP (2009a): “Kenya: Atlas of Our Changing Environment.” Division of Early Warning and Assessment (DEWA), *United Nations Environment Programme (UNEP), P.O. Box 30552, Nairobi 00100, Kenya pp 1 - 48*

UNEP, (2009b): Climate Change Science Compendium 2009, edited by Mcmullen C.P. and Jabbour J. *72*

UNEP/GOK, (2008): Mau Complex and Marmanet Forests: Environmental and Economic Contributions, Current Trends, Briefing *notes compiled by the team that participated in the reconnaissance flight on 7 May 2008, in consultation With relevant government departments, 33*

UNEP/KFWG, (2006): Eastern and South West Mau forest reserves; Assessment and way Forward; a presentation by: A presentation by United Nations Development Programme, *Kenya Forest Working Group, Department of Resource Surveys and Remote Sensing, EU – Biodiversity conservation Programme, 36*

UNEP/KWS/KFWG/ENSDA (2008): Mau complex under siege; Values and Threats; *A presentation by United Nations Development Programme, Kenya Wildlife Service, Kenya Forest Working Group, and Ewaso Nyiro Wouth Development Authority, May 2008, 25*

UNEP/ IVM (1998): Handbook on Methods for Climate Change Impact Assessment and Adaptation Strategies*; Edited by J.F. Feenstra, I. Burton, J.B. Smith, R.S.J. Tol, Version 2.0, October, 1998, 464*

UNESCO, (2000): Decision Time for Cloud Forests: Water-Related Issues and Problems of the Humid Tropics and other Warm Humid Regions IHP *Humid Tropics Programme Series No. 13*

UNFCCC, (2005): Compendium on methods and tools to evaluate impacts of, and vulnerability and adaptation to, climate Change, Final draft report; *UNFCCC Secretariat, Stratus Consulting Inc. January, 2005, 155*

USGS (2004): Shuttle Radar Topography Mission, 1 Arc Second scene SRTM_u03_n008e004, Unfilled Unfinished 2.0, *Global Land Cover Facility, University of Maryland, College Park, Maryland, February 2000.*

Van Liew, M.W. and T.L Veith, (2005): Guidelines for Using Sensitivity Analysis and Aut-Calibration Tools for Multi-Gage or Multi-Step Calibration in SWAT, *heartlandwq.iastate.edu, 30*

Van Griensven, A., P. Ndomba, S. Yalew, and F. Kilonzo (2012): Critical Review of SWAT Applications in the Upper Nile Basin Countries, *Hydrol. Earth Syst. Sci., 16, 3371–3381*

Van Griensven, A (2005): Sensitivity, Auto-Calibration, Uncertainty and Model Evaluation in SWAT2005 (DRAFT), *a.vangriensven@unesco-ihe.org*

Veith, T.L., Ghebremichael, L.T, (2009): How To: Applying and Interpreting the SWAT Auto-Calibration Tools. *In: Proceedings of the Soil and Water Assessment Tool International Conference, August 5-7, 2009, Boulder, Colorado. 26-33*

Whitehead P.G, Wilby R.L, Butterfield D, and Wade A.J, (2006): Impacts of climate change on in-stream nitrogen in a lowland chalk stream: *An appraisal of adaptation strategies. Journal of Science of the Total Environment, 365: 260-273*

Wilby, R. and K. Miller (2009): Technical Paper (3): Climate Models and Scenarios. *Water Research foundation and sponsors (UKWIR, WERF and NCAR), 2*

Wilks, D.S, (2006): Statistical Methods in the Atmospheric Sciences, *Second Edition. International Geophysics Series, Elsevier Oxford, UK 649*

Wilson, S., D. Hassel, D. Hein, R. Jones and R. Taylor (2009): Installing and using the Hadley Centre regional climate modelling system, PRECIS; version 1.8.2, precis.metoffice.com, September 11, 2009, *167*

Winchel M., R. Srinivasan, M. Di Luzio, J. Arnold (2010): ArcSWAT Interface for SWAT 2009 User's Guide, *Grassland Research and Extension Centre, Texas Agrilife research, 720 East Blackland Road-Temple, Texas 76502 490*

WMO, (2008): Guide to Hydrological Practices, Volume I Hydrology – From Measurements to Hydrological Information. *WMO – No. 168 Sixth Edition 2008*

WMO, (2009): Guide to Hydrological Practices, Volume II Management of Water Resources and Application of Hydrological Practices. *WMO – No. 168 Sixth Edition 2009*

WMO/UNEP, (2000): IPCC Special Report-Emissions Scenarios, a Special Report of IPCC Working Group III, *ISBN: 92-9169-113-5s*

Wong, L. T., W.K. Chow (2001): Solar radiation model, *Applied Energy 69 (2001) 191–224*

WRMA/GOK, (2009): Catchment Management Strategy; Lake Victoria South Catchment Area, *71*

Young, G.J (2009): Challenges for water managers: can science help solve the problem? The role of hydrology in water resources management (proceedings of a symposium held on the island of Capri, Italy, October 2008). *IAHS Publ. 327, 2009, 9 – 17*

Zhou, Q., (1999): Digital Image Processing and Interpretation: Remote Sensing and Image Interpretation, *Department of Geography, Hong Kong Baptist University, Kowloon Tong, Kowloon, Hong Kong, 50*